Heterometallic coordination polymers : toward luminescence modulation

Xiao Fan

▶ **To cite this version:**

Xiao Fan. Heterometallic coordination polymers : toward luminescence modulation. Inorganic chemistry. INSA de Rennes, 2015. English. NNT : 2015ISAR0007 . tel-01488883v2

HAL Id: tel-01488883

https://theses.hal.science/tel-01488883v2

Submitted on 21 Mar 2017

HAL is a multi-disciplinary open access archive for the deposit and dissemination of scientific research documents, whether they are published or not. The documents may come from teaching and research institutions in France or abroad, or from public or private research centers.

L'archive ouverte pluridisciplinaire **HAL**, est destinée au dépôt et à la diffusion de documents scientifiques de niveau recherche, publiés ou non, émanant des établissements d'enseignement et de recherche français ou étrangers, des laboratoires publics ou privés.

Résumé

Les polymères de coordination décrits dans cette thèse ont été préparés en accord avec les concepts de la chimie verte par réactions dans l'eau entre les sels de sodium des ligands et les ions lanthanides compris entre La et Lu (sauf Pm) plus Y. Deux types d'échantillons ont été préparés : des monocristaux et des poudres microcristallines. Les structures cristallines ont été résolues sur la base des monocristaux et les poudres microcristallines ont été utilisées pour étudier les propriétés physico-chimiques des composés : stabilité thermique, propriétés de luminescence et de magnétisme. Dans nos travaux, quatre systèmes de polymères de coordination ont été étudiés. Ils ont été obtenus à partir de quatre acides : acide chelidonique (H_2cda), acide 5-hydroxy-isophthalique (H_2hip), acide 5-nitroisophthalique (H_2nip) et acide 4-carboxyphenylboronique (Hcpb).

Dix nouveaux monocristaux ont été obtenus par diffusions lentes en tubes en U à travers des gels physique (Agar) ou chimiques (TMOS ou TEOS), par diffusion lente en tubes en H à travers de l'eau distillée ou par évaporation lente du filtrat obtenu après la synthèse des poudres microcristallines. Les poudres microcristallines ont été classées sur la base de leurs diagrammes de diffraction des rayons-X. Leurs propriétés de luminescence ou de magnétisme ont été étudiées à l'état solide. Les transferts d'énergie intermétalliques ont été discutés, en particulier pour les ligands H_2hip et Hcpb. Les composés hétéro-nucléaires (Gd / Tb et Eu / Tb) ont été préparés pour moduler les propriétés luminescentes de ces composés en variant les proportions relatives en ions lanthanides.

Les polymères de coordination à base de terres rares synthétisés et étudiés dans ce manuscrit fournissent des informations intéressantes pour la conception future de matériaux multifonctionnels.

Abstract

According to the concepts of Green Chemistry, the coordination polymers based on lanthanide ions were prepared by reactions in water between the sodium salts of ligands and lanthanide ions comprised between La and Lu (except Pm) plus Y. Two kinds of samples were prepared : single crystals and microcrystalline powders. The former ones are used to determine the single crystal structure, and the later ones are used to measure the physical-chemical properties : thermal stability, luminescence and magnetism properties. In our work, four ligands were explored: chelidonic acid (H_2cda), 5-hydroxy-isophthalic acid (H_2hip), 5-nitroisophthalic acid (H_2nip) and 4-carboxyphenylboronic acid (Hcpb).

As a result, 10 new single crystals were obtained by slow diffusion in U-shape tubes through physical gel (agar) or chemical gels (TMOS or TEOS), by slow diffusion in H-shape tubes through distilled water or by evaporation of the filtrate obtained after the synthesis of the microcrystalline powders. Microcrystalline powders were classified on the basis of their X-ray powder diffraction patterns. Their luminescent properties and magnetic properties were studied in the solid state. Intermetallic energy transfers were also discussed. Especially, for ligands H_2hip and H_2cpb. Hetero-nuclear compounds (Gd/Tb and Eu/Tb) were also prepared to tune luminescent properties by changing the relative ratios of the lanthanide ions.

Lanthanide coordination polymers described in this thesis provide information that could be useful as far as multifunctional materials are targeted.

Xiao FAN

N° d'ordre : 15ISAR 10 / D15 -10

Institut National des Sciences Appliquées de Rennes

20, Avenue des Buttes de Coësmes • CS 70839 • F-35708 Rennes Cedex 7

Tel : 02 23 23 82 00 - Fax : 02 23 23 83 96

Thèse

2015

THESE INSA Rennes

sous le sceau de l'Université européenne de Bretagne

pour obtenir le titre de

DOCTEUR DE L'INSA DE RENNES

Spécialité : Chimie

présentée par

Xiao FAN

ECOLE DOCTORALE : *SDLM*

LABORATOIRE : *ISCR/CSM*

Heterometallic coordination polymers : toward luminescence modulation

Françoise CONAN
Professeur à Université de Bretagne Occidentale / rapporteur
Carole DAIGUEBONNE
Maître de Conférences HDR à l'INSA de Rennes / Directrice de thèse / invitée

---

Thèse soutenue le 13.03.2015
devant le jury composé de :

Pierre MIALANE
Professeur à l'Université Versailles Saint Quentin / Président / Rapporteur
Corine SIMONNET
Maître de Conférences HDR à l'Université Versailles Saint Quentin / Examinateur
Eric LE FUR
Maître de Conférences HDR à ENSC Rennes / Examinateur
Olivier GUILLOU
Professeur à l'INSA de Rennes / Examinateur / Co-encadrant

Heterometallic coordination polymers: toward luminescence modulation

Xiao FAN

En partenariat avec

Document protégé par les droits d'auteur

Abstract

According to the concepts of Green Chemistry, the coordination polymers based on lanthanide ions were prepared by reactions in water between the sodium salts of ligands and lanthanide ions comprised between La and Lu (except Pm) plus Y. Two kinds of samples were prepared: single crystals and microcrystalline powders. The former ones are used to determine the single crystal structure, and the later ones are used to measure the physical-chemical properties: thermal stability, luminescence and magnetism properties. In our work, four ligands were explored: chelidonic acid (H_2cda), 5-hydroxy-isophthalic acid (H_2hip), 5-nitroisophthalic acid (H_2nip) and 4-carboxyphenylboronic acid (Hcpb).

As a result, 10 new single crystals were obtained by slow diffusion in U-shape tubes through physical gel (agar) or chemical gels (TMOS or TEOS), by slow diffusion in H-shape tubes through distilled water or by evaporation of the filtrate obtained after the synthesis of the microcrystalline powders. Microcrystalline powders were classified on the basis of their X-ray powder diffraction patterns. Their luminescent properties and magnetic properties were studied in the solid state. Intermetallic energy transfers were also discussed. Especially, for ligands H_2hip and H_2cpb. Hetero-nuclear compounds (Gd/Tb and Eu/Tb) were also prepared to tune luminescent properties by changing the relative ratios of the lanthanide ions.

Lanthanide coordination polymers described in this thesis provide information that could be useful as far as multifunctional materials are targeted.

Résumé

Les polymères de coordination décrits dans cette thèse ont été préparés en accord avec les concepts de la chimie verte par réactions dans l'eau entre les sels de sodium des ligands et les ions lanthanides compris entre La et Lu (sauf Pm) plus Y. Deux types d'échantillons ont été préparés : des monocristaux et des poudres microcristallines. Les structures cristallines ont été résolues sur la base des monocristaux et les poudres microcristallines ont été utilisées pour étudier les propriétés physico-chimiques des composés : stabilité thermique, propriétés de luminescence et de magnétisme. Dans nos travaux, quatre systèmes de polymères de coordination ont été étudiés. Ils ont été obtenus à partir de quatre acides : acide chelidonique (H_2cda), acide 5-hydroxy-isophthalique (H_2hip), acide 5-nitroisophthalique (H_2nip) et acide 4-carboxyphenylboronique (Hcpb).

Dix nouveaux monocristaux ont été obtenus par diffusions lentes en tubes en U à travers des gels physique (Agar) ou chimiques (TMOS ou TEOS), par diffusion lente en tubes en H à travers de l'eau distillée ou par évaporation lente du filtrat obtenu après la synthèse des poudres microcristallines. Les poudres microcristallines ont été classées sur la base de leurs diagrammes de diffraction des rayons-X. Leurs propriétés de luminescence ou de magnétisme ont été étudiées à l'état solide. Les transferts d'énergie intermétalliques ont été discutés, en particulier pour les ligands H_2hip et Hcpb. Les composés hétéro-nucléaires (Gd / Tb et Eu / Tb) ont été préparés pour moduler les propriétés luminescentes de ces composés en variant les proportions relatives en ions lanthanides.

Les polymères de coordination à base de terres rares synthétisés et étudiés dans ce manuscrit fournissent des informations intéressantes pour la conception future de matériaux multifonctionnels.

Acknowledgement

First and foremost, I sincerely thank Dr. DAIGUEBONNE Carole, my supervisor and Prof. GUILLOU Olivier. I appreciate that she gave me this opportunity to pursue my Ph. D. in laboratory ISCR/CSM of UMR6226 in INSA de Rennes. Thanks for their patient and professional advices in my work. I passed more than three years and half in this excellent research team. During my PH. D. period, I got not only the chemical professional skills or knowledge but also the friendship between the colleagues. This period will affect my whole life.

Thanks to Prof. MIALANE Pierre, CONAN Françoise, Dr. SIMONNET Corine, LE FUR Eric for accepting to review this work.

The thesis can hardly be done without the help of the scientists in our laboratory and in the collaborating laboratories. I acknowledge Dr. Guillaume Calvez, Dr. Kevin Bernot and M. Stéphane Freslon for their support and help in the physical properties measurements and thanks Laurent Le Pollès for the NMR measurement.

The colleagues in the laboratory have been always friendly and patient with me since I arrived. Thanks Stéphane Freslon and Florence Le Dret for their technical support in manipulations, and thanks our secretary, Isabelle Regis, for helping me in all the things of the live. Thanks the people from the companies I-Kr and OLNICA who work and celebrate all the happiness occurring in the lab - Mélissa Laurans, Nicolas Kerbellec , Aurélien Dif and Romain Guerandel.

I enjoyed my time in INSA de Rennes with my friends and the PhD students in the lab. Thanks Berenger Aranda, Yun Luo, Amandine Rojo, Xiaohui Yi, François Le Natur, Chrystelle Neaime, Camille Tandé, Gang Huang and Insa Badiane. They are dynamic, friendly and always useful when I have some troubles. I am very grateful for the friendship of them; I will keep these memories in my heart.

My gratitude to my friends: Xingrong, Cong, Jinlin, Linning，Hongquan, Hui, Yu, Shunying, Yi, Han, Wei, Yang, Hua, Tian, Jia, Yanping and Jiali.

Special Thanks to China Scholarship Council (CSC) for financial support.

At last, thanks for the support from my family: my parents, my brother, my wife (Dandan) and my little boy (Yuncong).

Résumé étendu

1. Lanthanides.

Les lanthanides désignent le groupe des 14 éléments qui suivent le lanthane dans le tableau périodique : La (57) -Lu (71). Du fait de leurs propriétés chimiques semblables, on y ajoute généralement l'yttrium (39) et le scandium (21) pour former la famille des terres rares. Les terres rares ont la particularité d'être la plus longue série d'élément ayant des propriétés chimiques semblables. Les ions lanthanides présentent en général un degré d'oxydation caractéristique +3.

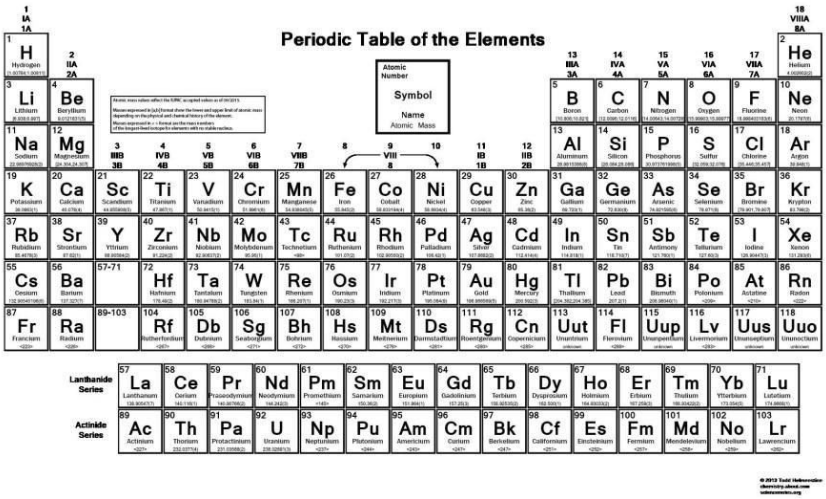

Figure R1 Tableau périodique des éléments.

2. Polymères de coordination.

Le terme de « polymère de coordination » désigne un assemblage périodique inorganique ou organométallique formé par itération de centres métalliques reliés entre eux par des ligands dans une, deux ou trois dimensions (Figure R2). Le terme anglophone de « MOF » (métal-organic framework) est souvent utilisé à la place de « polymère de coordination » pour évoquer les composés poreux ou 3D.

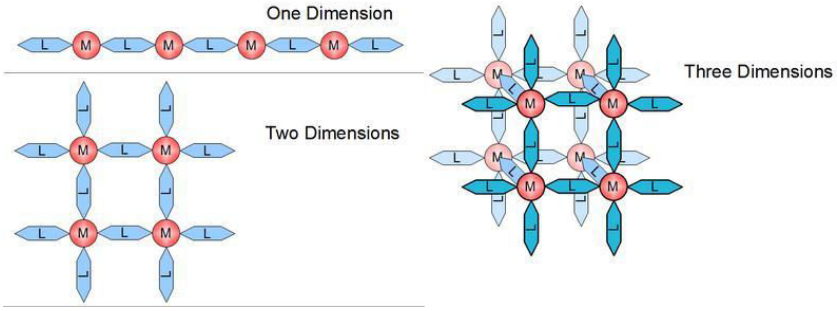

Figure R2 Polymères de coordination 1D, 2D et 3D.

3. Objectifs de nos travaux.

Notre équipe étudie les polymères de coordination à base de lanthanides depuis plus de dix ans. Nous nous consacrons à la synthèse de nouveaux polymères de coordination, l'étude de leurs propriétés physico-chimiques: thermogravimétrie, porosité, luminescence ou magnétisme. Quatre ligands ont été choisis (Figure R3) pour synthétiser les nouveaux polymères de coordination étudiés dans ce manuscrit.

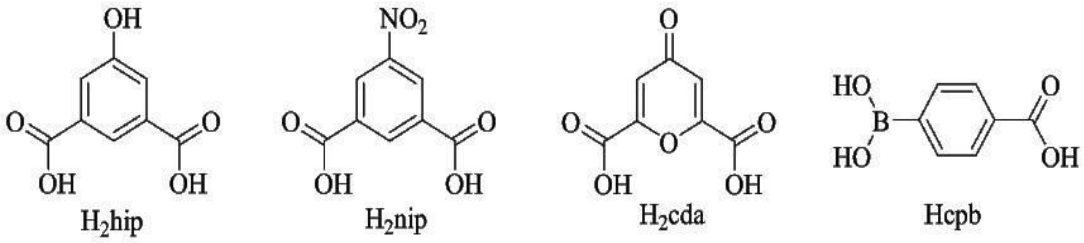

Figure R3 Les quatre ligands utilisés dans le cadre de cette thèse.

Ces composés ont été étudiés avec la méthodologie suivante :

1). La synthèse des poudres microcristalline est réalisée. Les poudres microcristallines sont classées en familles sur la base de leurs diffractogrammes de rayons X.

2). Les monocristaux de polymères de coordination sont obtenus par évaporation lente ou diffusion dans des tubes en H ou en U. Les structures cristallines sont ensuite déterminées.

3). Les diffractogrammes de rayons X des poudres microcristallines sont comparés avec les diagrammes de diffraction simulés à partir des structures cristallines. Les poudres microcristallines sont classées par familles de composés iso-structuraux.

4). Leurs propriétés physico-chimiques sont ensuite étudiées en détail.

4. Polymères de coordination à base de lanthanides et du ligand H_2cda.

Dans le chapitre 1, l'acide chelidonique (symbolisé par H_2cda) est utilisé comme ligand pour la synthèse de polymères de coordination. Après avoir préparé son sel di-sodique, les

poudres microcristallines des polymères de coordination à base de terres rares ont été synthétisées et classées en six familles (Table R1). Les structures cristallines de trois de ces familles étaient déjà connues. Seule la structure cristalline des composés qui constituent la famille 3 a pu être résolue.

Table R1 Familles de polymers de coordination à base de terres rares.

L=cda	La	Ce	Pr	Nd	Sm	Eu	Gd	Tb	Dy	Ho	Y	Er	Yb	Lu
RT														
RT														
100 °C														

Family 1	Published in *Cryst. Eng. Comm.*, **2010**, 12, 1809-1815. CCDC: 716750
Family 2	No crystal structure.
Family 3	Novel coordination polymers.
Family 4	Published in *Cryst. Eng. Comm.*, **2010**, 12, 1809-1815. CCDC: 715751
Family 5	Published in *Cryst. Growth Des.*, **2009**, 9, 4006-4016. CCDC: 748868
Family 6	No crystal structure.

Dans le cadre de ce travail, quatre nouvelles structures cristallines ont été résolues :

a). $[Na(Hcda)(H_2O)]_\infty$ qui est 2D.

b). $[Lu(cda)_{1.5}(H_2O)_5, 2H_2O]_\infty$ qui est 1D.

c). $[Yb_2(cda)_2(ox)(H_2O)_7, 6H_2O]_\infty$ qui est 1D.

d). $[Yb_2(ox)_3(H_2O)_4, 2H_2O]_\infty$ qui est 2D.

Les propriétés de luminescence des composés qui constituent les familles 2 et 6 ont été très succinctement étudiées. Les propriétés de luminescence et de magnétisme du composé $[Yb_2(cda)_2(ox)(H_2O)_7, 6H_2O]_\infty$ ont été étudiée (Figure R4 et Figure R5) plus en détail.

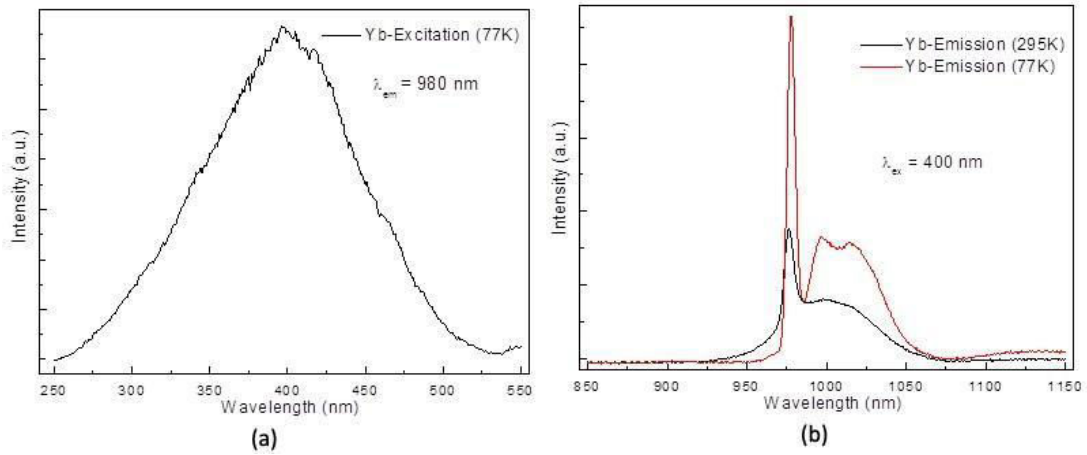

Figure R4 Spectre d'excitation à 77K et spectre d'émission à 295K et 77K du composé $[Yb_2(cda)_2(ox)(H_2O)_7, 6H_2O]_\infty$.

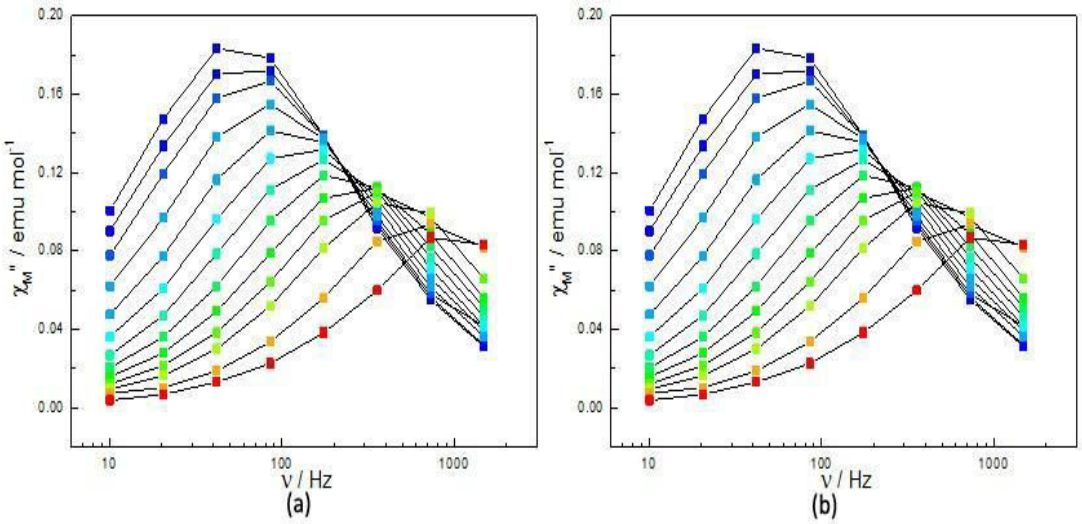

Figure R5 Dépendance en fréquence de la composante hors phase de la susceptibilité magnétique u composé $[Yb_2(cda)_2(ox)(H_2O)_7, 6H_2O]_\infty$.

5. Polymères de coordination à base de lanthanides et du ligand H_2hip.

Les poudres microcristallines obtenues à partir de l'acide 5-hydroxy-isophthalique (symbolisé par H_2hip) ont été classées en cinq familles de composés iso-structuraux. Les structures cristallines des composés constituant deux de ces familles (Famille 2 et Famille 3) ont été déterminées.

Table R2 Familles de polymères de coordination à base de terres rares.

L=hip	La	Ce	Pr	Nd	Sm	Eu	Gd	Tb	Dy	Ho	Y	Er	Yb	Lu
2°C														
RT														
100°C														

	Family 1 No crystal structure.
	Family 2 Novel coordination polymers.
	Family 3 Novel coordination polymers.
	Family 4 No crystal structure.
	Family 5 No crystal structure.

A partir du ligand H_2hip, deux nouvelles structures cristallines ont été obtenues :

a). $[Ce_2(hip)_3(H_2O)_9, 6H_2O)]_\infty$ qui est 1D.

b). $[La_2(hip)_2(H_2O)_{10}, hip), 4H_2O]_\infty$ qui est 1D.

Les propriétés de luminescence des composés homo- et hétéro-nucléaires appartenant à la famille 3 ont été étudiées en détail (Figure R6 et Figure R7).

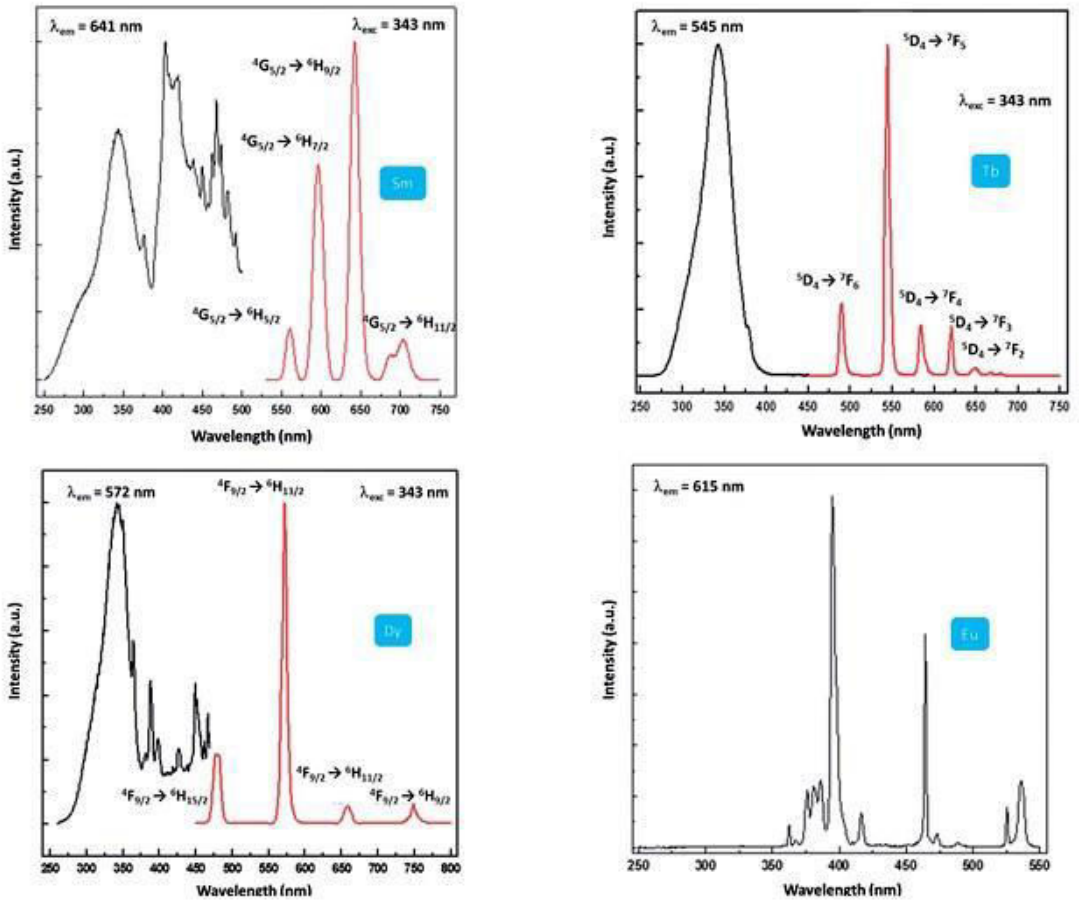

Figure R6 Spectres d'émission et excitation des composés de formule générale $[Ln_2(hip)_2(H_2O)_{10}, (hip), 4H_2O]_\infty$ (Ln=Sm, Tb and Dy) et spectre d'excitation du composé $[Eu_2(hip)_2(H_2O)_{10}, (hip), 4H_2O]_\infty$.

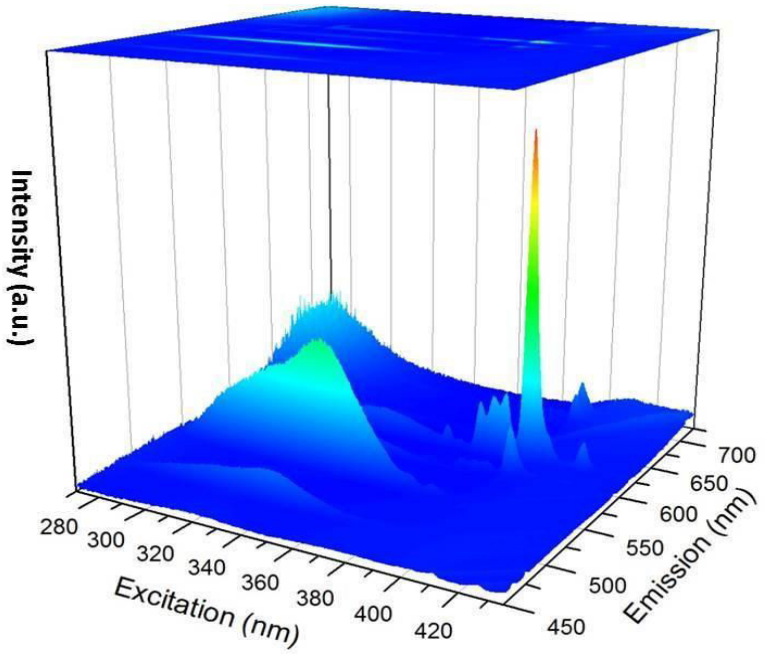

Figure R7 Excitation et émission 3D du composé $[Eu_1Tb_1(hip)_2(H_2O)_{10}, (hip), 4H_2O]_\infty$.

6. Polymères de coordination à base de lanthanides et du ligand H_2nip.

L'acide 5-nitroisophthalique (symbolisé par H_2nip) a également été utilisé comme ligand. Quatre familles de poudres microcristallines ont été obtenues.

Table R3 Familles de polymères de coordination à base de terres rares.

L=nip^{2-}	La	Ce	Pr	Nd	Sm	Eu	Gd	Tb	Dy	Ho	Y	Er	Yb
2°C													
RT													
100°C													

	Family 1 Novel coordination polymers
	Family 2 No crystal structure.
	Family 3 No crystal structure.
	Family 4 No crystal structure.

Dans ce système, deux nouvelles structures cristallines ont été obtenues :

a). $[Gd(nip)(Hnip)(H_2O)_4, 3H_2O]$ qui est 0D.

b). $[Gd_4(nip)_6(H_2O)_{14}, 5H_2O]_\infty$ qui est 1D.

Compte tenu de la proximité énergétique du premier état triplet excité du ligand et des niveaux émetteurs du Tb^{3+}, un processus de transfert en retour se produit qui empêche la luminescence du composé à base de terbium.

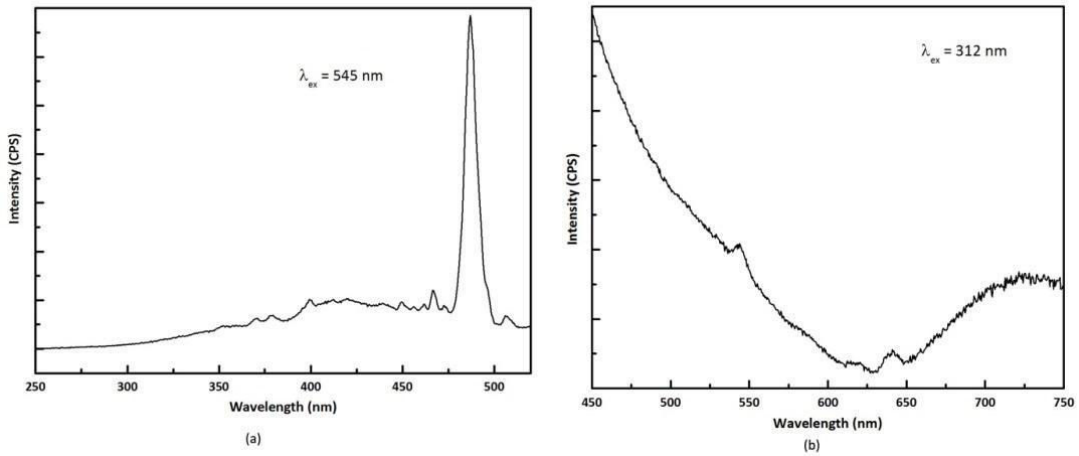

Figure R8 Spectres d'émission et excitation du composé $[Tb(nip)(Hnip)(H_2O)_4, 3H_2O]_\infty$.

7. Polymères de coordination à base de lanthanides et du ligand H_2hip.

L'acide 4-carboxyphenylboronique est un acide borique. C'est, à notre connaissance, la première fois qu'un acide borique est utilisé pour synthétiser un polymère de coordination à base de terre rare. Dans ce système, deux familles de poudres microcristallines ont été obtenues.

Table R4 Familles de polymères de coordination à base de terres rares.														
L=cpb$^-$	La	Ce	Pr	Nd	Sm	Eu	Gd	Tb	Dy	Ho	Y	Er	Yb	Lu
RT														
100°C														
	Family 1 ≡ crystal structure of $[La(cpb)_3(H_2O)_2]_\infty$.													
	Family 2 ≡ crystal structure of $[Tb(cpbOH)(H_2O)_2, (cpb)]_\infty$.													

Deux nouveaux composés ont été structuralement caractérisés :

a). $[La(cpb)_3(H_2O)_2]_\infty$ qui est 1D.

b). $[Tb(cpbOH)(H_2O)_2, (cpb)]_\infty$ qui est 2D.

Les propriétés de luminescence des composés homo- et hétéro-nucléaires qui constituent la famille 2 ont été étudiées en détail (Figure R9 et Figure R10). Les propriétés magnétiques des composés $[Dy(cpbOH)(H_2O)_2, (cpb)]_\infty$ et $[Yb(cpbOH)(H_2O)_2, (cpb)]_\infty$ ont également été étudiées (Figure R11).

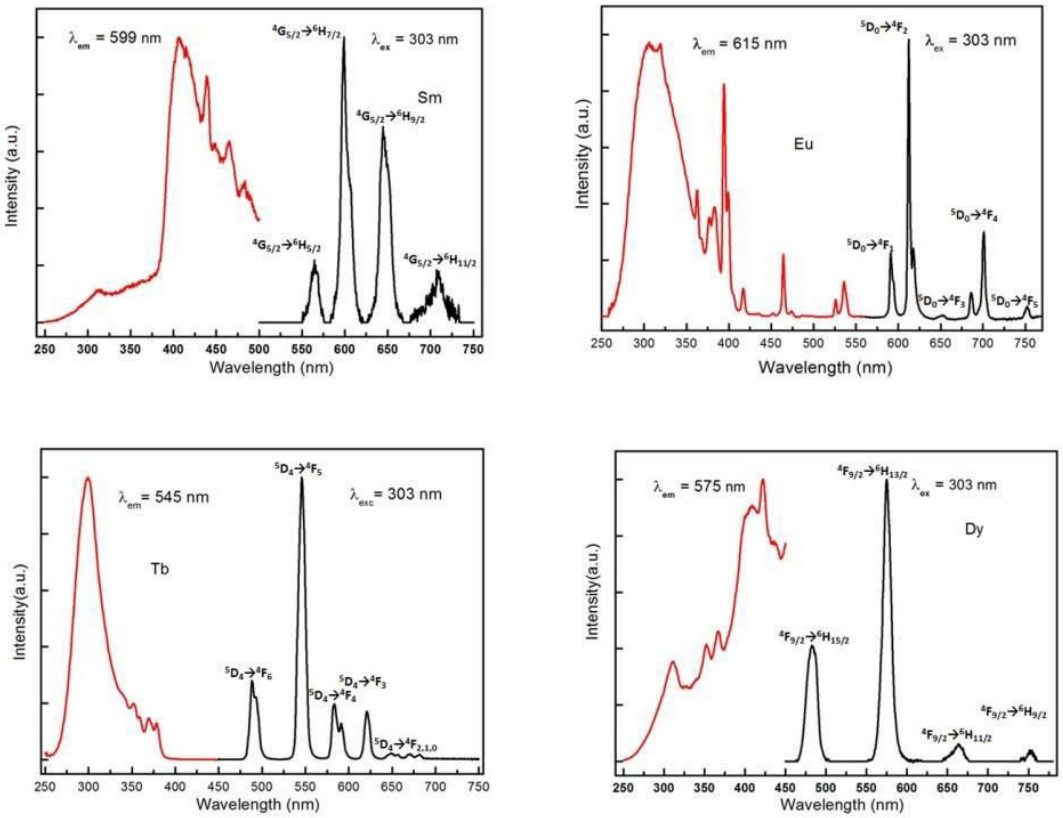

Figure R9 Spectres d'émission et excitation des composés
de formule chimique générale $[Ln(cpbOH)(H_2O)_2, (cpb)]_\infty$ (Ln=Sm, Eu, Tb and Dy).

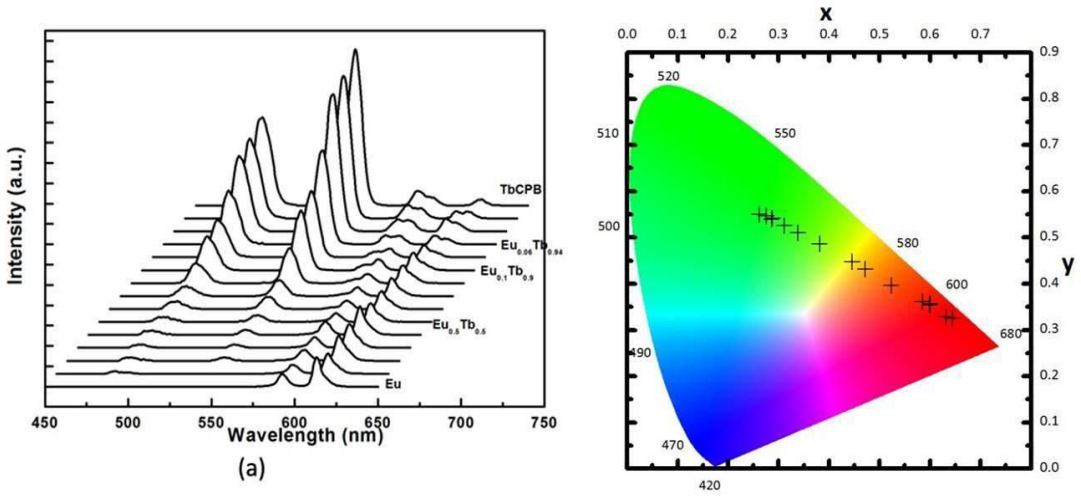

Figure R10 Spectres d'émission et coordonnées colorimétriques des composés de formules chimique générale $[Eu_{1-x}Tb_x(cpbOH)(H_2O)_2, (cpb)]_\infty$ $(0 \leq x \leq 1)$.

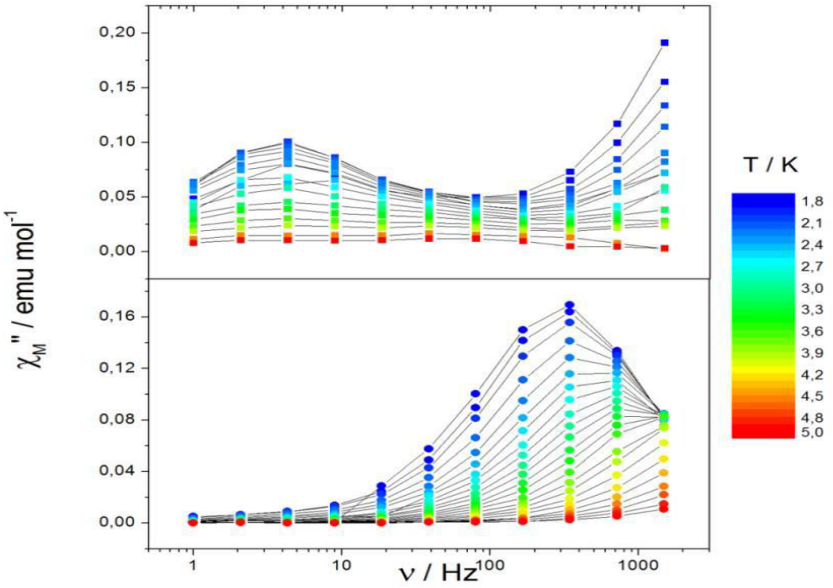

Figure R11 Dépendance en fréquence de la composante hors phase de la susceptibilité magnétique des composés $[Dy(cpbOH)(H_2O)_2,(cpb)]_\infty$ et $[Yb(cpbOH)(H_2O)_2,(cpb)]_\infty$

Conclusion

Ce travail a conduit à plusieurs polymères de coordination à base de lanthanides dont certains présentent des propriétés de luminescence ou de magnétisme intéressantes. Cette étude systématique nous a permis de mieux comprendre les mécanismes qui régissent la luminescence dans les polymères de coordination à base de lanthanides. Les résultats de cette étude pourront être utilisés par l'équipe comme une base de données pour de futurs travaux.

Contents

Introduction

According to the International Union of Pure and Applied Chemistry (IUPAC) recommendation (1968), lanthanides include elements from La (57) to Lu (71) ; when Sc (21) and Y (39) are added to the latter, then the resulting 17 elements should be termed rare earth.[1] For more than a decade, lanthanide-containing coordination polymers have attracted great attention because of their potential technological application due to their magnetic properties,[2] optical properties[3] and catalytic properties.[4] Especially, lanthanide-containing coordination polymers present bright and pure-color emission that depends on the involved lanthanide ion. Because of the inner character of their valence orbitals, lanthanide ions have similar chemical properties. It is thus possible to synthesize hetero-nuclear coordination polymers in which two or more lanthanide ions are randomly distributed over the metallic sites. This enables one to tune the intermetallic distances and therefore to modulate the color and the brightness of the emission.[5] The work described hereafter essentially consists on preparing homo-nuclear and hetero-nuclear lanthanide-containing coordination polymers and studying their luminescent properties.

Terminology of metal-organic frameworks and coordination polymers (IUPAC 2013).

Coordination polymer: An inorganic or organometallic polymer structure containing metal cations centers linked by organic ligands. More formally a coordination polymer is a coordination compound with repeating coordination entities extending in 1, 2, or 3 dimensions (Figure 1).

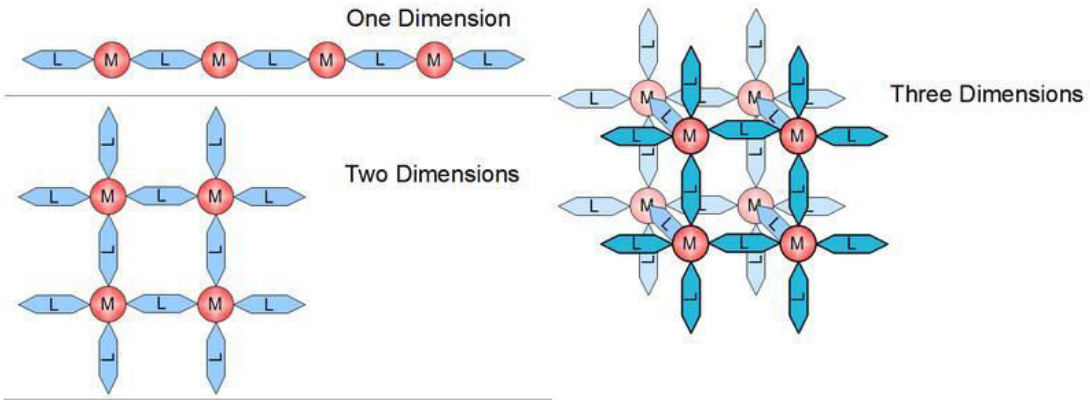

Figure 1 1D, 2D and 3D coordination polymers

Metal-organic frameworks (MOFs): A metal-organic framework, abbreviated to MOF, is a coordination polymer that presents potential voids.

Coordination number and Coordination geometry.

Coordination number (CN): The total number of points of attachment to the central element. For the lanthanide-containing coordination polymers, the coordination numbers generally range from 3 to 12.

Coordination geometry: The geometrical pattern formed by atoms around the central atom. The following table gives the coordination geometry from CN = 7 to 9 which are the common coordination numbers for lanthanide-containing coordination polymers and their site symmetry.[6]

CN=7	Shape	Symmetry
1	Heptagon	D_{7h}
2	Hexagonal pyramid	C_{6v}
3	Pentagonal bipyramid	D_{5h}
4	Capped octahedron	C_{3v}
5	Capped trigonal prism	C_{2v}
CN=8		
1	Octagon	D_{8h}
2	Heptagonal pyramid	C_{7v}
3	Hexagonal bipyramid	D_{6h}
4	Cube	O_h
5	Square antiprism	D_{4d}
6	Triangular dodecahedron	D_{2d}
7	Johnson - Gyrobifastigium (J26)	D_{2d}
8	Johnson - Elongated triangular bipyramid (J14)	D_{3h}
9	Johnson - Biaugmented trigonal prism (J50)	C_{2v}
10	Biaugmented trigonal prism	C_{2v}
11	Snub disphenoid (J84)	D_{2d}
12	Triakis tetrahedron	T_d
13	Elongated trigonal bipyramid (see 8)	D_{3h}
CN=9		
1	Enneagon	D_{9h}
2	Octagonal pyramid	C_{8v}
3	Heptagonal bipyramid	D_{7h}
4	trivacant cuboctahedron	C_{3v}
5	Capped cube	C_{4v}
6	Capped sq. antiprism	C_{4v}
7	Capped square antiprism	C_{4v}
8	Tricapped trigonal prism (J51)	D_{3h}
9	Tricapped trigonal prism	D_{3h}
10	Tridiminished icosahedron (J63)	C_{3v}
11	Hula-hoop	C_{2v}
12	Muffin	Cs

Ligands in coordination polymers.

Generally, coordination polymers are formed when ligands donate one pair of electrons to fill the orbitals of the metal cation. Thus, the ligands must be able to coordinate the metal centers and act as bridges between multiple metal centers. For effective energy transfer, the following principles should be respected: a). To achieve optimal luminescence quantum yields, a ligand with a first excited triplet state of appropriate energy should be chosen. The energy difference between the ligand's triplet state and the excited lanthanide states should be around 2500-3500 cm^{-1}. b). Excited ligand states at lower energy than excited f-states of the lanthanides do not allow ligand-to-metal energy transfer. c). At short distance (10 Å or less), when an antenna molecule is bonded to the lanthanide ion, a direct electron exchange via a Dexter mechanism is possible.

Our group has used a lot of ligands to prepare lanthanide-containing coordination polymers (Figure 2):

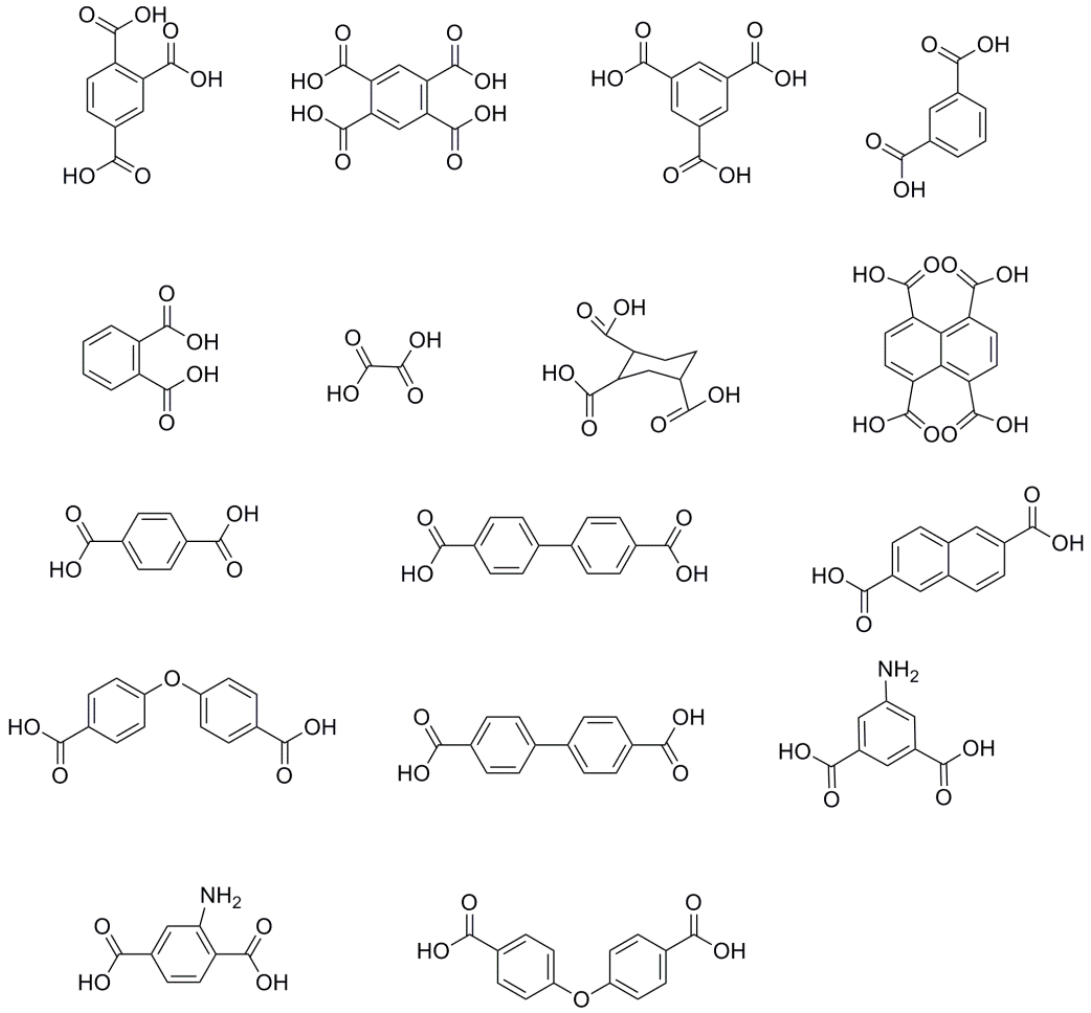

Figure 2 Ligands used by our group for preparing coordination polymers.

Coordination modes.

For carboxylates, there are 8 basic coordination modes in the coordination polymers (Figure 3):

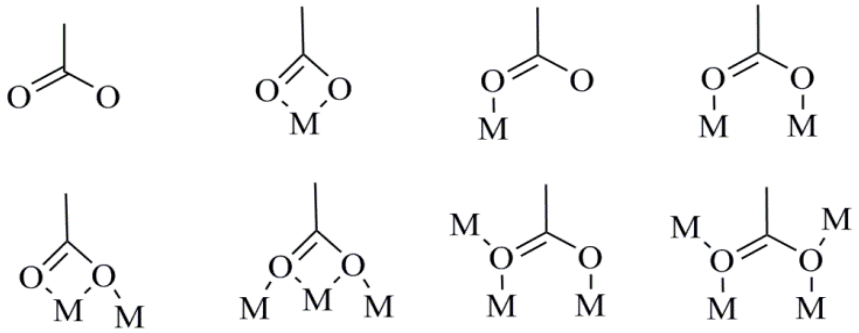

Figure 3 Basic coordination modes of carboxylate functions.

Targets of our work.

Our efforts have focused on the synthesis of lanthanide coordination polymers with novel structural characteristics and interesting physical properties.

Our work essentially consists on synthesizing new lanthanide coordination polymers with different ligands and studying their physico-chemical properties such as thermal, luminescent and magnetic properties. To achieve this objective, we have followed the strategy described below:

First, we have prepared the microcrystalline powders and classified them in different families depending on their powder X-ray diffraction patterns.

Second, single crystals were grown by different methods such as: slow diffusions trough gels in U-shaped tubes, slow diffusions in H-shaped tubes and slow evaporations.

Finally, microcrystalline powders which are iso-structural with single crystals were studied in details.

References:

[1]. Edited by N G Connelly and T Damhus (with R M Hartshorn and A T Hutton), ed. (2005). Nomenclature of Inorganic Chemistry: IUPAC Recommendations 2005. Cambridge: RSC Publ. ISBN 0-85404-438-8. Archived from the original on 2008-05-27. Retrieved 2012-03-13.

[2]. (a) X. Yi, K. Bernot, O. Cador, J. Luzon, G. Calvez, C. Daiguebonne, O. Guillou, Dalton Transactions, 42 (2013) 6728-6731. (b) X. Yi, K. Bernot, G. Calvez, C. Daiguebonne, O. Guillou, European Journal of Inorganic Chemistry, 2013 (2013) 5879-5885. (c) X. Yi, K. Bernot, V. Le Corre, G. Calvez, F. Pointillart, O. Cador, B. Le Guennic, J. Jung, O. Maury, V. Placide, Y. Guyot, T. Roisnel, C. Daiguebonne, O. Guillou, Chemistry – A European Journal, 20 (2014) 1569-1576.

[3]. (a) N. Kerbellec, C. Daiguebonne, K. Bernot, O. Guillou, X. Le Guillou, Journal of Alloys and Compounds, 451 (2008) 377-383. (b) Y. Luo, G. Calvez, S. Freslon, K. Bernot, C. Daiguebonne, O. Guillou, European Journal of Inorganic Chemistry, 2011 (2011) 3705-3716. (c) Y. Luo, G. Calvez, S. Freslon, C. Daiguebonne, T. Roisnel, O. Guillou, Inorganica Chimica Acta, 368 (2011) 170-178. (d) S. Freslon, Y. Luo, G. Calvez, C. Daiguebonne, O. Guillou, K. Bernot, V. Michel, X. Fan, Inorganic Chemistry, 53 (2014) 1217-1228.

[4]. J. Lee, O.K. Farha, J. Roberts, K.A. Scheidt, S.T. Nguyen, J.T. Hupp, Chemical Society Reviews, 38 (2009) 1450-1459.

[5]. (a) Dang, S.; Zhang, J. H.; Sun, Z. M. J. Mater. Chem. 2012, 22, 8868−8873. (b) Rodrigues, M. O.; Dutra, J. D. L.; Nunes, L. A. O.; de Sa, G. F.; de Azevedo, W. M.; Silva, P.; Paz, F. A. A.; Freire, R. O.; Junior, S. A. J. Phys. Chem. C 2012, 116, 19951−19957. (c) Le Natur, F.; Calvez, G.; Daiguebonne, C.; Guillou, O.; Bernot,K.; Ledoux, J.; Le Polles, L.; Roiland, C. Inorg. Chem. 2013, 52, 6720−6730.

[6]. (a) D. Casanova, P. Alemany, J. M. Bofill, S. Alvarez. Chem. Eur. J., 9, 1281 (2003). (b) D. Casanova, M. Llunell, P. Alemany, S. Alvarez. Chem. Eur. J., 11, 1479 (2005). (c)A. Ruiz-Martínez, D. Casanova, S. Alvarez. Chem. Eur. J., 14, 1291 (2008); Dalton Trans., 2583 (2008)

Chapter 1.
Basics of lanthanide

Chapter 1. Basics of lanthanide

IUPAC states that the lanthanide series contains the fifteen elements with atomic number comprised between 57 and 71, which is from lanthanum to lutetium.[1] In general, the fifteen elements plus the chemically similar scandium (21) and yttrium (39) are known as the rare earth elements (Figure 1.1). All the lanthanides are f-block elements except Lutetium that has the 4f electron sub-shell filled. All of them exhibit similar chemical properties.

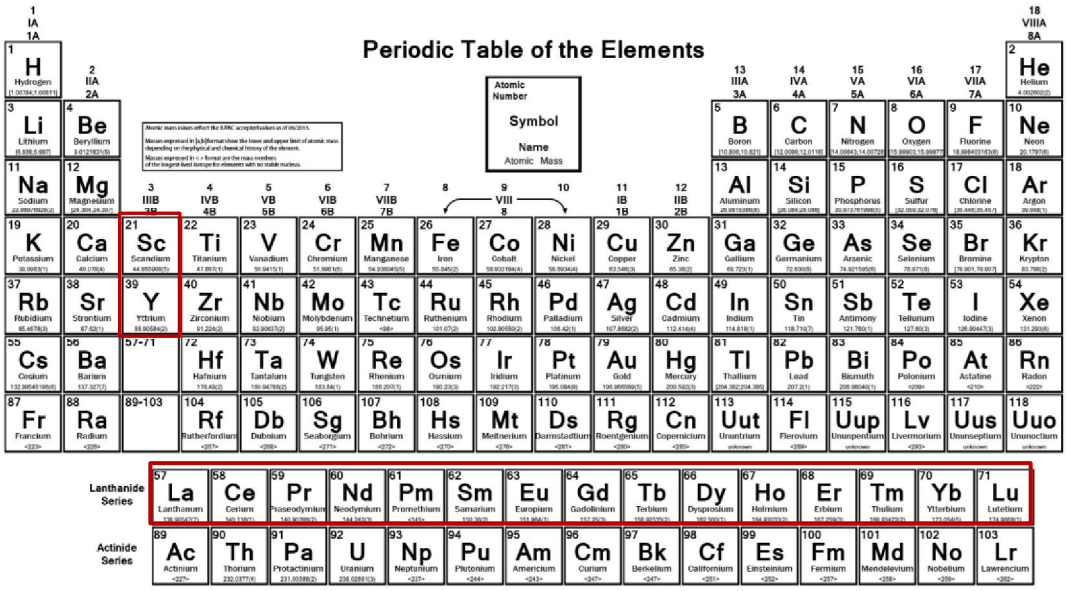

Figure 1.1 Periodic Table

Based on the electron configuration of each rare earth element, rare earths are often described as belonging to the "light group rare-earth element" (LREE)[2] (lanthanum to gadolinium plus scandium) or the "heavy-group rare-earth element" (HREE)[2] (terbium to lutetium plus yttrium) (Figure 1.2). Densities of LREEs range from 2.989 (scandium) to 7.9 g cm^{-3} (gadolinium) while those of the HREEs are from 8.2 to 9.8 g cm^{-3} except for yttrium (4.47 g cm^{-3}) and ytterbium (7 g cm^{-3}).

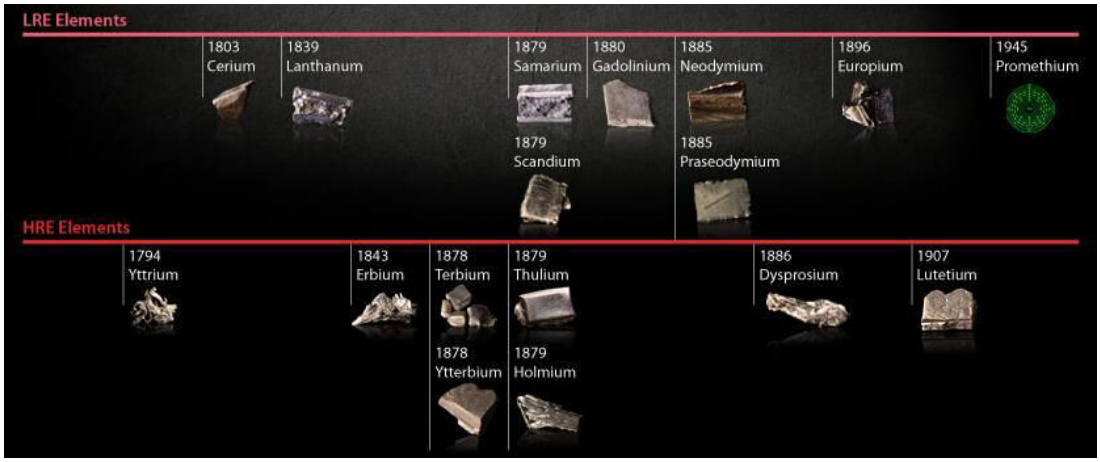

Figure 1.2 LRE elements and HRE elements and the year of their discovery.

In fact, rare earth elements except the radioactive promethium are relatively abundant in earth's crust : for example cerium is the 25th most abundant element, at 68 parts per million, similar to copper. In rock-forming minerals, rare earths mainly occur in compounds as Bastnasite $LnFCO_3$; Monazite $(Ln,Th)PO_4$ and Xenotime $(Y,Ln)PO_4$. However, because of their geochemical properties, rare earth elements are typically dispersed and not often found concentrated as rare earth minerals in economically exploitable ore deposits. As the US Geological survey's 2014 report on REEs show, a total of eight countries (Table 1.1) produce the chemical elements.[3]

Table 1.1 Total of eight countries produce REEs.

Country	Mine production (MT of REO)[a]
China	100,000
United States	4,000
India	2,900
Russia	2,400
Australia	2,000
Vietnam	220
Brazil	140
Malaysia	100

[a]Metric Tons of rare earth oxide.

1.1 Chemical properties of the elements.

1.1.1 Atomic orbitals.

The 4f orbitals of lanthanides are gradually filled which is the factor that distinguishes them. There are seven 4f orbitals (Figure 1.3) which are depicted in two different ways : the "cubic set" or the general set. The general set comprises $4f_{x(x^2-3y^2)}$, $4f_{y(3y^2-x^2)}$, $4f_{xyz}$, $4f_{z(x^2-y^2)}$, $4f_{xz^2}$, $4f_{yz^2}$, and $4f_{z^3}$; the cubic set is $4f_{xyz}$, $4f_{z(x^2-y^2)}$, $4f_{z(y^2-z^2)}$, $4f_{y(z^2-x^2)}$, $4f_{z^3}$, $4f_{x^3}$, and $4f_{y^3}$. The 4f orbitals are shielded by the [Xe] core and cannot significantly overlap with ligand orbitals and therefore do not much participate to bonding. This explains why crystal field effects are small and why 4f orbitals do not form π bonds.[4]

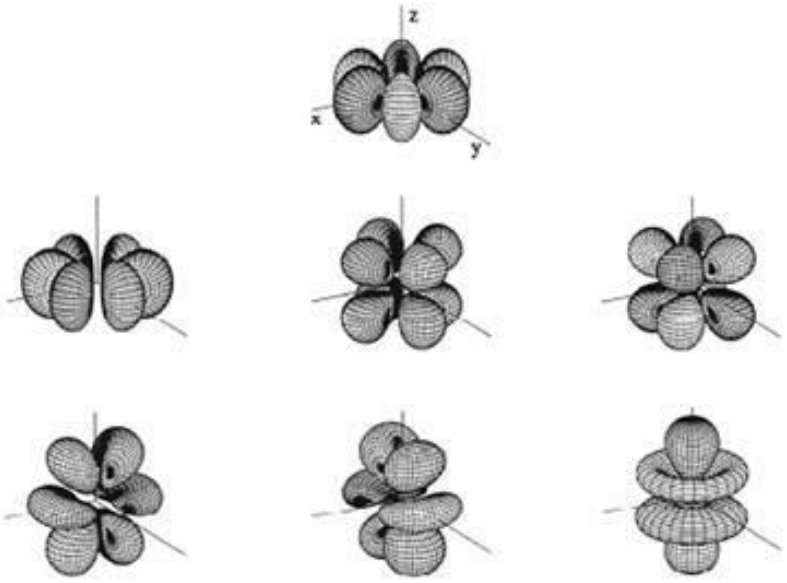

Figure 1.3 Top: Shape of the one-electron 4f orbitals in a Cartesian space. From *top* to *bottom* and *left* to *right*: $4f_{x(x^2-3y^2)}$, $4f_{y(3y^2-x^2)}$, $4f_{xyz}$, $4f_{z(x^2-y^2)}$, $4f_{xz^2}$, $4f_{yz^2}$, and $4f_{z^3}$.

1.1.2 Electronic configuration.

As more protons are added to the nucleus, the 4f orbitals contract rapidly and become more stable than the 5d orbitals (Figure 1.4). Therefore Ce has the electron configuration [Xe] $4f^1\,5d^1\,6s^2$ and the trend continues with Pr that has the arrangement [Xe] $4f^3\,6s^2$. This pattern continues for the elements Nd-Eu, all of which have configuration [Xe] $4f^n\,6s^2$ (n= 4-7). After europium, the stability of the half-filled 4f subshell is such that the next electron is added to the 5d orbitals, Gd being [Xe] $4f^7\,5d^1\,6s^2$; for terbium, however, the earlier pattern is resumed, with Tb having the configuration [Xe] $4f^9\,6s^2$, and succeeding elements to ytterbium being [Xe] $4f^{14}\,6s^2$ (n=10-14). The last, lutetium, where the 4f subshell is filled, is predictably [Xe] $4f^{14}\,5d^1\,6s^2$ (Table 1.2).

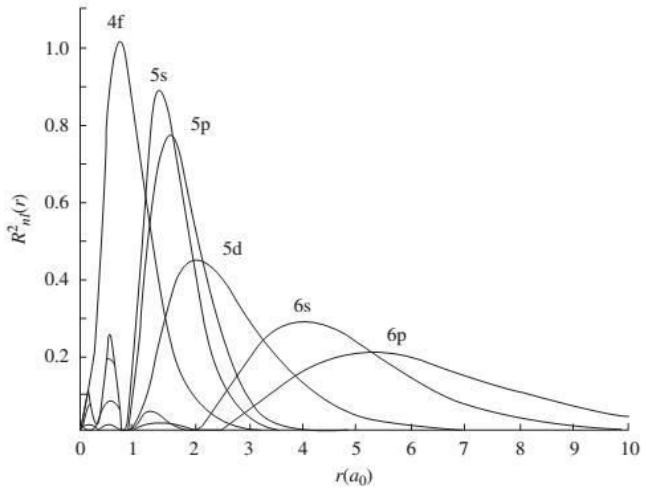

Figure 1.4 Radial distribution functions of 4f, 5s, 5p, 5d and 6s and 6p electrons for cerium.[5]

In forming the ions, electrons are removed first from the 6s and 5d orbitals, so that all the Ln^{3+} ions have [Xe] $4f^n$ configuration. Therefore all the lanthanide elements exhibit the

oxidation state +3. Although the chemistry of the lanthanides is dominated by the +3 oxidation state, the +4 and +2 oxidation states also exist. For example: Ce^{3+} can lose its single f electron to form Ce^{4+} which has the stable configuration [Xe]; Eu^{3+} can gain an electron to form Eu^{2+} with the extra-stability of a half-filled shell [Xe] $4f^7$ (Table 1.2).

Table 1.2 Electron configurations of the lanthanides and their common ions.

	Atom	Ln^{3+}	Ln^{4+}	Ln^{2+}
La	[Xe] $5d^1$ $6s^2$	[Xe]		
Ce	[Xe] $4f^1$ $5d^1$ $6s^2$	[Xe] $4f^1$	[Xe]	
Pr	[Xe] $4f^3$ $6s^2$	[Xe] $4f^2$	[Xe] $4f^1$	
Nd	[Xe] $4f^4$ $6s^2$	[Xe] $4f^3$	[Xe] $4f^2$	[Xe] $4f^4$
Pm	[Xe] $4f^5$ $6s^2$	[Xe] $4f^4$		
Sm	[Xe] $4f^6$ $6s^2$	[Xe] $4f^5$		[Xe] $4f^6$
Eu	[Xe] $4f^7$ $6s^2$	[Xe] $4f^6$		[Xe] $4f^7$
Gd	[Xe] $4f^7$ $5d^1$ $6s^2$	[Xe] $4f^7$		
Tb	[Xe] $4f^9$ $6s^2$	[Xe] $4f^8$	[Xe] $4f^7$	
Dy	[Xe] $4f^{10}$ $6s^2$	[Xe] $4f^9$	[Xe] $4f^8$	[Xe] $4f^{10}$
Ho	[Xe] $4f^{11}$ $6s^2$	[Xe] $4f^{10}$		
Er	[Xe] $4f^{12}$ $6s^2$	[Xe] $4f^{11}$		
Tm	[Xe] $4f^{13}$ $6s^2$	[Xe] $4f^{12}$		[Xe] $4f^{13}$
Yb	[Xe] $4f^{14}$ $6s^2$	[Xe] $4f^{13}$		[Xe] $4f^{14}$
Lu	[Xe] $4f^{14}$ $5d^1$ $6s^2$	[Xe] $4f^{14}$		
Y	[Kr] $4d^1$ $5s^2$	[Kr]		

1.1.3 Lanthanide contraction.

The lanthanide contraction is the phenomenon that the radius of lanthanide ions decreases gradually as the atomic number increases, resulting in regular changes in the properties of lanthanide elements as the atomic number increases. (Figure 1.5) Generally, the shielding effect originates from the inner electrons and decreases according to: s > p > d > f. For lanthanide elements, as the atomic number increases an electron is not added to the outermost shell but rather to the inner 4f shell. Because of their diffusive property, 4f electrons do not all distribute within the inner part of the 5s 5p shell. (Figure 1.4), so an increase in 4f electrons only partly shields the increase in nuclear charge. Therefore, as the atomic number increases the effective attraction between the nucleus and the outer electrons increases. This increased attraction causes shrinkage in the atomic or ionic radius which is called “Lanthanide contraction”.

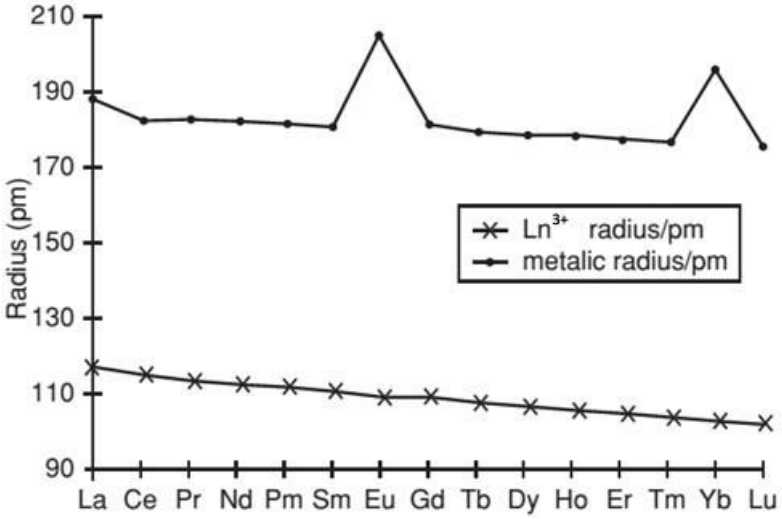

Figure 1.5 Atomic and ionic radii for the lanthanide series.

1.2 Coordination Chemistry.

1.2.1 Chemical bonding of rare earth elements.

As hard acids, lanthanide ions preferentially form chemical bonds with atoms of the hard base groups such as oxygen group that form RE-O, RE-S, RE-Se and Re-Te bonds; nitrogen group atoms that form RE-N and RE-P bonds; RE-As bond has not been observed. RE-C bonds are stable under water-free conditions but not stable under normal conditions; RE-Si bonds are very rare in the lanthanide chemistry.

About the nature of chemical bonds in lanthanide complexes, from the study of quantum chemistry, it is generally assumed that chemical bonds in lanthanide complexes exhibit polar covalent bond properties and that 4f electrons do not contribute too much to bonding, the major contribution being that of the 5d and 6s orbitals, while the 4f orbitals are highly localized.[6]

1.2.2 Coordination number of rare earth complexes.

Coordination number is defined as the number of donor atoms coordinated to a central atom.[7] Compared to the transition metals complexes (CN generally comprised between 4 and 6), lanthanide complexes have large coordination numbers (commonly 8 or 9) and diverse coordination numbers (from 2 to 12). Low coordination numbers are only observed in complexes that contain extremely bulky ligands (CN 2 for $Yb\{C(SiMe_3)_3\}_2$) and on the opposite those with very high coordination numbers involve sterically undemanding ligands.[7]

1.3 Optical properties of lanthanide-based coordination polymers.

Luminescence is the emission of light from any substance and occurs from electronically excited states. Depending on the nature of the ground and excited states, luminescence contains two categories: fluorescence that arises from the singlet excited states to the single ground state ($S_1 \rightarrow S_0$) and phosphorescence that arises from the triplet excited states to the singlet ground states ($T_1 \rightarrow S_0$). Luminescence spectroscopy relies on four

basic measurements: 1) absorption spectra, 2) emission spectra, 3) excitation spectra and 4) response to pulsed excitation.

1.3.1 Absorption Spectra.

When a photon is absorbed, its energy is transferred to an electron which may be pushed into an orbital with higher energy that is referred as excited state. Therefore, the purpose of absorption measurements is to set the energy levels scheme and to identify particular levels. Absorption of light by an electron moving around a nucleus occurs thanks to operators linked to the nature of light : the odd-parity electric dipole (ED), the even-parity magnetic dipole (MD) and electric quadrupole (EQ).

There are three types of electronic transitions involving lanthanide ions: a) 4f – 4f transitions; b) 4f -5d transitions; c) charge-transfer transitions, (Metal-to-Ligand MLCT or Ligand-to-Metal LMCT). Not all transitions are allowed. According to Laporte's rule, the f-f transitions are forbidden. However, when the lanthanide ion is under the influence of a ligand-field, non-centrosymmetric interactions allow the mixing of electronic states of opposite parity into the 4f wave functions and the transition becomes partially allowed. The other selection rules applying to *S*, *L* and *J* quantum numbers for f-f transitions between spectroscopic states are listed in Table 1.3. So for f-f transition, a forbidden transition has a low probability and an allowed transition has a high probability of occurring.

Table 1.3 Selection rules for f-f transitions between spectroscopic levels

Operator	Parity	Δ*S*	Δ*L*	Δ*J*[a]
ED	Opposite	0	≤ 6	≤ 6 (2, 4, 6 if *J* or *J*' = 0)
MD	Same	0	0	0, ±1
EQ	Same	0	0, ±1, ±2	0, ±1, ±2

[a] *J* = 0 to *J*' = 0 transitions are always forbidden

4f-5d transitions are parity allowed and their energies depend largely on the metal environment since 5d orbitals are external and interact directly with the ligand orbitals. 4f-5d transitions have high energies (Figure 1.6) and only those of Ce^{3+}, Pr^{3+} and Tb^{3+} can be observed.

The charge-transfer transitions (LMCT and MLCT) are allowed and have also high energies (Figure 1.6) so that only the LMCT of Eu^{3+} and Yb^{3+} (possibly $Sm^{3+}$and Tm^{3+}) are commonly observed in ordinary solvents.[9]

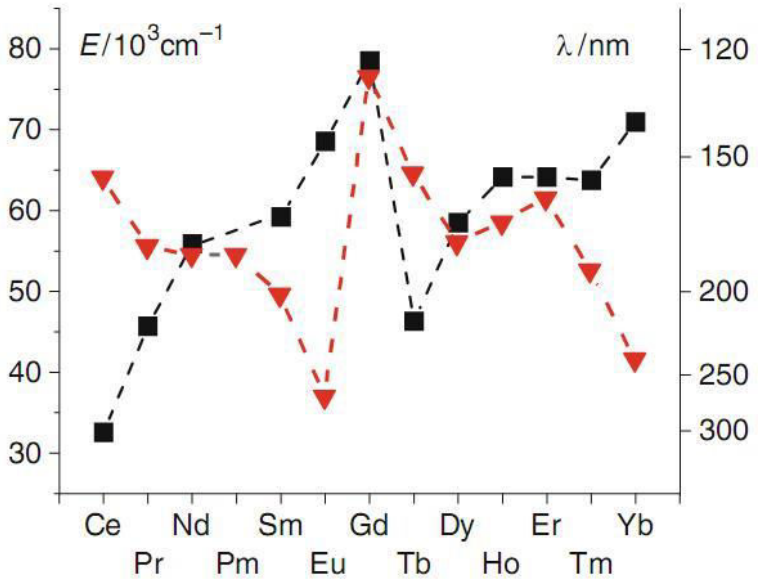

Figure 1.6 Energies of the 4f-5d transitions in Ln^{3+}:CaF_2 (squares[10]) and of the 2p-(O)-4f LMCT transition (triangles[11]).

1.3.2 Emission Spectra.

Emission spectra are used for identifying the luminescent states. They are useful for establishing energy levels, especially the position of the ground state multiplets. Emission spectra versus temperature measurements can provide information about thermal line broadening and thermal change of line positions. The threshold of quenching and up-conversion can be observed by measuring the spectral intensity versus the concentration of emission centers.

All trivalent lanthanide ions except La^{3+} and Lu^{3+} are luminescent and their f-f emission lines cover the entire spectrum from UV (Gd^{3+}) to visible (Pr^{3+}, Sm^{3+}, Eu^{3+}, Tb^{3+}, Dy^{3+}, and Tm^{3+}) and near-infrared (Pr^{3+}, Nd^{3+}, Ho^{3+}, Er^{3+}, and Yb^{3+}). Some ions are fluorescent ($\Delta S = 0$), others are phosphorescent ($\Delta S \neq 0$), and some are both. Because of the weak crystal field splitting, the f-f emission lines are sharp. From the energy level diagram for the lanthanide aquo ions (Figure 1.7)[12], the main emission transitions are listed in Table 1.4[13]. There are two important parameters characterizing the emission of light from a lanthanide ion: the **quantum yield Q** and **the lifetime of the excited state τ_{obs}**.

Table 1.4 Main luminescent transitions of trivalent lanthanide aquo ions[13]

Ln	Excited state[a]	Ground state[b]		Lumine.type[c]	λ\nm[d]	Emission color
Pr	$^1G_4$	^3H_J	J = 4-6	P	1300	NIR
	$^1D_2$	^3F_J	J = 2-4	P	890, 1060	NIR
	$^3P_0$	^3H_J	J = 4-6	F	525-680	Orange
Nd	$^4F_{3/2}$	^4I_J	J = 9/2-15/2	F	1060	NIR
Sm	$^4G_{5/2}$	^6H_J	J = 5/2-15/2	P	590	Orange
Eu	$^5D_0$	^7F_J	J = 0-6	P	620	Red
Gd	$^6P_{7/2}$	$^8S_{7/2}$		P	312	UV
Tb	$^5D_4$	^7F_J	J = 6-0	P	550	Green
Dy	$^4F_{9/2}$	^6H_J	J = 15/2-5/2	P	570	Yellow-organe
Ho	$^5F_5$	^5I_J	J = 8-4	F	970, 1450	NIR
	$^5S_2$	^5I_J	J = 8-4	F	540	Green
Er	$^4S_{3/2}$	^4I_J	J = 15/2-9/2	F		
	$^4I_{13/2}$	$^4I_{15/2}$		F	1530	NIR
Tm	$^1G_4$	^3H_J	J = 6-4	P		
Yb	$^2F_{5/2}$	$^2F_{7/2}$		F	980	NIR

[a] Most luminescent excited states.

[b] Range of J-values indicated on the right hand side.

[c] P: phosphorescence; F: florescence.

[d] Approximate wavelength of most intense emission lines or emission range.

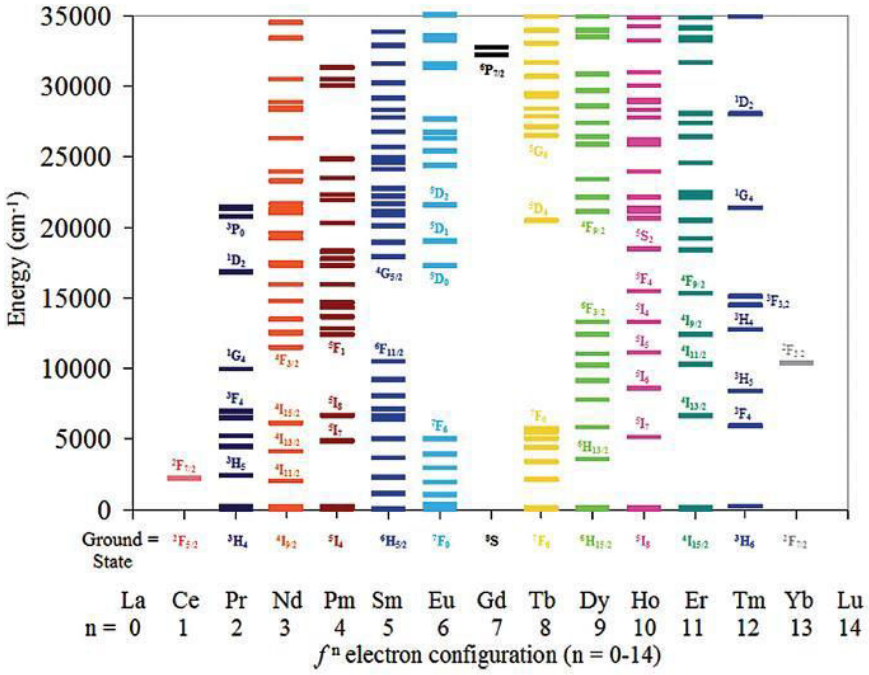

Figure 1.7 Energy level diagrams for Ln^{3+} ions doped in a low-symmetry crystal, LaF_3.[12]

Quantum yield is defined as the ratio of the number of emitted photons released in

the process of fluorescence to the number of photons absorbed.

$$Q = \frac{number\ of\ emitted\ photons}{number\ of\ absorbed\ photons}$$

For lanthanide complexes, they are two relevant quantum yields: Q_{Ln}^{L} andQ_{Ln}^{Ln}. Both are defined in details in the following.

The lifetime of the level from which the transition originates is defined as the decay constant τ of an exponentially decaying luminescence signal. It includes two parts: τ_{rad} and $\tau_{non\text{-}rad}$.

$$\frac{1}{\tau} = \frac{1}{\tau_{rad}} + \frac{1}{\tau_{non-rad}(T)}$$

Where $\frac{1}{\tau_{rad}}$ is the radiative rate constant (κ^{rad}) and $\frac{1}{\tau_{non-rad}(T)}$ is referred as the probability of non-radiative decay. $\frac{1}{\tau_{non-rad}(T)}$ is affected by the temperature of the sample. If τ is found to be independent of the temperature:

$$\frac{1}{\tau_{non-rad}} = 0$$

The decay pattern of a luminescence signal may not be exponential when the excitation energy reaches the luminescence level after undergoing a number of downward steps. If the number of this step is n, then the decay signal will contain (n+1) exponentials. But it is difficult to find all the exponentials because the components that are faster than the response time of the detecting apparatus leave no trace.[14]

1.3.3 Luminescence sensitization or “antenna effects” .

Because f-f transitions are forbidden by Laporte’s rule, the absorbance of lanthanide ions is inherently weak. To enhance the luminescence, one generally uses a ligand which strongly absorbs a suitable wavelength of radiation (as an antenna) and then transfers the energy to the lanthanide ion and excites it to the emissive states. This phenomenon is called ‘Antenna effects’ (Figure 1.8).[15]

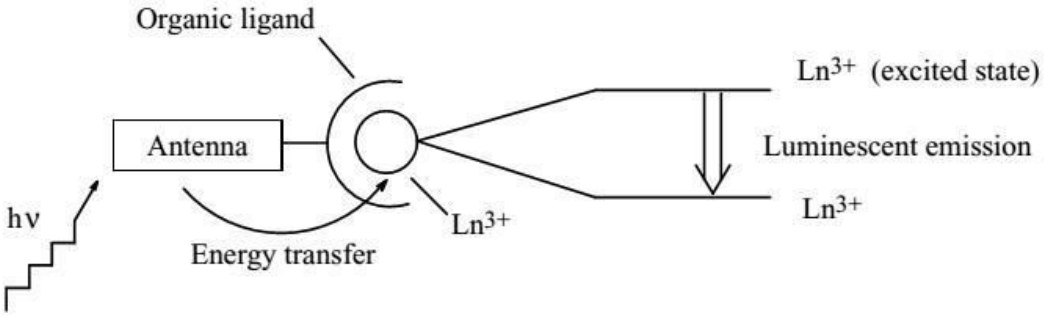

Figure 1.8 The Antenna Effect.

The process of the energy migration can be illustrated by a Jablonski’s diagram (Figure 1.9). The mechanism of luminescence sensitization (antenna effects) presents three steps: first, light is absorbed by the organic ligand; second, energy is transferred to the lanthanide

ions and finally luminescence is generated from the lanthanide ions.

Because of the energy transfer from the ligand to the lanthanide ion, fluorescence and phosphorescence of the ligand are not observed. If such energy transfer is not very efficient, the lanthanide-centered luminescence and the ligand luminescence can be simultaneously observed. The diagram below is not exhaustive, since LMCT, MLCT and 4d-5f transitions can also funnel energy onto the lanthanide ions. Moreover back-energy transfer can also occurs when the excited lanthanide ion and the ligand triplet levels lay close to each other in energy. This results in poor luminescent properties.

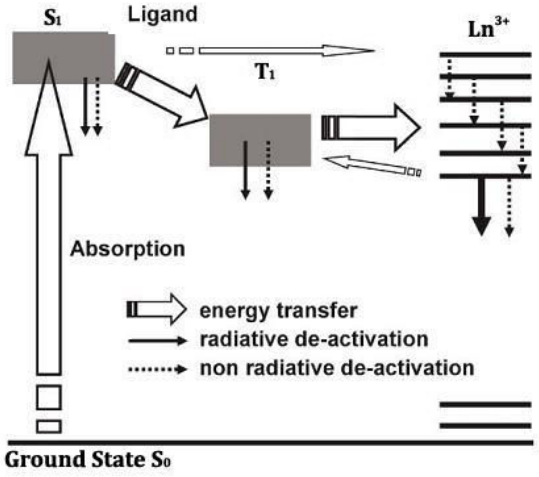

Figure 1.9 the main energy flow paths during sensitization of lanthanide luminescence via organic ligand.[16]

1.3.4 Energy transfer mechanisms in lanthanide-based complexes.

Generally, two 'donor (D) - acceptor (A)' theoretical models are used to explain the energy transfers in lanthanide complexes: Dexter energy transfer mechanism[17] (DET) and Förster resonance energy transfer mechanism[18] (FRET). (Figure 1.10) Both strongly depend on the distance *d* between the donor D and the acceptor A.

Dexter energy transfer is a double-electron exchange mechanism in which an excited electron is transferred from one molecule (donor) to a second molecule (acceptor) *via* non-radiative pathways. This process requires an overlap of the orbitals of the donor and the acceptor which only occurs at short distances (within 10 Å).

Förster energy transfer is an electrostatic multipolar mechanism in which a donor group, initially in its excited state, may transfer energy to an acceptor through non-radiative dipole-dipole coupling. This mechanism depends on the electrostatic interactions between electrons. Thus the relative distance of columbic interaction between the donor and acceptor can be bigger than for Dexter energy transfer. The efficiency with which this mechanism occurs is quantified by the following equation:

$$E = \frac{1}{1 + (R/R_0)^6}$$

where R is the distance between the donor and the acceptor and R_0 is the characteristic

distance that induces 50% transfer efficiency. Because of the sixth power of the distance, Förster energy transfer is extremely sensitive to small changes in distance. This mechanism occurs within 10 to 100 Å.

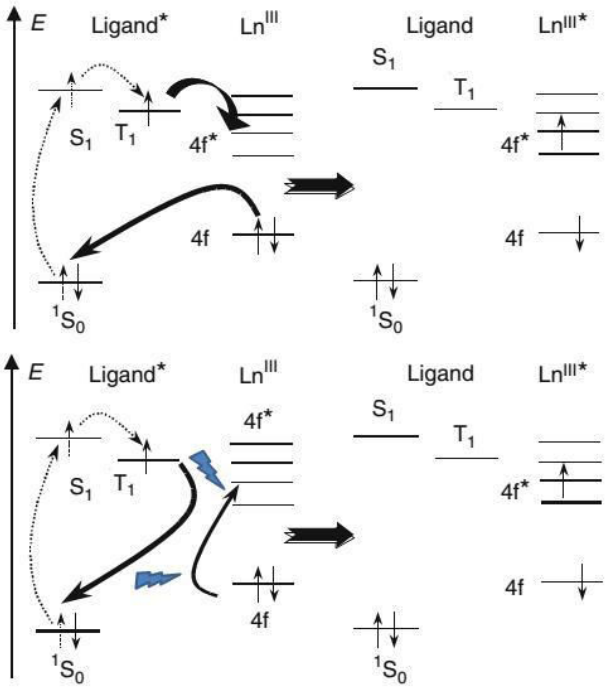

Figure 1.10 Dexter energy transfer mechanism (Top) and Förster energy transfer mechanism (Bottom).

Dexter mechanism (top of Figure 1.10), involves two electrons transfers. One-electron transfer occurs from the triplet state of the donor onto the excited state of the acceptor, while another electron transfer occurs from the highest occupied energy level of the acceptor onto the ground state of the donor.

On the opposite (bottom of Figure 1.10), for Förster mechanism, after excitation into the ligand singlet state and suitable intersystem crossing to the ligand triplet state the dipole moment associated with de-excitation of the triplet state couples with the dipole moment of the 4f orbitals and energy flows from the donor to the acceptor.

1.3.5 Quantum yield and lifetimes in lanthanide complexes.

Quantum yield is related to the efficiency of the luminescence process. There are two relevant quantum yields for lanthanide complexes: the overall quantum yield (Q_{Ln}^{L}) and the intrinsic quantum yield (Q_{Ln}^{Ln}). The overall quantum yield is the quantum yield of the metal-centered luminescence upon ligand excitation. The intrinsic quantum yield reflects the extent of radiative deactivation process of the metal ion upon direct excitation of the rare earth ion. The following equation represents their relation:

$$Q_{Ln}^{L} = \eta_{isc}\,\eta_{et} Q_{Ln}^{Ln} = \eta_{sens} Q_{Ln}^{Ln}$$

η_{isc} represents the efficacy of the intersystem crossing process .
η_{et} represents the effectiveness of the $^{3}\pi\pi^{*}$-Ln^{3+} transfer.
η_{sens} is the overall sensitization efficiency which represents the efficacy of the overall ligand-

to-metal energy transfer.

If the main energy transfer pathway involves a dipole-dipole transfer, its efficiency is given by equation:

$$\eta_{et} = 1 - \frac{\tau_{obs}}{\tau_0} = E_{(FRET)}$$

where τ_{obs} and τ_o are the lifetimes of the donor in presence and in absence of acceptor, respectively.

To calculate the sensitization efficiency, we need both the overall and intrinsic quantum yields. Overall quantum yield is easy to determine through an absolute method with an integration sphere.[19] On the opposite, intrinsic quantum yield is difficult to obtain by experimental methods because of the very small molar absorption coefficients of the f-f transitions (< 10 M^{-1} cm^{-1}, but very often in the range 0.1-1 mol^{-1} L cm^{-1}). Therefore the quantity is often calculated by the equation:

$$Q_{Ln}^{Ln} = \frac{k^{rad}}{k_{obs}} = \frac{\tau_{obs}}{\tau^{rad}}$$

k_{obs} is the sum of the rates of the various deactivation processes:

$$k_{obs} = k^{rad} + \sum_n k_n^{nr} = k^{rad} + \sum_i k_i^{vibr}(T) + + \sum_j k_j^{pet}(T) + + \sum_k k_k' nr$$

k^{rad} is the radiative rate constant and k^{nr} is the non-radiative rate constants. The superscript *vibr* points to vibration-induced processes, while *pet* refers to photo-induced electron transfer processes rate constants. k' is associated with the remaining deactivation pathways. If there is no non-radiative de-activation processes $\kappa^{rad} = \kappa_{obs}$, and the intrinsic quantum yield is equal to 1, which is very rare (this is the case for a Tb-benzoate complex[20]).

τ^{rad} is the radiative lifetime, if the absorption spectrum corresponding to an emission spectrum is known , the radiative lifetime can be calculated from an equation that arises from the Judd-Ofelt theory (JO theory). Herein we do not introduce this equation because in our work we never used it. Reference 21 contains more details about it.[21]

For Eu^{3+}-containing compounds a simplified equation leads to the radiative lifetime[22]:

$$\frac{1}{\tau^{rad}} = A_{MD,0} \cdot n^3 \left(\frac{I_{tot}}{I_{MD}}\right)$$

where $A_{MD,0}$ is the deactivation rate which is equal to 14.65 s^{-1}. n is the refractive index. I_{tot}/I_{MD} is the ratio of the total integrated emission from $^5D_0 \rightarrow {}^7F_J$ (J=0-6) to the integrated intensity of the MD transition $^5D_0 \rightarrow {}^7F_1$. Thus, it is very useful to study Eu^{3+}-containing compounds.

1.4 Choice of the ligand.

Until now, there is no efficient theoretical model. People have to rely on the abundant experimental data for establishing some rules to design efficient lanthanide-containing

luminescent compounds.

1) For the antenna effects, the ligand should have high molar absorption coefficient which can absorb enough energy and transfer onto the center lanthanide ions ;

2) The ligand should have a strong donor group in order to coordinate efficiently with the lanthanide ions ; [23]

3) In 1995, Reinhoudt and his co-workers demonstrated that intersystem crossing process becomes effective when the singlet-triplet energy gap (ΔE ($^1\pi\pi^*$-$^3\pi\pi^*$) is at least 5000 cm^{-1}.[24] ;

4) In 1997, Latva and co-workers prepared more than 40 Eu^{3+} and Tb^{3+} polyaminocarboxylates and show that the overall quantum yield increases considerably when the energy of the triplet state is close to resonance with excited levels of lanthanide ions. For Eu^{3+} ion, 2500 cm^{-1} < ΔE ($^3\pi\pi^*$- $^5D_0$) < 3500 cm^{-1} and E (LMCT) > 25000cm^{-1}; for Tb^{3+} 2500 cm^{-1} < ΔE ($^3\pi\pi^*$- $^5D_0$) < 4000 cm^{-1}.[25]

1.5 Luminescent properties of homo and hetero-nuclear lanthanide-based compounds.

Homo-nuclear compounds contain only one metal ion in their structure while hetero-nuclear compounds contain two or more different metal ions. Because of the inner character of the 4f valence orbitals and similar chemical properties of lanthanide ions, it is sometimes possible to synthesize iso-structural hetero-nuclear in which the different lanthanide ions are randomly distributed over the metallic sites of the crystal structure (Figure 1.11). These compounds can exhibit tunable optical properties.[26]

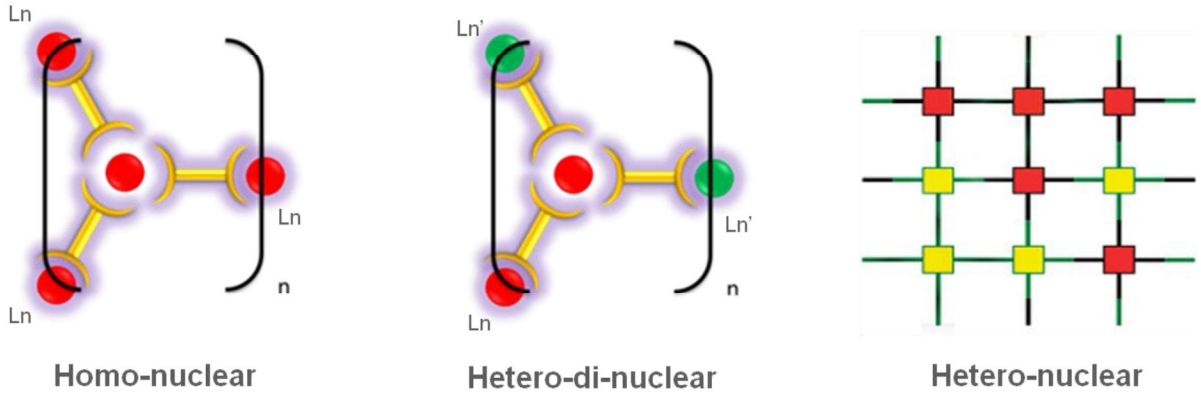

Figure 1.11 homo-nuclear and hetero-nuclear compounds.

1.5.1 Emission spectra of homo-nuclear lanthanide-based compounds.

Emission properties of the lanthanide ions cover the whole spectral range from UV, the visible to the NIR. Typical emission spectra of some lanthanide ions are briefly described below. Depending on the chemical environment of the ions, the shape of the spectra may be slightly different from one to another, but the energies of the transitions remain relatively unchanged.

a). **Gd^{3+} ion.**

The Gd^{3+} ion has a very stable ground state ($^8S_{7/2}$) and the excited level ($^6P_{7/2}$) energy is

higher than 32 0000 cm^{-1}. Hence the emission of Gd^{3+} is in the ultraviolet spectral region (Figure 1.12). The ground state $^8S_{7/2}$ cannot be split by the crystal field which limits the low-temperature fluorescent spectrum to one line. Therefore, the phosphorescent band of Gd-containing compound's emission spectra at 77K is useful for estimating the triplet state of the ligand energy.[26]

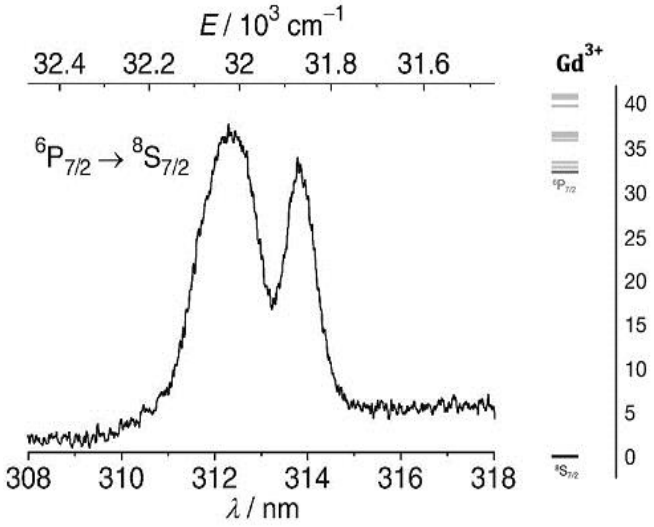

Figure 1.12 Emission spectrum and energy diagram of a Gd^{3+} ion.

b). Eu^{3+} ion.

The Eu^{3+} emission is usually observed in the red region. Lines correspond to transitions from the excited state ($^5D_0$) (≈ 17 000 cm^{-1}) to the ground state (^7F_J J=0-6) (Figure 1.13). Because the $^5D_0$ level cannot be split by the crystal field (J=0), emission transitions correspond to 580 nm ($^5D_0 \rightarrow {}^7F_0$), 592 nm ($^5D_0 \rightarrow {}^7F_1$), 615 nm ($^5D_0 \rightarrow {}^7F_2$), 650 nm ($^5D_0 \rightarrow {}^7F_3$), 693 nm ($^5D_0 \rightarrow {}^7F_4$), 741 nm ($^5D_0 \rightarrow {}^7F_5$) and 805 nm ($^5D_0 \rightarrow {}^7F_6$). The main emission of Eu^{3+} ion is most often concentrated in the transition $^5D_0 \rightarrow {}^7F_2$, while the peak at 805 nm is usually difficult to observe. Sometimes one can also observe emission from higher ^5D levels, such as $^5D_1$ and $^5D_2$.

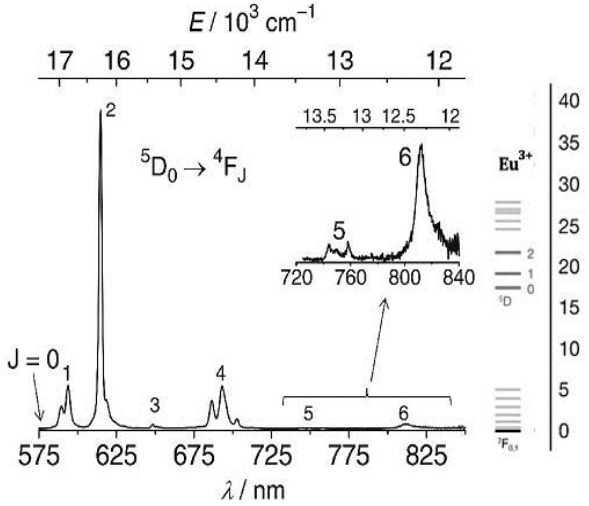

Figure 1.13 Emission spectrum and energy diagram of a Eu^{3+} ion.

***c).* Tb^{3+} ion.**

The Tb^{3+} ion is usually a good green emitter. The emission lines correspond to transitions from the excited state ($^5D_4$) (≈ 20 000 cm^{-1}) to the ground state (^7F_J J=6-0) (Figure 1.14). Because of the high J values, the crystal field splits levels in many sublevels which results in a complicated emission spectrum. The emission peaks are usually observed at 490 nm ($^5D_4 \rightarrow {}^7F_6$), 550 nm ($^5D_4 \rightarrow {}^7F_5$), 585 nm ($^5D_4 \rightarrow {}^7F_4$), 624 nm ($^5D_4 \rightarrow {}^7F_3$), 653 nm ($^5D_4 \rightarrow {}^7F_2$), 670 nm ($^5D_4 \rightarrow {}^7F_1$), and 684 nm ($^5D_4 \rightarrow {}^7F_0$) and the transition $^5D_4 \rightarrow {}^7F_5$(550 nm) is dominant. Therefore terbium complexes are commonly used as bright green emitters.

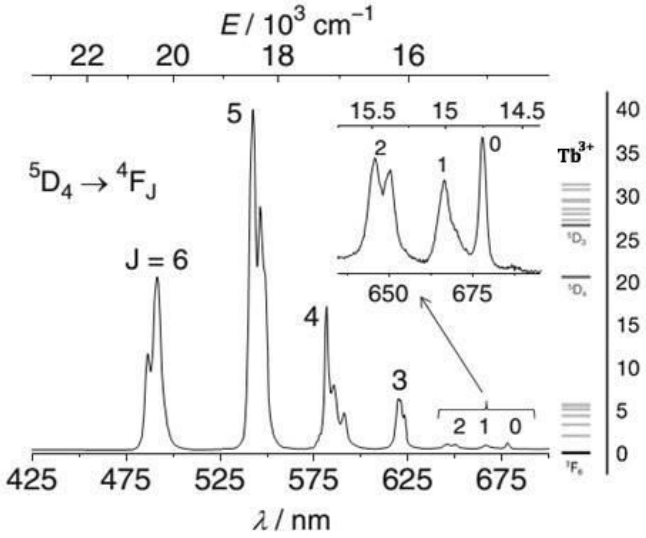

Figure 1.14 Emission spectrum and energy diagram of a Tb^{3+} ion.

***d).* Sm^{3+} ion.**

The emission of Sm^{3+} ions is situated in the red–orange spectral region and consists of transition from the excited state $^4G_{5/2}$(≈ 18 000 cm^{-1}) to the ground state ^6H_J (J=5/2,7/2,9/2 and 11/2). The emissions based on Sm^{3+} ion peak at about 564 nm ($^4G_{5/2} \rightarrow {}^6H_{5/2}$), 598 nm ($^4G_{5/2} \rightarrow {}^6H_{7/2}$), 645 nm ($^4G_{5/2} \rightarrow {}^6H_{7/2}$), and 710 nm($^4G_{5/2} \rightarrow {}^6H_{9/2}$) respectively (Figure 1.15).

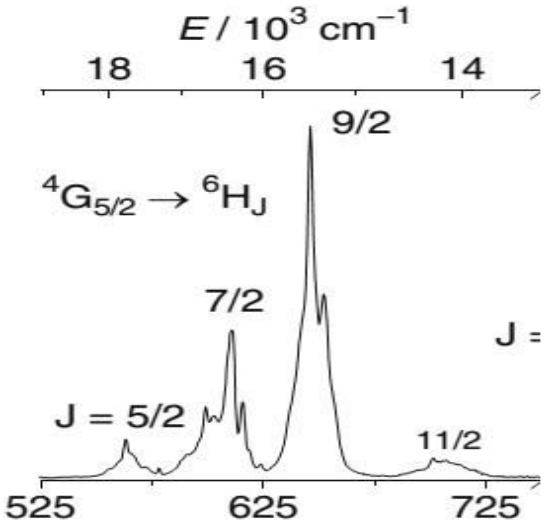

Figure 1.15 Emission spectrum and energy diagram of a Sm^{3+} ion.

***e).* Dy^{3+} ion.**

The emission of Dy^{3+} originates from $^4F_{9/2}$ (≈21 000 cm^{-1}) to ^6H_J (J=15/2, 13/2, 11/2, and 9/2). They locate at 480 nm ($^4F_{9/2}\rightarrow{}^6H_{15/2}$), 575 nm ($^4F_{9/2}\rightarrow{}^6H_{13/2}$), 660 nm ($^4F_{9/2}\rightarrow{}^6H_{13/2}$), and 760 nm ($^4F_{9/2}\rightarrow{}^6H_{9/2}$), respectively (Figure 1.16)..

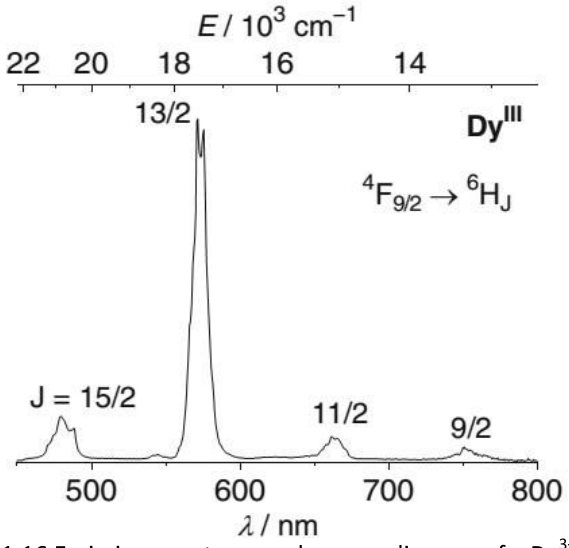

Figure 1.16 Emission spectrum and energy diagram of a Dy^{3+} ion.

1.5.2 Emission spectra of f-f Hetero-nuclear lanthanide-based compounds.

In the f-f hetero-nuclear lanthanide-based compounds, the energy can transfer from one lanthanide center to another which leads to interesting spectral and emission properties involving the f-f levels. The f-f hetero-nuclear compounds present highly tunable luminescence properties. Actually, the intensity of the luminescence can be significantly enhanced or diminished in the solid state or in solution, and the emission color of the compounds can be easily tune through by changing the ratio between the different ions.[27] Because there are a lot of types of hetero-nuclear compounds, we just refer some typical examples to highlight their tunable luminescence properties.

***a).* Eu^{3+}-Tb^{3+} hetero-dinuclear compounds.**

The first mixed lanthanide ions luminescent materials are the Eu/Tb compounds [(Eu, Tb)$(C_6H_8O_4)_3(H_2O)_2$],$(C_{10}H_8N_2)$ reported by C. L. Cahill et al in 2009.[28] They characterized their luminescence spectra and studied the pathways of the energy transfers in the mixed-lanthanides system, but they didn't give details about the color change, emission spectra and energy transitions.

Our group prepared the coordination polymers with general chemical formula $[Eu_{2-2x}Tb_{2x}(C_8O_4H_4)_3(H_2O)_4]_\infty$ and studied their luminescence properties in details.[29] This study reveals that there are double energy-transfer process in the system (Ligand → Tb and Tb → Eu) (Figure 1.17) and that evolution of the colorimetric and spectroscopic properties versus the Tb/Eu ratio is non-linear.

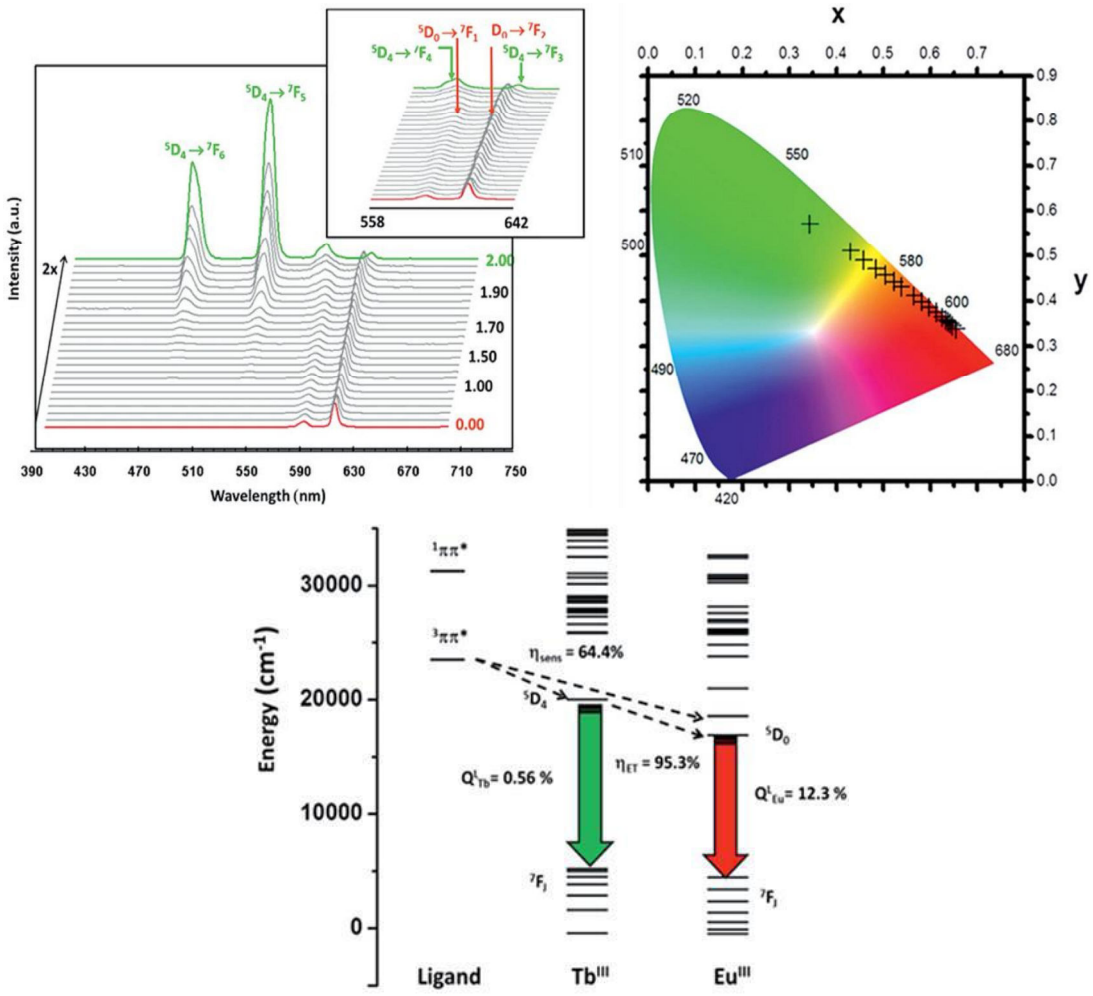

Figure 1.17 The tunable luminescent properties and the energy transfer pathway in the hetero nuclear compounds $[Eu_{2-2x}Tb_{2x}(C_8O_4H_4)_3(H_2O)_4]_\infty$

For these Eu/Tb mixed compounds, we can calculate the yield of this Tb-to-Eu energy transfer (η_{ET}) from the following equation:

$$\eta_{ET} = \frac{1}{1 + (R_{Ln-Ln'}/R_0)^6}$$

So the yield of the energy transfer depends on the distance between the different ions, and it is commonly admitted that dipole-dipole intermetallic energy transfer is efficient if the metallic ions are less than 10 Å apart from each other. In general, the luminescence of Tb^{3+} is intensively quenched and this of Eu^{3+} is highly enhanced in Eu/Tb system.

There is another equation which can also be used to calculate the yield:

$$\eta_{ET} = 1 - \frac{\tau_{obs}}{\tau_0}$$

Herein, τ_{obs} and τ_o are the lifetimes of the donor in presence and in absence of acceptor, respectively.[30] Because the Gd^{3+} ion excited levels are higher than the excited level of Tb^{3+} ion and the ligand triplet state, it cannot act as an acceptor. Therefore, the design of the Tb/Gd hetero-dinuclear compound allows one to measure the lifetime τ_o and then calculates η_{ET}.

***b).* Gd^{3+}-Tb^{3+} or Gd^{3+}-Eu^{3+} hetero-dinuclear compounds.**

The optically non-active rare ion Gd^{3+} acts as an optical dilutor in the hetero-nuclear compounds. From the study of the mixed Gd/Tb compounds, τ_o can be obtained and used to calculate the yield of the energy transfer in the hetero-nuclear Tb/Eu compounds. And this study (Figure 1.18) also reveals that: (1). the addition of an optically inactive rare earth ion (Gd) provokes an increase in the mean distance between the luminescent ion (Tb^{3+} or Eu^{3+}) without perturbing the crystal structure. (2). For some antenna ligand, a dilution is beneficial up to a point, than further dilution resulted in a decrease in the luminescence intensity.[31] Therefore people can use a cheaper optically non-active ion (Gd^{3+}, La^{3+} or Y^{3+}) to enhance the luminescence intensity by replacing expensive luminescent ions (Tb^{3+} or Eu^{3+}).

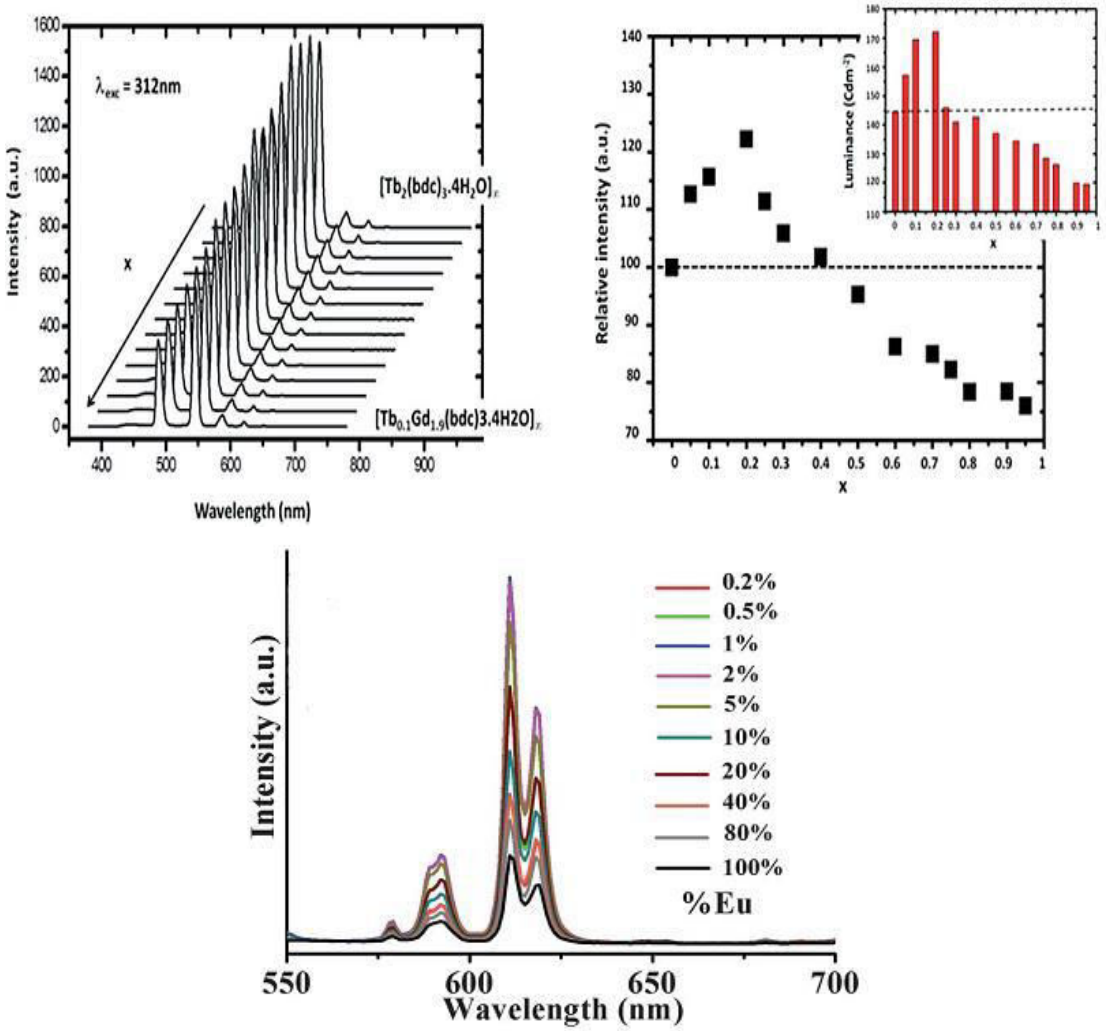

Figure 1.18 the tunable luminescent properties and luminescent intensity in hetero dinuclear compounds $[Tb_{2-2x}Gd_{2x}(C_8O_4H_4)_3(H_2O)_4]_\infty$ or $Eu_xGd_{1-x}(C_{29}NO_{10}H_{26})$.

***c).* Other types of hetero-nuclear compounds.**

Nowadays, due to their fascinating luminescent properties, a lot of hetero-nuclear lanthanide-based compounds were prepared. So, Zheng Z.-P. synthesized a series of hetero-trinuclear compounds $\{[La_xEu_yTb_{1-x-y}(BTPCA)(H_2O)],2DMF,3H_2O\}_\infty$ (BTPCA symbolizes 1,1',1''-(benzene- 1,3,5-triyl)tripiperidine-4-carboxylic acid) for white light emission.[32] C. V. Rodrigues

et al prepared $\{[(La_{0.9}Eu_{0.05}Tb_{0.05})_2(PDC)_3(H_2O)_4],2H_2O\}_\infty$ (PDC symbolizes pyrazole-3,5-dicarboxylate) which can be excited by different excitation wavelengths and displayed tunable emitted color from red through orange to green.[33] K. Müller-Buschbaum and co-workers synthesized a series of compounds with general chemical formula $\{[Gd_{2-x-y}Eu_xTb_yCl_6(bipy)_3],2bipy\}_\infty$ (bipy symbolizes 4,4'-bipyridine), which exhibit a linear color variation from green to orange-red with no changes in the quantum yield.[34] Our group also studied the hetero-nuclear compounds with general chemical formula $[Er_{2-2x}Yb_{2x}(C_8O_4H_4)_3(H_2O)_4]_\infty$ for their near-IR luminescent properties[35] and prepared a large number of compounds with general chemical formula compounds $[Tb_{2-x-y}Eu_xLa_y(C_8O_4H_4)_3(H_2O)_4]_\infty$ which present a wide variety of luminescent properties (Figure 1.19).[36]

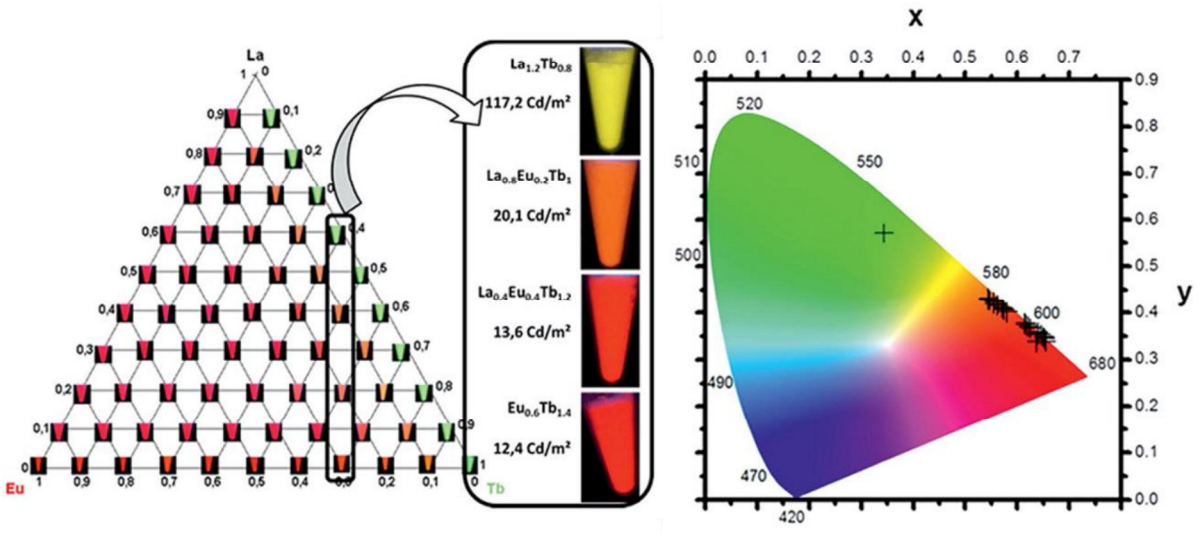

Figure 1.19 Photoluminescence and Colorimetric coordinates in $[Tb_{2x}Eu_{2y}La_{2-2x-2y}(C_8O_4H_4)_3(H_2O)_4]_\infty$.

1.6 Application.

The rare earth and lanthanide-based coordination polymers find their application in different domains because of their original chemical or physical properties: gas storage,[37] catalysts,[38] molecular magnetism,[39] bio-analyses and imaging,[40] laser[41] and OLEDs.[42] All these fields have led to a very abundant literature.[43] That is why we don't present them in details in this manuscript.

References:

[1]. IUPAC Provisional Recommendations for Nomenclature of Inorganic Chemistry, 2004.

[2]. a) Gschneider, Karl A., Jr. 1966. Rare Earths-The Fraternal Fifteen. Washington, DC, US atomic Energy Commission, *Divisions of Technical Information*, 42 pages. b) Hedrick, James B. "REE Handbook -- The ultimate guide to Rare Earth Elements,". Rare Metal Blog. Toronto, Canada.

[3]. Joseph Gambogi, U.S. Geological Survey, *Mineral Commodity Summaries*, February 2014.

[4]. Cotton, Simon. *Lanthanide and Actinide Chemistry*. John Wiley & Sons Ltd, 2006.

[5]. Z. B. Goldschmidt," Atomic Properties (Free Atom)" *Handbook on the Physics and Chemistry of Rare Earth*. Volume 1, 1978.

[6]. (a) Lemin, L., Jingqiang, R., and Guangxian, X. *International Journal of Quantum Chemistry*, XXIII, 1305–1316; 1983 (b) Jingqing, R. and Guangxian, X. () *International Journal of Quantum Chemistry*, XXIX, 1017–1024; 1986 (c) Jingqing, R. and Guangxian, X. *Lanthanide and Actinide Research*, 2, 67–78, 1987.

[7]. IUPAC, *Compendium of Chemical Terminoloy*, 2nd ed. (the "Gold Book"), 1997.

[8]. Stuart R. Batten, Suzanne M. Neville and David R. Turner. *Coordination Polymers: Design, Analysis and Application*. RSC, 2009.

[9]. P. Hanninen and H. Harma. *Lanthanide Luminescence: Phototical, Ananlytical and Biological Aspects*. Springer, 2011.

[10]. Dorenbos P. *J Lumin*, 91, 91-106, 2000.

[11]. Shionoya S, Yen WM, *Phosphor Handbook*, CRC,Boca Raton, Hh. 235, 1999.

[12]. W.T. Carnall, G.L. Goodman, K. Rajnak, R.S. Rana, , *J. Chem. Phys.*, 90, 3443, 1989.

[13]. a). W.T. Carnall, P.R. Fields and K.Rajnak, *J. Chem. Phys.*, 49, 4424, 1968. b). W.T. Carnall, P.R Fields and K.Rajnak, *J. Chem. Phys.*, 49, 4443, 1968. c). W.T. Carnall, P.R. Fields and K.Rajnak, *J. Chem. Phys.*, 49, 4447, 1968. d). W.T. Carnall, P.R. Fields and K.Rajnak, *J. Chem. Phys.*, 49, 4450, 1968.

[14]. D. B. Daldassare, C. John. *Handbook of Applied solid State Spectroscopy*. Chapter 12, Springer, 2006.

[15]. M. Kawa, J.M.J. Fréchet. Chem. Mater, 10, 286, 1998.

[16]. J.-C. G.Bünzli and C. Piguet. *Chem. Soc. Rev.* 34, 1048, 2005.

[17]. D. L. Dexter. *The Journal of Chemical Physics*, 21, 836-850, 1953.

[18]. T. Förster. *Comprative Effects of Radiation*, John Willey & Son, 1960.

[19]. (a). G. Weber and F. W. J. Teale, *Trans. Faraday Soc.*, 53, 646, 1957. (b). M.S.Wrighton, D. S.Ginley and D. L.Morse. *J. Chem. Phys*., 78, 2229, 1974.

[20]. B. Michael, K. UIrich and R.Cornelis. *Adv. Mater.*, 3, 361, 1991.

[21]. A. Aebischer, F. Gumy and J.C G.Bünzli, Phys Chem Chem Physic, 11, 1346, 2009.

[22]. M.H.V. Weerts, R.T.F. Jukes and J.W. Verhoeven. Phys Chem Chem Phys, 4, 1542, 2002.

[23]. J.-C. G.Bünzli, In: Rqre Earths, eds; R. Saez Puche and P. Caro. (Editorial Complutense; Madrid), P 233, 1998.

[24]. F.J. steemers, W. Verboom, D.N. Reinhoudt, E.B. Ban der Tol and J.W. Verhoeven, J. Am. Chem. Soc. 117, 9408, 1995.

[25]. M. Latva, H. Takalo, V.-M. Mukkala, C. Matachescu J. C. Rodriguez-Ubis and J. Kankare. J. Lumin. 75, 149, 2005.

[26]. (a). N. Kerbellec, D. Kustaryono, V. Haquin, M. Etienne, C. Daiguebonne, and O. Guillou, Inorg. Chem. 48, 2837, 2009. (b). V. Haquin, F. Gumy, C. Daiguebonne, J.-C. G.Bünzli and O. Guillou, Eur. J. Inorg. Chem. 2009, 491.

[27]. (a). S. Quici, M. Cavazzini, G. Marzanni, G. Accorsi, N. Armaroli, B. Ventura and F. Barigelletti, Inorg. Chem., 44, 529, 2005. (b). M. Shi, F. Li, T. Yi, D. Zhang, H. Hu and C.-H. Huang, Inor. Chem. 44, 8929, 2005. (c). L. Prodi, M. Maestri, R. Ziessel and V. Balzani, Inorg. Chem. 30, 3798, 1991.

[28]. D. T. de Lille, A. de Bettencourt-Dias and C. L. cahill, Inorg. Chem. 46, 3960, 2007.

[29]. V. Haquin, M. Etienne, C. Daiguebonne, S. Freslon, G. Calvez, K. Bernot, L. Le Polles, S.E. Ashbrook, M.R. Mitchell, J.-C. G. Bünzli, S.V. Elisseva, and O. Guillou, Eur. J. Inorg. Chem. 2013, 3464.

[30]. S.V. Eliseeva, and J.-C. G. Bünzli, Chem. Soc. Rev. 9, 189, 2010.

[31]. S. Dang, J.-H. Zhang and Z.-M. Sun, J. Mater. Chem., 22, 8868, 2012.

[32]. Q. Tang, S.-X. Liu, Y.-W. Liu, D.-F. He, J. Miao, X.-Q. Wang, Y.-J. Ji, and Z.-P. Zheng, Inorg. Chem. 53, 289, 2014.

[33]. C.V. Rodrigues, L.L. Luz, J. Diogo L. dutra, S.A. Junior, O. L. Malta, C.C. Gatto, H. C. Streit, R. O. Freire, C. Wickleder and M. O. Rodrigues, Phys. Chem. Chem. Phys, 16, 14858, 2014.

[34]. P. R. Matthes, C.J. Höller, M. Mai, J. Heck, S. J. Sedlmaier, S. Schmiechen, C. Feldmann, W. Schnick and K. Müller-Buschbaum, J. Mater. Chem, 22, 10179, 2012.

[35]. V. Haquin, F. Gumy, C. Daiguebonne, J.-C. G. Bünzli, and O. Guillou, Eur. J. Inorg. Chem. 2009, 1099.

[36]. N. Kerbellc, D. Kustaryono, V. Haquin, M. Etienne, C. Daiguebonne and O. Guillou, Inorg. Chem. 7, 2837, 2009.

[37]. (a). M. P. Suh, H. J. Park, T. K. Prasad and D.-W. Lim, Chem. Rev. 112, 782, 2012. (b). B. Mu, F. Li, Y. Huang and K.S. Walton, J. Mater. Chem, 22, 10172, 2012, (c). O. M. Yaghi and H. L. Li, J. Amm. Soc., 117, 10401, 1995.

[38]. (a). M. G. Walter, E. L. Warren, J. R. McKone, S. W. Boettcher, Q. Mi, E.A. Santori and N. S. lewis, Chem. Rev. 110, 6446, 2010, (b). G. F. Feng, S. W. Liu, Z.L. Xiu, Y. Zhang, J. X.Yu, Y. G. Chen, P. Wang and X. J. Yu. J. Phys. Chem. C, 112, 13692, 2008. (c). J. Lee, O.K. Farha, J. Roberts, A. Scheidts, S. T. Nguyen and J. T. Hupp, Chem. Soc. Rev. 38, 1450, 2009. (d). L. Yun, K. Bernot, G. Calvez, S. freslon, C. Daiguebonne, O. Guillou, N. Kerbellec, T. Roisnel, Crys. Eng. Comm., 15, 1882, 2013.

[39]. (a). X. Yi, K. Bernot, F. Pointillart, G. Poneti, G. Clavez, C. Daiguebonne, O. Guillou, and R. Sessoli, Chem.- Chem. Eur. J. 18, 11379, 2012, (b). K. Beron, F. Pointillart, P. Rosa, M. Etienne, R. Sessoli and D. Gatteschi, Chem. Commun. 46, 6458, 2010. (c). M. Andruh, J.-P Costes, C. Diaz and S. Gao, Inorg. Chem., 48, 3342, 2009.

[40]. (a). S. Viswanathan, Z. Kovacs, K. N. Green, S. J. Ratnakar and A. D. Sherry, Chem. Rev. 110, 2960, 2010. (b). K.N. Allen and B. Imperiali, Curr. Opin. Chem. Biol. 14, 247, 2010.

[41]. (a). X. Zhu and N. Peyghambarian, Adv. Opto. Electron., 501956, 2010. (b). R. A. S. Ferreira, P. S. Andre and L. D. Carlos, Opt. Mater., 32, 1937, 2010.

[42]. (a). Q. Y. Zhang and X.Y. Huang, Prog. Mater. Sci. 55, 353, 2010. (b). N. Guo, Y. Huang, H. You, M. Yang, Y. Song, K. Liu and Y. Zheng, Inorg. Chem. 49, 10907, 2010.

[43]. (a). S. V. Eliseeva and J.-C. G. Bünzli, New. J. Chem. 35, 1165, 2011. (b). J. Heine and K. Muller-Buschbaum, Chem. Soc. Rev., 42, 9232, 2013. (c). F. A. Alemeida Paz, J. Klinowski, S. M. F. Viela, J. P. C. Tome, J. A. S. Cavaleiro, J. Rocha, Chem. Soc. Rev., 41, 1088, 2012. (d). J. Feng and H. G. Zhang, Chem. Soc. Rev., 42, 387, 2013.

Chapter2.

Bibliography:

coordination polymers based on ligands

(H_2cda, H_2hip, H_2nip and Hcpb)

Chapter 2. Bibliography: coordination polymers based on ligands (H_2cda, H_2hip, H_2nip and Hcpb)

Our work is based on four carboxylic acids used as ligands. We used these four ligands to synthesize rare earth-based coordination polymers: 5-hydroxy-isophthalic acid (hereafter symbolized as H_2hip); 5-nitro-isophthalic acid (hereafter symbolized as H_2nip); chelidonic acid (hereafter symbolized as H_2cda) ; 4-carboxyphenylboronic acid (hereafter symbolized as Hcpb)[1] (Figure 2.1). Some works involving these ligands for lanthanide-based compounds have been previously published. In this chapter, these works are briefly presented.

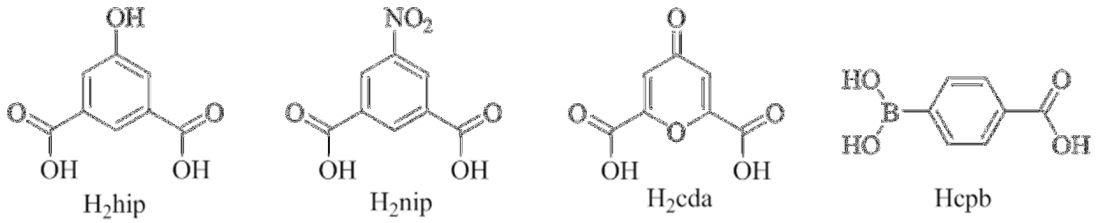

Figure 2.1 Schematic representation of the four ligand used in this work.

2.1 Ligand hip^{2-}.

According to the hard-soft acid-base theory, lanthanide atoms have high affinity for oxygen donor atoms. Therefore, multicarboxylate ligands are often employed in the construction of lanthanide-based coordination polymers. Among these compounds, 5-hydroxy-isophthalic acid (H_2hip) has attracted great interest because of the following characteristics:

1) it presents two carboxylic groups which may exhibit diverse coordination modes ;
2) its hydroxyde group can be acceptor or donor for hydrogen bonding ;
3) its hydroxyde group may also provide an additional binding site for metal atoms.

Some transition metal-based compounds involving this ligand have been published.[2] Some other compounds with mixed ligands involving hip^{2-} have also been reported.[3] Herein, the compounds that are only based on H_2hip ligand and lanthanide ions have attracted our interest. They are briefly summarized below.

In 2004, Li Y.D. *et al.* reported for the first time, five rare earth-based coordination polymers using H_2hip acid as ligand ($[Ln(C_8H_4O_5)(H_2O)_5$, (H_2O), $(C_8H_4O_5)_{1/2}]_\infty$,with Ln = Eu; Gd; Tb; Dy and Er).[4] These five isomorphic complexes were synthesized by hydrothermal method. They crystallize in the monoclinic system, space group *C/2c* (Table 2.1). In the crystal structure, there are one half uncoordinated hip^{2-} ligand and one crystallographically independent Ln^{3+} ion which is nine-coordinated by four oxygen atoms from carboxylate groups of the hip^{2-} ligand and five oxygen atoms from coordination water molecules (Figure 2.2).

Table 2.1 Crystallographic data for $[Ln(C_8H_4O_5)(H_2O)_5, (H_2O), (C_8H_4O_5)_{1/2}]_\infty$,with Ln = Eu; Gd; Tb; Dy and Er.

	1	2	3	4	5
formula	$C_{12}H_{18}O_{13.5}Eu$	$C_{12}H_{18}O_{13.5}Gd$	$C_{12}H_{18}O_{13.5}Tb$	$C_{12}H_{18}O_{13.5}Dy$	$C_{12}H_{18}O_{13.5}Er$
Mw	530.22	535.51	535.17	540.67	545.44
Crystal system	Monoclinic	Monoclinic	Monoclinic	Monoclinic	Monoclinic
Space group	C2/c	C2/c	C2/c	C2/c	C2/c
a(Å)	19.838(16)	19.823(7)	19.770(4)	19.632(2)	19.648(7)
b(Å)	10.529(8)	10.552(4)	10.519(2)	10.492(2)	10.480(3)
c(Å)	17.752(14)	17.762(6)	17.698(4)	17.617(3)	17.598(6)
α(°)	90	90	90	90	90
β(°)	107.503(14)	107.443(6)	107.52(3)	107.470(12)	107.502(6)
ϒ(°)	90	90	90	90	90
V ($Å^3$)	1610.6(6)	3544(2)	3509.6(12)	3461.4(10)	3455.9(19)
Z, ρ_{calc} (g/cm^3)	8, 1.992	8, 2.007	8, 2.026	8, 2.002	4, 2.024
GOF on F^2	0.953	0.987	0.842	1.02	1.025
R	0.0413	0.0426	0.0399	0.0512	0.0372
Rw	0.1028	0.1056	0.0987	0.1229	0.0828
CCDC number	210810	210983	213616	213730	207075

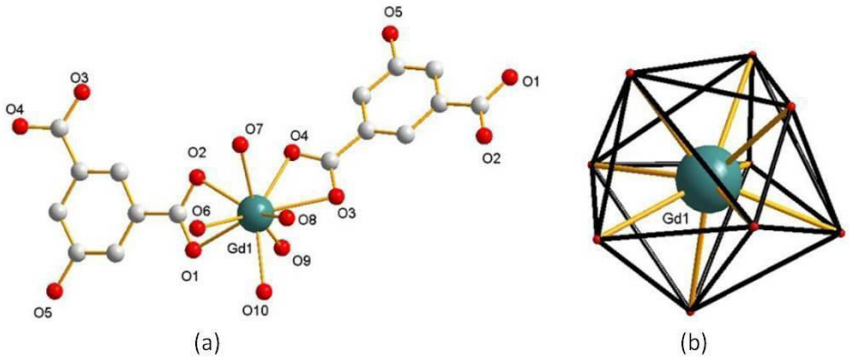

Figure 2.2 (a) Molecular structure and (b) coordination geometry of the lanthanide ions in $[Gd(C_8H_4O_5)(H_2O)_5, (H_2O), (C_8H_4O_5)_{1/2}]_\infty$.

The carboxylate groups of hip^{2-} chelate the Gd^{3+} ions to form 1D helical cationic chains which are further arranged to form 2D anion / cation layers with the uncoordinated hip^{2-} ligands (Figure 2.3). The hydrogen bonds which are formed by water molecules and carboxylate groups of the uncoordinated hip^{2-} ligands ensure the stability of the open framework.

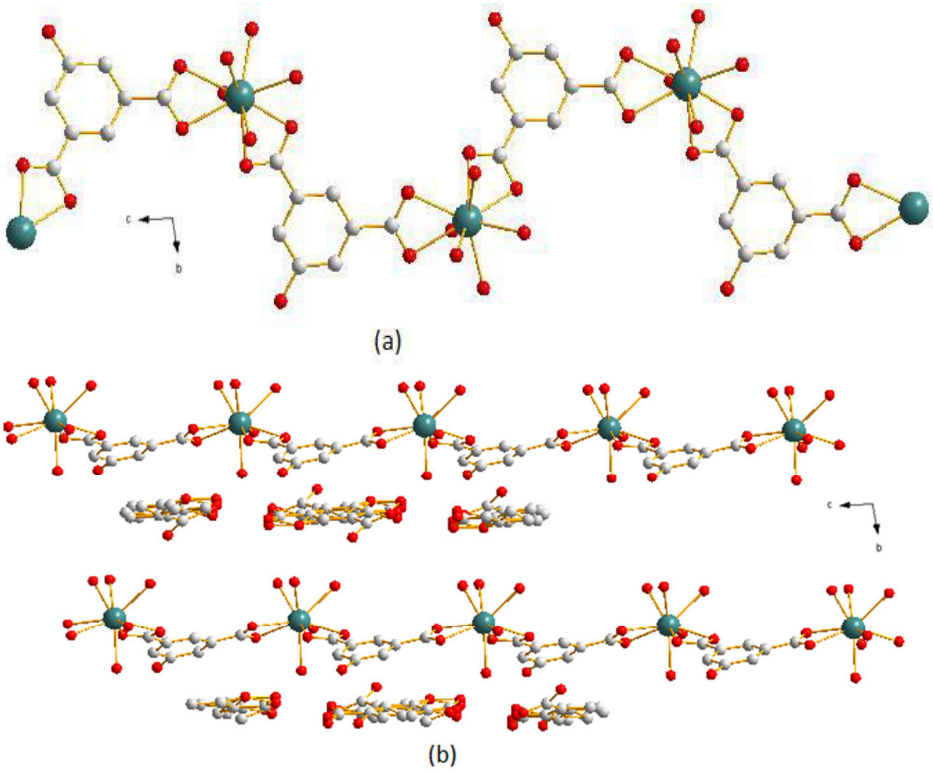

Figure 2.3 (a) 1D molecular chain and (b) 2D packing layers of $[Gd(C_8H_4O_5)(H_2O)_5, (H_2O), (C_8H_4O_5)_{1/2}]_\infty$.

Luminescent properties of these compounds have been studied. The UV-vis absorption spectra are similar (Figure 2.4), which indicates that excitation of the ligand can be done through an antenna effect. Emission spectra of the Tb- and Dy-containing complexes have been studied (Figure 2.4) upon different excitation wavelength (λ_{ex}=336nm and λ_{ex}=309 nm for the Tb- and Dy-containing compounds respectively).

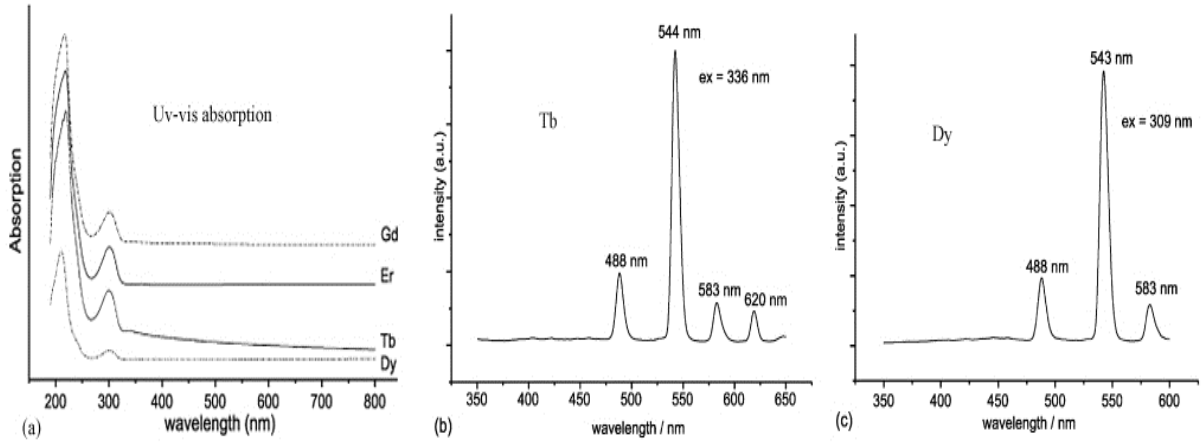

Figure 2.4 (a) UV-vis absorption spectra for the Gd-, Er-, Tb- and Dy- containing compounds. (b) Emission spectrum of the Tb-containg compound and (c) emission spectrum of the Dy containing compound.

In 2008, the team of Yan reported a series of lanthanide coordination polymers with general chemical formula $\{[Ln(hip)(Hhip)(H_2O)_2], 2H_2O\}_\infty$ with Ln=La, Sm, Tb and Er.[5] These four coordination polymers are isostructural. They crystallize in the triclinic system, space group *P*1 (Table 2.2). In this crystal structure, there is only one crystallographically independent Tb^{3+} ion which is nine-coordinated by five oxygen atoms from four hip^{2-} ligands,

two oxygen atoms from one $Hhip^-$ ligand, and two oxygen atoms from two coordination water molecules. The coordination polyhedron of the Tb^{3+} ion is close to a distorted capped square antiprism (Figure 2.5). Carboxylate groups of hip^{2-} ligand act as bridges to form 1D Tb-O-C-O-Tb chains (Figure 2.6a). Then the chains are cross-linked by the phenylene moieties to lead to 2D layers (Figure 2.6b), that further form a pseudo 3D framework through hydrogen bonds and π-π interactions (Figure 2.6c).

Luminescent properties of the Tb-containing compound have been studied. It exhibits bright green photoluminescence upon UV radiation in the solid state at room temperature. The excitation spectrum (λ_{em} = 545 nm) and emission spectrum (λ_{ex} = 336 nm) have been recorded (Figure 2.7).

Table 2.2 Crystallographic data of $\{[Ln(hip)(Hhip)(H_2O)_2], 2H_2O\}_\infty$ with Ln=La, Sm, Tb and Er.

	1	2	3	4
formula	$C_{16}H_{17}O_{14}La$	$C_{16}H_{17}O_{14}Tb$	$C_{16}H_{17}O_{14}Er$	$C_{16}H_{17}O_{14}Sm$
Mw	572.21	592.22	600.56	583.65
Crystal system	Triclinic	Triclinic	Triclinic	Triclinic
Space group	*P*1	*P*1	*P*1	*P*1
a(Å)	9.1578(7)	9.0089(7)	8.9767(8)	9.0534(8)
b(Å)	9.9548(8)	9.7974(9)	9.7531(11)	9.8512(8)
c(Å)	12.6503(11)	12.5504(9)	12.5276(11)	12.5830(11)
α(°)	102.1310(10)	102.6980(10)	102.7960(10)	102.5440(10)
β(°)	103.2110(10)	103.1190(10)	103.1610(10)	103.1040(10)
ϒ(°)	109.3780(10)	109.4130(10)	109.4070(10)	109.4140(10)
V ($Å^3$)	1006.47(14)	963.50(13)	953.13(16)	977.19(15)
Z, ρ_{calc} (g/cm^3)	2, 1.888	2, 2.041	2, 2.093	2, 1.984
GOF on F^2	1.06	1.063	1.124	1.032
R	0.0205	0.0182	0.0238	0.0250
Rw	0.0486	0.0445	0.0605	0.0611
CCDC number	638119	638120	638121	630261

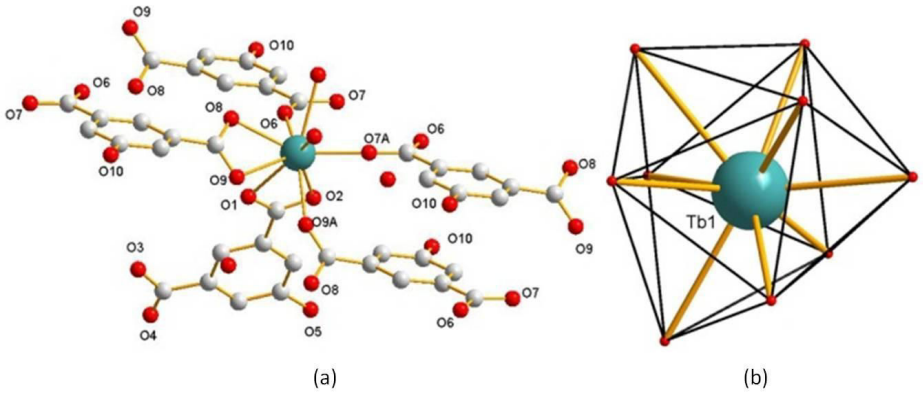

Figure 2.5 (a) Coordination environment and (b) coordination geometry of $\{[Tb(hip)(Hhip)(H_2O)_2], 2H_2O\}_\infty$.

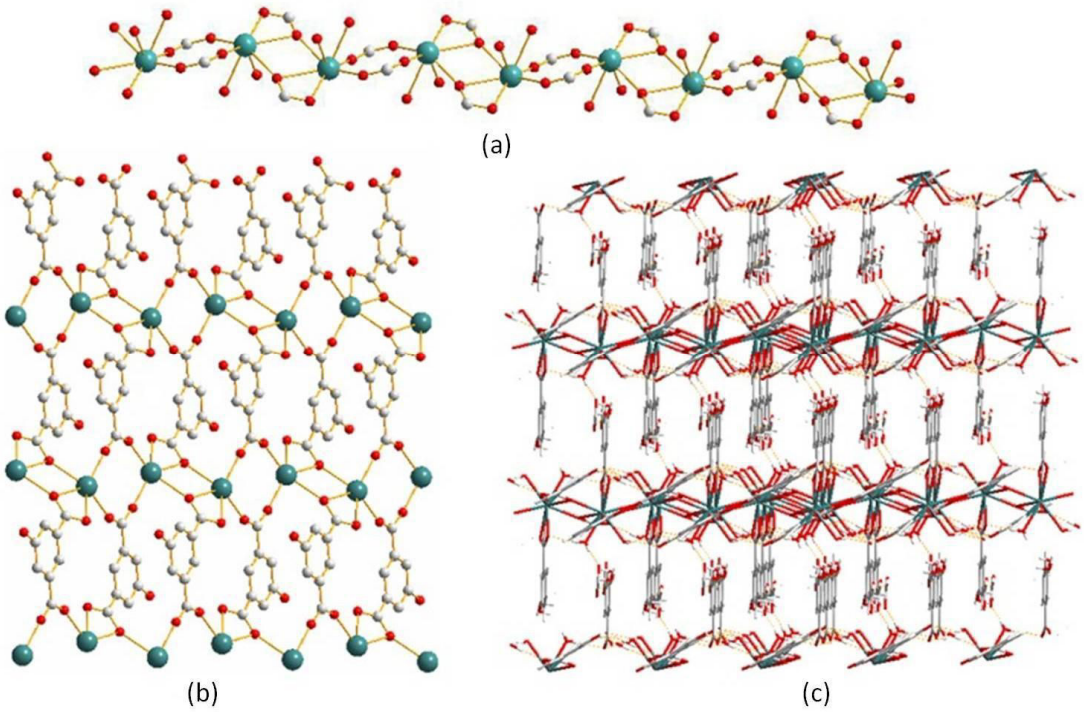

Figure 2.6 (a) 1D chain Tb-O-C-O-Tb, (b) 2D-layer structure and (c) 3D structure of compound $\{[Tb(hip)(Hhip)(H_2O)_2], 2H_2O\}_\infty$

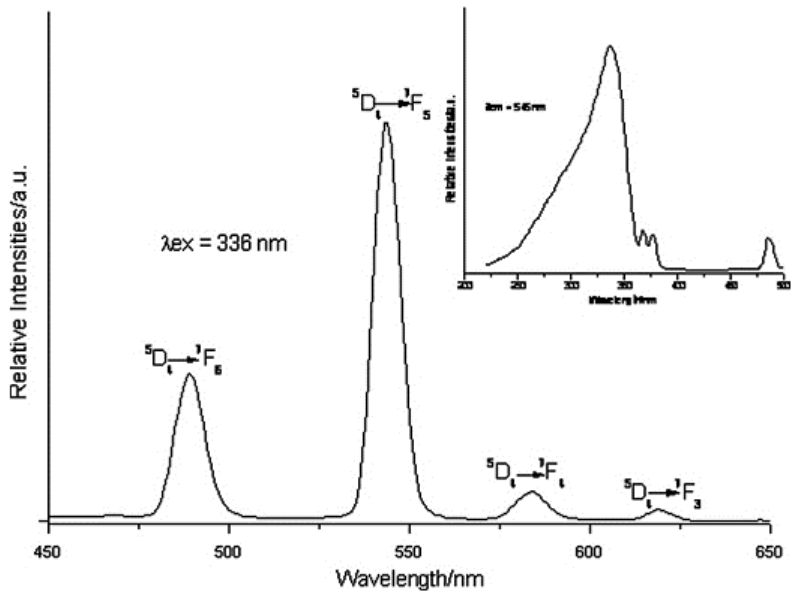

Figure 2.7 Excitation spectrum (λ_{em} = 545 nm) and emission spectrum (λ_{exc} = 336 nm) of $\{[Tb(hip)(Hhip)(H_2O)_2], 2H_2O\}_\infty$.

Recently, in 2012, Liu C.S. *et al.* prepared two novel coordination polymers $[La(hip)(OH)]_\infty$ and $\{[Ho_2(hip)_3(H_2O)_2], H_2O\}_\infty$ by hydrothermal reactions.

$[La(hip)(OH)]_\infty$ crystallizes in the monoclinic system, space group P2(1)/c (Table 2.3). The crystal structure consists of one La^{3+} ion which is nine-coordinated and surrounded by eight oxygen atoms from six hip^{2-} ligands and one oxygen atoms from one coordination water molecule. The central La^{3+} ion shows distorted tricapped trigonal prism coordination geometry (Figure 2.8).

Table 2.3 Crystallographic data of $[La(hip)(OH)]_\infty$ and $\{[Ho_2(hip)_3(H_2O)_2], H_2O\}_\infty$

	1	2
formula	$C_8H_5O_6La$	$C_{24}H_{18}O_{18}Ho_2$
Mw	336.03	924.24
Crystal system	Monoclinic	Monoclinic
Space group	P2(1)/c	P2(1)/c
a(Å)	9.9715(5)	10.7636(11)
b(Å)	11.7086(6)	14.3485(13)
c(Å)	7.3056(3)	17.528(2)
α(°)	90	90
β(°)	91.439(4)	102.116(11)
ϒ(°)	90	90
V ($Å^3$)	852.68(7)	2646.7(5)
Z, ρ_{calc} (g/cm^3)	4, 2.618	4, 2.319
GOF on F^2	1.129	1.069
R	0.0245	0.0578
Rw	0.0505	0.1628
CCDC number	853405	853406

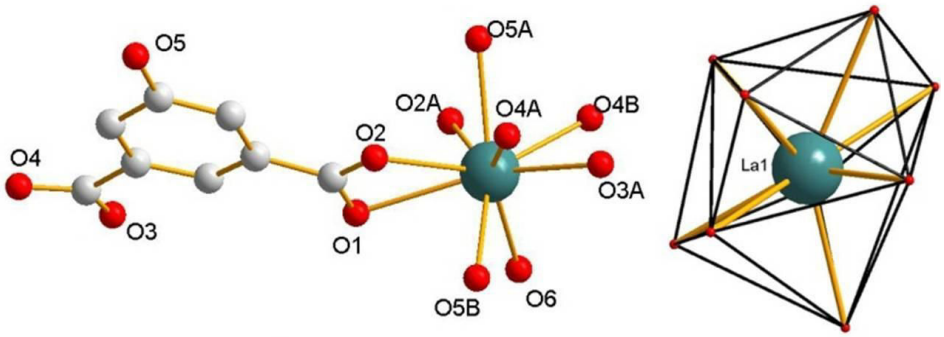

Figure 2.8 (a) Coordination environment and (b) Coordination geometry of the La^{3+} ion in $[La(hip)(OH)]_\infty$.

In compound $[La(hip)(OH)]_\infty$, the carboxylate groups of H_2hip ligand are fully deprotonated. The hydroxide group (O5) and two carboxylate groups act as bridges to connect La^{3+} ions forming a 1D molecular chain (Figure 2.9a). Based on the linkage of carboxylate groups, the 1D chains generate infinite 2D layers (Figure 2.9b), and then the hydroxyde groups further bridge the 2D layers to form a 3D network (Figure 2.9c). The authors explained the structure from the topology, and defined the structure as a bimodal (6,6)-connected network with the point (Schläfli) symbol of $(4^9.6^6)(4^{12}.6^3)$. [7]

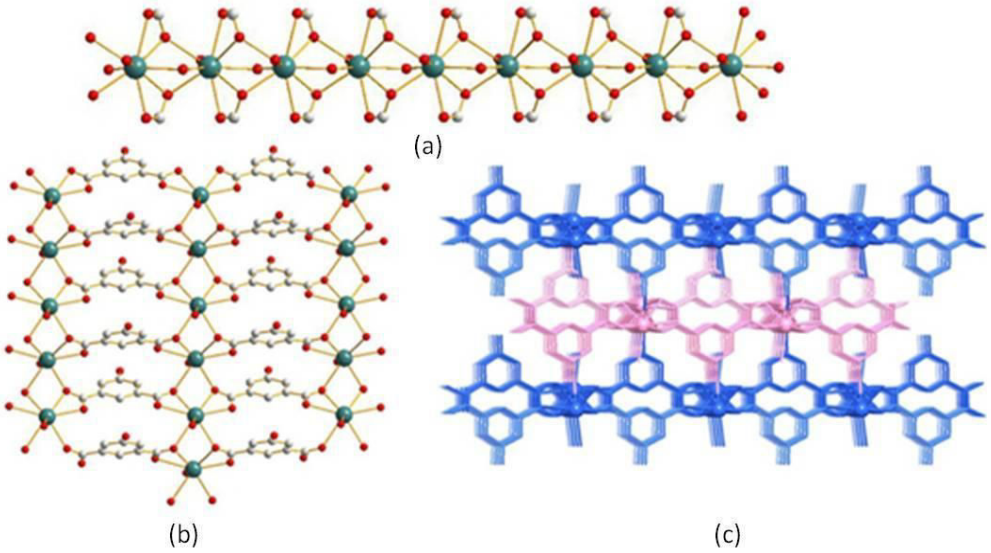

Figure 2.9 (a) 1D chain Tb-O-C-O-Tb, (b) 2D layer structure and (c) 3D structure of $[La(hip)(OH)]_{\infty}$.

$\{[Ho_2(hip)_3(H_2O)_2],H_2O\}_{\infty}$ features a 2D coordination framework, and the crystal structure contains two crystallographically independent Ho^{3+} ions which are both seven-coordinated and show distorted pentagonal-bipyramidal geometries. The two Ho^{3+} ions have different coordination environments. One is surrounded by seven oxygen atoms from six distinct hip^{2-} ligands and the other one is surrounded by five oxygen atoms from five different hip^{2-} ligands and two oxygen atoms from two coordination water molecules (Figure 2.10).

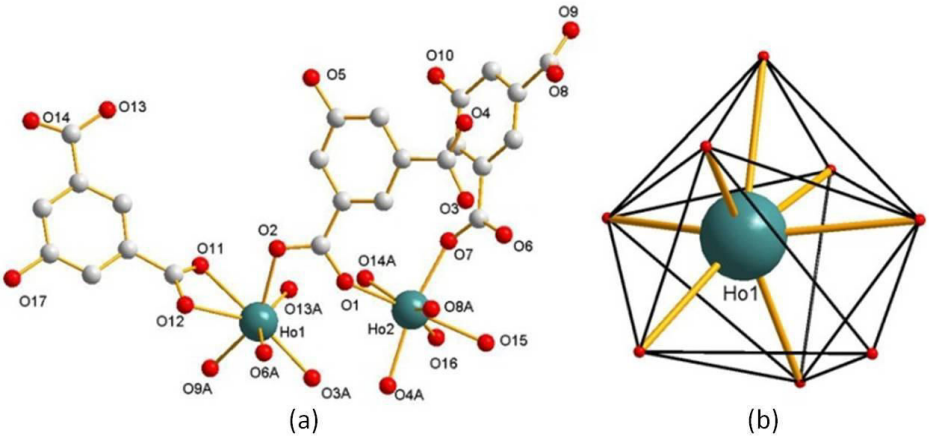

Figure 2.10 (a) Coordination environment and (b) coordination geometry for $\{[Ho_2(hip)_3(H_2O)_2], H_2O\}_{\infty}$.

In the Ho-containing compound, the carboxylate groups are deprotonated and bind Ho^{3+} ions according to two coordination modes (Figure 2.11). Mode 1 acts as a bridge to form infinite 1D chains (Figure 2.12a). Then, 1D molecular chains are connected together through the linkage of mode 2 to generate a 2D layered molecular structure (Figure 2.12b). $\{[Ho_2(hip)_3(H_2O)_2], H_2O\}_{\infty}$ was defined as a 2D (3,6)-connected $(3^2.4)(3^4.4^3.5^3.6^5.7)$ topological net.

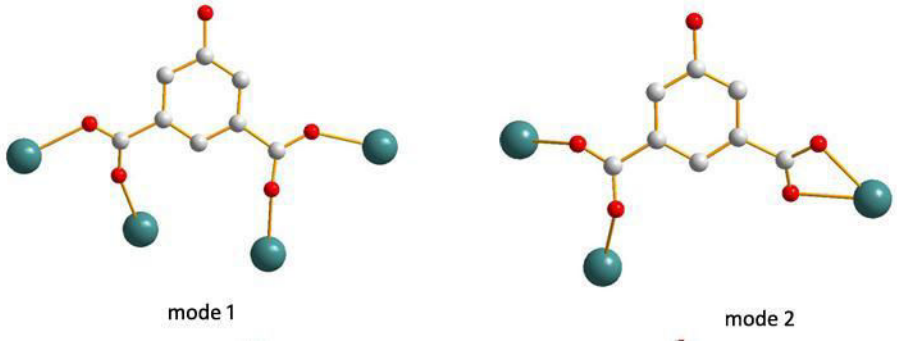

Figure 2.11 Coordination modes of hip^{2-} ligands in $\{[Ho_2(hip)_3(H_2O)_2], H_2O\}_\infty$.

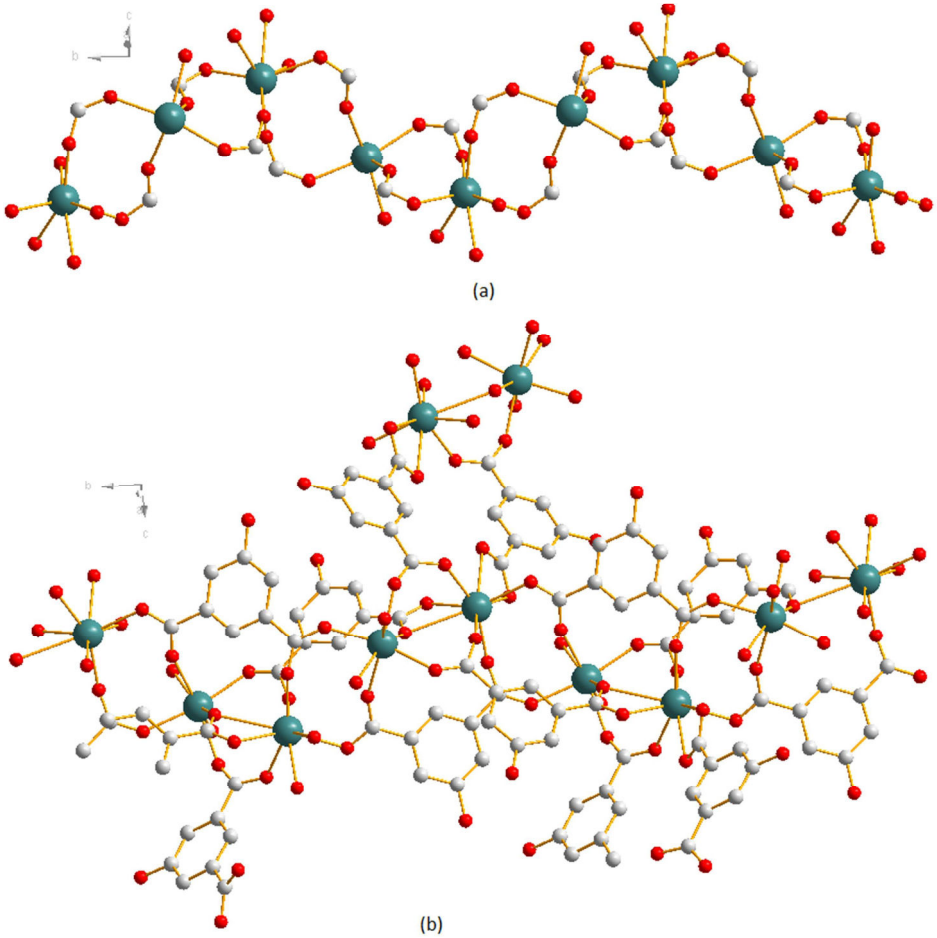

Figure 2.12 (a) 1D chain Ho-O-C-O-Ho, (b) 2D layer structure of $\{[Ho_2(hip)_3(H_2O)_2], H_2O\}_\infty$.

2.2 Ligand nip^{2-}.

The ligand 5-Nitroisophthalic acid (H_2nip) has been chosen because it has the good following characteristics:

1) It is a rigid benzene-polycarboxylate ligand and possesses good chemical and thermal stabilities;[8]
2) Its dicarboxlate groups can adopt various modes to coordinate metal ions and is suitable for the design of high-dimensional coordination polymers;
3) The nitrite group ($-NO_2$) is an electron-withdrawing group .[9]

There are a lot of reports about transitional metal coordination compounds with H_2nip acid only[10] or with H_2nip acid and other organic ligands [11] We have restricted our interest to the works devoted to rare earth coordination compounds based on ligand nip^{2-} only. In addition, some crystals which have been prepared in organic solvent[12] are not summarized here.

The first series of rare earth coordination polymers based on acid H_2nip was reported by Y. X. Ren's group in 2006[13] and 2008[14]. They synthesized six coordination polymers $[Ln(nip)(Hnip)(H_2O)_2,\ 2H_2O]_\infty$ (Ln = Sm, Gd, Dy, Y, Ho and Er) by hydrothermal reactions. X-ray diffraction measurements reveal that all six compounds are isomorphic. They crystallize in the triclinic system, space group P-1 (Table 2.4). The crystallographically independent lanthanide ion is eight-coordinated by two oxygen atoms from $Hnip^-$ anions, four oxygens atoms from nip^{2-} and two oxygen atoms from coordination water molecules. Its coordination geometry can be described as an antiprismatic geometry (Figure 2.13).

Table 2.4 Crystallographic data of $[Ln(nip)(Hnip)(H_2O)_2,\ 2H_2O]_\infty$ with Ln = Sm, Gd, Dy, Ho, Y or Er

	1	2	3	4	5	6
formula	$C_{16}H_{15}N_2O_{16}Sm$	$C_{16}H_{15}N_2O_{16}Gd$	$C_{16}H_{15}N_2O_{16}Dy$	$C_{16}H_{15}N_2O_{16}Y$	$C_{16}H_{15}N_2O_{16}Ho$	$C_{16}H_{15}N_2O_{16}Er$
Mw	641.65	648.55	653.8	580.21	656.23	658.56
Crystalsystem	Triclinic	Triclinic	Triclinic	Triclinic	Triclinic	Triclinic
Space group	P-1	P-1	P-1	P-1	P-1	P-1
a(Å)	9.6894 (9)	9.6834 (2)	9.637 (3)	9.6585(2)	9.6566(3)	9.6437(8)
b(Å)	10.5183 (1)	10.4879 (2)	10.431 (3)	10.4244(2)	10.4267(3)	10.4200(8)
c(Å)	13.5770 (1)	13.6043 (2)	13.585 (4)	13.5887(2)	13.5848(5)	13.5737(1)
α(°)	69.9480 (1)	67.5660 (1)	112.537 (5)	112.3460(1)	112.328(2)	112.2460(1)
β(°)	70.1000 (1)	69.7990 (1)	91.310 (5)	91.4400(1)	91.414(2)	91.4280(1)
Υ(°)	65.1870 (1)	65.0960 (1)	114.953 (4)	115.0090(1)	115.046(2)	115.0320(1)
V ($Å^3$)	1136.27 (2)	1129.89 (4)	1115.6 (6)	1118.23(2)	1117.84(6)	1115.66(2)
Z,ρ_{calc}(g/cm^3)	2, 1.875	2, 1.906	2, 1.946	2, 1.723	2, 1.950	2, 1.960
GOF on F^2	1.038	1.097	1.054	1.06	1.08	1.073
R	0.021	0.0177	0.0789	0.0311	0.0286	0.0237
Rw	0.0556	0.0472	0.2114	0.0854	0.0685	0.0599
CCDCnumber	294552	294553	294556	294554	294555	294557

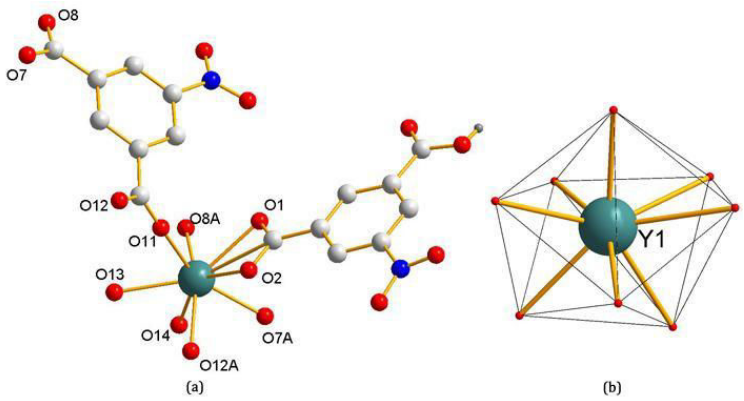

Figure 2.13 (a) Coordination environment and (b) coordination geometry for the lanthanide ion in $[Y(nip)(Hnip)(H_2O)_2,\ 2H_2O]_\infty$.

These eight-numbered rings link into 1D chains. Then, adjacent chains join with each other through the same nip^{2-} ligands to form a 2D molecular layer (Figure 2.14). In the crystal structure, there are two types of π-π stacking interactions: 1). a π-π stacking interaction between the nip^{2-} ligands with a face to face distance of about 3.4 Å; 2). another π-π stacking between $Hnip^{-}$ ligands between adjacent layers with a face to face distance of about 3.5 Å. There are also hydrogen bonds between the mono-chelate $Hnip^{-}$ ligands and the coordination water molecules (Figure 2.15). Both π-π stacking interactions and hydrogen bonds ensure layers packing to form a 3D molecular framework.

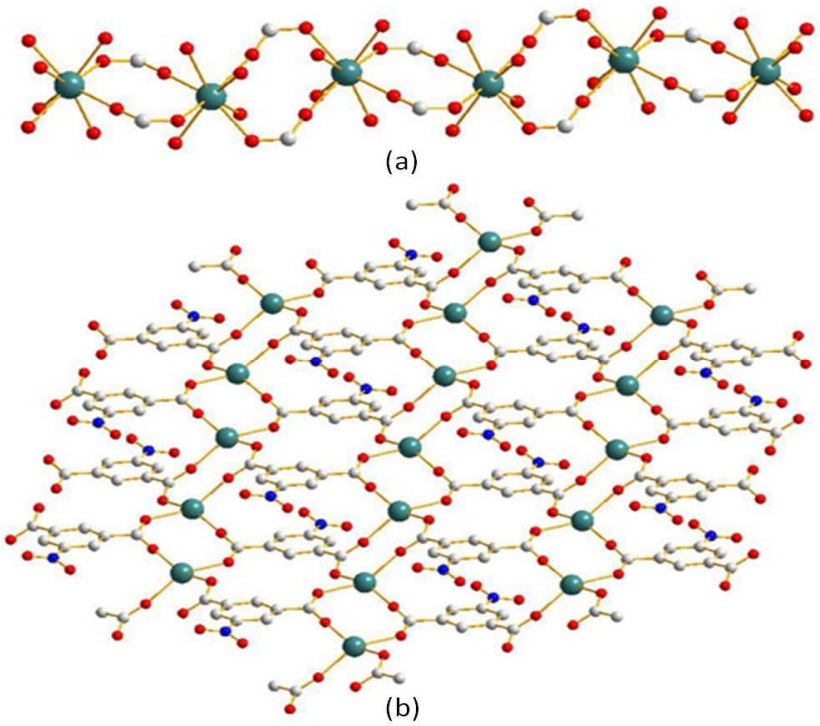

Figure 2.14 1D chain and 2D layer for $[Y(nip)(Hnip)(H_2O)_2,\ 2H_2O]_\infty$.

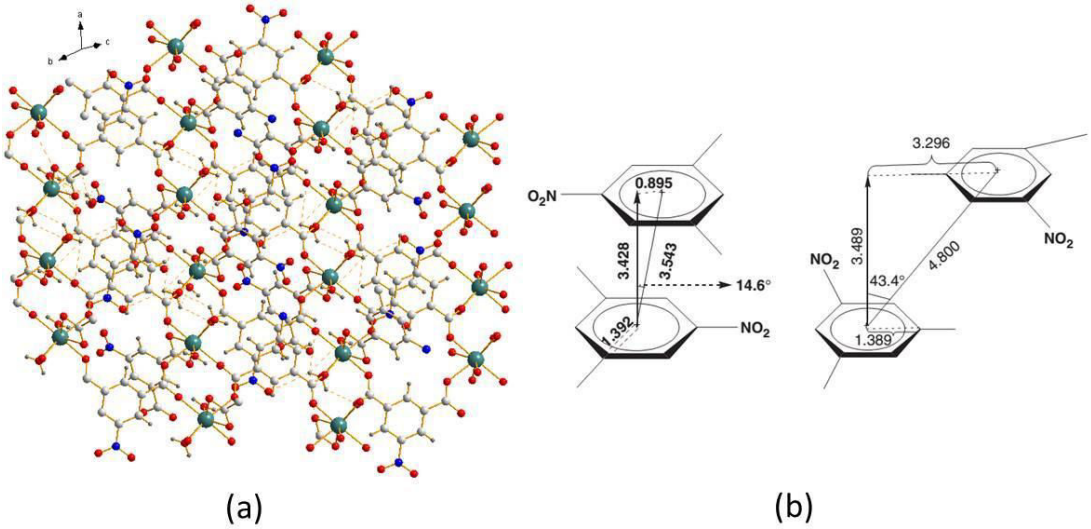

Figure 2.15 Hydrogen bonds and π-π stacking types in $[Y(nip)(Hnip)(H_2O)_2,\ 2H_2O]_\infty$.

In 2009[15], Bing Y. *et al* synthesized three new lanthanide coordination polymers with chemical formulae $[Y(nip)(Hnip)(H_2O), H_2O]_\infty$ and $[Ln(nip)(Hnip)(H_2O)_2, 2H_2O]_\infty$ with Ln= Eu or Tb by hydrothermal methods. Luminescent properties of the Eu- and Tb-compounds were also investigated.

$[Y(nip)(Hnip)(H_2O), \cdot H_2O]_\infty$ crystallizes in the monoclinic system, space group $P2_1/n$ (Table 2.5). There is one crystallographically independent Y^{3+} ion in the crystal structure. It is eight-coordinated by two oxygen atoms from a nip^{2-} ligand, three bridging oxygen atoms from three nip^{2-} ligands, two bridging oxygen atoms from two $Hnip^-$ ligands, and one oxygen atom from a coordination water molecule. Its coordination geometry is close to a trigonal dodecahedron (Figure 2.16).

Table 2.5 Crystallographic data of $[Y(nip)(Hnip)(H_2O), H_2O]_\infty$ and $[Ln(nip)(Hnip)(H_2O)_2, 2H_2O]_\infty$ with Ln= Eu or Tb

	1	2	3
formula	$C_{16}H_{11}N_2O_{14}Y$	$C_{16}H_{15}N_2O_{16}Eu$	$C_{16}H_{15}N_2O_{16}Tb$
Mw	544.18	643.26	650.22
Crystal system	Monoclinic	Triclinic	Triclinic
Space group	P2(1)/n	$P\bar{1}$	$P\bar{1}$
a(Å)	13.9587(15)	9.6860(6)	9.6561(14)
b(Å)	8.7386(9)	10.5102(7)	10.4608(12)
c(Å)	16.6299(18)	13.5884(8)	13.5963(14)
α(°)	90	67.7540(10)	67.4990(10)
β(°)	106.4220(10)	69.9160(10)	69.7850(10)
ϒ(°)	90	65.0680(10)	65.0350(10)
V ($Å^3$)	1945.8(4)	1132.86(12)	1122.2(2)
Z, ρ_{calc} (g/cm^3)	4, 1.858	2, 1.886	2, 1.924
R	0.0392	0.0192	0.0240
Rw	0.1051	0.0452	0.0532
GOF on F^2	1.034	1.036	1.039
CCDC number	644528	653117	653118

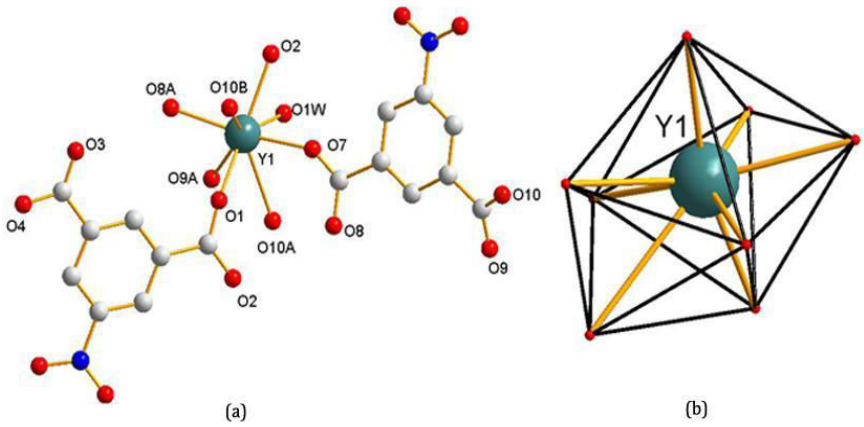

Figure 2.16 (a) Coordination environment and (b) coordination geometry of yttrium ions in $[Y(nip)(Hnip)(H_2O), H_2O]_\infty$.

Two kinds of anions, $Hnip^-$ and nip^{2-} exist in the asymmetric unit. They act as bridges to form three helical strands: one is formed from $Hnip^-$ ligand and the two others are formed from nip^{2-} ligands. The three kinds of helical-shaped chains are same-handed and intersect each other through Y^{3+} ions, thus forming a unique Y-carboxylate chain. These chains are further linked to lead to 2D layers (Figure 2.17). The 2D layers are connected by hydrogen bonds to form a 3D molecular framework which is further stabilized by π-π stacking interactions.

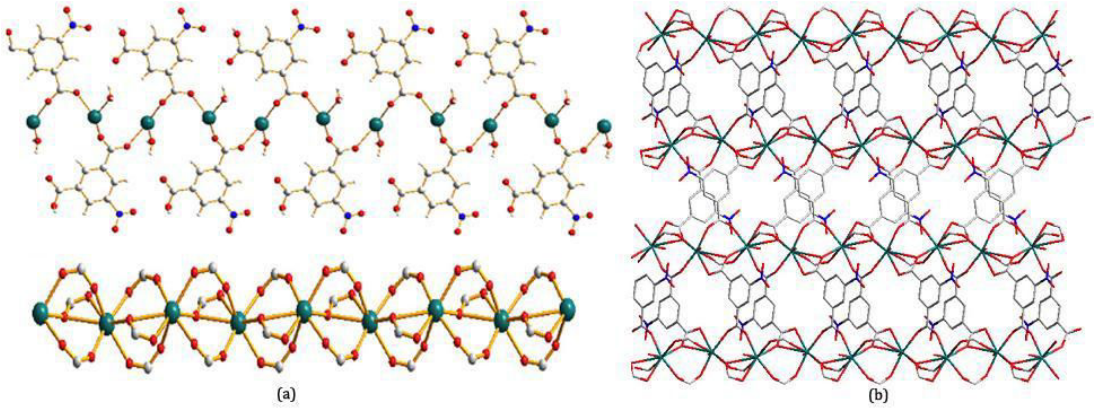

Figure 2.17 Helical-shaped chains and 2D layer structures in $[Y(nip)(Hnip)(H_2O), H_2O]_\infty$.

$[Eu(nip)(Hnip)(H_2O)_2,2H_2O]_\infty$ and $[Tb(nip)(Hnip)(H_2O)_2, 2H_2O]_\infty$ are iso-structural. They crystallize in the triclinic system, space group P-*1* (Table 2.5). The lanthanide (Eu^{3+} or Tb^{3+}) ion is eight-coordinated by two oxygen atoms from one $Hnip^-$ ligand, four bridging oxygen atoms from four nip^{2-} ligands and two oxygen atoms from two coordination water molecules. Its coordination geometry is closed to a bicapped trigonal prism (Figure 2.18). In this crystal structure, only the carboxylate groups of nip^{2-} ligands bridge lanthanide ions to form 1D molecular chains. Adjacent chains are further cross-linked to lead to 2D layers (Figure 2.19). 2D layers are connected by hydrogen bonds to form a pseudo 3D molecular framework.

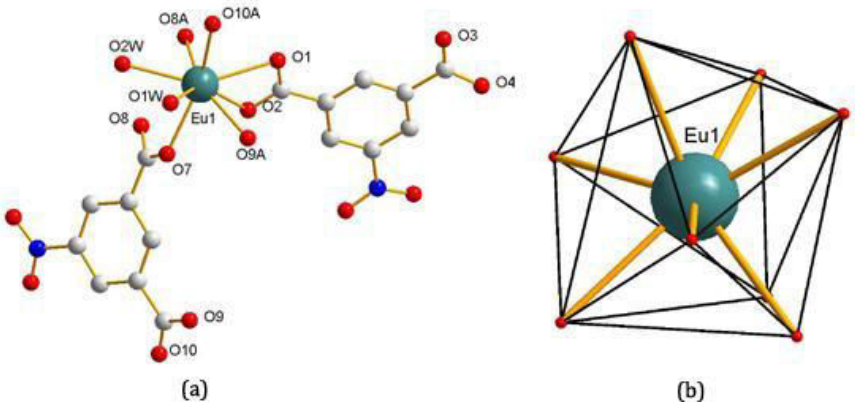

Figure 2.18 (a) Coordination environment and (b) coordination geometry for lanthanide ions in $[Eu(nip)(Hnip)(H_2O)_2, 2H_2O]_\infty$.

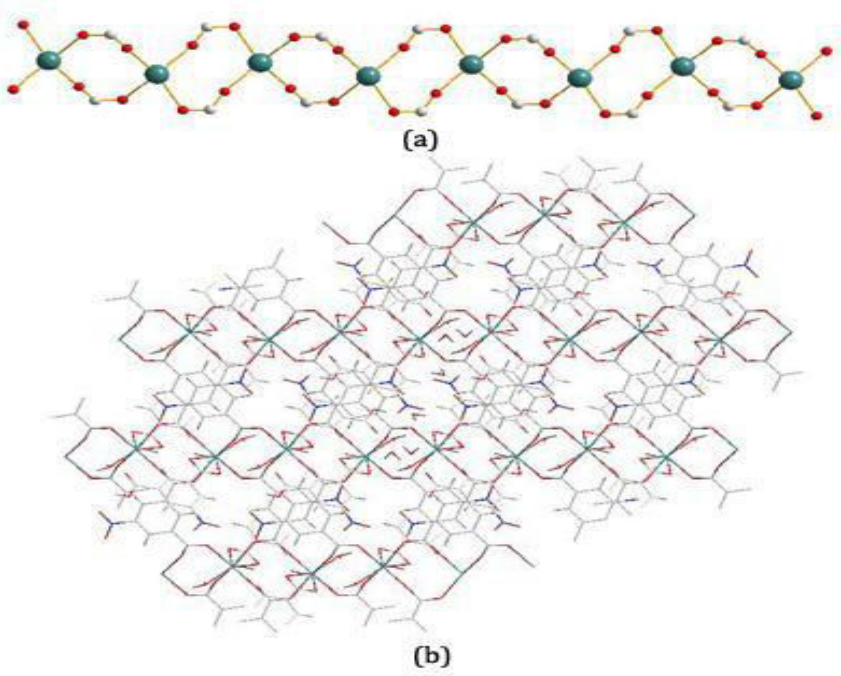

Figure 2.19 1D chain and 2D layer structures in $[Eu(nip)(Hnip)(H_2O)_2, 2H_2O]_\infty$.

Luminescent properties of the Eu- and Tb-based compounds have been studied in this publication. The isostructural $[Gd(nip)(Hnip)(H_2O)_2, 2H_2O]_\infty$ has also been synthesized and the triplet level of H_2nip (about 21786 cm^{-1}) estimated (Figure 2.20). Because the lowest triplet state is close to Tb^{3+} feeding levels, a back-energy transfer process occurs and the luminescence of the Tb-containing compound is not observed at room temperature. On the contrary, the Eu-containing compound exhibits red luminescence in the solid state at room temperature under direct excitation (at 392 nm) of Eu^{3+} ion. Excitation and emission spectra of compound $[Eu(nip)(Hnip)(H_2O)_2, 2H_2O]_\infty$ are reported in Figure 2.20.

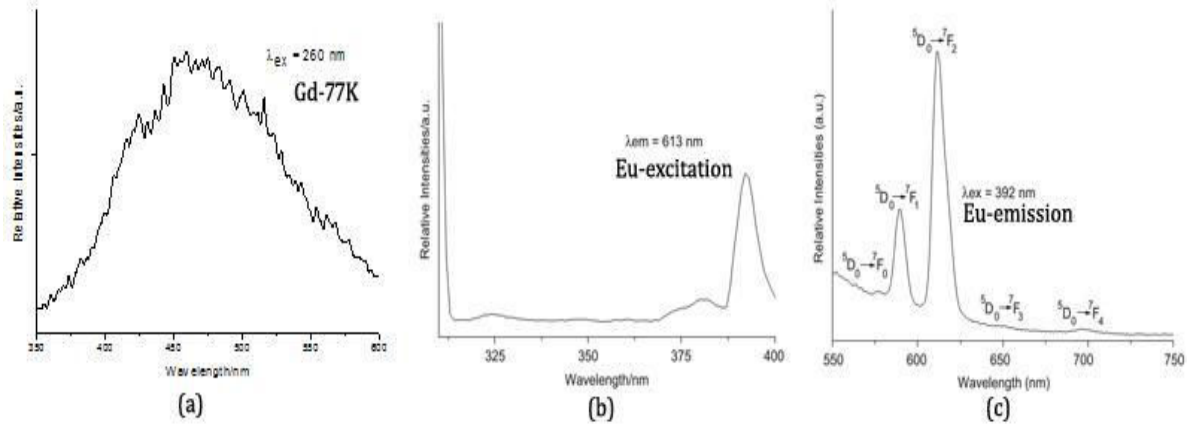

Figure 2.20 (a) Emission spectrum of $[Gd(nip)(Hnip)(H_2O)_2, 2H_2O]_\infty$ at 77K. (b,c) Excitation and emission spectra of compound $[Eu(nip)(Hnip)(H_2O)_2, 2H_2O]_\infty$.

Recently, in 2012, a new lanthanum-containing coordination polymer with chemical formula $[La_6(nip)_9(H_2O)_4, 4H_2O]_\infty$ has been reported by X.-F. Wang *et al.*[16] This compound was prepared under hydrothermal conditions and crystallizes in the orthorhombic system, space group *Ima2* (Table 2.6). In the crystal structure, there are three crystallographically

independent La^{3+} ions. La1 and La3 have the same coordination environments (Figure 2.21a). La (2) has another coordination environment (Figure 2.21b). La(1) and La(3) are deca-coordinated by nine oxygen atoms from carboxylate groups of seven nip^{2-} ligands and one oxygen atom from a coordination water molecule. La (2) is also deca-coordinated but all of its ten oxygen atoms belong to carboxylate groups from six nip^{2-} ligands. The three La^{3+} ions display dodecahedral geometries (Figure 2.21c). The La (1) and La (3) ions are bridged by three oxygen atoms from carboxylate groups and further connect La (1) ion by carboxylate groups to form a S-shaped molecular chain (Figure 2.22a). These S-shaped chains connect into two-dimensional layers and then such layers are covalently connected through carboxylate groups forming a three-dimensional molecular framework (Figure 2.22b).

Table 2.6 Crystallographic data of $[La_6(nip)_9(H_2O)_4, 4H_2O]_\infty$

	1
formula	$C_{72}H_{43}N_9O_{62}La_6$
Mw	2859.61
Crystal system	Orthorhombic
Space group	*I*ma2
a(Å)	9.7769(12)
b(Å)	28.239(3)
c(Å)	21.149(2)
α(°)	90
β(°)	90
ϒ(°)	90
V ($Å^3$)	5839.1(11)
Z, ρ_{calc} (g/cm^3)	2, 1.626
GOF on F^2	1.083
R	0.0413
Rw	0.1191
CCDC number	807014

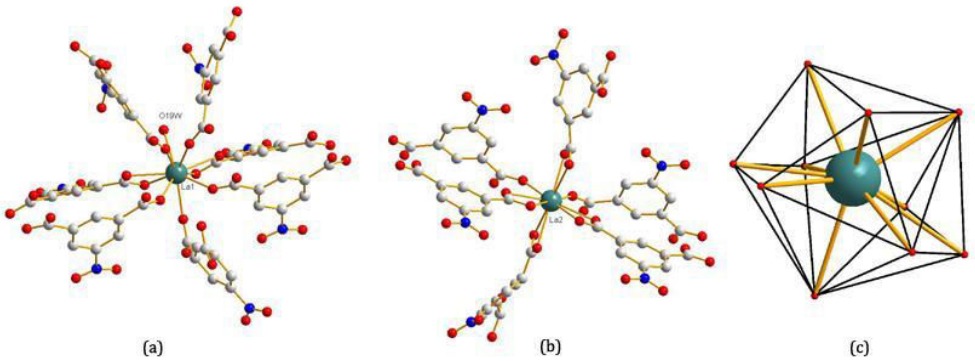

Figure 2.21(a, b) coordination environments of La(1) and La(2); (c) coordination geometry for the lanthanide ions in $[La_6(nip)_9(H_2O)_4, 4H_2O]_\infty$.

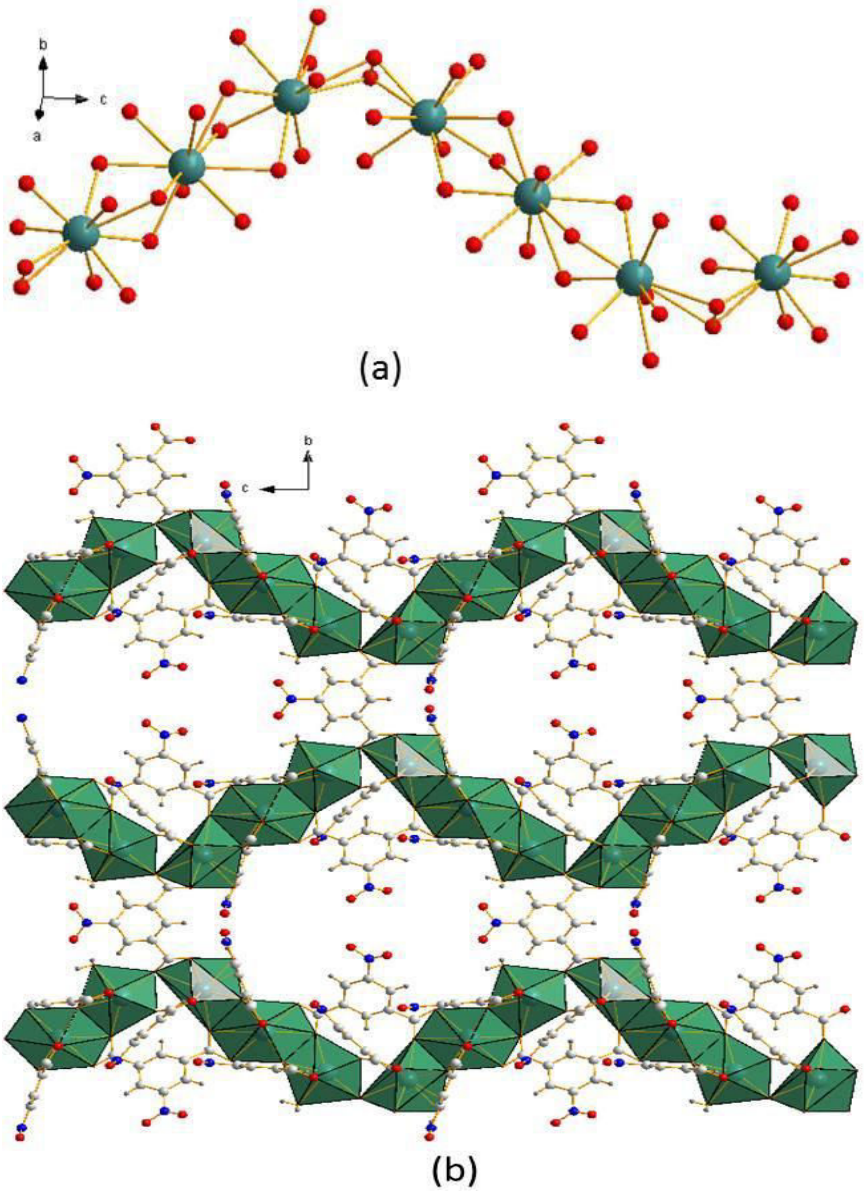

Figure 2.22 (a) S-shaped molecular chain and (b) 3D structure of $[La_6(nip)_9(H_2O)_4,4H_2O]_\infty$.

This crystal structure presents large channels with 2.3 × 2.0 nm^2 cross-section area. Luminescence of this compound has also been measured. As expected, the ligand and the compound $[La_6(nip)_9(H_2O)_4, 4H_2O]_\infty$ present similar emission spectra upon excitation at 284 nm in solid state at room temperature. This confirms that the luminescence behavior of $[La_6(nip)_9(H_2O)_4, 4H_2O]_\infty$ is a ligand–based emission.

2.3 Acid Hcpb.

Because 4-carboxyphenylboronic acid (Hcpb) acid presents both the acidic character of a Bronstëd acid and of a Lewis acid, it has been chosen as ligand to prepare new lanthanide-based coordination compounds. Pedireddi's team published the study of transition metals-based compounds[17] and the solid-state crystal structures of Hcpb and its hydrates[18] in 2006 and 2007, respectively. To the best of our knowledge, there is no lanthanide-based crystal structure which has been reported.

2.4 Ligand cda^{2-}.

The benzene core carboxylic acids have been often used to prepare coordination polymers. They have been proved to be good candidates for their rich coordination modes.[19] However, some N- or O- heterocyclic dicarboxylic acids such as pyridine or pyran-dicarboxylic acids have begun to attract people's interest because both their carboxylate oxygen atoms and nitrogen or oxygen atoms that belong to the heterocycle can coordinate the metal ions to form interesting frameworks.[20] Chelidonic acid (H_2cda) has been chosen because of its distinctive characteristics:

(1). the rigidity and high symmetry of H_2cda can cause the generation of ordered structures and at the same time reduce the possibility of lattice interpenetration.
(2). H_2cda has plenty coordination groups: two carboxylic groups, one ketone oxygen, and one pyran oxygen that can coordinate transition metal ions or lanthanide ions.
(3). H_2cda has two carbon-carbon double bonds within its heterocyclic ring. When H_2cda coordinate with metal ions, π-π stacking can occur.
(4). H_2cda present various linking modes with metal ions which can lead to a great diversity of crystal structures.

Some coordination polymers based on transition metals ions[21] or rare earths ions have been reported. We have summed up below the published works that involve rare earths.

As early as 1980, M. A. V. De Almeida *et al.* tried to use H_2cda to prepare lanthanide complexes for X-ray crystal structure determination. Unfortunately this expectation was not fulfilled, and only microcrystalline powders were obtained. Emission spectra of the Eu^{3+}-containing compounds show a very intense luminescence with characteristic sharp lines and allowing the symmetry of the chemical environment to be assigned. This work was cursory but constituted the first attempt of obtaining lanthanide-based coordination compounds with H_2cda as ligand.[22]

In 2005, S. Alves *et al.* prepared the complex $[Gd(cda)_3]^{3-}$, nH_2O and recorded its solid state emission spectrum (Figure 2.23) at 77k to estimate the energy of the triplet state of ligand cda^{2-} (about 21413 cm^{-1}).[23]

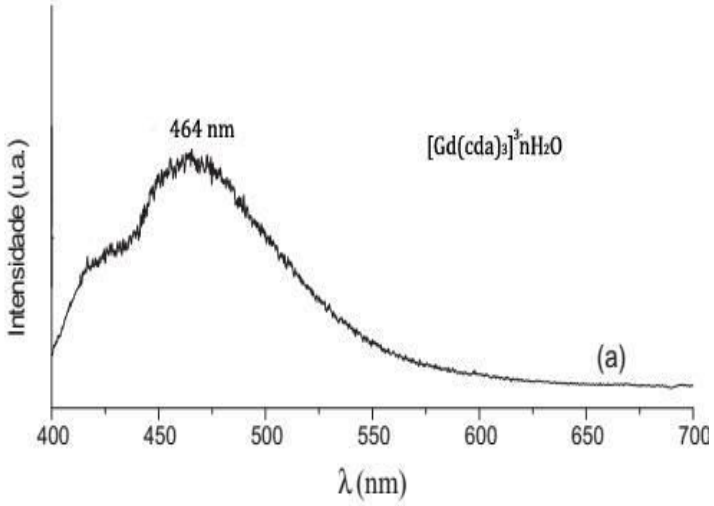

Figure 2.23 Solid state emission spectrum of $[Gd(cda)_3]^{3-}$, nH_2O at 77K.

In 2009, B. Zhao *et al.* succeeded in synthesizing the first three novel families of lanthanide-based coordination polymers with H_2cda as ligand under hydrothermal conditions. The three families have respective chemical formula: $[Ln(C_7O_6H_2)(OH)]_\infty$ (Ln= Pr, Nd, Sm) (Family 1), $[Ho(C_7O_6H_2)(OH)]_\infty$ (Family 2) and $[Pr(C_7O_6H_3)(C_2O_4)_{0.5}(H_2O)_2]_\infty$ (Family 3), respectively.[24]

Family 1 $Ln(C_7O_6H_2)$ (Ln= Pr, Nd, Sm). Single crystal X-ray diffraction analysis reveals that the three compounds are isostructural. They crystallize in the orthorhombic system, space group *Pnma* (Table 2.6).

Table 2.6 Crystallographic data $[Ln(C_7O_6H_2)(OH)]_\infty$ (Ln= Pr, Nd, Sm) (Family 1), $[Ho(C_7O_6H_2)(OH)]_\infty$ (Family 2) and $[Pr(C_7O_6H_3)(C_2O_4)_{0.5}(H_2O)_2]_\infty$ (Family 3)

	Family 1	Family 2	Family 3
Formula	$C_7H_2O_6Pr$	$C_7H_4O_7Ho$	$C_8H_7O_{10}Pr$
Mr	323	365.03	404.05
crystal system	orthorhombic	orthorhombic	monoclinic
space group	*Pnma*	*Pnma*	*C2/c*
a(Å)	7.9153(18)	19.476(5)	21.507(2)
b(Å)	10.228(2)	10.024(3)	6.8401(8)
c(Å)	9.528(2)	4.3060(12)	16.2843(19)
α(°)	90	90	90
β(°)	90	90	120.453(2)
ϒ(°)	90	90	90
V ($Å^3$)	771.4(3)	840.6(4)	2065.1(4)
Z, ρ_{calc} (g/cm^3)	4, 2.781	4, 2.884	8, 2.599
GOF on F^2	1.163	1.127	1.295
R	0.0218	0.0404	0.0307
Rw	0.0535	0.1009	0.0649
CCDC number	748868	748871	748872

In this crystal structure, there is one crystallographically independent Ln^{3+} ion and one cda^{2-} ligand in the asymmetric unit. Six oxygen atoms from carboxylate groups of five cda^{2-} ligands and two oxygen atoms from ketone functions (O3A and O3B) from another two

cda^{2-} ligands constitute the coordination sphere of Ln^{3+} ions. (Figure 2.24a) The coordination geometry for the lanthanide ion can be described as a distorted bicapped trigonal prism in which O3 act as the capping atom (Figure 2.24b). In the c direction, the Ln^{3+} ions forms a 1D molecular chain by the bridging of carboxylate and ketone oxygen atoms. It is further connected into a 3D molecular framework by carboxylate groups (Figure 2.25).

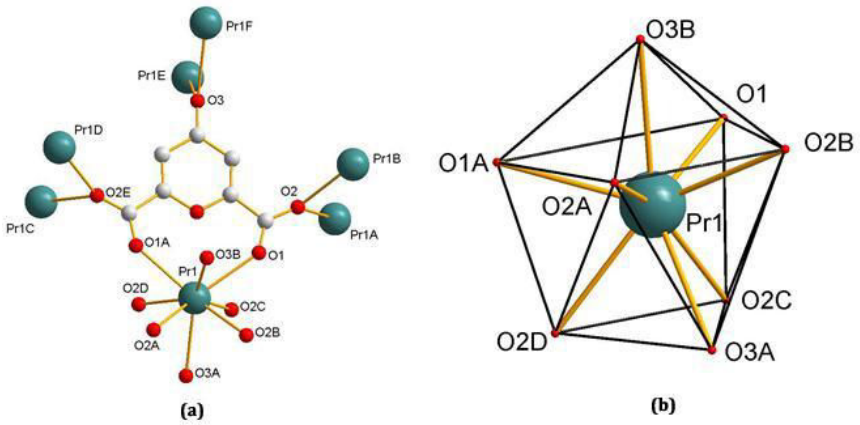

Figure 2.24 (a) cda^{2-} environment and (b) coordination geometry of the lanthanide ion for $[Pr(C_7O_6H_2)(OH)]_\infty$.

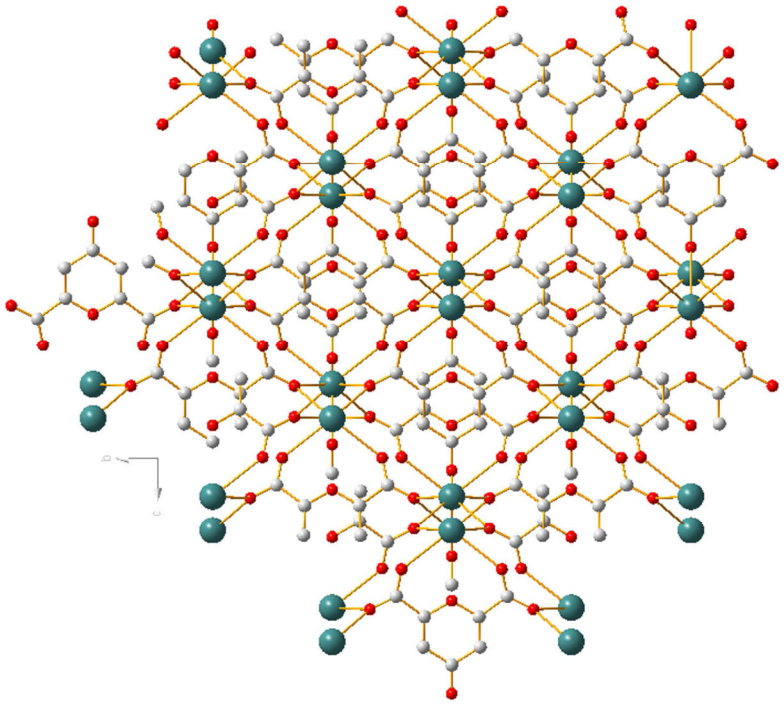

Figure 2.25 Projection view of the 3D molecular framework of $[Pr(C_7O_6H_2)(OH)]_\infty$.

The authors also studied the UV absorption in solid state for the Pr^{3+}- and Nd^{3+}-containing compounds (Figure 2.26). The UV-visible spectra show typical f-f transitions of Pr^{3+} and Nd^{3+} ions. The Pr-containing compound has four main absorption peaks : 592 ($^3H_4 \rightarrow {}^1D_2$), 485 ($^3H_4 \rightarrow {}^3P_0$), 471 ($^3H_4 \rightarrow {}^3P_1$), and 446nm ($^3H_4 \rightarrow {}^3P_2$). The Nd-containing compound presents the typical peaks of Nd^{3+} ions: 867 ($^4I_{9/2} \rightarrow {}^4F_{3/2}$), 798 ($^4I_{9/2} \rightarrow {}^4F_{5/2}+{}^2H_{9/2}$), 742 ($^4I_{9/2} \rightarrow {}^4S_{3/2}+{}^2F_{7/2}$), 679 ($^4I_{9/2} \rightarrow {}^4F_{9/2}$), 627 ($^4I_{9/2} \rightarrow {}^2H_{11/2}$), 580 ($^4I_{9/2} \rightarrow {}^2G_{7/2}+{}^2G_{5/2}$), 523 ($^4I_{9/2} \rightarrow {}^2K_{13/2}+{}^4G_{7/2}+{}^4G_{9/2}$), and 461-475 nm ($^4I_{9/2} \rightarrow {}^2K_{15/2}+{}^4D_{3/2}+{}^2G_{9/2}$).

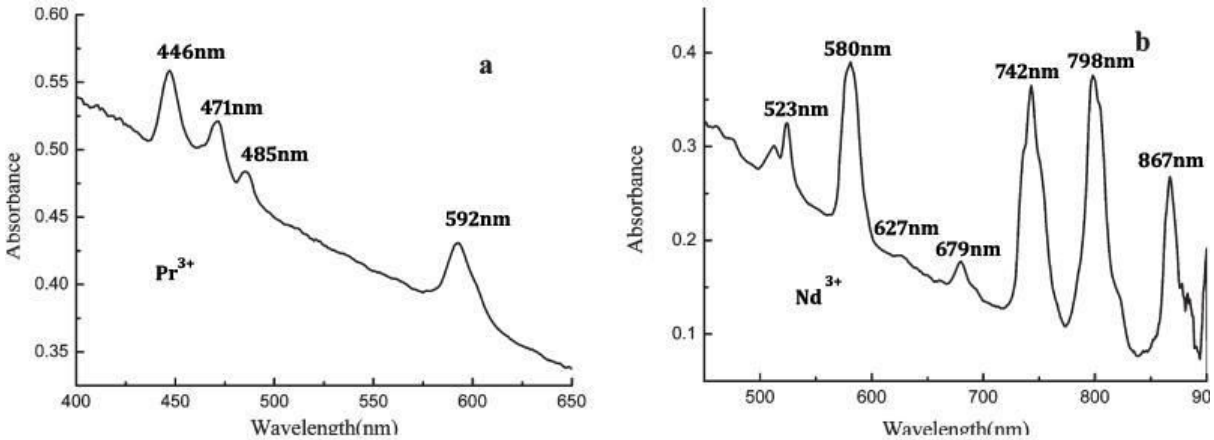

Figure 2.26 The UV-vis absorption spectra of $[Pr(C_7O_6H_2)(OH)]_\infty$ and $[Nd(C_7O_6H_2)(OH)]_\infty$ in the solid state.

Family 2 $[Ho(C_7O_6H_2)(OH)]_\infty$ X-ray structural analysis shows that $[Ho(C_7O_6H_2)(OH)]_\infty$ also crystallizes in the orthorhombic system, space group *Pnma* (Table 2.6). In this crystal structure, four carboxylate oxygen atoms, one ketone oxygen atom and one coordination water molecule oxygen atom (O5) constitute a six-coordinated sphere of Ho^{3+} (Figure 2.27a). The coordination geometry can be described as a very distorted octahedron (Figure 2.27b). The cda^{2-} ligand acts as a μ_5 ligand. Each carboxylate group has one oxygen atom coordinated to two Ho^{3+} ions and the ketone oxygen atom is coordinated to one Ho^{3+} ion.

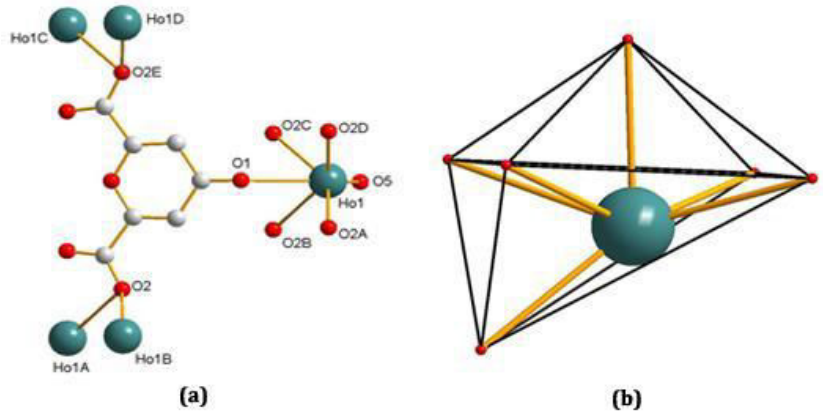

Figure 2.27 (a). cda^{2-} environment and (b). coordination geometry of the Ho^{3+} ionin $[Ho(C_7O_6H_2)(OH)]_\infty$.

From this figure, one can notice that the coordination polyhedron of the Ho^{3+} ion is quite strange and should be confirmed.

The Ho^{3+} ions are connected into a 1D molecular chain through carboxylic oxygen atoms, and then further assembled into a 2D double-layer structure by the linking of the ligand (Figure 2.28). The authors didn't study any physical property of this compound.

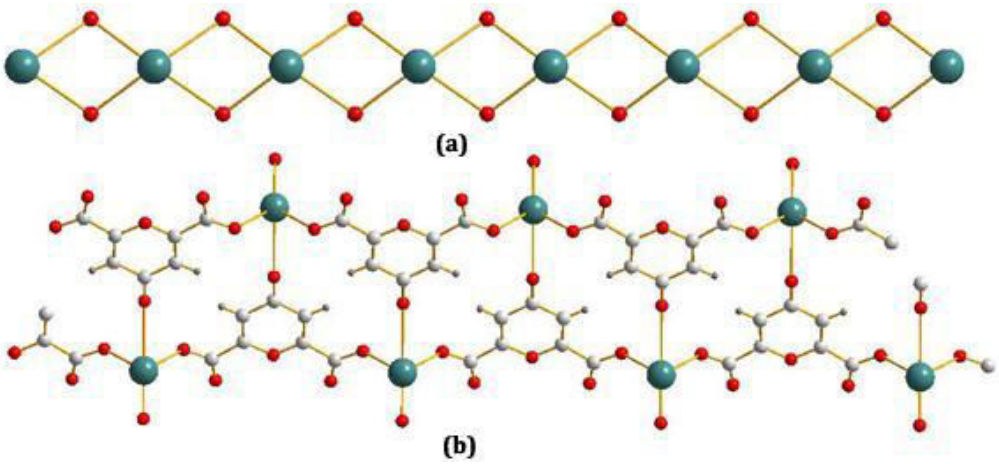

Figure 2.28 View along the a direction of the 1D molecular chain and of the 2D double-layer for $[Ho(C_7O_6H_2)(OH)]_\infty$.

Family 3 $[Pr(C_7O_6H_2)(C_2O_4)_{0.5}(H_2O)_2]_\infty$. Single crystal X-ray diffraction analysis reveals that the compound crystallizes in the monoclinic system, space group *C2/c* (Table 2.6). In this crystal structure, one crystallographically independent Pr^{3+} ion is coordinated to one cda^{2-} ligand; half oxalate which is the product of the decomposition of the ligand, and two coordination water molecules. Coordination geometry can be described as a distorted bicapped square antiprism (Figure 2.29).

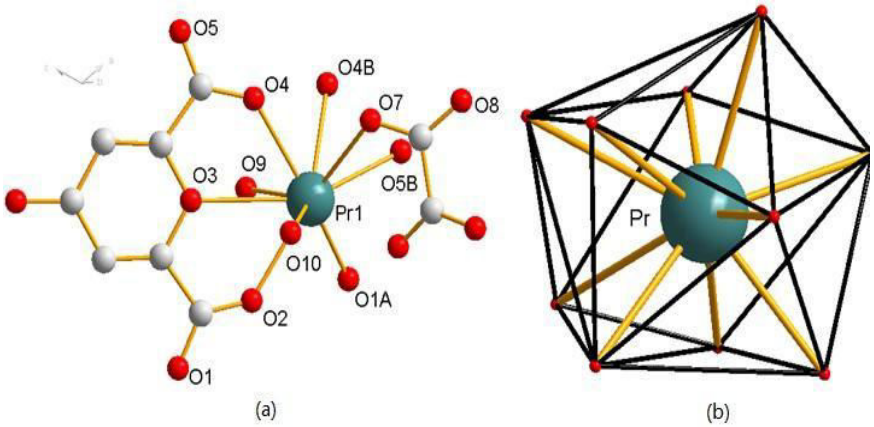

Figure 2.29 Pr^{3+} environment and coordination geometry in $[Pr(C_7O_6H_2)(C_2O_4)_{0.5}(H_2O)_2]_\infty$.

In the crystal structure, two carboxylic oxygen atoms from two cda^{2-} ligands and two oxalate groups act as bridges that alternatively link the Pr^{3+} ions to form a 1D zigzag molecular chains. The 1D chains are further assembled into a 2D layer by carboxylate bridges. Then the 2D layer are further connected into a 3D molecular framework by other carboxylate bridges (Figure 2.30).

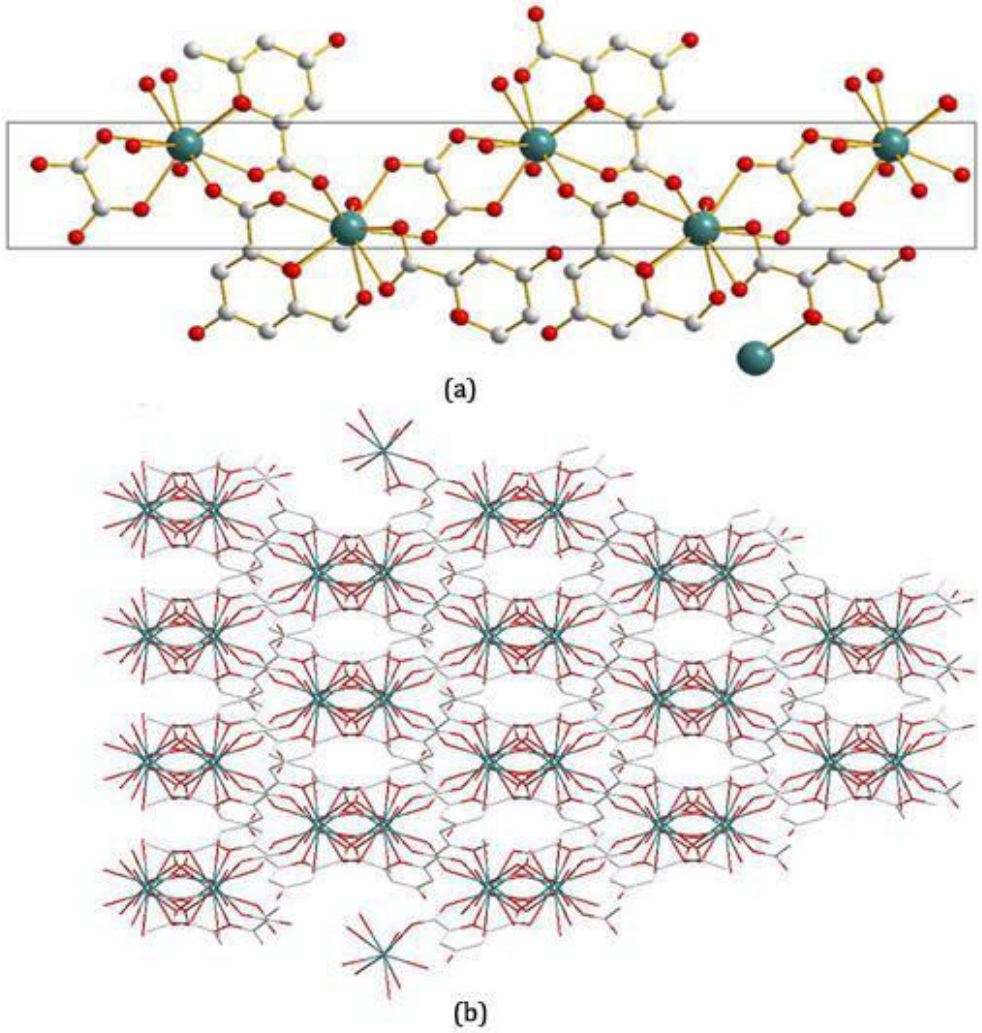

Figure 2.30 Projection views of the 1D chain and 3D molecular framework of $[Pr(C_7O_6H_2)(C_2O_4)_{0.5}(H_2O)_2]_\infty$.

The magnetic susceptibility of this compound was mesured from 2 to 300 K under 100 Oe field. $\chi_M T$ value is equal to 1.72 cm^3 K mol^{-1} at room temperature which is close to the theoretical value (1.60 cm^3 K mol^{-1}). Then, $\chi_M T$ value slowly desceases on cooling and reaches a minimun value of 0.12 cm^3 K mol^{-1} at 2K.

In 2010, W. Shi's team published four new series of lanthanide-based coordination polymers with chelidonic acid (H_2cda) as ligand. The crystal structrures in this publication depend on the involved lanthanide ions : Type I (1D) for the lighter rare earth (Nd) ; Type II (2D) for the middle rare earth (Eu, Gd, Tb, Dy and Ho) ; Type III (binuclear) and Type IV (two independent chains) for the heaviest rare earths (Er and Tm; or Yb).[25]

Table 2.7 Crystallographic data of the four crystal structures (Type I to IV).

	Type I	Type II	Type III	Type IV
Formula	$C_{21}H_{38}Nd_2O_{34}$	$C_{21}H_{30}Eu_2O_{30}$	$C_{16}H_{32}Er_2O_{30}$	$C_{16}H_{26}Yb_2O_{27}$
Mw	1122.99	1066.37	1038.92	996.45
Crystal system	Triclinic	Triclinic	Triclinic	Triclinic
Space group	P-1	P-1	P-1	P-1
a(Å)	7.641(2)	9.4966(19)	6.3385(13)	7.4895(15)
b(Å)	13.150(4)	9.6020(19)	10.340(2)	11.093(2)
c(Å)	18.236(5)	10.144(2)	13.700(3)	16.875(3)
α(°)	77.837(14)	69.48(3)	108.60(3)	86.68(3)
β(°)	80.450(14)	68.52(3)	94.42(3)	80.69(3)
ϒ(°)	80.031(15)	83.79(3)	106.38(3)	77.65(3)
V ($Å^3$)	1748.3(9)	805.9(3)	802.6(3)	1351.1(4)
Z, ρcalc (g/cm^3)	2, 2.133	1, 2.197	2, 2.112	2, 2.449
GOF on F^2	1.085	1.112	1.048	1.06
R	0.0459	0.0653	0.0255	0.0360
Rw	0.1073	0.1668	0.0653	0.1005
CCDC number	716750	716751	716757	716759

Type I $\{[Nd_2(C_7O_6H_2)_3(H_2O)_{11}], 5H_2O\}_\infty$. This compound crystallizes in the triclinic system, space group $P\bar{1}$ (Table 2.7). There are two crystallographically independent Nd^{3+} ions in the asymetric unit. Nd1 is nine-coordinated. Its coordination geometry is best described by a monocapped square antiprism. Nd2 is also nine-coordinated (two carboxylate oxygen from three independent cda^{2-} ligands, one ketone oxygen atom from one cda^{2-} ligand (O4) and six oxygen atoms from coordination water molecules) (Figure 2.31). Powder X-ray diffraction diagrammes of the other complexes of light rare earths (La^{3+}, Ce^{3+}, and Pr^{3+}) revealed that they are isomorphic with $\{[Nd_2(cda)_3(H_2O)_{11}], 5H_2O\}_\infty$. In this crystal structure, there is one novel μ_3 lingking mode. μ_3 lingking mode constitutes the bridge between Nd^{3+} ions to construct the 1D chain structure (Figure 2.32).

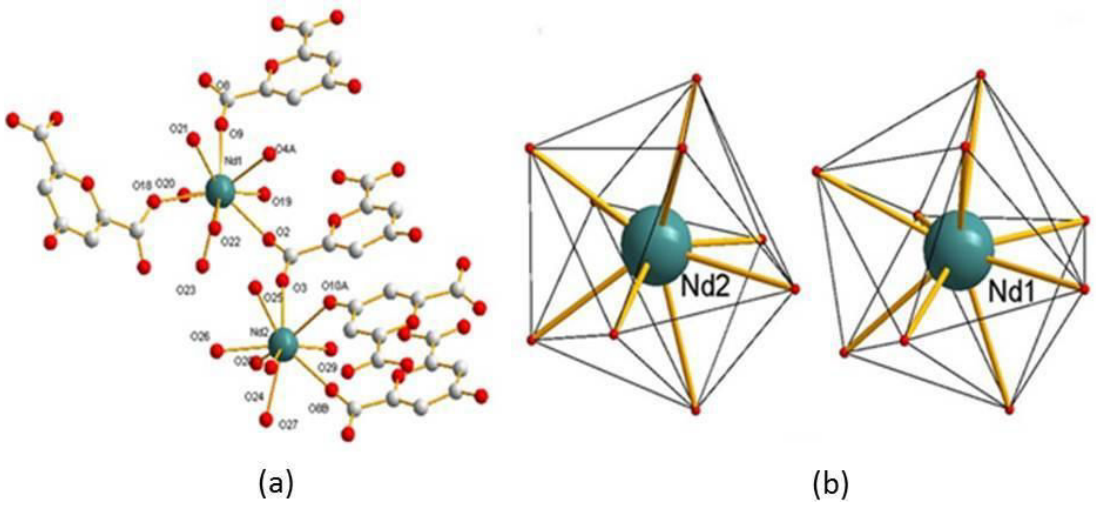

Figure 2.31 Pr^{3+} environments and coordination geometries in $\{[Nd_2(C_7O_6H_2)_3(H_2O)_{11}], 5H_2O\}_\infty$.

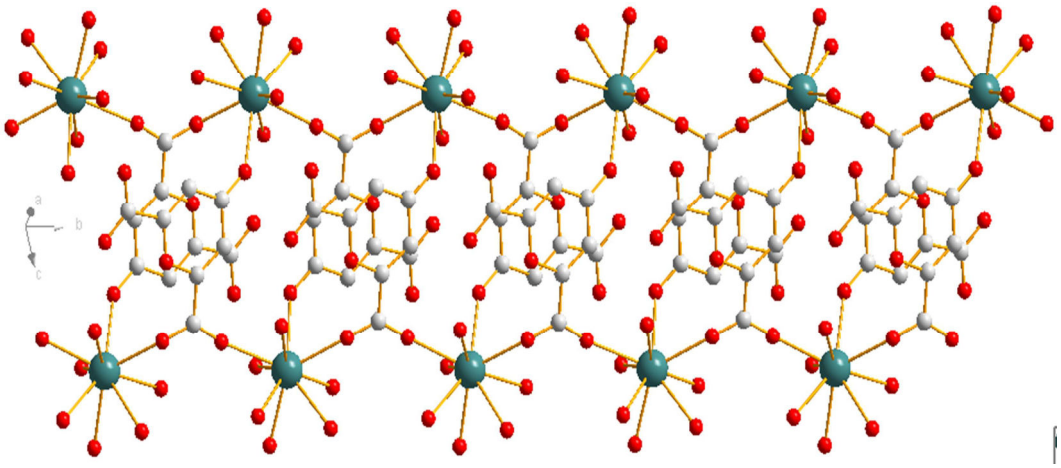

Figure 2.32 Projection view showing the 1D polymeric chains and the μ_3 lingking mode bridge.

Type II $\{[Ln_2(C_7O_6H_2)_3(H_2O)_7],6H_2O\}_\infty$ with Ln = Eu Gd, Tb, Dy and Ho. These compounds also crystallize in the triclinc system, space group $P\bar{1}$ (Table 2.7). Eu^{3+} ions are eight-coordinated. The coordination polyhedron can be described as a distorted double-capped trigonal prism (Figure 2.33). cda^{2-} ligands adopt monocoordinated mode and μ_4 linking mode to coordinate Eu^{3+} ions.(Figure 2.34).

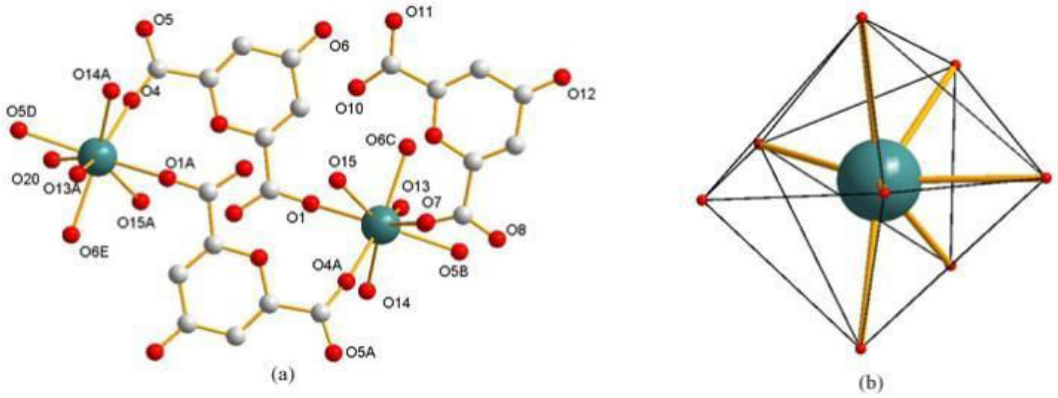

Figure 2.33 Eu^{3+} environment and coordination geometry in $\{Eu_2(C_7O_6H_2)_3(H_2O)_7]\cdot 6H_2O\}_\infty$.

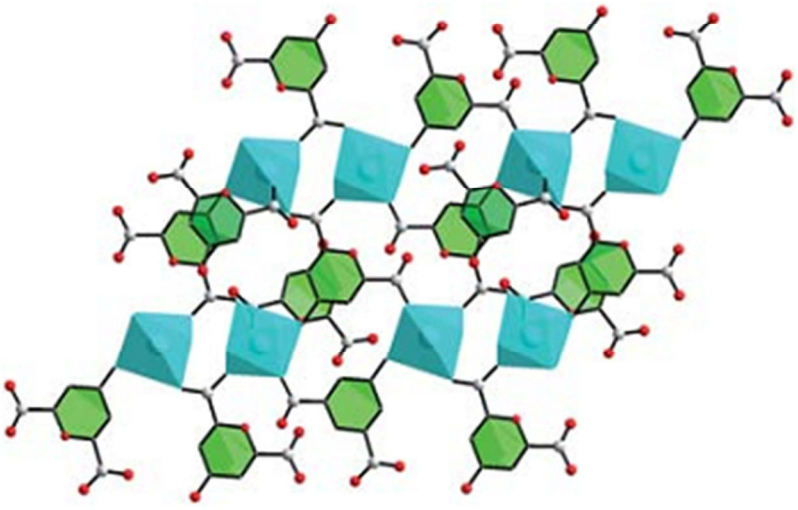

Figure 2.34 Projection view of a 2D layer with cda^{2-} μ_3 lingking mode.

Luminescent properties of the Eu-, Tb- and Dy-containing compounds were also studied in the solid state at room temperature (Figure 2.35).

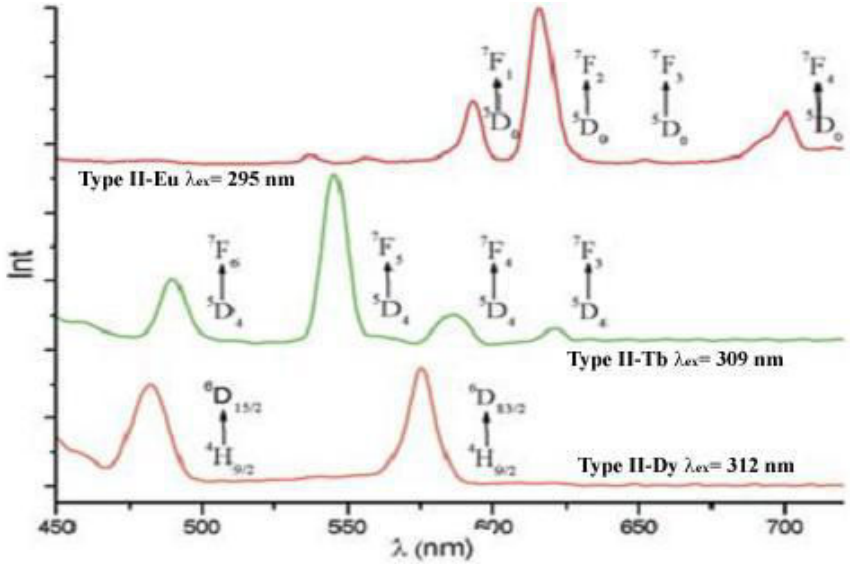

Figure 2.35 Solid-state luminescence spectra of - the Eu-, Tb-, and Dy-based compounds of Type II.

Type III $\{[Ln_2(C_2O_4)(C_7O_6H_2)_2(H_2O)_8],6H_2O\}_\infty$ with Ln = Er and Tm. These compounds crystallize in the triclinic system, space group $P\bar{1}$ (Table 2.7). In this crystal structure, cda^{2-} ligands partly decompose into oxalate, which bridge two lanthanide ions. Lanthanide ion is nive-coordinated and present a distorted monocapped square antiprismatic geometry. The coordination environment is composed of one cda^{2-} ligand (two carboxlate oxygen atoms and one pyran oxygen atom), half an oxalate group and four coordination water molecules (Figure 2. 36). In this crystal structure, all cda^{2-} ligands adopt the tridentate mode to chelate lanthanide ions, which are further bridged by oxlate to form a binuclear structure, and then are interlinked by weak hydrogen-bonds to form a pseudo 3D molecular framework. (Figure 2.37)

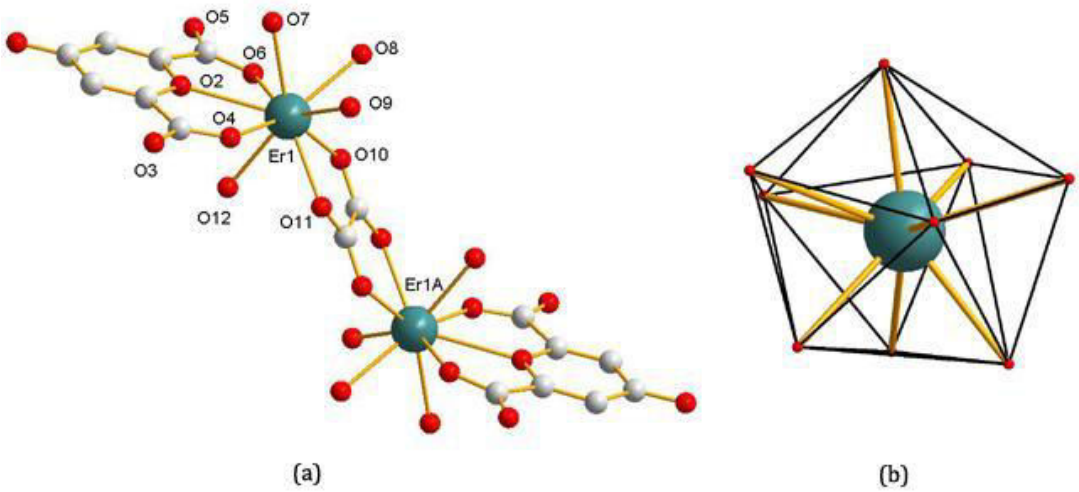

Figure 2.36 Er^{3+} environment and coordination geometry in $\{Er_2(C_2O_4)(C_7O_6H_2)_2(H_2O)_8]\cdot 6H_2O\}_\infty$.

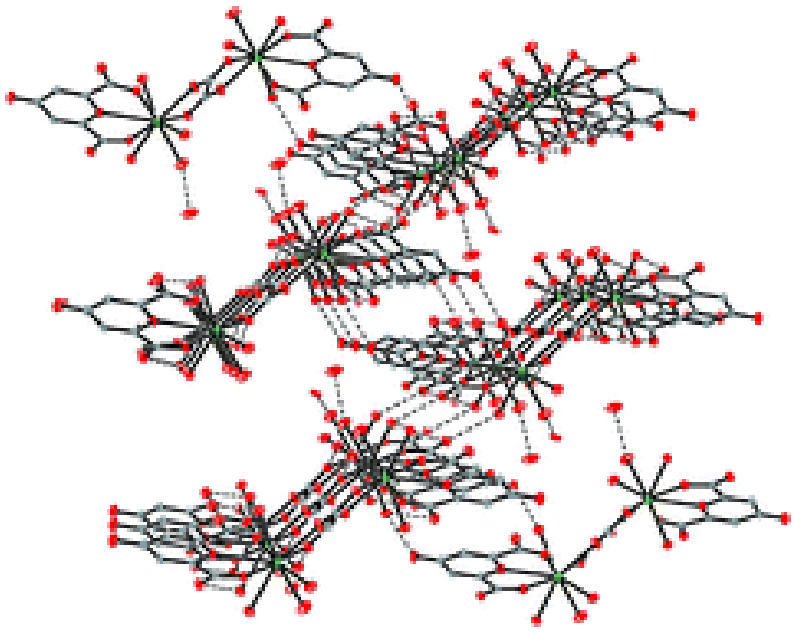

Figure 2.37 Perspective view of the pseudo 3D framework of $\{Er_2(C_2O_4)(C_7O_6H_2)_2(H_2O)_8],6H_2O\}_\infty$.

Type IV $\{[Yb(C_2O_4)(H_2O)_4][Yb(C_7O_6H_2)_2(H_2O)_4],3H_2O\}_\infty$ crystallizes also in the triclinic system, space group P-1 (Table 2.7). In this crystal structure, cda^{2-} ligand also partly decompose into oxalate, but oxalate group and cda^{2-} ligand produce two independent 1D chains. In the oxalate-based chain, Yb1 ion is eight-coordinated and present a distorted double-capped trigonal prism geometry formed by four oxygen atoms from two different oxalate groups and four oxygen atoms from coordination water molecules. In the cda^{2-}-based chain, Yb2 is also eight-coordinated and present a double-capped trigonal prism geometry formed by one ketone oxygen atom, three carboxylate oxygen atoms from three different cda^{2-} ligands, and six oxygen atoms from coordination water molecules (Figure 2.38). cda^{2-}-based chain carries a positive charge, whereas the oxalate-based chain a negative one. Therefore both the interchain weak classical hydrogen-bonding interactions and the elctrostatic interactions form the pseudo 3D molecular framework (Figure 2.39).

In this publication, a decomposition mechanism of ligand cda^{2-} is proposed. The experimental data show that only the heavy rare earth elements (Ho, Er, Tm and Yb) act as catalysis for the formation of oxalate at high temperature and with long reaction time. When Ln^{3+} ions coordinate with cda^{2-} ligands, the ligation causes a decrease of electron density on the pyran ring (weakly conjugated) and promote nucleophilic attack by water molecules. The hydrolysis reaction may occur at C-O bond, and the oxidation reaction may happen at C=C double bond and the Ln^{3+} ions act as Lewis acid in the reaction (Figure 2.40).

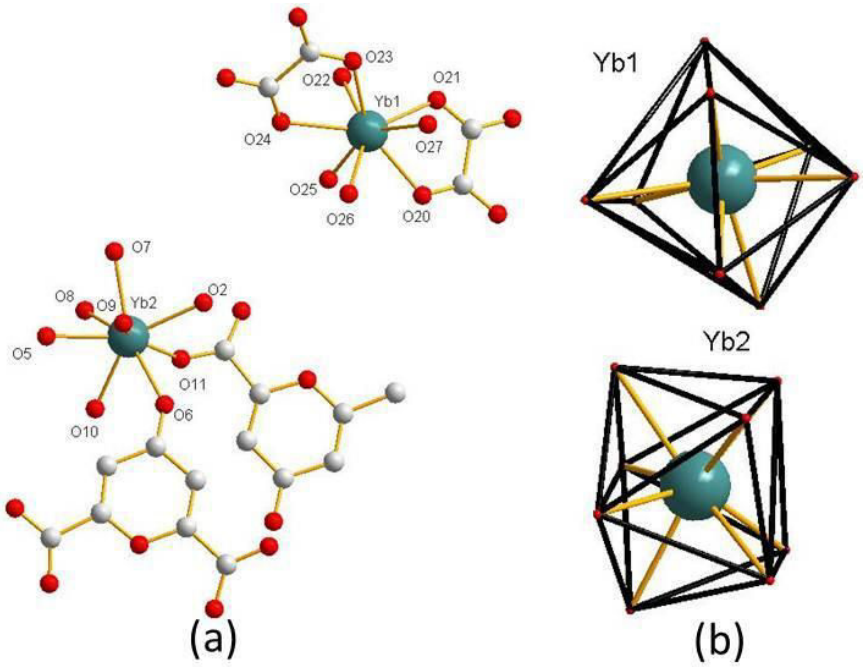

Figure 2.38 Coordination environments and coordination geometries of Yb^{3+} ions in the two indenpendent chains in $\{[Yb(C_2O_4)(H_2O)_4][Yb(C_7O_6H_2)_2(H_2O)_4]\cdot 3H_2O\}_\infty$.

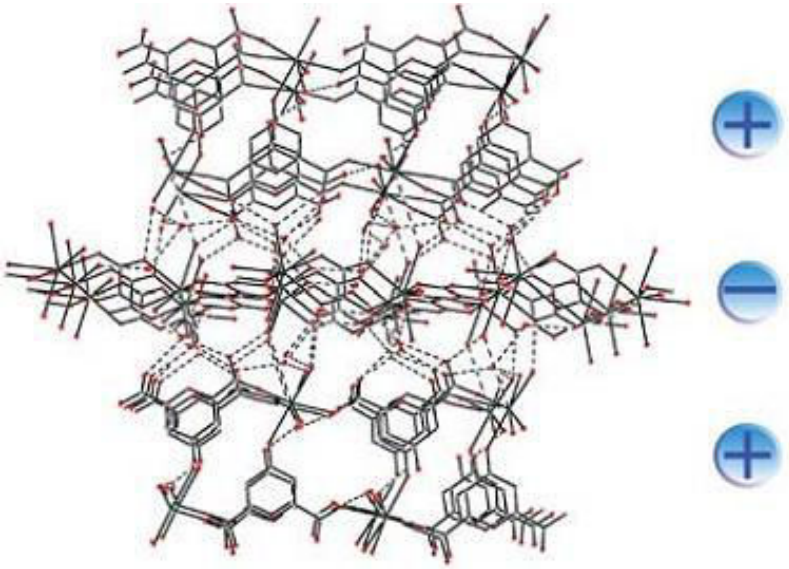

Figure 2.39 Perspective view of the pseudo 3D framework consolidated by the interchain weak classical hydrogen-bonding interactions and the elctrostatic interactions.

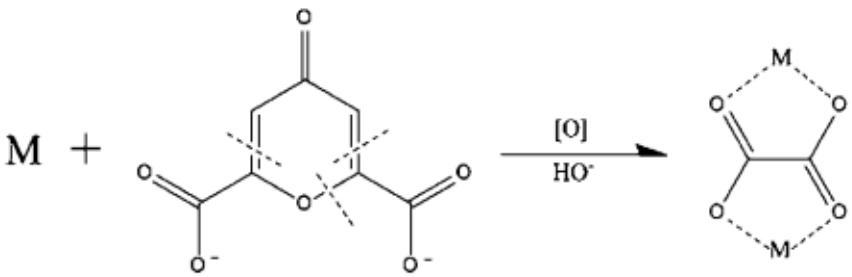

Figure 2.40 Decomposition mechanism of ligand cda^{2-}.

References:

[1]. (a). 5-hydroxyisophthalic acid, cas number: 618-83-7. (b). 5-nitroisophthalic acid, cas number: 618-88-2. (c). Chelidonic acid, cas number: 99-32-1. (d). 4-carboxyphenylboronic acid, cas number: 14047-29-1.

[2]. (a). Q. Shuai, S.P. Chen, X.W. Yang, S.L. Gao, Thermochimica Acta, 447, 2006, 45. (b). Q. Shuai, S.P. Chen, S.L. Gao, Inorganica Chimica Acta, 360, 2007, 1381. (c). R.K. Feller, A.K. Cheetham, Dalton Transactions, 2008, 2034. (d). J.D. Lin, S.T. Wu, Z.H. Li, S.W. Du, Dalton Transactions, 39, 2010, 10719. (e). K.L. Zhang, J.B. Zhang, C.Y. Jing, L. Zhang, R.I. Walton, P.Z. Zhu, S.W. Ng, Journal of Solid State Chemistry, 211, 2014, 8.

[3]. (a). Z.-B. Han, J.-W. Ji, H.-Y. An, W. Zhang, G.-X. Han, G.-X. Zhang, L.-G. Yang, Dalton Transactions, 2009, 9807. (b). F. Zhang, X.T. Huang, Y.Y. Tian, Y.X. Gong, X.Y. Chen, J.J. Lin, D.S. Lu, Y.L. Zhang, R.H. Zeng, S.R. Zheng, Journal of Coordination Chemistry, 66, 2013, 2659. (c). X.J. Li, T.N. Guan, X.F. Guo, X.X. Li, Z.J. Yu, European Journal of Inorganic Chemistry, 2014, 2014, 2307.

[4]. H.T. Xu, Y.D. Li, Journal of Molecular Structure, 690, 2004, 137

[5]. (a) Y. Huang, B. Yan, M. Shao, Journal of Molecular Structure, 876, 2008, 211. (b) Y. Huang, B. Yan, M. Shao, Journal of Solid State Chemistry, 181, 2008, 2935.

[6]. M. Chen, C. Wang, M. Hu, C.S. Liu, Inorganic Chemistry Communications, 17, 2012, 104.

[7]. V.A. Blatov, TOPOS, Multipurpose Crystallochemical Analysis with the program Package, Samara State University, Russia, 2006.

[8]. (a). J.W. Ye, P. Zhang, K.Q. Ye, W.R. Yin, L. Ye, G.D. Yang, Y. Wang, Inorg. Chem. Commun. 9, 2006, 744. (b). J.J. Shiers, G.J. Clarkson, M. Shipman, J.F. Hayes, Chemical Communications, 6, 2006, 649.

[9]. X. Yin, J. Tao, R.B. Huang, L.S. Zheng, Main Group Met. Chem. 2002, 691.

[10]. (a). J. Tao, X. Yin, Y.B. Jiang, L.F. Yang, R.B. Huang, L.S. Zheng, European Journal of Inorganic Chemistry, 2003, 2003, 2678. (b). H. Abourahma, B. Moulton, V. Kravtsov, M.J. Zaworotko, Journal of the American Chemical Society, 124, 2002, 9990. (c). X. Li, R. Cao, W. Bi, Y. Wang, Y. Wang, X. Li, Z. Guo, Crystal Growth & Design, 5, 2005, 1651.

[11]. (a). J.W. Ye, Y. Liu, Y.F. Zhao, X.Y. Mu, P. Zhang, Y. Wang, Crystengcomm, 10, 2008, 598. (b). J.W. Ye, J.Y. Zhang, L. Ye, D. Xie, T. Xu, G. Li, G.L. Ning, Dalton Transactions, 2008, 5342.

[12]. (a). Y. Ren, S. Chen, G. Xie, S. Gao, Q. Shi, Inorganica Chimica Acta, 359, 2006, 2047. (b). J.W. Ye, J. Wang, J.Y. Zhang, P. Zhang,Y.Wang,Crystengcomm, 9 (2007) 515-523. (c). H.P. Xiao, R. Rahimi, Y.Q. Cheng, A. Morsali, W.B. Zhang, J.G. Wang, Journal of Coordination Chemistry, 62, 2009, 3921. (d). S.P. Chen, Y.X. Ren, W.T. Wang, S.L. Gao, Dalton Transactions, 39, 2010, 1552. (e). X. Zhang, Q. Fang, G. Zhu, Journal of Molecular Structure, 969, 2010, 208. (f). J. Fan, T.T. Xiao, J. Wang, S.R. Zheng, J.B. Tan, W.G. Zhang, J. Inorg. Organomet. Polym. Mater., 21, 2011, 723. (g). J.-Y. Gao, X.-H. Xiong, C.-J. Chen,

W.-P. Xie, X.-R. Ran, S.-T. Yue, Y.-L. Liu, Y.-P. Cai, Inorganic Chemistry Communications, 31, 2013, 5.

[13]. Y.X. Ren, S. Chen, S. Gao, Journal of Coordination Chemistry, 59, 2006, 2135.

[14]. S.P. Chen, Y.X. Ren, S.L. Gao, Russian Journal of Coordination Chemistry, 34, 2008, 301.

[15]. Y. Huang, B. Yan, M. Shao, Journal of Solid State Chemistry, 182, 657, 2009.

[16]. Y.Q.X. X.F. Wang, X.Q. Huang, C.W. Hu, Chinese J. Struct. Chem., 31, 2012, 1194.

[17]. N. SeethaLekshmi, V.R. Pedireddi, Inorganic Chemistry, 45, 2006, 2400.

[18]. N. SeethaLekshmi, V.R. Pedireddi, Crystal Growth & Design, 7, 2007, 944.

[19]. (a). L.-P. Sun, S.-Y. Niu, J. Jin, G. –D Yang, L. Ye, Inorg. Chem. Commun, 9, 2006, 679. (b). H.W. Roesky, M, Andruh, Coord. Chem. Rev., 236, 2003, 91. (c). K. Biradha, Cryst. Eng. Comm. 5, 2003, 374. (d). X.M. Chen, G.F. Liu, Chem. Eur. J., 8, 2002, 4811.

[20]. (a). J.F. Eubank, V.C. Kravtsov. M. Eddaoudi, J. Am. Chem. Soc. 129, 2007, 5820. (b). Xia. B. Zhao, H.-S. Wang, W. Shi, Y. Ma, H.-B. Song, P. Cheng, D.-Z. Liao, S.-P. Yan, Inorg. Chem. 46, 2007, 3450..(c). X.-X. Zhou, M. –S. Liu, X.-M. Lin, H.-C. Fang, J.- Q. Chen, D.-Q. Yang, Y. –P. Cai, Inorg. Chim. Acta. 362, 2009, 1441.

[21]. (a).L. Manojlovic-Muir, K.W. Muir, R.A. Campbell, J.E. McKendrick, D.J. Robins, Acta Crystallographica Section C, 55, 1999, 178. (b). V. Yasodha, S. Govindarajan, V. Manivannan, O. Büyükgüngör, Acta Crystallographica Section E, 63, 2007, m2720. (c). V. Yasodha, S. Govindarajan, J.N. Low, C. Glidewell, Acta Crystallographica Section C, 63, 2007, m207. (d). M. Fainerman-Melnikova, J.K. Clegg, A.A.H. Pakchung, P. Jensen, R. Codd, CrystEngComm, 12, 2010, 4217. (e). V. Yasodha, S. Govindarajan, W. Starosta, J. Leciejewicz, Journal of Chemical Crystallography, 41, 2011, 1988. (f). A.B. Lago, R. Carballo, N. Fernández-Hermida, S. Rodríguez-Hermida, E.M. Vázquez-López, Journal of Molecular Structure, 1003, 2011, 121.

[22]. M.A.V. Dealmeida, G.F. Desa, Journal of Inorganic & Nuclear Chemistry, 42, 1980, 1503.

[23]. P.P. Lima, O.L. Malta, S. Alves, Quimica Nova, 28, 2005, 805.

[24]. M. Fang, L. Chang, X. Liu, B. Zhao, Y. Zuo, Z. Chen, Crystal Growth & Design, 9, 2009, 4006.

[25]. Z.-J. Zhang, S.-Y. Zhang, Y. Li, Z. Niu, W. Shi, P. Cheng, Cryst Eng Comm, 12, 2010, 1809.

Chapter 3.
Lanthanide coordination polymers based on ligand H_2cda

Chapter 3. Lanthanide coordination polymers based on ligand H_2cda

Because chelidonic acid (hereafter symbolized by H_2cda) has six oxygen atoms from one pyran function (O1), one ketone group (O2), and two carboxyl groups (O3, O4, O5 and O6), it presents various coordination modes. Figure 3.1 shows six fundamental linking modes with metal ions. In fact, two or more modes generally coexist in lanthanide coordination polymers.

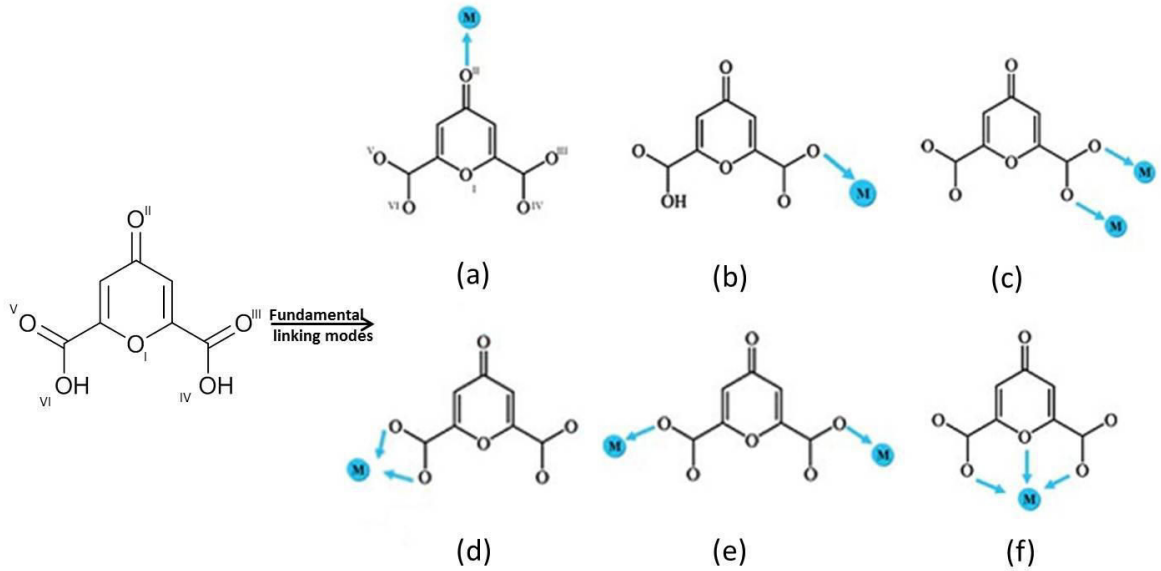

Figure 3.1: Fundamental linking modes with metal ions for the deprotonated chelidonic acid.

Some lanthanide-based coordination polymers have been published, but it doesn't mean that the exploration of H_2cda is finished. We try to find new types of lanthanide coordination polymers based on H_2cda.

3.1 Preparation of the sodium salt of chelidonic acid (H_2cda).

An aqueous solution of sodium hydroxide (0.21 mol in 50mL of water) was added to an aqueous suspension of H_2cda (0.1 mol in 50mL of water) under magnetic stirring. Then the obtained limpid solution was evaporated to dryness. A small amount of ethanol was added to the resulting solid and the suspension was stirred and refluxed for 1h. After the suspension was cooled to room temperature, a lot of ethoxyethane was added and precipitation occurred. After filtration and drying, the yellow powder of the di-sodium salt of H_2cda was obtained in 90% yields. X-ray diffraction and TGA of were recorded (Figure 3.2). TGA reveals that the salt is mono-hydrated (Figure 3.2b).

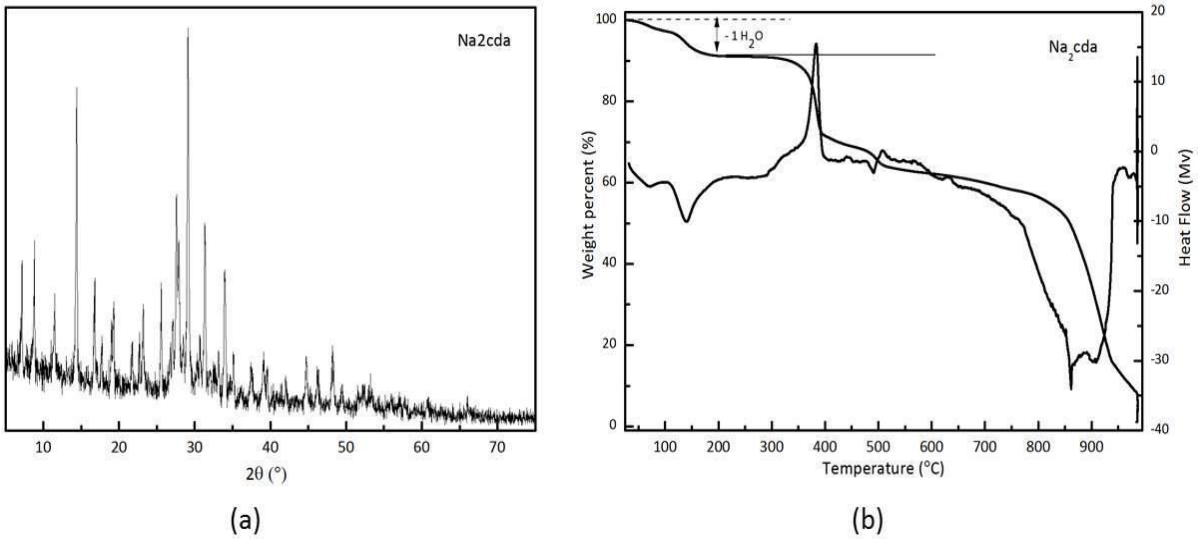

Figure 3.2 (a) XRPD patterns and (b) TGA/TDA curves for microcrystalline powder of Na_2cda, H_2O.

UV-vis absorption spectrum of an aqueous solution of Na_2cda, H_2O (1×10^{-5} mol.L^{-1}) was recorded. It shows a broad absorption band centered at 287 nm (Figure 3.3).

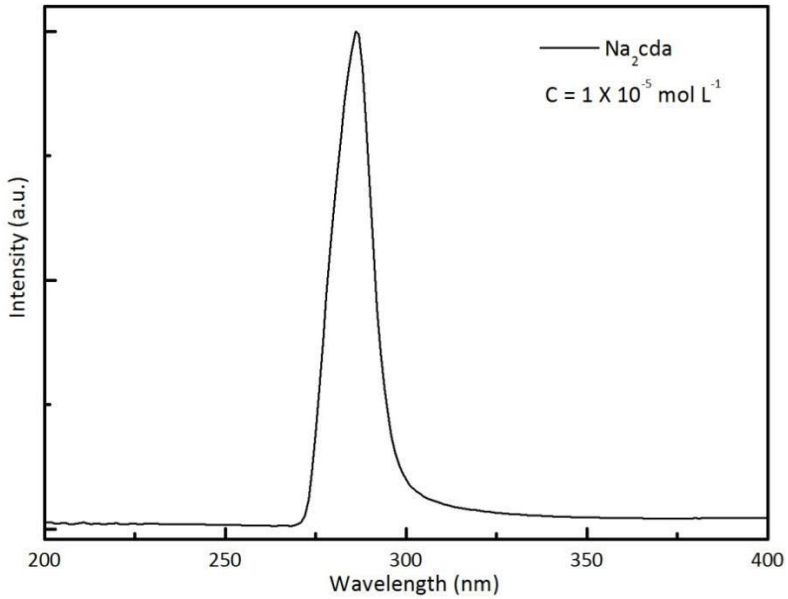

Figure 3.3: UV-vis absorption spectrum of an aqueous solution of Na_2cda,H_2O.

3.2 Preparation of microcrystalline powders.

Microcrystalline powders of lanthanide-based (La to Lu plus Y except Pm) compounds were synthesized with the same stoichiometric amounts at different temperatures (room temperature or 100 °C).

Clear aqueous solutions of lanthanide chloride (0.5 mmol in 10mL H_2O) were added to aqueous solutions of the di-sodium salt of H_2cda (0.75 mmol in 10 mL H_2O). At room temperature, precipitations occurred after 30 min (from La to Tb) and after 2h (from Dy to Lu plus Y). At 100 °C, precipitations occurred after 10 min whatever the used lanthanide ion. Precipitations were filtered and dried at room temperature. Yellow resulting powders were obtained in 80% yields. The microcrystalline powders were classified by families (Table 3.1)

of iso-structural compounds on the basis of their X-ray powder diffraction diagrams (Figure 3.4).

Table 3.1 Families of Lanthanide-based compounds.

L=cda	La	Ce	Pr	Nd	Sm	Eu	Gd	Tb	Dy	Ho	Y	Er	Yb	Lu
RT														
RT														
100 °C														

Family 1	Published in *Cryst. Eng. Comm*., **2010**, 12, 1809-1815. CCDC: 716750
Family 2	No crystal structure.
Family 3	Novel coordination polymer.
Family 4	Published in *Cryst. Eng. Comm*., **2010**, 12, 1809-1815. CCDC: 715751
Family 5	Published in *Cryst. Growth Des.*, **2009**, 9, 4006-4016. CCDC: 748868
Family 6	No crystal structure.

Family1

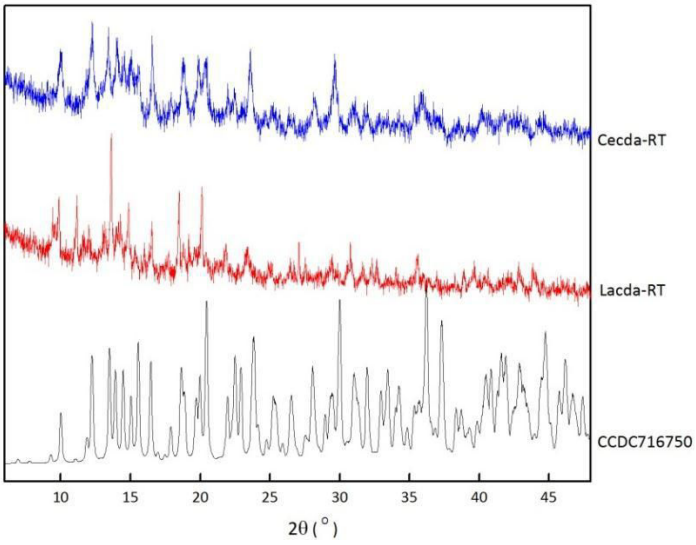

Family2

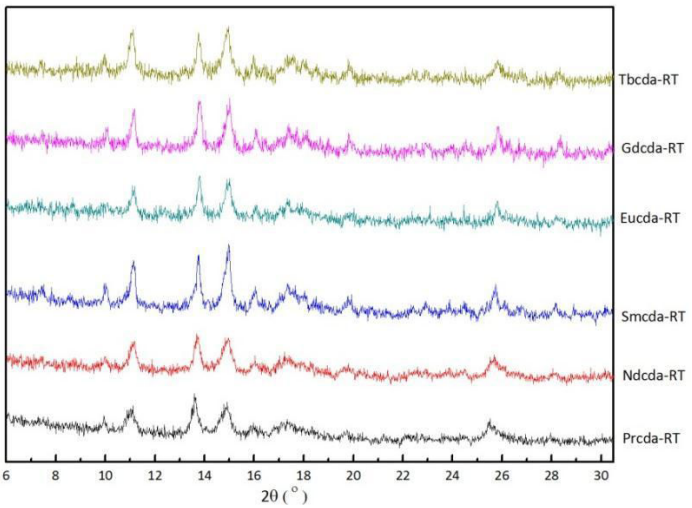

Family3

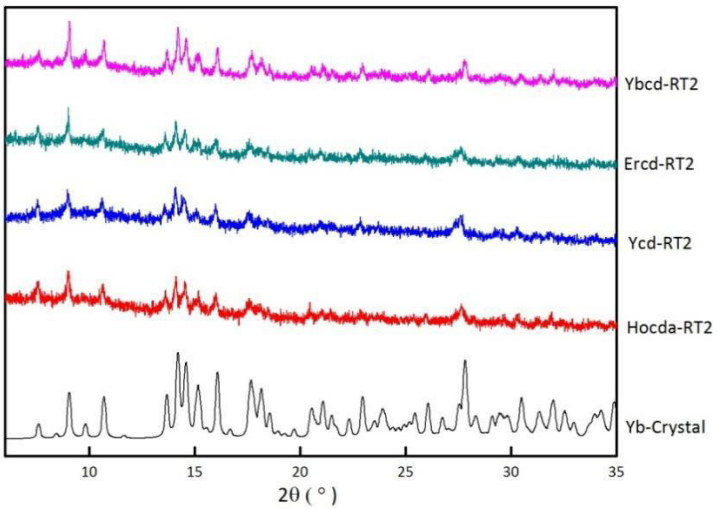

Family4

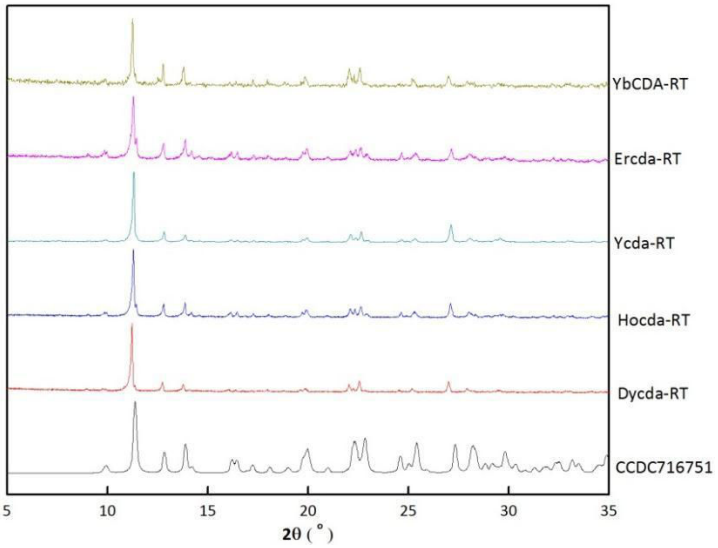

Family5

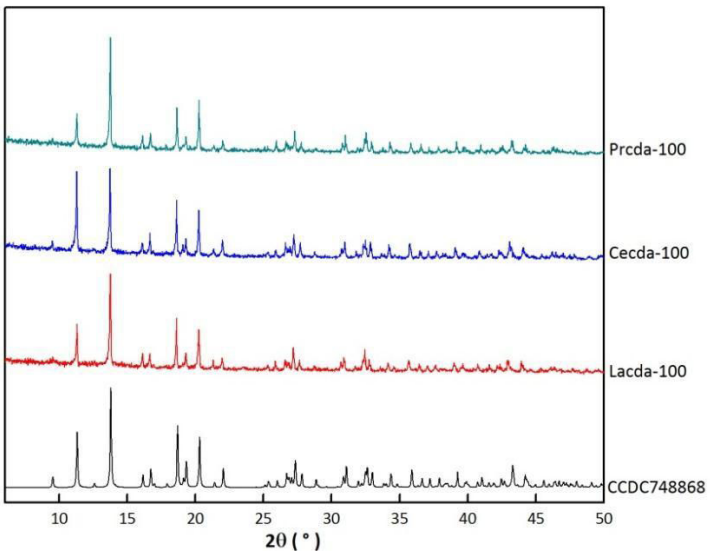

Family6

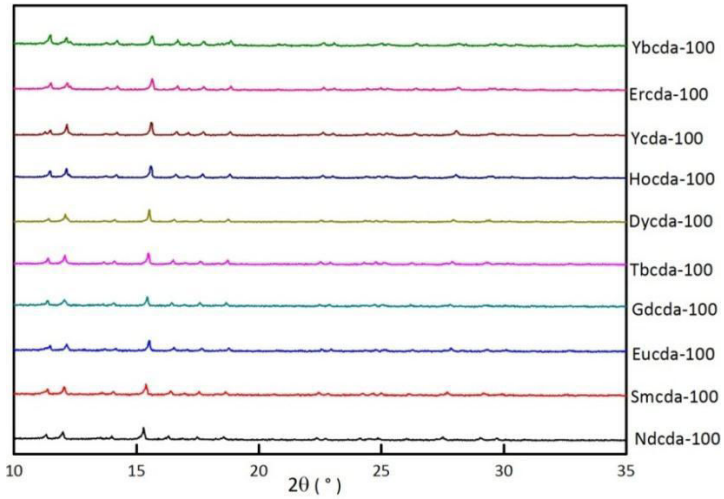

Figure 3.4: XRPD patterns of the microcrystalline powders for all families and simulated XRD diagrams from their iso-structural crystals.

For the heavy lanthanide elements (Ho, Er, Yb and Lu), prolonged reactive time (1 month) leads to a novel family of coordination polymers whom crystal structure has been solved and the new crystal is iso-structural with family 3.

In family 3, some cda^{2-} ligand decomposed into oxalate. This reaction mechanism (Figure 3.5) has been published, but the authors reported that the process of decomposition occurred at the high temperature and for long reaction times.[1] In the present case we find that the decomposition also occurs at room temperature.

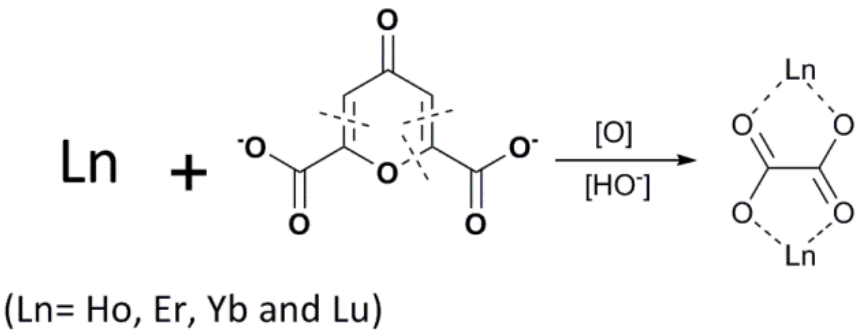

Figure 3.5: Decomposition mechanism of cda^{2-} ligand.[1]

Compounds that constitute family 2 are not stable. Actually, microcrystalline powders of family 2 have been suspended into water and the suspension was heated at 40 °C for 12h. Powder XRD patterns of the resulting solids prove that a phase transition occurred that led to compounds belonging to family 4 (Figure 3.6). All single crystals that were obtained by slow evaporation of the filtrates from the filtration of family 2 belonged to the family 4.

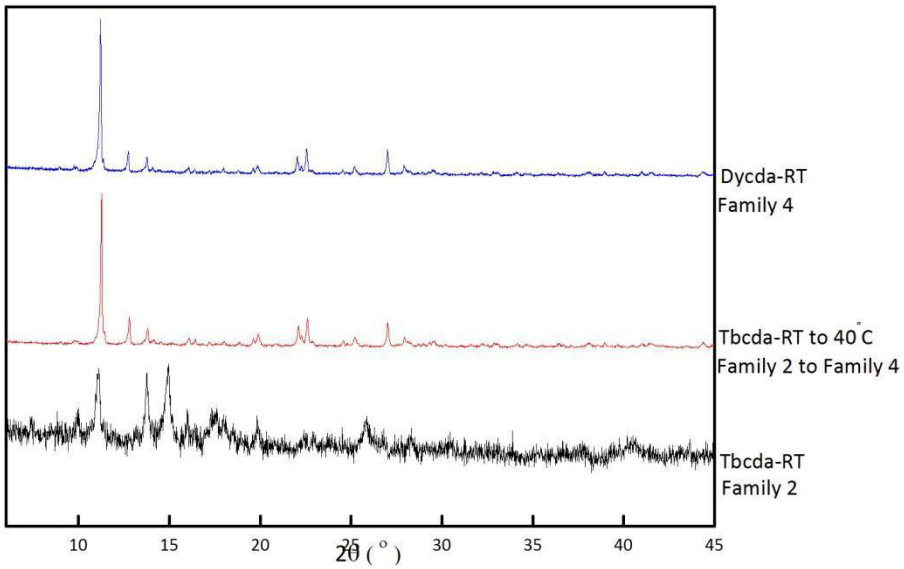

Figure 3.6 : XPRD patterns of the Tbcda-RT compound before and after its suspension in water at 40°C.

3.3 Syntheses of single crystals.

Usually, in our group, single crystals of lanthanide-based compounds are grown by slow diffusions of lanthanide chloride (0.5 mmol in 10 mL H_2O) and Na_2cda, H_2O (0.5 mmol in 10 mL H_2O) aqueous solutions in H-shaped tubes as well as in U-shaped tubes containing a gel (Agar- Agar, TMOS or TEOS). Details are given in Appendix I.

For cda^{2-} ligand, these two methods didn't work and we can't get good single crystals suitable for X-ray diffraction. We tried to put the U tubes with chemical gels (TMOS or TEOS) into a 40 ^{o}C water bath for improving the quality of the crystals. Unfortunately, the cda^{2-} ligand completely decomposed to oxalate. A single crystal of a compound with chemical formula $[Yb_2(ox)_3(H_2O)_4,\ 2H_2O]_\infty$ was obtained. Despite similar chemical formula it crystallizes with different cell parameters than a previously reported compound. [2]

In general, slow evaporation of the filtrates after reaction is also used to get single crystals of good quality. By this way, we obtained three new crystal structures. The chemical formulae are $[Na(Hcda)(H_2O)]_\infty$, $[Lu(cda)_{1.5}(H_2O)_5,2H_2O]_\infty$ and $[Yb_2(cda)_2(ox)(H_2O)_7,6H_2O]_\infty$. Their cell parameters and selected refinement parameters are listed in Table 3.2. All these crystals are thin plate-shaped (Figure 3.7). All single crystals were sealed in glass capillaries for X-ray single crystal data collection in order to avoid potential dehydration.

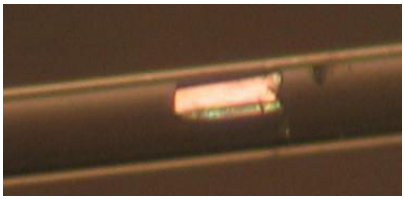

Figure 3.7: Picture of a single crystal of $[Yb_2(cda)_2(ox)(H_2O)_7,\ 6H_2O]_\infty$ in a glass capillary. Dimension: 0.14 x 0.04 x 0.05 cm^3.

Table 3.2 Crystal data of compounds.

formula	$C_7O_6H_5Na$	$C_{10.5}O_{14}H_{13}Lu$	$C_{16}O_{30}H_{32}Yb_2$	$C_6O_{18}H_{12}Yb_2$
MW ($g.mol^{-1}$)	208.09	538.17	1050.49	718.22
Crystal system	Monoclinic	Monoclinic	Monoclinic	Triclinic
Space group	C2/c (15)	C 2/c (15)	P 21/n (14)	P-1 (2)
a(Å)	10.8579(2)	19.3529(3)	10.9245(2)	6.2741(3)
b(Å)	10.3714(2)	11.2104(2)	23.2870(5)	6.6538(3)
c(Å)	7.3610(15)	18.3675(2)	12.7852(2)	9.6164(3)
α(°)	90	90	90	75.062(4)
β(°)	92.061(3)	119.0573(7)	113.245(10)	80.650(4)
ϒ(°)	90	90	90	81.688(4)
V ($Å^3$)	828.40(3)	3483.34(9)	2988.52(10)	380.51(3)
Z, ρ_{calc} ($g.cm^{-3}$)	4, 1.773	2, 2.125	4, 2.237	1, 3.082
R(%)	4.42	3.85	3.36	2.45
Rw(%)	15.11	9.72	8.85	5.51
GOF on F^2	1.113	1.051	0.967	1.036

3.4 Description of the crystal structures.

3.4.1 $[Na(Hcda)(H_2O)]_\infty$.

This single crystal $[Na(Hcda)(H_2O)]_\infty$ was gotten by slow evaporation of the filtrate obtained during the synthesis of the Lu-containing compounds at room temperature.

The single crystal X-ray diffraction ananlysis reveals that the compound with chemical formula $[Na(Hcda)(H_2O)]_\infty$ crystallizes in the monoclinic system, space group C2/c, with the cell paramenters: a = 10.8579(2) Å, b = 10.3714**(**2**)** Å, c = 7.3610(15) Å and β = 92.061(3)° (Table 3.2). Atomic parameters and selected bond lengths and angles are listed in Appendix II.

In this crystal structure, there is one crystallographically independent Na^+ ion which is six coordinated by six oxygen atoms from two carboxylic groups of two different cda^{2-} ligands, two ketone functions (O6 and O6A) from another two cda^{2-} ligands and two water molecules. The coordination geometry of the central Na^+ ion is closed to octahedral geometry (0.046 calculated by SHAPE 2.0 software) (Figure 3.8).[3] Na-O distances are in the range 2.357-2.443 Å, and the cda^{2-} ligand acts as a tetradentate linker (Figure 3.9). Two oxygen atoms from carboxylate groups bridge two Na^+ ions so forming an infinite 1D chain along the a direction. Oxygen atoms from ketone function coordinate two Na^+ ions to form another infinite 1D chain along the c direction. The two 1D chains are further assembled into an infinite 2D layer structure by the linking of the ligand (Figure 3.10).

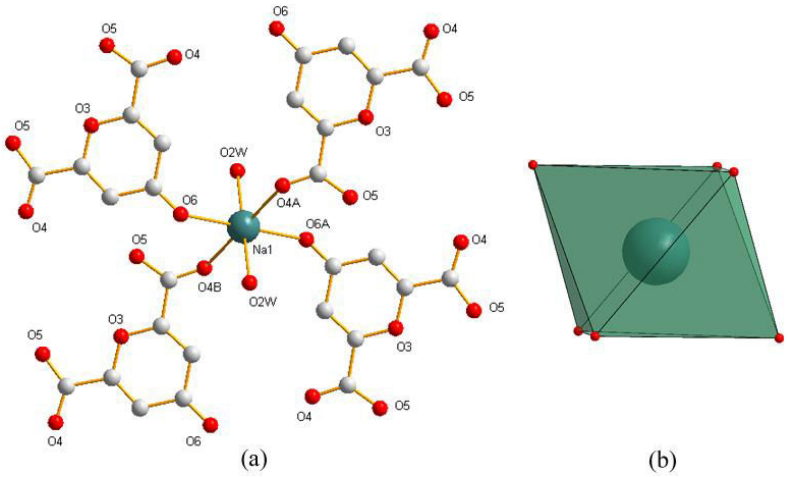

Figure 3.8: (a) extended asymmetric unit and (b) coordination geometry of the Na^{+} ion in $[Na(Hcda), (H_2O)]_{\infty}$.

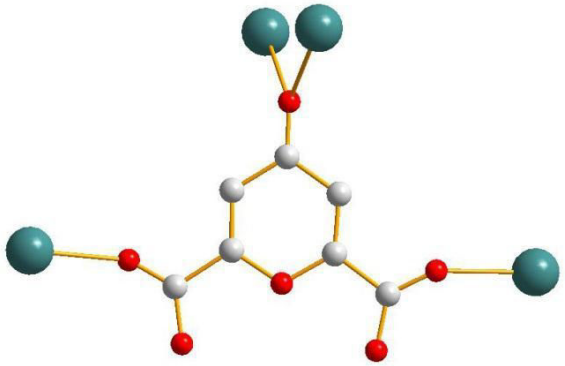

Figure 3.9: Tetradentate linking modes of cda^{2-} ligand. (mode a and mode e) in $[Na(Hcda), (H_2O)]_{\infty}$.

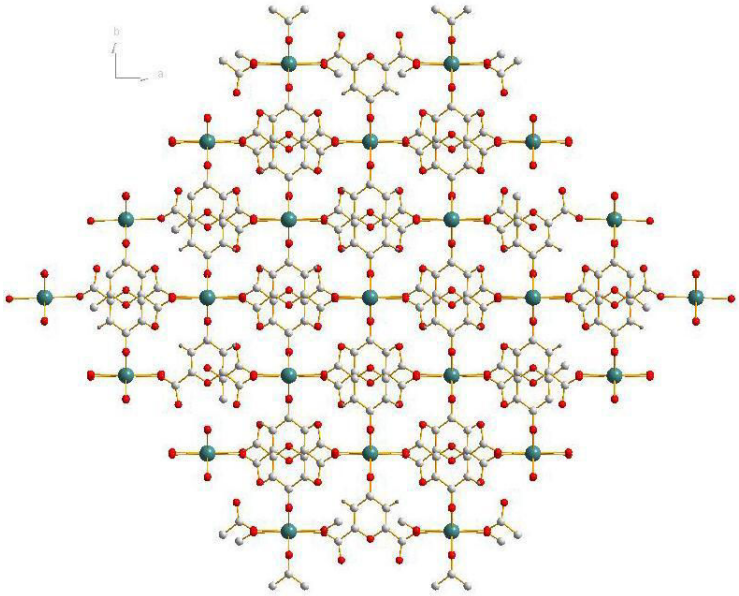

Figure 3.10: 2D layer structure of $[Na(Hcda), (H_2O)]_{\infty}$.

We compared the simulated XRD pattern of $[Na(Hcda), (H_2O)]_{\infty}$ with the experimental XPRD pattern of the synthesized di-sodium salt of H_2cda acid (Figure 3.11). They are clearly different. The reason may be that the crystals of $[Na(Hcda), (H_2O)]_{\infty}$ were accidentally obtained by slow evaporation of the filtrate obtained during the synthesis of the

Lu-containing compounds at room temperature. Growth of single crystals of di-sodium salt of H_2cda acid is in progress.

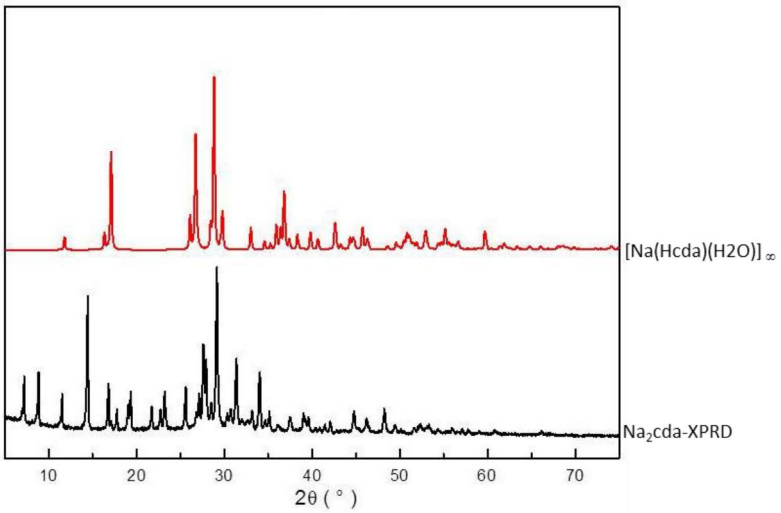

Figure 3.11: The XPRD pattern of Na_2cda, H_2O and simulated XRD patterns of crystal [Na(Hcda), $(H_2O)]_\infty$.

3.4.2 $[Lu(cda)_{1.5}(H_2O)_5,2H_2O]_\infty$.

The single crystal $[Lu(cda)_{1.5}(H_2O)_5,2H_2O]_\infty$ was grown by slow evaporation of the filtrate after reaction at room temperature.

Single crystal X-ray diffraction analysis reveals that the compound $[Lu(cda)_{1.5}(H_2O)_5, 2H_2O]_\infty$ crystallizes in the monoclinic system, space group C2/c, with the cell paramenters: a = 19.3529(3) Å, b = 11.2104(2) Å, c = 18.3675(2) Å,β = 119.0573(7)°and Z = 2 (Table 3.2). Atomic parameters and selected bond lengths and angles are listed in Appendix II.

The crystal structure is mono-dimensional. There is one crystallographically independent Lu^{3+} ion. Three carboxylic oxygen atoms (O5A, O6 and O12) and five oxygen atoms from coordination water molecules (O7, O8, O9, O10 and O11) constitute its eight coordinated sphere. The coordination geometry can be described as a distorted square antiprism (0.717 calculated by SHAPE 2.0 software) (Figure 3.12).[3] Lu-O distances are in the range 2.250 - 2.309 Å.

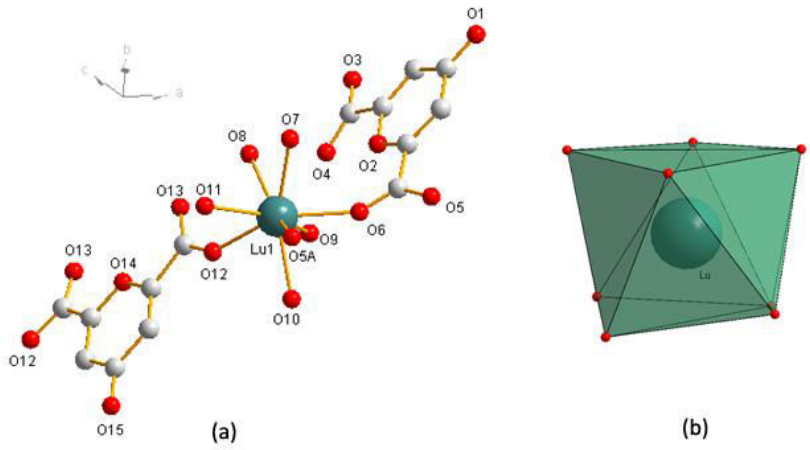

Figure 3.12: (a) extended asymmetric unit and (b) coordination geometry of the Lu^{3+} ion in $[Lu(cda)_{1.5}(H_2O)_5, 2H_2O]_\infty$.

In this crystal structure, cda^{2-} ligand presents two coordinating modes (Figure 3.13). Two oxygen atoms belonging to the same carboxylate group bridge two Lu^{3+} ions (mode c); two other oxygen atoms from two different carboxylate groups (mode e) act as a hand-to-hand bridge for Lu^{3+} ions. These two coordination modes alternate along the infinite 1D chain (Figure 3.14).

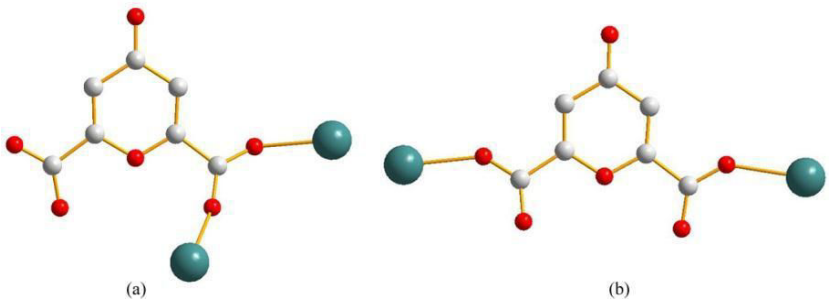

Figure 3.13: Coordination modes of cda^{2-} ligands (mode c and mode e).

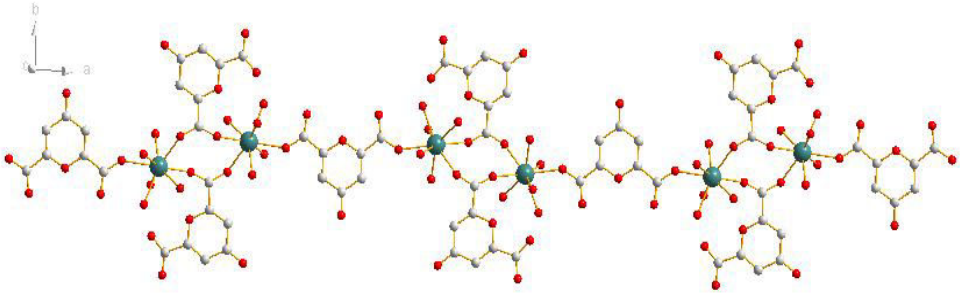

Figure 3.14: Bridging modes and 1D molecular chain of compound $[Lu(cda)_{1.5}(H_2O)_5, 2H_2O]_\infty$

3.4.3 $[Yb_2(cda)_2(ox)(H_2O)_7, 6H_2O]_\infty$.

The single crystal $[Yb_2(cda)_2(ox)(H_2O)_7, 6H_2O]_\infty$ was grown by slow evaporation of the filtrate after reaction at 100 ^{O}C.

This compound crystallizes in the monoclinic system, space group P 21/n (Table 3.2). There are two crystallographically independent Yb^{3+} ions, two cda^{2-} ligands, one oxalate ligand, seven coordination water molecules and six crystallization water molecules in this crystal structure. Two oxygen atoms (O3 and O9) from two carboxylate groups belonging to two different cda^{2-} ligands, two oxygen atoms (O13 and O15) from one oxalate group and four oxygen atoms from coordination water molecules (O17, O18, O19 and O20) constitute the eight coordinated environment of Yb1. The coordination geometry of Yb1 is closed to a triangular dodecahedron (0.397 calculated by SHAPE 2.0 software) (Figure 3.15).[3] Yb1-O distances are in the range 2.235-2.372 Å. Yb2 has nine coordinated environment: two oxygen atoms (O4 and O5) from carboxylate groups that belong to the same cda^{2-} ligand, one oxygen atoms (O2) from the pyran group of the same cda^{2-} ligand and one oxygen atom (O7) from a ketone function belonging to another cda^{2-} ligand, two oxygen atoms (O14 and O16) from one oxalate group and three oxygen atoms (O21, O22 and O23) from three coordination water molecules. The coordination geometry of Yb2 can be described as a

distorted spherical capped square antiprism (0.926 SHAPE 2.0 software) (Figure 3.16).[3] Atomic parameters and selected bond lengths and angles are listed in Appendix II.

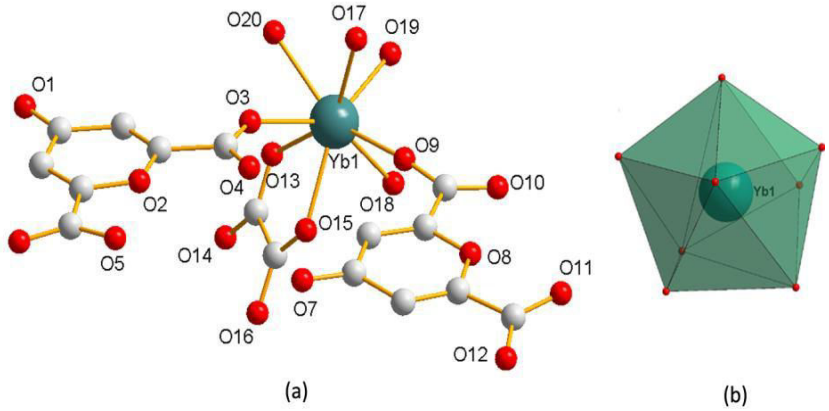

Figure 3.15: (a) Coordination environment and (b) coordination geometry of Yb1 in $[Yb_2(cda)_2(ox)(H_2O)_7, 6H_2O]_\infty$.

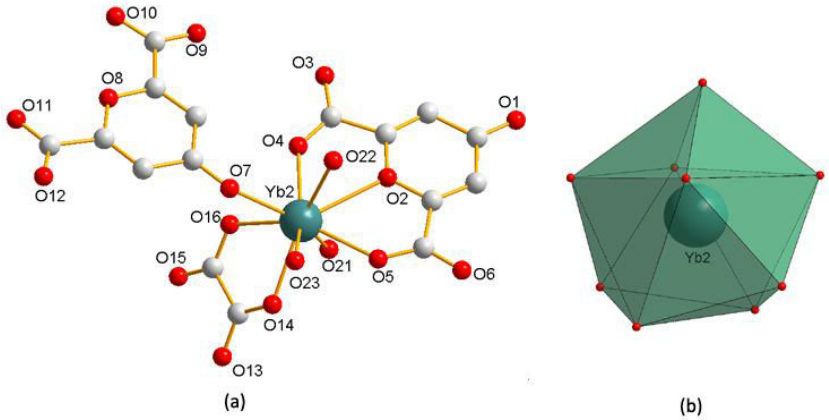

Figure 3.16: (a) Coordination environment and (b) coordination geometry of Yb2 in $[Yb_2(cda)_2(ox)(H_2O)_7, 6H_2O]_\infty$.

In this crystal structure, the cda^{2-} ligand presents two coordination modes (Figure 3.17). The cda^{2-} ligand is partly decomposed into oxalate. In the *bc* plane, two oxygen atoms from one carboxylate group of the cda^{2-} ligand (Mode b) and the oxygen atoms from an oxalate ligand act as bridges, that alternatively link the Yb^{3+} ions to form a 1D zigzag chain (Figure 3.18). Another cda^{2-} ligand by its ketone oxygen atom and one carboxylate oxygen atom (Mode a) coordinate with Yb^{3+} ions to decorate the 1D chain at the outside and furthermore complete the 1D chain (Figure 3.19).

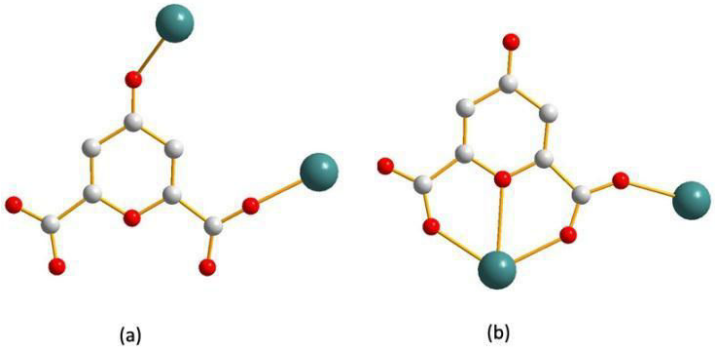

Figure 3.17: Linking modes of cad^{2-} ligands: Left: modes a and b. Right : modes b.

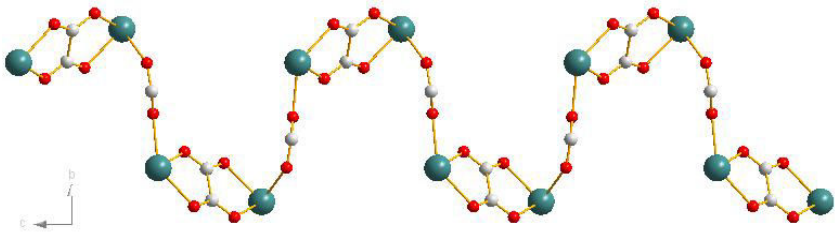

Figure 3.18: Bridges in a 1D zigzag chain in $[Yb_2(cda)_2(ox)(H_2O)_7, 6H_2O]_\infty$.

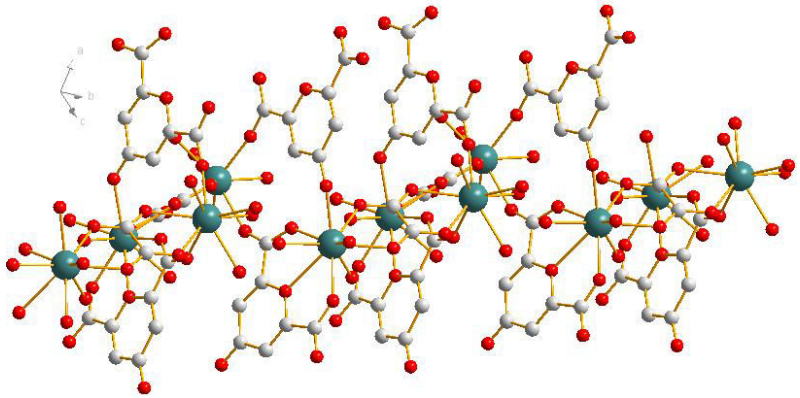

Figure 3.19: 1D chain structure of $[Yb_2(cda)_2(ox)(H_2O)_7, 6H_2O]_\infty$.

3.4.4 $[Yb_2(ox)_3(H_2O)_4, 2H_2O]_\infty$.

U-shaped tubes filled with a chemical gel (TMOS or TEOS) have been put in a 70 °C water bath for growing crystals. cda^{2-} ligands completely decomposed and single crystals suitable for X-ray diffraction appeared.

Crystal structure was solved and these compounds revealed to be lanthanide-based (La, Sm or Yb) oxalate coordination polymers. A similar crystal structure has already been published. It had different cell parameters.[2] The crystal structure of the Yb-containing compound with chemical formula $[Yb_2(ox)_3(H_2O)_4, 2H_2O]_\infty$ is described below.

This compound crystallizes in the triclinic system, space group P-1 (Table 3.2), with the cell parameters: a = 6.2741(3) Å, b = 6.6538(3) Å, c= 9.6164(3) Å, α= 75.062(4) °, β= 80.650(4) °, ϒ= 81.688(4) ° and Z = 1. Atomic parameters and selected bond lengths and angles are listed in Appendix II.

There are two crystallographically independent Yb^{3+} ions, but they have the same coordination environment and geometry. Both Yb^{3+} ions are surrounded by six oxygen atoms from three different oxalate groups and two coordination water molecules to complete the eight coordinated environment. The coordination geometry is closed to a triangular dodecahedron (1.021 and 1.146 calculated by SHAPE 2.0 software respectively) (Figure 3.20).[3] Yb-O distances are in the range of 2.290-2.36 Å. This crystal structure can be described on the basis of a 2D layer (Figure 3.21).

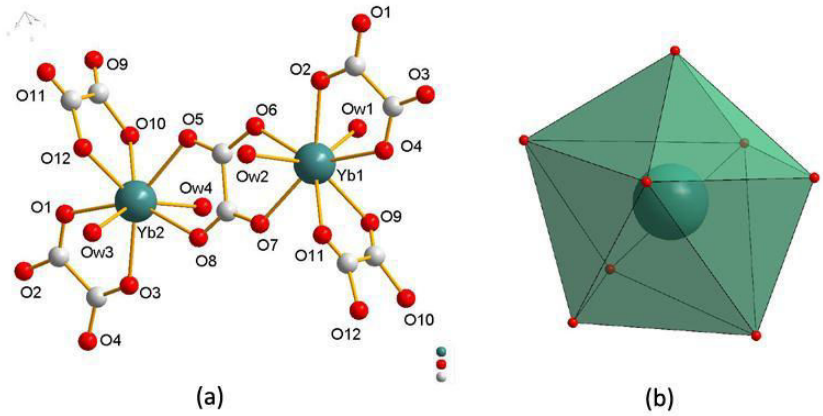

Figure 3.20: Coordination environment and geometry of Yb^{3+} ions in $[Yb_2(ox)_3(H_2O)_4, 2H_2O]_\infty$.

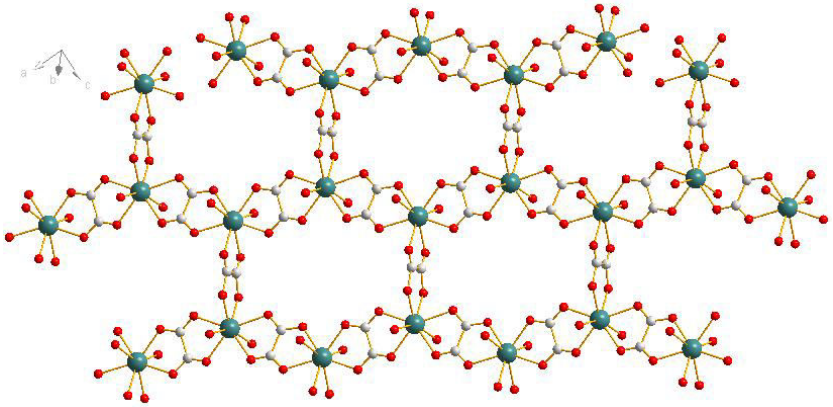

Figure 3.21: 2D layer of $[Yb_2(ox)_3(H_2O)_4, 2H_2O]_\infty$.

3.5 Study of the thermal stability.

Thermal stabilities of families 1,4 and 5 have been reported in the litterature.[4] Thermal stabilities of families 2, 3 and 6 were investigated by TGA/TDA experiments in the 25 - 995°C temperature range under N_2 atmosphere. Thermal analysis of family 3 ($[Yb_2(ox)(cda)_2(H_2O)_7, 6H_2O]_\infty$) is described as an example. Thermal analyses of families 2 and 6 are reported in Appendix II.

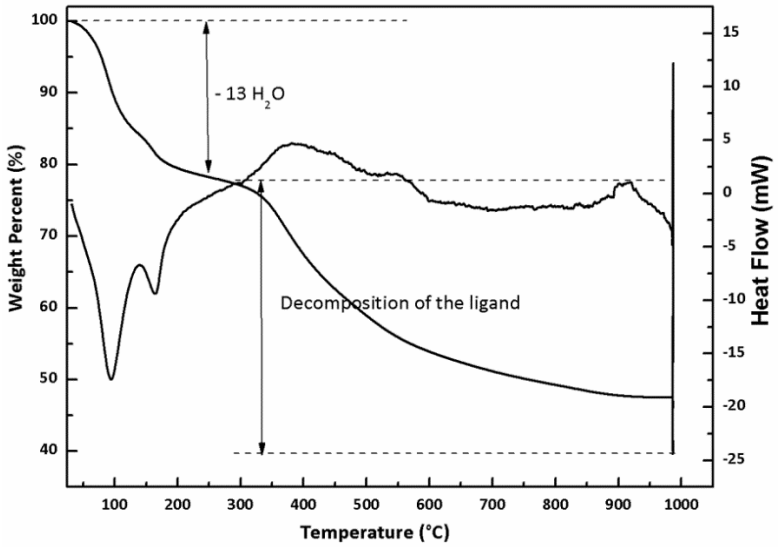

Figure 3.22: TGA/TDA analyses for a microcrystalline powder of Family 3 ($[Yb_2(ox)(cda)_2(H_2O)_7,6H_2O]_\infty$.).

The TGA (Figure 3.22) curve exhibits an obvious weight loss of 22% from room temperature to 210°C, cooresponding to the whole loss of coordination and crystallization water molecules (calc. 24%). The anhydrous phase is stable between 210 to 310°C and then decomposes until 995°C (the Ytterbium oxide Yb_2O_3 is finally obtained).

3.6 Luminescent properties.

3.6.1 Tb- and Eu-containing compounds of Families 2 and 6.

Although we can't obtain the crystal structures of families 2 and 6, the Tb- and Eu-containing compounds exhibit visible emission (green and red respectively) under UV radiation. We briefly characterized their luminescent properties under UV radiation (λ_{exc} = 300 nm). Emission spectra and colorimetric coordinates of the Tb- and Eu-containing compounds of family 2 are reported (Figure 3.23, 3.24 and 3.25). Emission spectra and colorimetric coordinates of the Tb- and Eu-containing compounds of family 6 are reported in Appendix II.

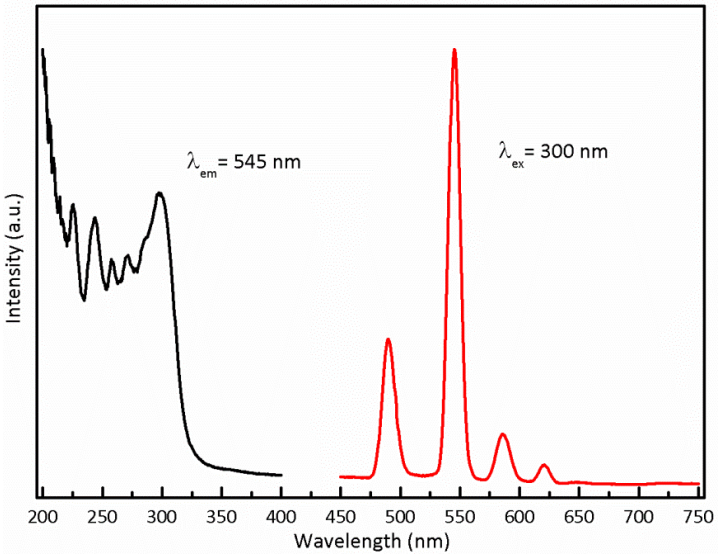

3.23: Emission and excitation spectra of the Tb-containing compound of Family 2.

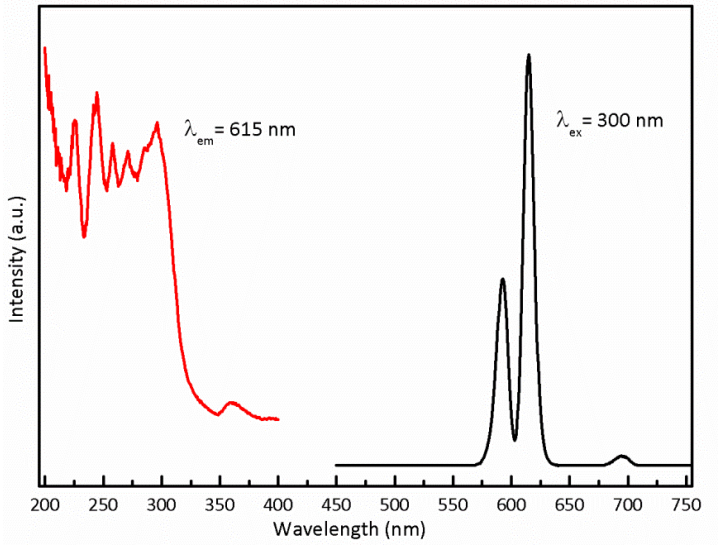

3.24: Emission and excitation spectra of the Eu-containing compound of Family 2.

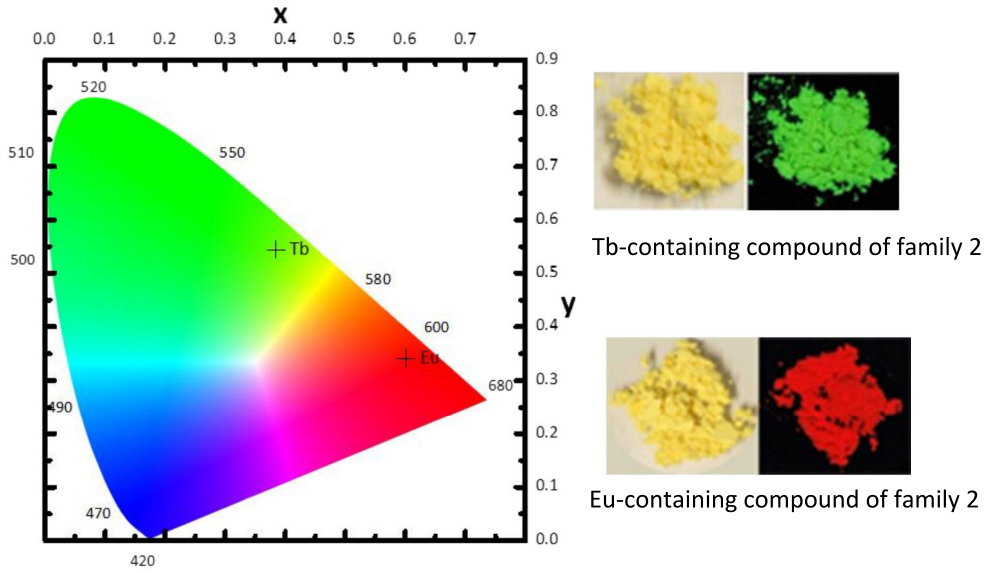

Figure 3.25: Colorimetric coordinates and pictures of the Tb- and Eu-containing compounds of family 2 under 312 nm irridiation (right).

Emission spectrum of the Tb-containing compound shows typical $^5D_4 \rightarrow {}^7F_J$ with J = 6-0 transitions. The more intense emission peaks are located at 490 nm ($^5D_4 \rightarrow {}^7F_6$), 545 nm ($^5D_4 \rightarrow {}^7F_5$), 590 nm ($^5D_4 \rightarrow {}^7F_4$), 620 nm ($^5D_4 \rightarrow {}^7F_3$), respectively. Under day light the Tb-containing compound is yellow. Under UV radation (312 nm), it emits green light (Figure 3.25) which is confirmed by its colorimetric coordinates (0.384, 0.544) (Figure 3.25).

Emission spectrum of the Eu-containing compound shows typical $^5D_0 \rightarrow {}^7F_J$ with J = 0-6 transions. The more intense emission peaks are located at 590 nm ($^5D_0 \rightarrow {}^7F_1$), 615 nm ($^5D_0 \rightarrow {}^7F_2$), 695 nm ($^5D_4 \rightarrow {}^7F_4$), respectively. Under day light, the Tb-containing compound is yellow. Under UV radation (312 nm), it emits red light (Figure 3.25) which is confirmed by its colorimetric coordinates (0.601, 0.342) (Figure 3.25).

Their luminescent behaviors can be explained by the energy transfer between the triplet state of the ligand and the lanthanides receiving energy levels.[4] The lowest excited singlet state was estimated on the basis of the wavelength of the UV-vis absorbance edges of the di-sodium salt of H_2cda (305 nm ≈ 32 800 cm^{-1}),[5] and the triplet states had already been reported (464 nm ≈ 21 400 cm^{-1})[6]. Therefore the energy gap ΔE ($^1\pi\pi^* \rightarrow {}^3\pi\pi^*$) is about 11 000 cm^{-1}. According to Reinhoudt's empirical rules the inter-system crossing is efficient when ΔE ($^1\pi\pi^* \rightarrow {}^3\pi\pi^*$) is greater than 5000 cm^{-1}, and depending to Latva's rules, the lowest excited triplet state is supposed to favor efficient ligand-to-metal energy transfer without singnificant back-transfer for Eu^{3+}- and Tb^{3+}-containing compounds (Figure 3.26).

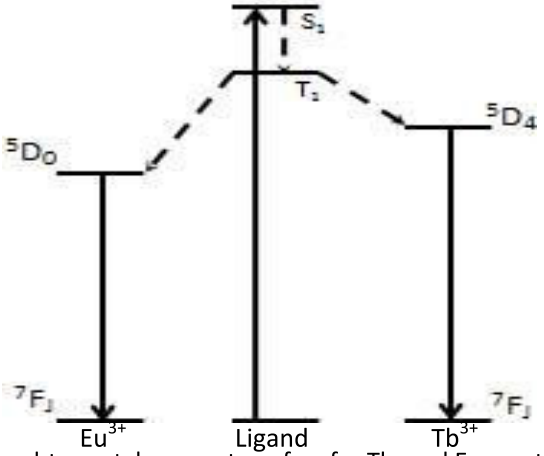

Figure 3.26: Intramolecular Ligand-to-metal energy transfers for Tb- and Eu- containing compounds of family 2.

These results indicate that in the Tb- and Eu-containing compounds, central Tb^{3+} or Eu^{3+} ions can be efficiently sensitized by the ligand through antenna effect.

3.6.2 Yb-containing compound of Family 3.

Yb^{3+}, because of its f^{13} configuration, presents a simple electronic structure. Its emission properties are rather unexplored compared with other lanthanides which exhibit visible emission. The first excited state $^2F_{5/2}$ of Yb^{3+} ion exhibits emission around 980 nm directly to the ground state $^2F_{7/2}$. We studied the near-infrared luminescence of the Yb-containing compound of Family 3 at room temperature and 77 K (Figure 3.27).

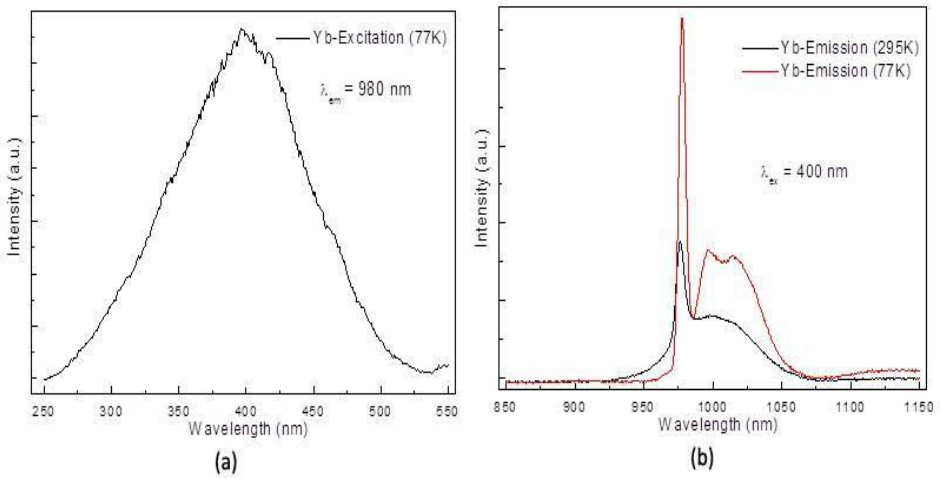

Figure 3.27: Solid state (a) excitation spectrum at 77K (λ_{em}=980 nm) and (b) emission spectrum at 295K and 77K (λ_{ex}=400 nm) of $[Yb_2(cda)_2(ox)(H_2O)_7,6H_2O]_\infty$.

The typical $^2F_{5/2} \rightarrow {}^2F_{7/2}$ transition at 980 nm has been detected. This transition is a promising probe for fluoro-immuno assays and vivo applications. It is worth noting that the Yb^{3+} ion emission band is not a single sharp transition but an envelope of bands arising at lower energies than the primary 980 nm band, because of the crystal field splitting.[8] A similar phenomenon has also been reported in literature.[9] Compared to the emission spectrum recorded at the emission spectrum recorded at 77K is well resolved. This indicates that the energy transfer between the ligands and the ytterbium ion is highly temperature dependent. For cda^{2-} ligand, the large energy difference between the triplet state (21400

cm^{-1}) and the resonance $^2F_{5/2}$ level (10235 cm^{-1}) of Yb^{3+} ion eliminates any possible energy matching.[10] Thus, the sensitization mechanism ligand-to-Yb^{3+} is not the antenna effect. It may occur via phonon-assisted energy-transfer process pointed out by Güdel and coworkers.[11]

3.7 Magnetic properties

We also have interest in the magnetic properties of compounds $[Yb_2(cda)_2(ox)(H_2O)_7, 6H_2O]_\infty$. Static measurements have been performed at solid state. The room temperature value of the χT product is 2.16 emu mol^{-1}, slightly lower than the calculated 2.57 cm^3 mol^{-1} K for a single Yb^{3+} ion ($^2F_{7/2}$, L=3, J = 7/2, g = 8/7).[12] On lowering the temperature, the curve decreases due to the progressive thermal depopulation of the excited-state Stark sublevel (Figure 3.28). [13]

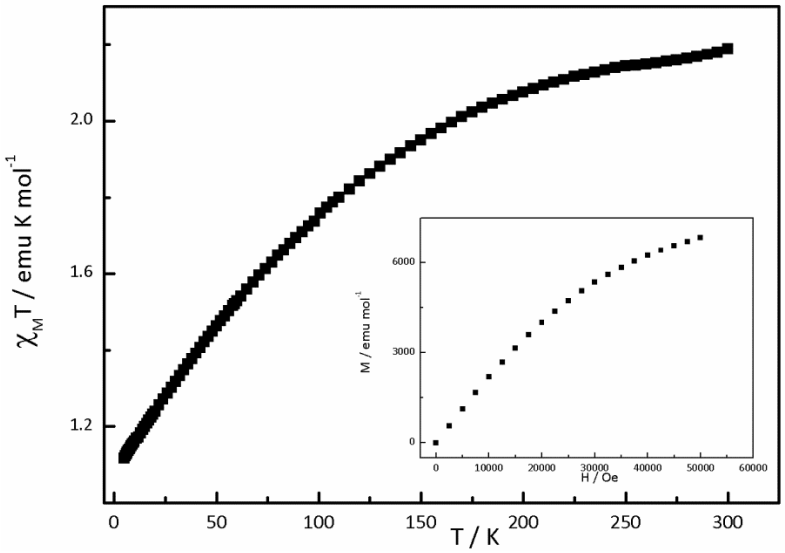

Figure 3.28 Temperature dependence of the χT product at 1000 Oe for compound $[Yb_2(cda)_2(ox)(H_2O)_7, 6H_2O]_\infty$.

The dynamic magnetic behavior is investigated from 1.8 K to 4.4 K in the 10-1500 Hz frequency range in an external magnetic field. Strong frequency dependence of the in-phase (χ_M') and out-of-phase (χ_M'') component of the magnetization is observed (Figure 3.29). The dynamic relaxation time τ is extracted from the Arrhenius plot shown in Figure 3.30. Best fit of the high temperature region afforded an energy barrier of 13 K, and $\tau_0 = 9.35 \times 10^{-6}$ s. In the low temperature region the Arrhenius plot goes flattening to a frequency of 55.65 Hz (2.86×10^{-3} s) at 1.8 K for the non-thermally activated regime.

Cole plots of the in- and out-phase components of the magnetization have been normalized over the isothermal susceptibility from 1.8 K to 3.6 K (Figure 3.31). By fitting the plot with a Debye model, the distribution of the relaxation time is indicated by the value of α = 0.13 which indicates a single relaxation mechanism.

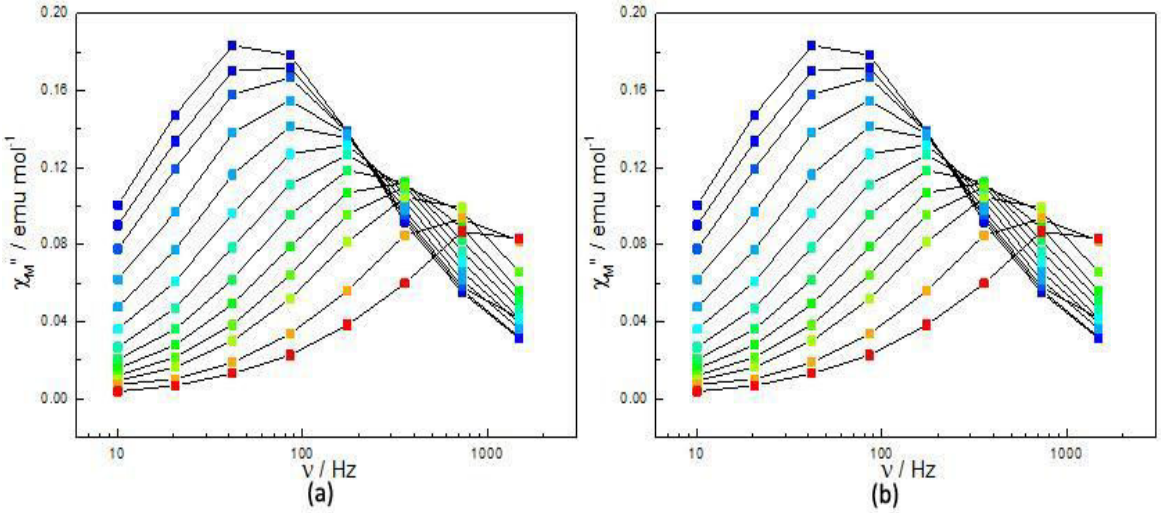

Figure 3.29: Frequency dependence of the in-phase χ' (a) and out-of-phase (b) χ'' ac susceptibility signals under a 1600 Oe optimum dc-field.

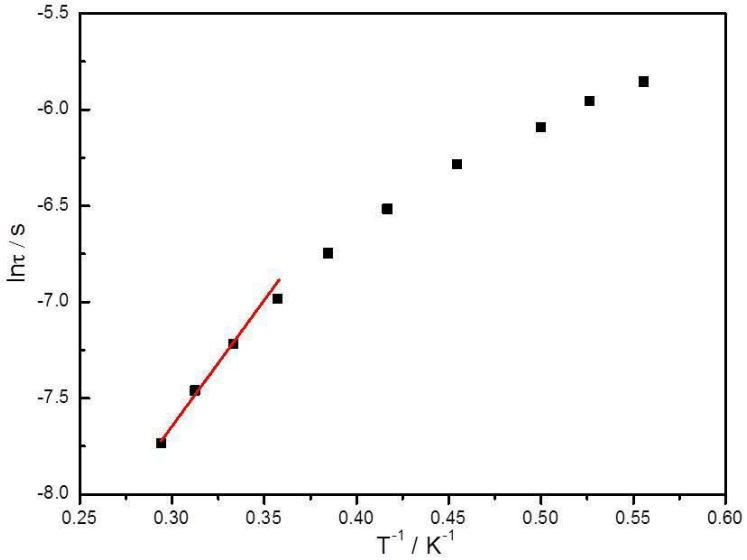

Figure3.30: Plot of ln(τ) versus T^{-1} fitted with the Arrhenius law.

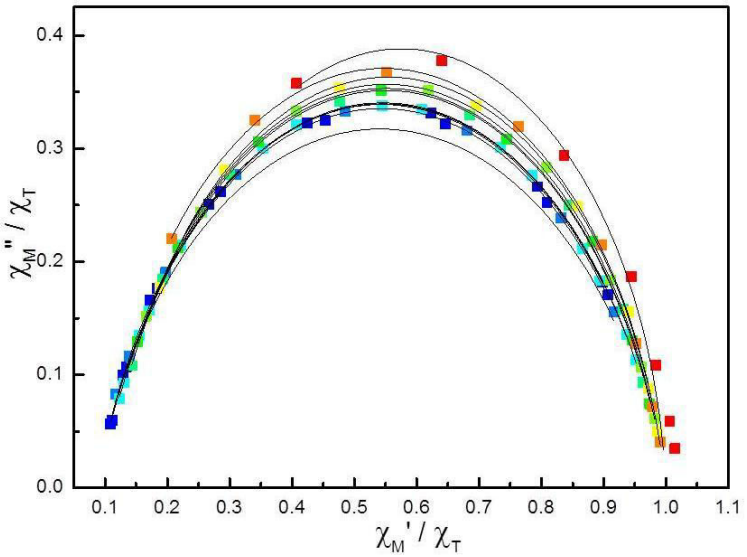

Figure 3.31 Normalized Argand diagram in the 1.8-3.6K temperature range. Lines represent the best fits calculated with an extended Debye model.

Conclusion

We synthesized the microcrystalline powders of all the rare earth elements, and classified them into structural families according to their XPRD patterns. There are three families already published and three new families. Unfortunately, we only obtained the crystal structure of Family 3. We got three novel crystal structures based on cda^{2-} ligand. We briefly studied the luminescent properties of the Tb- and Eu-containing compounds of family 2 and 6 and of the Yb-containing compound of family 3. Photoluminescence of the Tb- and Eu-containing compounds evidences an antenna effect. Magnetic study of the $[Yb_2(cda)_2(ox)(H_2O)_7, 6H_2O]_\infty$ has also been performed.

References

[1].Z.-J. Zhang, S.-Y. Zhang, Y. Li, Z. Niu, W. Shi, P. Cheng, Cryst. Eng. Comm., 12, 2010, 1809.

[2].E. Hansson. Acta Chemica Scandinavica., 27, 1973, 823.

[3].M. Llunell, D. Casanova, J. Cirera, P. Alemany and S. Alvarez, SHAPE v. 2.1 University of Barcelona, 2010.

[4].J. C. G, Bünzli and S. V. Eliseeva, in Lanthanide Luminescence, ed. P. Hänninen and H. Härmä, Springer, Berlin, Heidelberg, 2010, pp. 1-45.

[5].(a) M. Shi, F. Li, T. Yi, D. Zhang, H. Hu and C.-H. Huang, Inorg. Chem., 2005, 44, 8929. (b) S. Quici, M. Cavazzini, G. Marzanni, G. Accorsi, N. Armaroli, B. Ventura and F. Barigelletti, Inorg. Chem. 2005, 44, 529.

[6].P.P. Lima, O.L. Malta, S. Alves, Quimica Nova, 28, 2005, 805.

[7].(a) A. Beeby, R. S.Dickins, S. Faulkner, D. Parker, J.A.G. Williams, Chem. Commum., 1997, 1401; (b) M.H.V. Werts, J.W. Hofstraat, F.A.J. Geurts, J.W. Verhoeven, Chem. Phy. Lett. 1997, 276, 196.

[8].W.G. Perkins, G.A. Crosby, The Journal of Chemical Physics, 42, 1965, 407.

[9].(a) M.P. Tsvirko, G.F. Stelmakh, V.E. Pyatosin, K.N. Solovyov, T.F. Kachura, Chem. Phys. Lett. 1980, 73, 80. (b) M. Asano-Someda, Y.Kaizu, J. Photochem. Photobiol. A. 2001, 139, 161.

[10].(a) O.M. Khreis, W.P. Gillin, M. Somerton, R.J. Curry, Organic Electronics, 2, 2001, 45. (b) X. Guo, H. Guo, L. Fu, L.D. Carlos, R.A.S. Ferreira, L. Sun, R. Deng, H. Zhang, The Journal of Physical Chemistry C, 113 (2009) 12538-12545.

[11].C. Reinhard, H.U. Güdel, Inorganic Chemistry, 41, 2002, 1048.

[12].O. Kahn, Molecular magnetism, 1993.

[13].J. D. Rinehart and J. R. Long, Chem. Sci., 2011, 2, 2078.

Chapter 4.
Lanthanide coordination polymers based on ligand H_2hip

Chapter 4. Lanthanide coordination polymers based on ligand H_2hip

5-hydroxy-isophthalic acid (H_2hip) (Figure 4.1) is a rigid ligand. It has one hydroxyde group and two carboxylate groups at its 1, 3 and 5 positions. The two carboxylate groups can lead to various coordination modes with lanthanide ions, and the hydroxyde group may be involved in hydrogen bonding and then reinforces the stability of the molecular networks. Moreover, the hydroxyde group can also affect the luminescent properties of the lanthanide containing coordination polymers. The ligand which has two carboxylate groups in iso-position is defined as a V-shaped ligand. Our group has reported on two V-shaped ligands: isophthalic acid (H_2ip) and 5-amino-isophthalic acid (H_2aip) (Figure 4.1).[1] They present different luminescent properties because of a photo-induced electron transfer mechanism (PET).[2] To further understand this mechanism, the series of lanthanide containing coordination polymers based on H_2hip ligand was prepared and characterized.

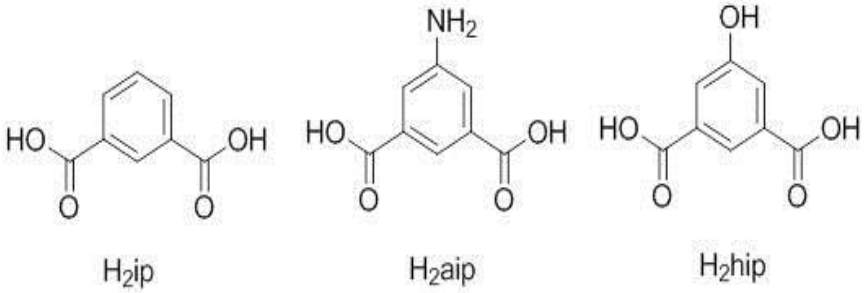

Figure4.1 Isophthalic acid, 5-amino-isophthalic acid, and 5-hydroxy-isophthalic acid.

4.1 Preparation of di-sodium salt of 5-hydroxylisophthalic acid.

The synthesis of the di-sodium salt of 5-hydroxy-isophthalic acid (H_2hip) is similar to that of Na_2cda (Chapter 3) except that chelidonic acid (H_2cda) is replaced by 5-hydroxy-isophthalic acid (H_2hip). After filtration and drying, the white powder of the di-sodium salt of H_2hip acid was obtained in 90% yields. The UV-vis absorption spectrum of Na_2hip aqueous solution (1×10^{-5} mol.L^{-1}) was measured. It shows a broad absorption band centered at 300 nm (Figure 4.2).

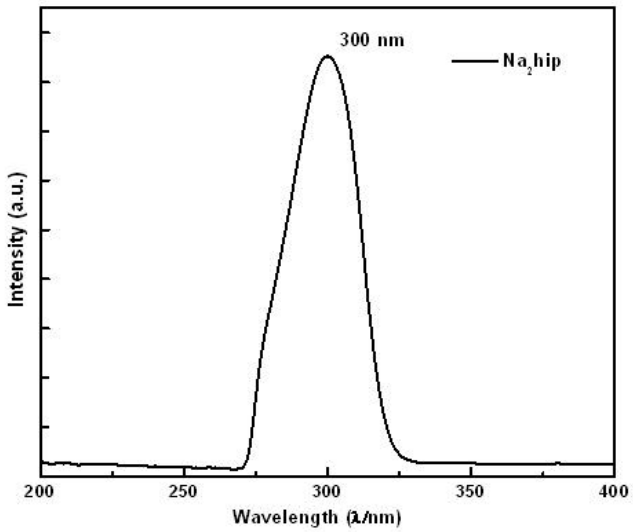

Figure 4.2 UV-vis absorption spectrum of a Na_2hip aqueous solution.

4.2 Preparation of microcrystalline powders of lanthanide-based coordination polymers.

4.2.1 Synthesis of microcrystalline powders of homo-nuclear compounds.

Microcrystalline powders of lanthanide-based (La to Lu plus Y) compounds are synthesized with the same stoichiometric amounts at different temperatures (2°C, room temperature or 100 °C).

A clear solution of lanthanide chloride (0.5 mmol in 10mL H_2O) was added to an aqueous solution of the di-sodium salt of H_2hip (0.75 mmol in 10 mL H_2O). Precipitation immediately occurred at 2°C, room temperature and 100 ^{O}C. The precipitations were filtered and dried at room temperature. The white resulting powders were obtained in 90% yields. The microcrystalline powders were classified by families (Table 4.1) of iso-structural compounds on the basis of their X-ray powder diffraction diagrams (Figure 4.3).

Table 4.1 Families of Lanthanide-based compounds.

L=hip	La	Ce	Pr	Nd	Sm	Eu	Gd	Tb	Dy	Ho	Y	Er	Yb	Lu
2°C														
RT														
100°C														

	Family 1 No crystal structure.
	Family 2 Novel coordination polymers.
	Family 3 Novel coordination polymers.
	Family 4 No crystal structure.
	Family 5 No crystal structure.

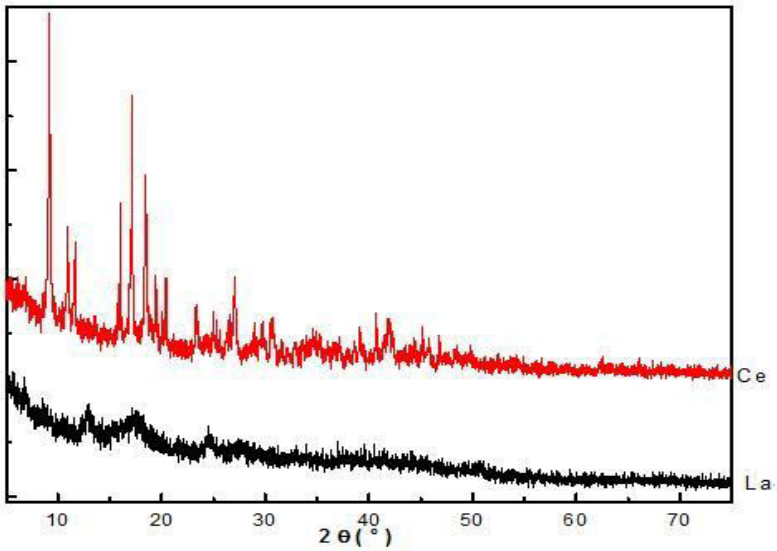
Ce
La
10
20
30
40
50
60
70
2 θ (°)

(a)

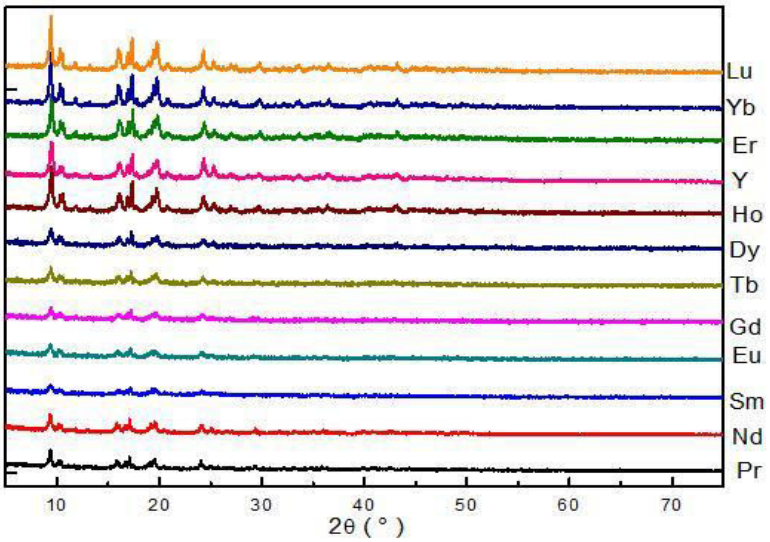
Lu
Yb
Er
Y
Ho
Dy
Tb
Gd
Eu
Sm
Nd
Pr
10
20
30
40
50
60
70
2θ (°)

(b)

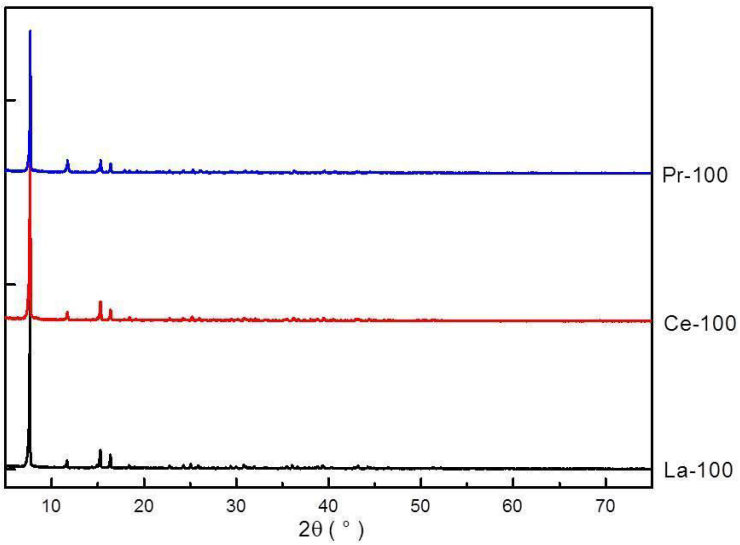
Pr-100
Ce-100
La-100
10
20
30
40
50
60
70
2θ (°)

(c)

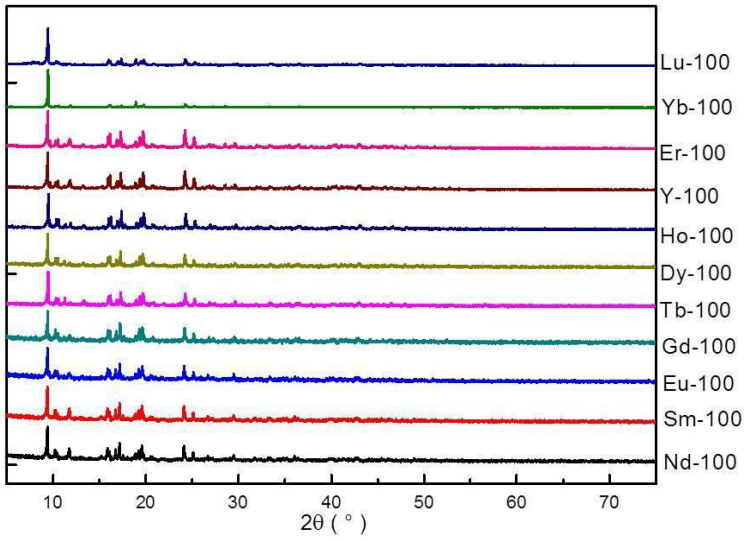

(d)

Figure 4.3 XPRD patterns of microcrystalline powders (a) Family 1 and 2 (RT), (b) Family 3 (RT), (c) Family 4 (100 °C) and (d) Family 5 (100 °C).

4.2.2 Synthesis of microcrystalline powders of hetero-nuclear compounds of Family 3.

Microcrystalline powders of the hetero-nuclear (Eu/Tb, Tb/Gd, and Y/Lu) compounds were obtained according to similar procedures by simply replacing the lanthanide chloride solution by the appropriate mixture of lanthanide chloride solution in the synthetic process. For hetero-nuclear compounds the relative ratios between the two different lanthanide ions were measured by EDS (Appendix I), and the results are listed in Table 4.2.

Table 4.2 Relative ratios between Ln and Ln' for some $[Eu_{2-2x}Tb_{2x}(hip)_2(H_2O)_{10}, (hip), 4H_2O]_\infty$ and $[Gd_{2-2x}Tb_{2x}(hip)_2(H_2O)_{10}, (hip), 4H_2O]_\infty$ compounds with $0 \leqslant x \leqslant 1$.

$[Eu_{2-2x}Tb_{2x}(hip)_2(H_2O)_{10}, (hip), 4H_2O]_\infty$			$[Gd_{2-2x}Tb_{2x}(hip)_2(H_2O)_{10}, (hip), 4H_2O]_\infty$		
Tb[a](%)	Eu[a](%)	X[b]	Tb[a](%)	Gd[a](%)	X[b]
100	0	1.00	100(2)	0	1.00
89(2)	11(2)	0.90	90(2)	10(2)	0.90
80(2)	20(2)	0.80	79(2)	21(2)	0.80
75(2)	25(2)	0.75	68(2)	32(2)	0.70
66(2)	34(2)	0.70	60(2)	40(2)	0.60
64(2)	36(2)	0.65	49(2)	51(2)	0.50
57(2)	43(2)	0.60	40(2)	60(2)	0.40
54(2)	46(2)	0.55	29(2)	71(2)	0.30
48(2)	52(2)	0.50	21(2)	79(2)	0.20
37(2)	63(2)	0.40	10(2)	90(2)	0.10
29(2)	71(2)	0.30	0	100	0.00
18(2)	82(2)	0.20			
11(2)	89(2)	0.10			
0	100	0.00			

a: experimental values (metal fractions found by elemental analyses).

b: Theoretical values (metal fractions used during the syntheses)

XPRD patterns of the hetero-nuclear compounds (Figure 4.4) reveal that they are iso-structural to the corresponding homo-nuclear compounds (Family 3).

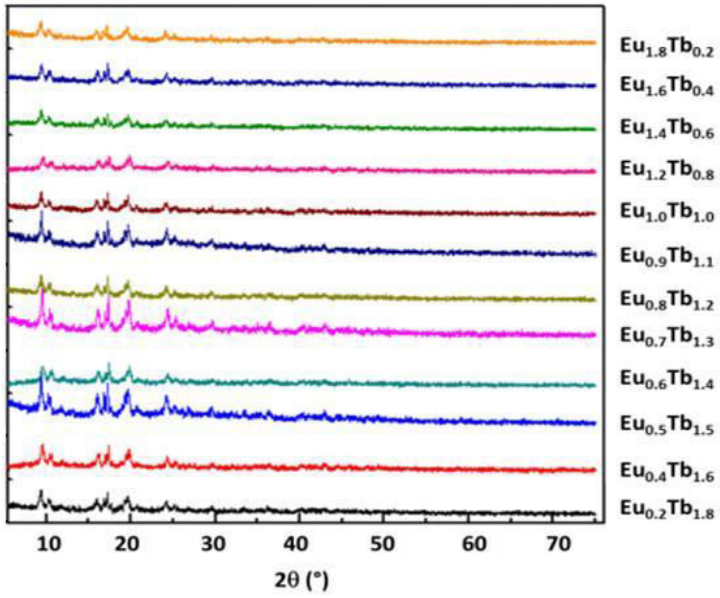

Figure 4.4a XPRD patterns for hetero-nuclear (Eu/Tb) compounds

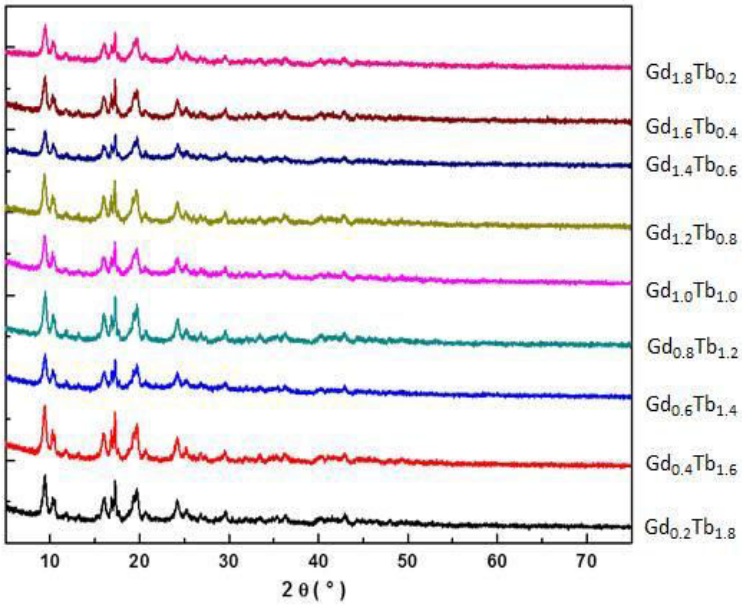

Figure 4.4b XPRD patterns for hetero-nuclear (Gd/Tb) compounds.

4.3 Distribution of the lanthanide ions over the metallic sites in the hetero-nuclear compounds.

To confirm that the distribution of the lanthanide ions over the metallic sites in the hetero-nuclear compounds is random, both the X-ray powder diffraction and solid state ^{89}Y RMN spectroscopy (Appendix I) have been used to verify the phenomenon at the X-ray scale and the local scale.

4.3.1 Distribution at X-ray scale.

Four samples have been prepared and their powder X-ray diffraction diagrams compared (Figure 4.5):

1). Two homo-nuclear compounds involving two lanthanide ions with very different ionic radii- $[Nd_2(hip)_2(H_2O)_{10}, (hip), 4H_2O]_\infty$ and $[Y_2(hip)_2(H_2O)_{10}, (hip), 4H_2O]_\infty$.
2). A fifty-fifty mixture of homo-nuclear compounds: $0.5[Nd_2(hip)_2(H_2O)_{10}, (hip), 4H_2O]_\infty$ and $0.5[Y_2(hip)_2(H_2O)_{10}, (hip), 4H_2O]_\infty$.
3). The 50/50 hetero-nuclear compound $[NdY(hip)_2(H_2O)_{10}, (hip), 4H_2O]_\infty$.

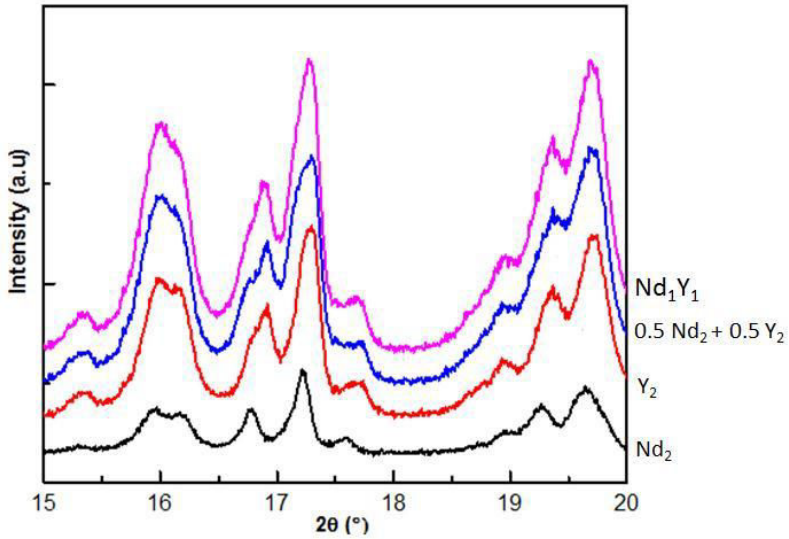

Figure 4.5 XPRD patterns of $[Nd_2(hip)_2(H_2O)_{10}, (hip), 4H_2O]_\infty$, $[Y_2(hip)_2(H_2O)_{10}, (hip), 4H_2O]_\infty$, $0.5[Nd_2(hip)_2(H_2O)_{10}, (hip), 4H_2O]_\infty$+$0.5[Y_2(hip)_2(H_2O)_{10}, (hip), 4H_2O]_\infty$, and $[NdY(hip)_2(H_2O)_{10}, (hip), 4H_2O]_\infty$.

The powder X-ray diffraction diagrams of these four samples show that the diffraction peaks of the hetero-nuclear compounds are not split and are located between the corresponding diffraction peaks of the homo-nuclear (Nd and Y) compounds. Meanwhile, the powder X-ray diffraction patterns of the hetero-nuclear (Eu/Tb and Gd/Tb) compounds (Figure 4.4) indicate that there is neither a long range order nor segregation in the hetero-nuclear compounds. Both exhibit that distribution of the lanthanide ions over the metallic sites in the hetero-nuclear compounds is random at the X-ray scale.

4.3.2 Distribution at the local scale.

^{89}Y NMR spectroscopy is a useful probe of local ordering in solid state compounds which have been reported by some papers.[3] Diamagnetic lanthanide ions (Lu^{3+}) were chosen to synthesize the hetero-nuclear (Y/Lu) compounds with the general chemical formula $[Y_{2-2x}Lu_{2x}(hip)_2(H_2O)_{10}, (hip), 4H_2O]_\infty$ (x=0, 0.4 and 0.7) for achieving high resolution solid state NMR experiments (Figure 4.6).

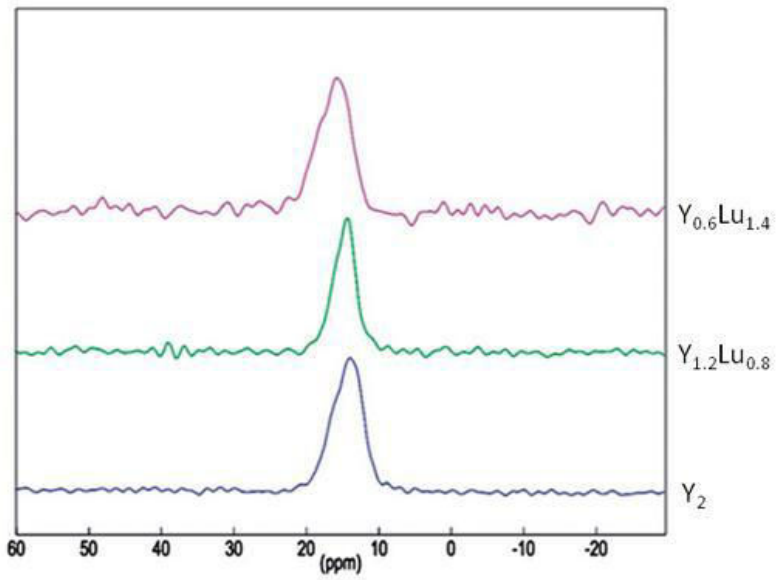

Figure 4.6 ^{89}Y MAS NMR spectra recorded at a spinning rate of 4KHz using a CPMAS pulse sequence for three compounds $[Y_{2-2x}Lu_{2x}(hip)_2(H_2O)_{10}, (hip), 4H_2O]_\infty$ (x=0, 0.4 and 0.7).

NMR spectra clearly show that regardless of Lutetium rate, the magnetic signal remains almost identical, this indicates that the local environment of the Y^{3+} ions remains unchanged, but the NMR spectra of Y/Lu mixed compounds cannot be described as the superimposition of the pure yttrium compound.

These measurements show no evidence for local ordering and support the interpretation of randomly distributed yttrium and lutetium ions over the metallic sites in the hetero-nuclear compounds at the local scale.

All these characterizations at the X-ray diffraction scale and the NMR scale demonstrate that the particles constituting the microcrystalline powders are homogenous in composition and each one contains the whole information.

4.4 Synthesis of single crystals.

Single crystals of lanthanide-based compounds were synthesized by slow diffusions of lanthanide chloride (0.5 mmol in 10 mL H_2O)and Na_2hip (0.5 mmol in 10 mL H_2O) solutions in H-shaped tubes as well as in U-shaped tubes containing gel (Agar-Agar, TMOS or TEOS).[4] Details are reported in Appendix I. After a few weeks, single-crystals were obtained in the U-shaped tubes that were fill with 7.5% gel (TMOS or TEOS) or Agar-Agar (0.3% or 0.5%). Slow evaporation of the filtrates obtained in the syntheses of the corresponding micro-crystalline powders also offers single crystals of good quality. Single crystals suitable for crystal structure characterizations of Family 2 $\{[Ce_2(hip)_3(H_2O)_9, 6H_2O)]_\infty\}$ and Family 3 $\{[Ln_2(hip)_2(H_2O)_{10}, (hip), 4H_2O]_\infty\}$ have been obtained.

These crystals are needle-like shaped (Figure 4.7). Single crystals were sealed in glass capilaries for single crystals X-ray data collection in order to avoid potential dehydration. Compounds of Families 1, 4 and 5 have only been obtained as microcrstalline powders and

despite great efforts no single crystal suitable for X-ray caracterization has been obtained. The work is still in process.

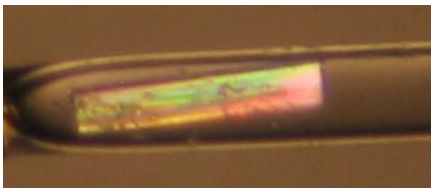

Figure 4.7 Picture of a single crystal sealed in a glass capillary.

4.5 Description of the crystal structures.

4.5.1 $[Ce_2(hip)_3(H_2O)_9, 6H_2O)]_\infty$.

The single crystal $[Ce_2(hip)_3(H_2O)_9, 6H_2O)]_\infty$ was gotten by solw evaporating the filtrate after reaction at room temperature.

$[Ce_2(hip)_3(H_2O)_9, 6H_2O)]_\infty$ crystallizes in the monoclinic system, space group $P2_1$, with the cell parameters: a = 10.7150(3) Å, b = 11.1039(2) Å, c = 16.3611(4) Å, β = 100.975(2) ° and Z = 2 (Table 4.3). Atomic parameters and selected bond lengths and angles are listed in Appendix II.

Table 4.3 Crystal data for$[Ce_2(hip)_3(H_2O)_9, 6H_2O)]_\infty$ and $[La_2(hip)_2(H_2O)_{10}, (hip), 4H_2O]_\infty$.

formula	$C_{24}H_{42}O_{30}Ce_2$	$C_{24}H_{37}O_{29}La_2$
Mw	1090.82	1067.36
Crystal system	monoclinic	monoclinic
Space group	P 21	P 21/n
a(Å)	10.7150(3)	17.906(5)
b(Å)	11.1039(2)	21.419(5)
c(Å)	16.3611(4)	19.917(5)
α(°)	90	90
β(°)	100.975(2)	107.658(5)
ϒ(°)	90	90
V ($Å^3$)	1911.01(8)	7279(3)
Z, ρ_{calc} (g/cm^3)	2, 1.896	8, 1.948
GOF on F^2	1.06	1.132
R	0.0423	0.0864
Rw	0.0838	0.0875
CCDCC	995942	962512

In this crystal structure, the asymmetric unit contains two Ce^{3+} ions, three hip^{2-} ligands, nine coordination water molecules and six crystallization water molecules. The two Ce^{3+} ions are nine-coordinated. Ce1 is coordinated by four oxygen atoms from the carboxylate groups of two different hip^{2-} ligands and five oxygen atoms from coordination water molecules that generate a tricapped trigonal-prismatic geometry (2.036 calculated by SHAPE2.0 software). The coordination environment of the other Ce^{3+} ion (Ce2) is similar,

except that one oxygen atom from a coordination water molecule is replaced by an oxygen atom from an additional hip^{2-} ligand. The coordination polyedron is best described as a distorted capped square-antiprism (2.016 calculateded by SHAPE2.0 software)[5] (Figure 4.8).

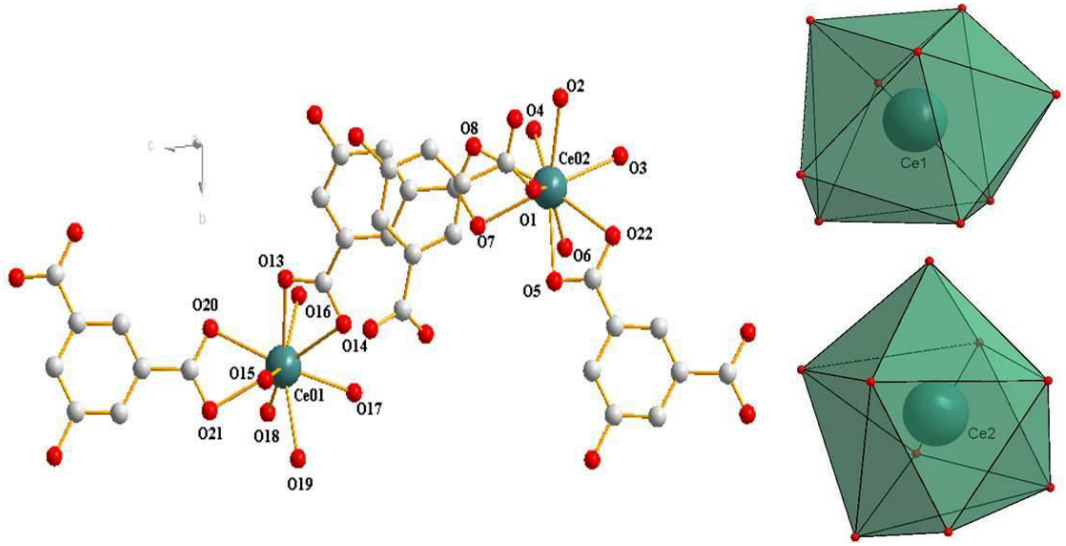

Figure 4.8 (a) Coordination environments and (b) coordination geometries of Ce^{3+} ions in $[Ce_2(hip)_3(H_2O)_9, 6H_2O)]_\infty$.

The crystal structure can be described on the basis of 1D molecular chains (Figure 4.9c). There are two coordinated mode for hip^{2-} ligand (Figure 4.9a and b). Mode a is bis-bidentate and acts as a bridge to connect two Ce^{3+} ions ; Mode b is mondentate and only links Ce2 to decorate the chain.

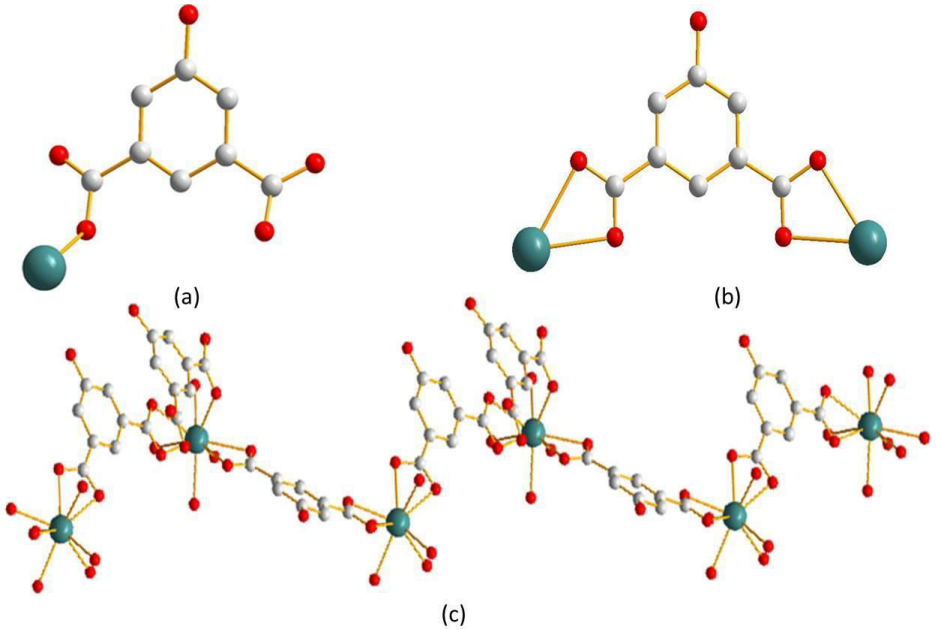

Figure 4.9 (a,b) coordinating modes of hip^{2-} ligandsand (c) 1D molecular chain of $[Ce_2(hip)_3(H_2O)_9, 6H_2O)]_\infty$.

The short distances between some oxygen atoms (in the range 2.7-2.8 Å) indicate that quite strong hydrogen bond interactions further assemble neighborings chain forming a double-chains molecular motif (Figure 4.10). Hydrogen bonds also stabilize the crystal

packing.

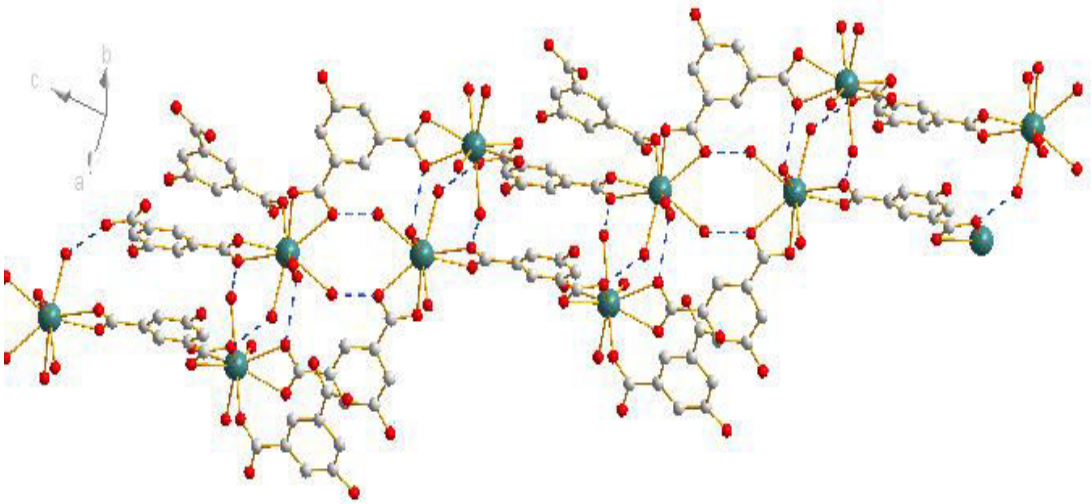

Figure 4.10 Hydrogen-bonds (doted lines) leading to double-chains molecular motifs.

XRPD pattern of the micro-crystalline powder of the Ce-containing compound is similar to the X-ray diffraction diagram simulated on the basis of the crystal structure (Figure 4.11).

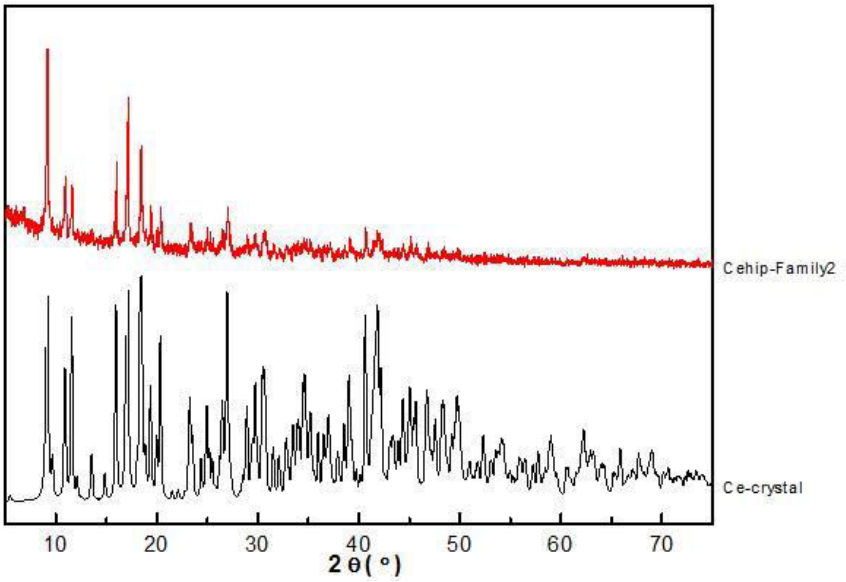

Figure 4.11 XRPD pattern of the Ce-containg compound of Family 2 and the simulated XRD diagram of $[Ce_2(hip)_3(H_2O)_9, 6H_2O)]_\infty$.

4.5.2 $[La_2(hip)_2(H_2O)_{10}, (hip), 4H_2O]_\infty$.

The single crystal $[La_2(hip)_2(H_2O)_{10}, (hip), 4H_2O]_\infty$ was gotten by diffusion in the U-shaped tubes which contains gels (Agar-Agar or TMOS).

$[La_2(hip)_2(H_2O)_{10}, (hip), 4H_2O]_\infty$ crystallizes in the monoclinic system, space group P21/n, with a = 17.906(5) Å, b = 21.419(5) Å, c = 19.917(5) Å, β = 107.658(5)° and Z = 8 (Table 4.3). Atomic parameters and selected bond lengths and angles are listed in Appendix II.

In this crystal structure, there are two crystallographically independent La^{3+} ions which are located in two different chains. They have the same coordination environments and geometries. Both are nine coordinated by four oxygen atoms from two different hip^{2-} ligands and five oxygen atoms from five coordination water molecules (Figure 4.12a). Their coordination geometry is close to muffin geometry (1.915 and 1.396 calculated by the SHAPE 2.0 softwarefor La1 and La2 respectively)[5] (Figure 4.12b).

The crystal structure is 1D and can be described as a juxtaposition of stair-like molecular double-chain motifs. There is only one coordinated mode for hip^{2-} ligand: bis-bidentate acting as a bridge to connect La^{3+} ions and form a chain. Each molecular double–chain motif is constituted by two molecular chains held together by a network of strong hydrogen bonds and π-stacking interactions (Figure 4.13) Hydrogen bonds and π-stacking interactions distances are listed in Appendix II.

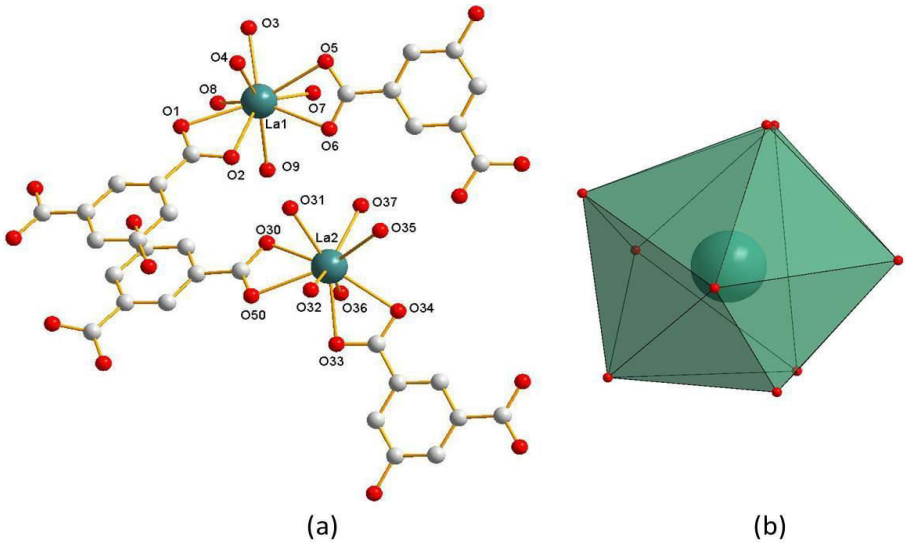

Figure 4.12 (a) Coordination environment and (b) geometry of La^{3+} ions in $[La_2(hip)_2(H_2O)_{10}, (hip), 4H_2O]_\infty$.

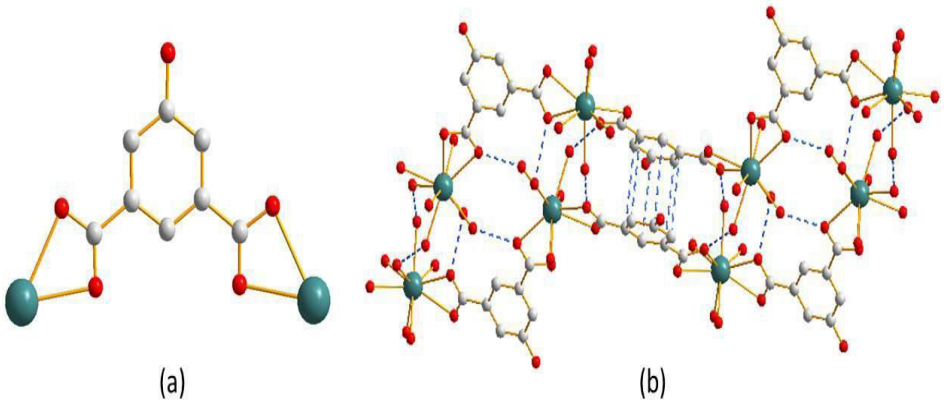

Figure 4.13(a) Coordination mode for hip^{2-} ligand and(b) stair-like double-chain molecular motif of $[La_2(hip)_2(H_2O)_{10}, (hip), 4H_2O]_\infty$.

Crystallization water molecules and free deprotonated hip^{2-} ligands lay between the double-chain molecular motifs. Deprotonated hip^{2-} ligands insure the electric neutrality of the network. Free deprotonated hip^{2-} ligand and crystallization water molecules also generate H-bonds and π-stacking interactions that ensure the crystal packing of the cationic molecular double-chains (Figure 4.14).

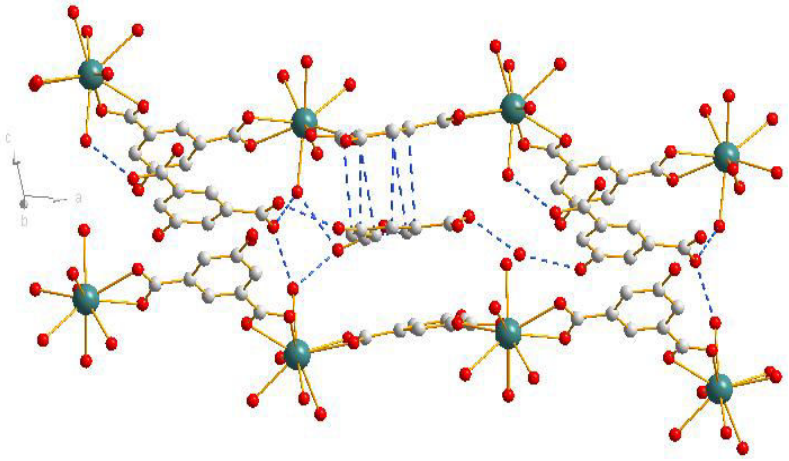

Figure 4.14 Packing of two double chain molecular motifs ensured by H-bonds and π-π stacking involving free hip^{2-} ligands and crystallization water molecules.

The crystal structure is similar to the one of the previously reported compounds with the general chemical formula $[Ln\,(hip)\,(H_2O)_5,\,(hip)_{1/2},\,H_2O]_\infty$ (Ln=Eu, Gd, Tb, Dy or Er).[6] The main difference between the two crystal structures is related to the free hip^{2-} ligand: In the previously reported crystal structure a disorder model was used for describing it while no disorder is observed in our crystal structure (Figure 4.15). Moreover, there is one more crystallization water molecule in our crystal structure.

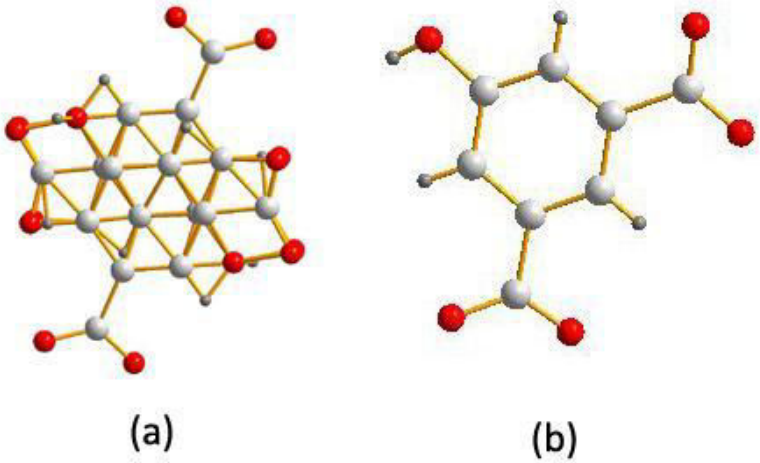

Figure 4.15 (a) Disorder model of the free ligand in $[Ln\,(hip)\,(H_2O)_5,\,(hip)_{1/2},\,H_2O]_\infty$and (b) no-disordered free hip^{2-} ligand in $[La_2(hip)_2(H_2O)_{10},\,(hip),\,4H_2O]_\infty$.

The shortest distances between La^{3+} ions that belong to the same zig-zag chain are

close to 10 Å. The shortest contacts between La^{3+} ions belonging to different chains of the double chain molecular motif are about 6 Å (Figure 4.16). These distances are almost similar in the crystal structures based on ip^{2-} and aip^{2-} ligands.[1]

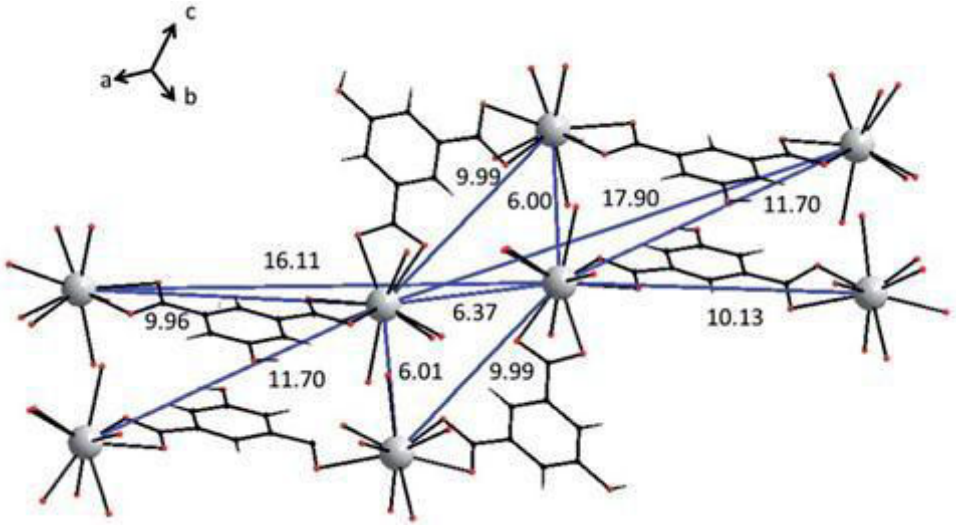

Figure 4.16 shortest intermetallic distances for $[La_2(hip)_2(H_2O)_{10}\cdot(hip)\cdot 4H_2O]_\infty$.

The mean diameter of the microcrystalline powders ($[Y_2(hip)_2(H_2O)_{10}\cdot(hip)\cdot 4H_2O]$) of Family 3 measured by laser granulometry (4.17a) is about 3.2 µm. The result is in agreement with what is observed in SEM pictures (Appendix I). All the microcrystalline powders of Family 3 are similar and are constituted by small particles in SEM pictures (Figure 4.17b).

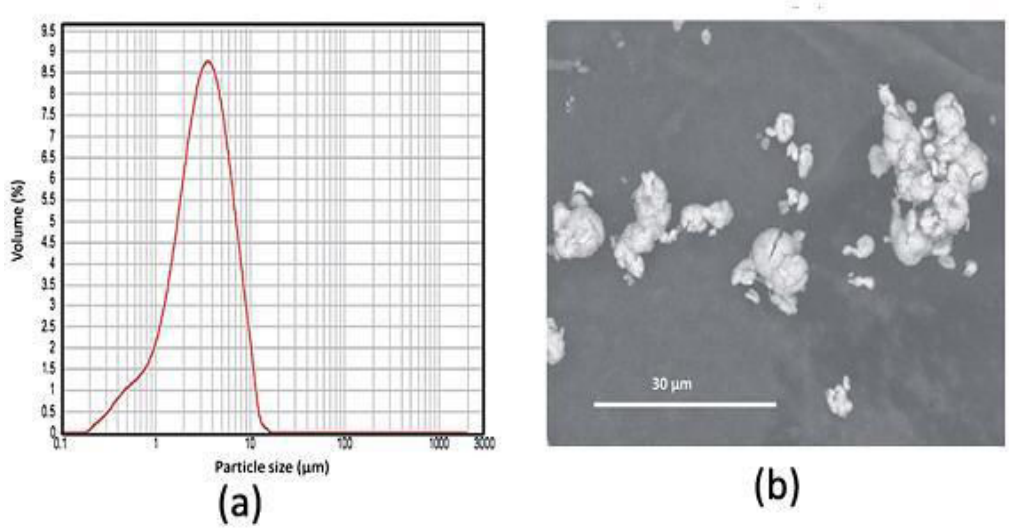

Figure 4.17 (a) particle size distribution and (b) SEM picture of microcrystalline powder of $[La_2(hip)_2(H_2O)_{10}\cdot(hip)\cdot 4H_2O]_\infty$.

Comparison of the simulated X-ray diffraction diagram $[La_2(hip)_2(H_2O)_{10}$, (hip), $4H_2O]_\infty$ with the powder X-ray diffraction diagrams (Figure 4.18) of the compounds that constitute Family 3 reveals that they are all iso-structural to $[La_2(hip)_2(H_2O)_{10}$, (hip), $4H_2O]_\infty$. Their cell

parameters (Table 4.4 and Figure 4.19) were refined on the basis of their powder X-ray diffraction patterns by the software Celref 3[7] (Appendix I). Refined cell parameters (a,b,c and β) are almost the same which indicates a weak influence of the involved lanthanide ion on the cell parameters compounds that belong to Family 3. The cell parameters of the hetero-nuclear (Eu/Tb and Gd/Tb) compounds ($[Ln_{2x}Ln'_{2-2x}(hip)_2(H_2O)_{10}\cdot(hip)\cdot 4H_2O]_\infty$) were also refined using the same method (Table 4.5, 4.6 and Figure 4.20,4.21), and the results also verified the conclusion: a weak influence of the involved lanthanide ion on the cell parameters.

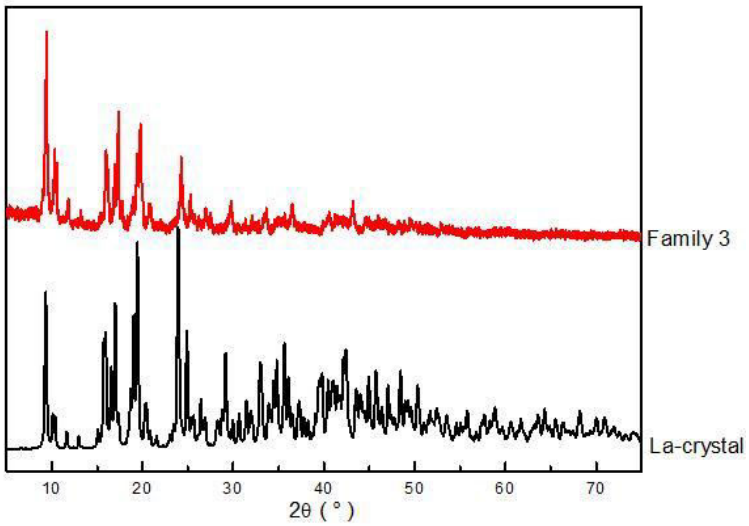

Figure 4.18Characteristic experimental powder XRD pattern of compounds belonging to Family 3 and simulated XRD diagram from the crystal structure of $[La_2(hip)_2(H_2O)_{10}, (hip), 4H_2O]_\infty$.

Table 4.4 Refined cell parameters for $[Ln_2(hip)_2(H_2O)_{10}, (hip), 4H_2O]_\infty$ (Ln= Pr-Lu plus Y).

Ln	a (Å)[a]	b (Å)[a]	c (Å)[a]	β (°)[a]
Pr	17.90	21.42	19.92	107.67
Nd	17.91	21.43	19.91	107.66
Sm	17.89	21.43	19.91	107.66
Eu	17.90	21.42	19.92	107.65
Gd	17.91	21.42	19.91	107.65
Tb	17.91	21.44	19.87	107.66
Dy	17.91	21.41	19.92	107.66
Ho	17.90	21.42	19.91(1)	107.63
Y	17.90	21.42	19.92(1)	107.63
Er	17.90	21.41	19.92	107.64
Yb	17.89	21.42	19.91	107.63
Lu	17.90	21.41	19.92	107.63

a. calculated values (cell parameters calculate by software Celref).

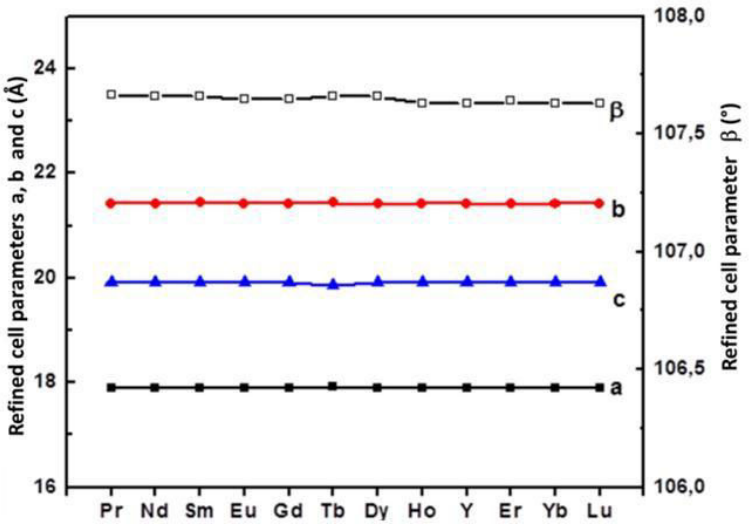

Figure 4.19 Refined cell parameters for $[Ln_2(hip)_2(H_2O)_{10}, (hip), 4H_2O]_\infty$ (Ln= Pr-Lu plus Y).

Table 4.5 Refined cell parameters for $[Eu_{2-2x}Tb_{2x}(hip)_2(H_2O)_{10}, (hip), 4H_2O]_\infty$ with 0 < x <1.

x	a (Å)[a]	b (Å)[a]	c (Å)[a]	β(°)[a]
0.1	17.90	21.41	19.94	107.66
0.2	17.91	21.41	19.91	107.64
0.3	17.89	21.42	19.92	107.63
0.35	17.92	21.41	19.91	107.65
0.4	17.90	21.39	19.91	107.62
0.45	17.89	21.39	19.92	107.63
0.5	17.90	21.41	19.91	107.62
0.55	17.90	21.40	19.92	107.64
0.6	17.90	21.41	19.92	107.63
0.7	17.92	21.42	19.91	107.63
0.8	17.91	21.41	19.91	107.62
0.9	17.89	21.42	19.91	107.62

a. calculated values (cell parameters calculate by software Celref).

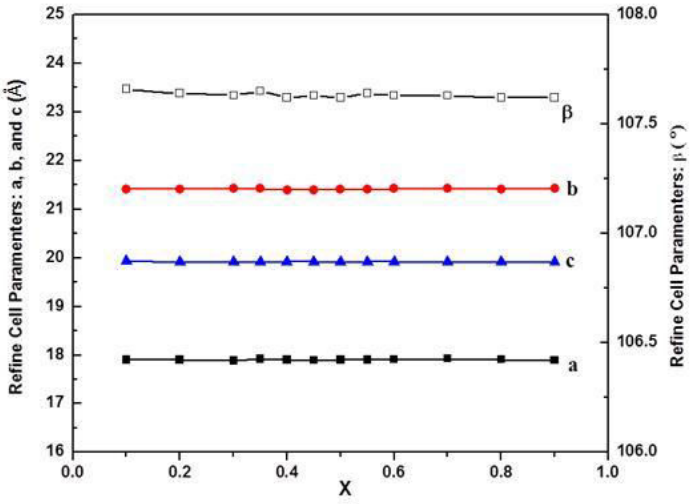

Figure 4.20 Refined cell parameters for $[Eu_{2-2x}Tb_{2x}(hip)_2(H_2O)_{10}, (hip), 4H_2O]_\infty$, $0.1 \leq x \leq 0.9$.

Table 4.6 Refined cell parameters for $[Gd_{2-2x}Tb_{2x}(hip)_2(H_2O)_{10}, (hip), 4H_2O]_\infty$ with $0 < x < 1$				
x	a (Å)[a]	b (Å)[a]	c (Å)[a]	β (°)[a]
0.1	17.91	21.42	19.92	107.65
0.2	17.91	21.40	19.91	107.64
0.3	17.91	21.42	19.91	107.64
0.4	17.9	21.41	19.92	107.63(1)
0.5	17.91	21.41	19.91	107.63
0.6	17.90	21.42	19.91	107.64
0.7	17.90	21.41	19.91	107.63
0.8	17.90	21.42	19.91	107.63
0.9	17.91	21.41	19.91	107.64
a. calculated values (cell parameters calculate by software Celref).				

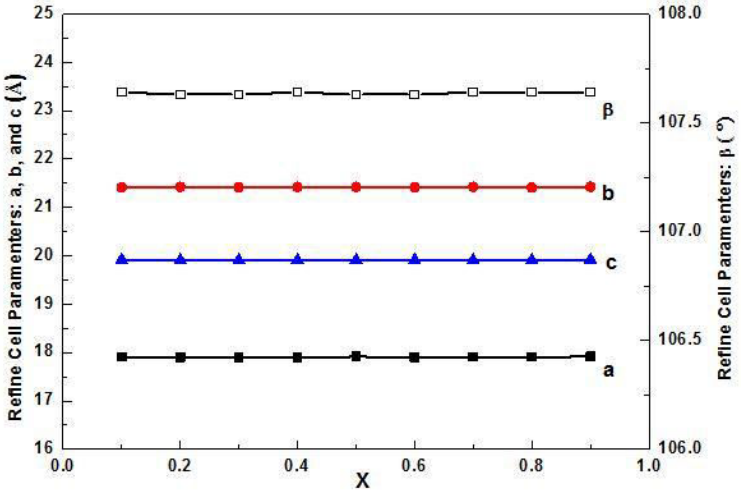

Figure 4.21 Refined cell parameters for $[Gd_{2-2x}Tb_{2x}(hip)_2(H_2O)_{10}, (hip), 4H_2O]_\infty$, $0.1 \leq x \leq 0.9$.

4.6 Study of the thermal stabilities.

Thermal stabilities of all families were investigated by TGA/TDA experiments in the 25-995°C temperature range under N_2 atmosphere. Program details about TGA/TDA are given in Appendix I. The curves of the Gd-containing compound of family 3 is treated as an example (Figure 4.22). Curves of the other families are reported in Appendix II.

Thermal analysis shows a 22.4% weight loss form room temperature to 150°C that corresponds to the departure of 14 water molecules (calc. 22.9%). The anhydrous phasis is stable between 150 to 300°C and then the weight loss that occurs above 300°C is attributed to the decomposition of the ligand. Finally, above 990°C Gd_2O_3 forms.

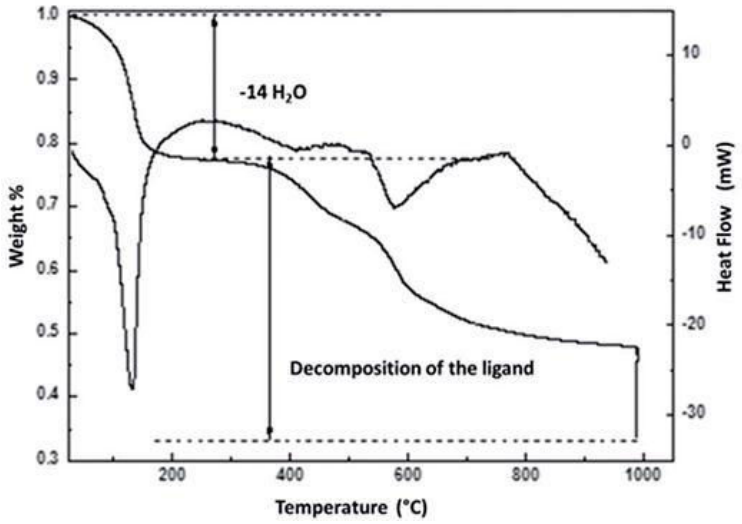

Figure 4.22 TGA/TDA curves for a microcrystalline sample of $[Gd_2(hip)_2(H_2O)_{10}$, (hip), $4H_2O]_\infty$.

TDXD diagrams of $[Gd_2(hip)_2(H_2O)_{10}$, (hip), $4H_2O]_\infty$ confirm the results of the thermal analysis (Figure 4.23). The sample has been heated from room temperature to 850°C under N_2 flux. The crystal structure is unchanged from room temperature to 75°C. From 100 to 350°C, the crystal structure collapses upon dehydration leading to an amorphous phasis, this is in agreement with the mono-dimensional character of the crystal structure. At last, the sample completely decomposes and crystallizes into Gd_2O_3..

Dehydration-rehydration experiments were performed for a study of the thermal stability of the molecular network. The Tb-containing compound $[Tb_2(hip)_2(H_2O)_{10}$, (hip), $4H_2O]_\infty$ was heated at 250°C for 2 hours to obtain the dehydrated phasis. XPRD pattern of the dehydrated phasis has broadened and some of the characteristic peaks have disappeared. Then the dehydrated compound was put into distilled water. After filtration and drying at room temperature, the rehydrated phasis was obtained back. Actually XPRD pattern of the rehydrated phasis was similar to the one of the original sample $[Tb_2(hip)_2(H_2O)_{10}$, (hip), $4H_2O]_\infty$ (Figure 4.24). This experiment demonstrates that the dehydrated material reversibly binds water reforming the hydrated phasis when exposed under a wet medium and the molecular network is not destroyed upon dehydration.

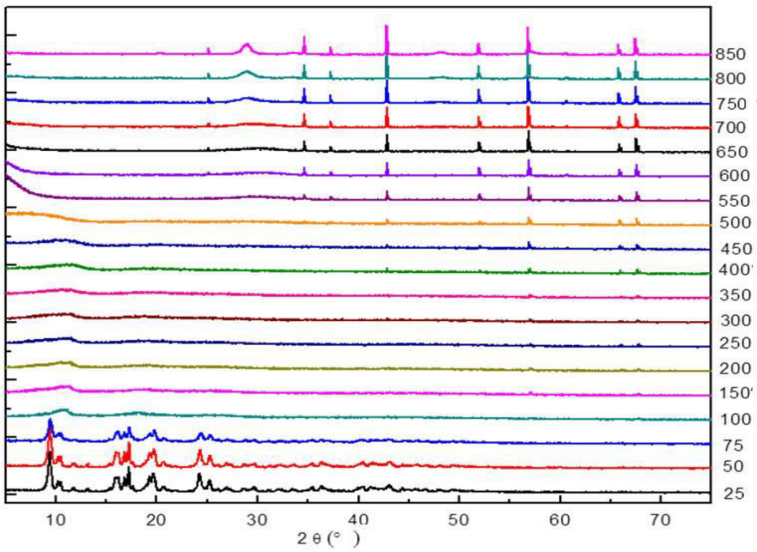

Figure 4.23TDXD diagrams under N_2 flux between room temperature and 850°C for $[Gd_2(hip)_2(H_2O)_{10}, (hip), 4H_2O]_\infty$.

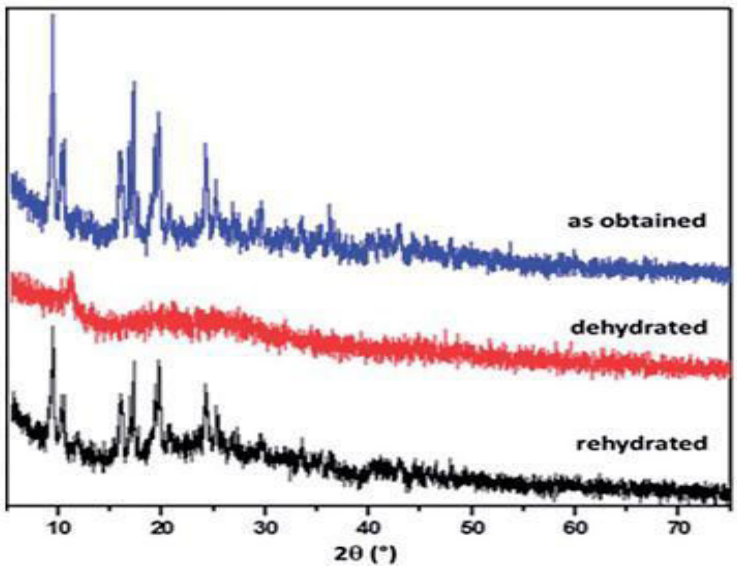

Figure 4.24 XPRD patterns of $[Tb_2(hip)_2(H_2O)_{10}, (hip), 4H_2O]_\infty$ before dehydration,after dehydration and after rehydration.

4.7 UV-vis absorption measurements.

Solid-state UV-vis absorption spectrum of $[Gd_2(hip)_2(H_2O)_{10}, (hip), 4H_2O]_\infty$ has been recorded for estimating the energy of the lowest singlet excited state of hip^{2-} ligand (Figure 4.25) on the basis of the wavelength of the UV-vis absorbance edge (310 nm ≈32 250 cm^{-1}).[8]

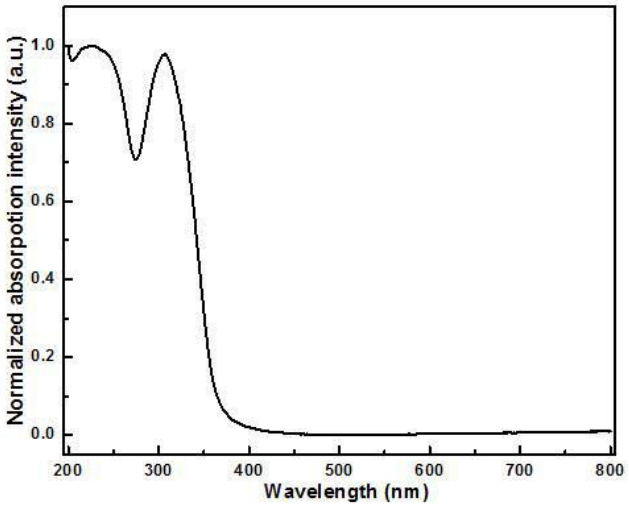

Figure 4.25 Solid state absorption spectrum of $[Gd_2(hip)_2(H_2O)_{10}, (hip), 4H_2O]_\infty$.

Highly luminescent compounds must present an important absorption cross-section. Because of the insolubility of the compound in common solvents, the molar absorption coefficient could not be determined, which prevented us to estimate luminescent efficiency: $f_{lum} \approx Q_{Ln}^{ligand} \times \varepsilon_\lambda$ where f_{lum} is the luminescence efficiency, Q_{Ln}^{ligand} is the overall quantum yield and ε_λ is the molar absorption coefficient.[9] Therefore, the molar absorption coefficient of the deprotonated ligand has been calculated from a series of dilute aqueous solution (Table 4.7) of its di-sodium salt (Figure 4.26).

Table 4.7 Absorbance of dilute aqueous solutions of di-sodium salt of H_2hip acid.

mol.L^{-1}	absorbance
$6.25.10^{-4}$	1.72
$3.91.10^{-4}$	1.07
$3.13.10^{-4}$	0.91
$1.56.10^{-4}$	0.47
$1.25.10^{-4}$	0.35
$7.80.10^{-5}$	0.21
$6.25.10^{-5}$	0.19
$3.90.10^{-5}$	0.12

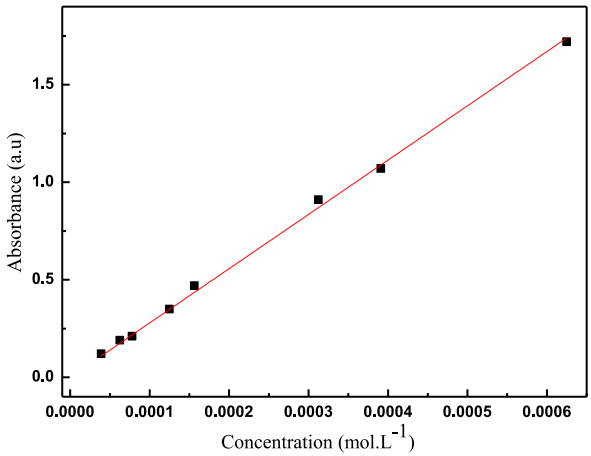

Figure 4.26 Absorbance versus concentration of dilute aqueous solutions of Na_2hip.

Calculated molar absorption coefficient of the deprotonated hip^{2-} ligand was ε_{max}=2800 L mol^{-1} cm^{-1}. This is quite sizeable and may explain the large luminance of the lanthanide coordination polymers based on this ligand.

4.8 Luminescent properties of the homo-nuclear compounds.

Before working on hetero-nuclear compounds, we firstly studied the luminescence properties of the homo-nuclear compounds with general chemical formula $[Ln_2(hip)_2(H_2O)_{10}$,

(hip), $4H_2O]_\infty$ (Ln=Sm, Eu, Tb, or Dy). Solid-state excitation and emission spectra were recorded (Figure 4.27).

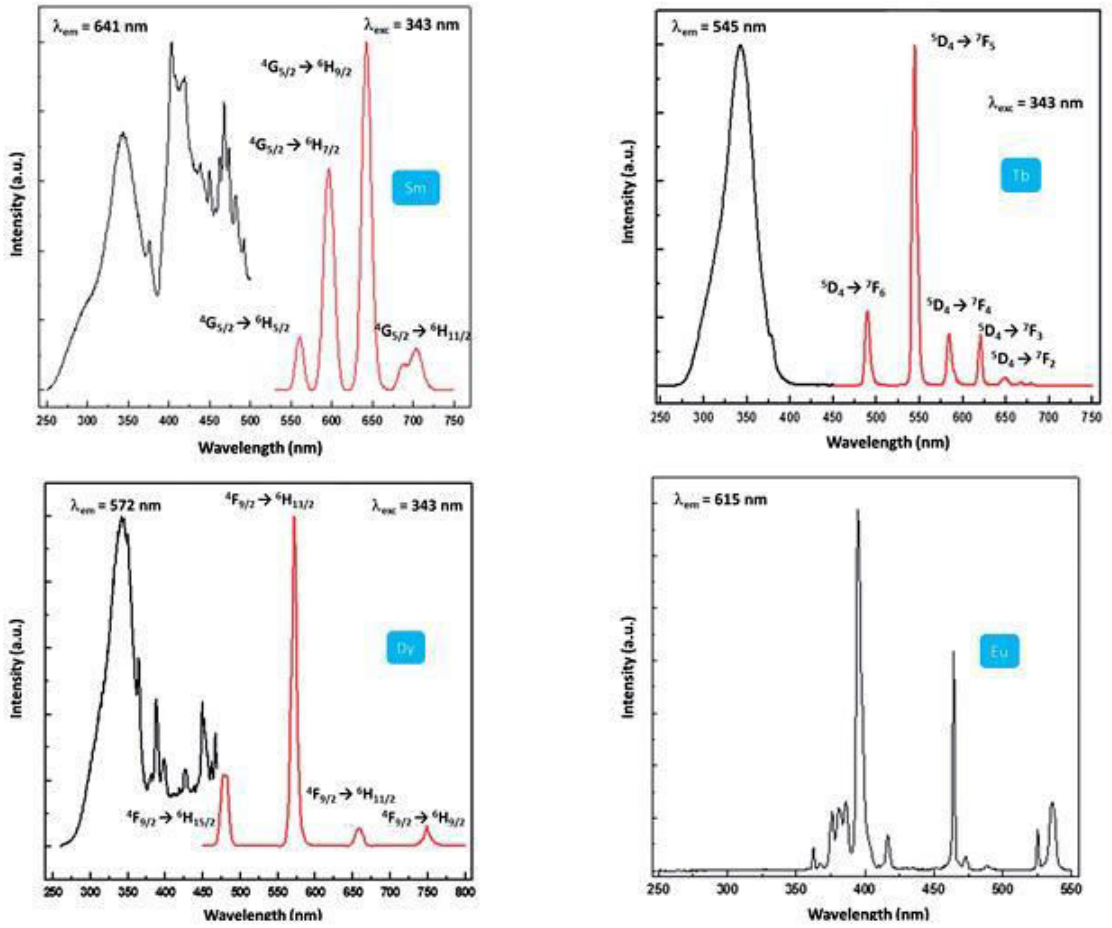

Figure 4.27 Excitation and emission spectra for $[Ln_2(hip)_2(H_2O)_{10}$, (hip), $4H_2O]_\infty$ (Ln=Sm, Tb and Dy) and excitation spectrum for $[Eu_2(hip)_2(H_2O)_{10}$, (hip), $4H_2O]_\infty$.

Excitation spectra of the Sm- Tb- and Dy-containing compounds show a broad band centered at 343 nm. This confirms that for these three ions the ligand presents an efficient antenna effect. On the other hand, the excitation spectrum of the Eu-containing compounds does not present any band that can suggest the presence of an antenna effect. All the excitation peaks correspond to the typical excitation peaks of Eu^{3+} ion. This excitation spectrum supports the presence of a photo-induced electron transfer (PET) mechanism. The PET mechanism strongly depends on the temperature so the excitation spectrum of $[Eu_2(hip)_2(H_2O)_{10}$, (hip), $4H_2O]_\infty$ at room temperature and at 77 K were recorded and compared (Figure 4.28). At 77 K, the broad band centered at 343 nm obviously appears. This strongly suggests the presence of the PET mechanism for $[Eu_2(hip)_2(H_2O)_{10}$, (hip), $4H_2O]_\infty$. Therefore, emission spectra of the Tb-, Sm- and Dy-containing compounds were recorded under excitation at 343 nm, and that of the Eu-containing compound was recorded under irradiation at 395 nm which is a wavelength that corresponds to a direct excitation of the

Eu^{3+} ions ($^7F_0 \rightarrow {}^5D_3$ transition).

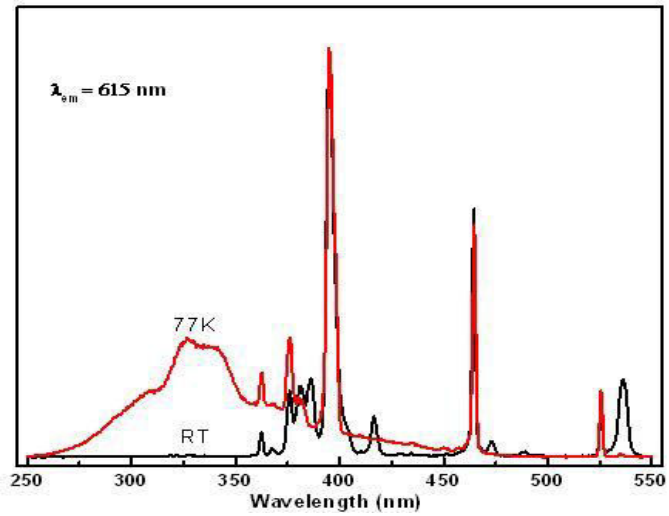

Figure 4.28 Excitation spectra of $[Eu_2(hip)_2(H_2O)_{10}, (hip), 4H_2O]_\infty$ recordedat room temperature and at 77K.

The Sm-containing microcrystalline powder exhibits four emission peaks at 560, 596, 642 and 703 nm which respectively correspond to the typical transitions: $^4G_{5/2} \rightarrow {}^6H_{5/2}$, $^4G_{5/2} \rightarrow {}^6H_{7/2}$, $^4G_{5/2} \rightarrow {}^6H_{9/2}$ and $^4G_{5/2} \rightarrow {}^6H_{11/2}$ under irradiation at 343 nm (Figure 4.29a). Its overall quantum yield is 0.11% and the observed luminescent lifetime is about 0.008 ms. Its luminescent decay rate is mono-exponential (Figure 4.29b).

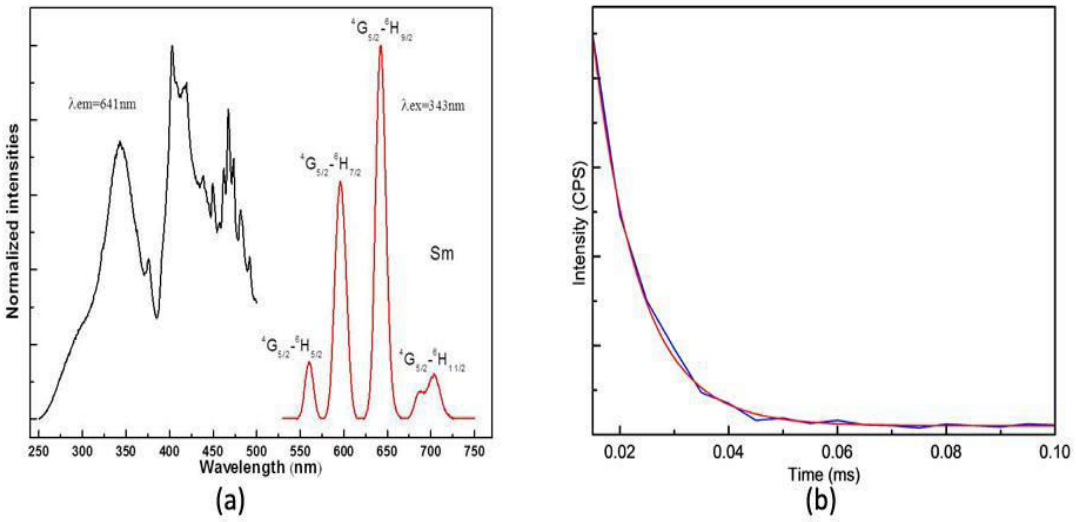

Figure 4.29 (a) Excitation and emission spectra and (b) the luminescent decay for $[Sm_2(hip)_2(H_2O)_{10}, (hip), 4H_2O]_\infty$.

The Tb-containing microcrystalline powder exhibits seven emission peaks at 490, 545, 585, 621, 650, 665 and 678 nm which respectively correspond to the typical transitions: $^4D_4 \rightarrow {}^7F_6$, $^4D_4 \rightarrow {}^7F_5$, $^4D_4 \rightarrow {}^7F_4$, $^4D_4 \rightarrow {}^7F_3$, $^4D_4 \rightarrow {}^7F_2$, $^4D_4 \rightarrow {}^7F_1$ and $^4D_4 \rightarrow {}^7F_0$ under irradiation at 343 nm (Figure 4.30a).). Its overall quantum yield is 24% and the observed luminescent lifetime is about 0.52 ms. Its luminescent decay rate is also mono-exponential (Figure 4.30b). The Tb-containing compound emits bright green light.

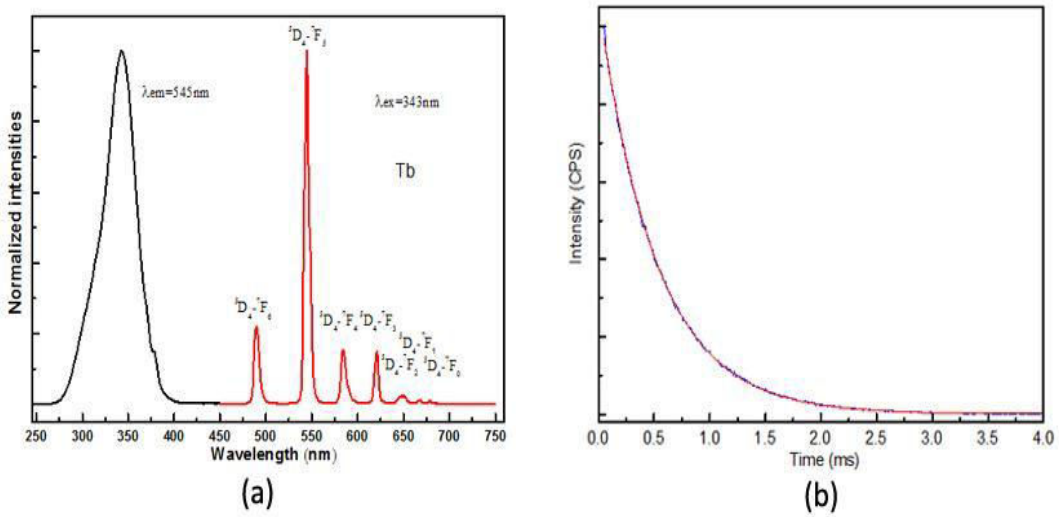

Figure 4.30 (a) Excitation and emission spectra and (b) luminescent decayfor $[Tb_2(hip)_2(H_2O)_{10}, (hip), 4H_2O]_\infty$.

The Dy-containing microcrystalline powder exhibit four emission peaks at 478, 572, 660 and 750 nm which respectively correspond to the typical transitions: $^4F_{9/2}\rightarrow{}^6H_{15/2}$, $^4F_{9/2}\rightarrow{}^6H_{13/2}$, $^4F_{9/2}\rightarrow{}^6H_{11/2}$ and $^4F_{9/2}\rightarrow{}^6H_{9/2}$ under irradiation at 343nm (Figure 4.31a). Its overall quantum yield is 0.34% and the observed luminescent lifetime is about 0.007 ms. Its luminescent decay rate is also mono-exponential (Figure 4.31b).

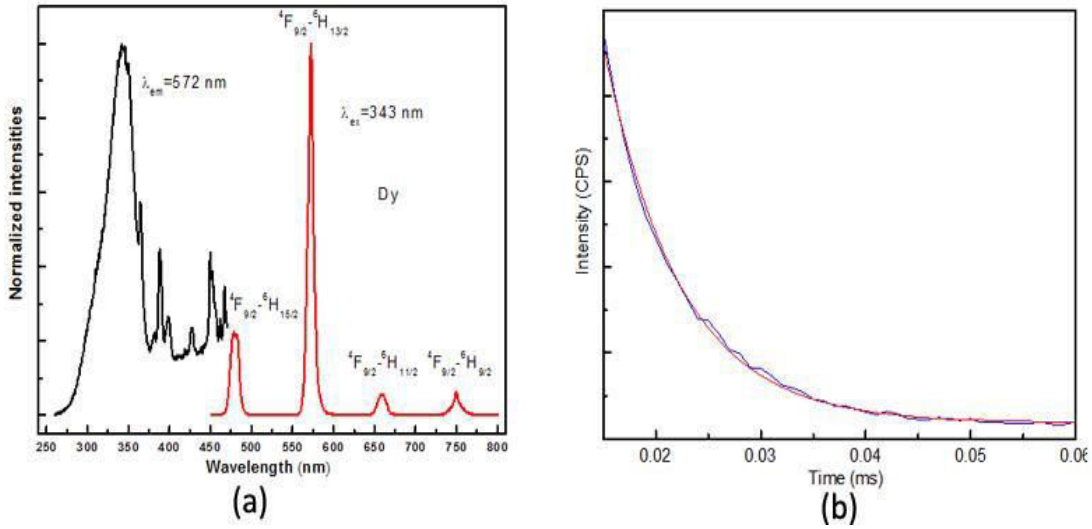

Figure 4.31 (a) Excitation and emission spectra and (b) luminescent decayfor $[Dy_2(hip)_2(H_2O)_{10}, (hip), 4H_2O]_\infty$.

The Eu-containing compound exhibits no luminescence under irradiation at 343nm, so the emission spectrum of $[Eu_2(hip)_2(H_2O)_{10}, (hip), 4H_2O]_\infty$ was recorded under irradiation at 395nm. The microcrystalline powder exhibits five emission peaks at 592, 615, 650, 688/693 and 752nm which respectively correspond to the typical transitions: $^4D_0\rightarrow{}^7F_1$, $^4D_0\rightarrow{}^7F_2$, $^4D_0\rightarrow{}^7F_3$, $^4D_0\rightarrow{}^7F_4$ and $^4D_0\rightarrow{}^7F_5$ (Figure 4.32a). Its intrinsic quantum yield is 0.53% and the observed luminescent lifetime is about 0.0172 ms. Its luminescent decay rate is also mono-exponential (Figure 4.32b).

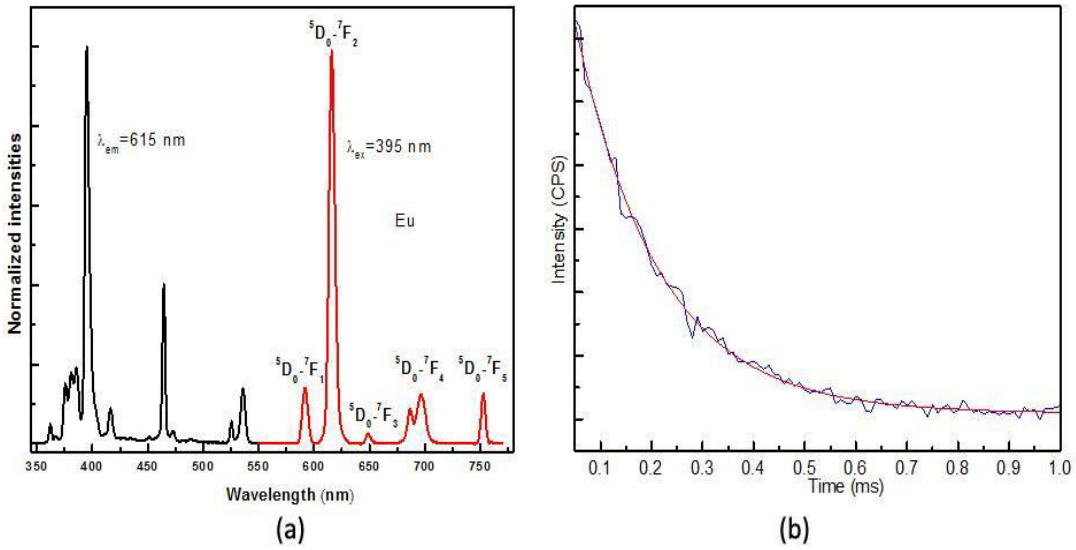

Figure 4.32 (a) Excitation and emission spectra and (b) luminescent decayfor $[Eu_2(hip)_2(H_2O)_{10}, (hip), 4H_2O]_\infty$.

This spectrum confirms that the PET mechanism is present and that back-transfer in not responsible for the absence of luminescence. To support this conclusion, Ligand-to-Ln energy transfer was studied. The triplet state of hip^{2-} ligand was estimated on the basis of the shortest wavelength of the phosphorescent band of the emission spectrum of $[Gd_2(hip)_2(H_2O)_{10}, (hip), 4H_2O]_\infty$ at 77K with λ_{ex}=343 nm (425 nm ≈ 23500 cm^{-1})(Figure 4.33).

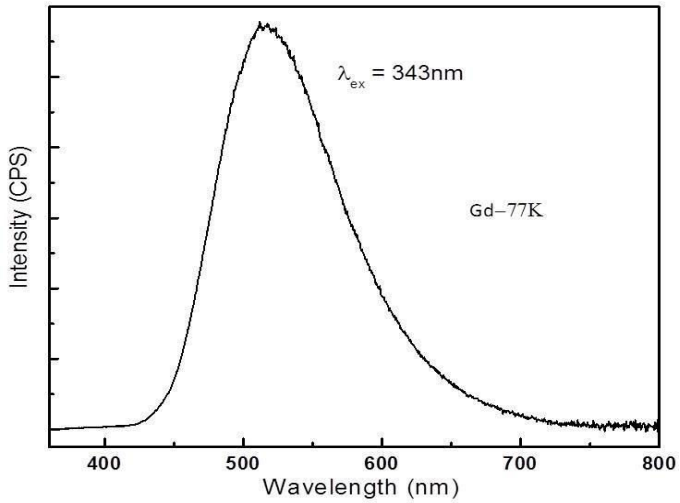

Figure 4.33Emission spectrum of $[Gd_2(hip)_2(H_2O)_{10}, (hip), 4H_2O]_\infty$at 77K under irradiation at 343nm.

The singlet excited and triplet state of hip^{2-} ligand were thus 32250 cm^{-1} and 23500 cm^{-1} respectively. Therefore, the energy gap $\Delta E(^1\pi\pi^* \rightarrow {}^3\pi\pi^*)$ is about 8750 cm^{-1}. According to Reinhoudt's empirical rules,[10] the inter-system crossing is efficient when $\Delta E(^1\pi\pi^* \rightarrow {}^3\pi\pi^*)$ is greater than 5000 cm^{-1}. Moreover, according to Latva's rules,[11] the lowest excited triplet (23500 cm^{-1}) state is supposed to favor efficient ligand-to-metal energy transfer without significant back-transfer for Eu^{3+} (17300cm^{-1}) and Tb^{3+} (20500cm^{-1}) containing compounds.

3D excitation/emission scan of Tb- and Eu-containing compounds were recorded.

This scan is promising as far as modulation of the emission *versus* excitation wavelength is aimed.

The 3D scan (Figure 4.34a) of the Tb-containing compound was measured (250nm ≤ λ_{ex} ≤ 420nm and 450nm ≤ λ_{em} ≤ 700nm). It shows that the compound can emit luminescence between 280 and 380 nm excitation wavelengths, and that the intensity reaches a maximum under 345 nm excitation wavelength.

The 3D scan (Figure 4.34b) of the Eu-containing compound was measured (360nm ≤ λ_{ex} ≤ 420nm and 450nm ≤ λ_{em} ≤ 750nm). It shows that the compound can emit luminescence between 370 and 415 nm excitation wavelengths, and that the intensity is maximum under the 395 nm excitation wavelength.

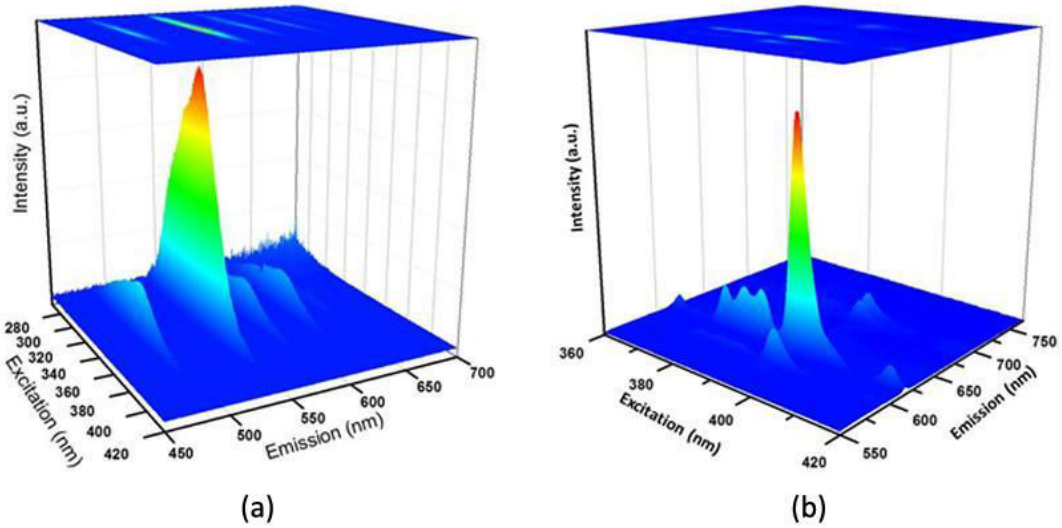

Figure 4.34 3D excitation/emission scans for (a) $[Tb_2(hip)_2(H_2O)_{10}, (hip), 4H_2O]_\infty$ and (b) $[Eu_2(hip)_2(H_2O)_{10}, (hip), 4H_2O]_\infty$.

The complex luminescent behaviors of the Tb- and Eu-containing compounds have encouraged us to study the luminescent properties of hetero-nuclear compounds.

4.9 Luminescent properties of the hetero-nuclear compounds.

4.9.1 $[Gd_{2-2x}Tb_{2x}(hip)_2(H_2O)_{10}, (hip), 4H_2O]_\infty$.

According to the crystal structure, lanthanides ions are close enough (≤ 10 Å) to give rise to intermetallic quenching. Some hetero-metallic coordination polymers that involve Tb^{3+} ions (luminescent lanthanide ions) and Gd^{3+} ions (optically non-active lanthanide ions) as optical dilutors were synthesized. Their emission spectra and luminance were measured (Appendix I).

Emission spectra (Figure 4.35)show that the luminescent properties of the compounds $[Gd_{2-2x}Tb_{2x}(hip)_2(H_2O)_{10}, (hip), 4H_2O]_\infty$ do not depend on the optically inactive lanthanide ions (Gd^{3+}) ratio and the colorimetric data of these hetero-nuclear compounds are all similar (Tab 4.8 and Figure 4.36). Because the lanthanide ions are randomly

distributed over the metallic sites of the crystal structure (**4.3**), the addition of an optically inactive lanthanide ion provokes an increase in the mean distance between the luminescent ions without perturbing the crystal structure.

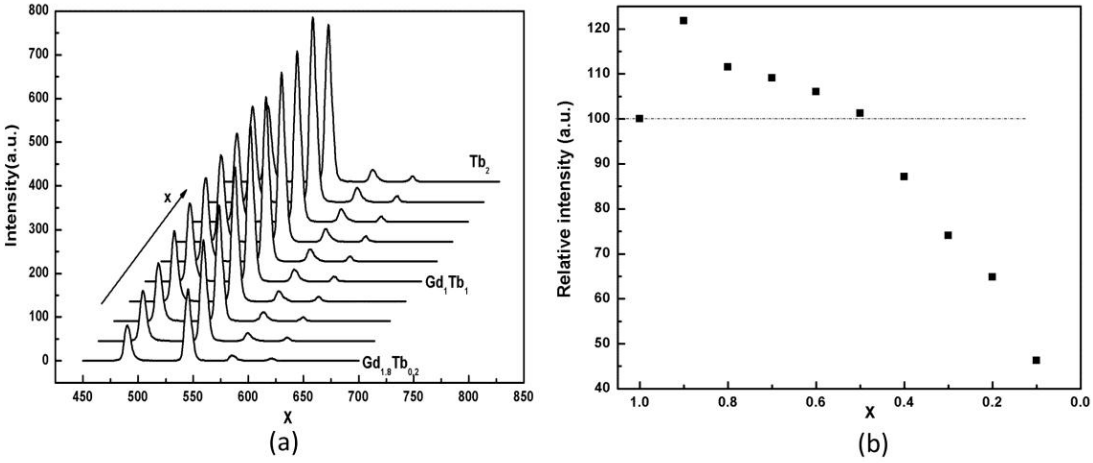

Figure 4.35 Emission spectra under UV irradiation (345 nm) and integrated intensity of the emission transitions (545 nm) of $[Gd_{2-2x}Tb_{2x}(hip)_2(H_2O)_{10}, (hip), 4H_2O]_\infty$ versus x.

Table 4.8 Colorimetric data for $[Gd_{2-2x}Tb_{2x}(hip)_2(H_2O)_{10}, (hip), 4H_2O]_\infty$ ($0.1 \leq x \leq 1$) under irradiation at 345 nm.

Compounds	Colorimetric coordinates	
x	x	y
1	0.34(1)	0.60(1)
0.9	0.34(1)	0.60(1)
0.8	0.34(1)	0.60(1)
0.7	0.34(1)	0.60(1)
0.6	0.34(1)	0.60(1)
0.5	0.34(1)	0.60(1)
0.4	0.33(1)	0.60(1)
0.3	0.33(1)	0.60(1)
0.2	0.33(1)	0.60(1)
0.1	0.33(1)	0.61(1)

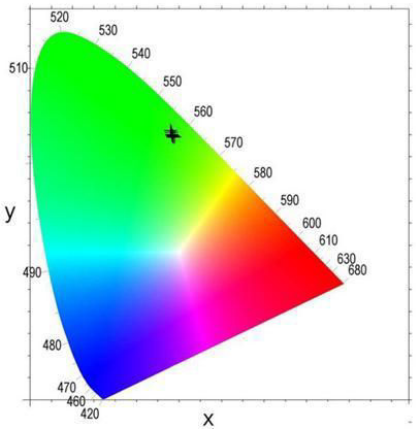

Figure 4.36 Colorimetric coordinates compounds of $[Gd_{2-2x}Tb_{2x}(hip)_2(H_2O)_{10}, (hip), 4H_2O]_\infty$ ($0.1 \leq x \leq 1$) under irradiation at 345 nm.

However, these compounds exhibit different luminance (Figure 4.37), a dilution up to x = 0.9 is beneficial, whereas further dilution resulted in a decrease in the luminance to a value that is comparable to the one of the pure Tb-containing compound for x = 0.5. While $x \leq 0.4$, the effect becomes detrimental. The results also correspond to integrated peaks (545 nm) in the emission spectra (Figure 4.35b).

These results confirm that some intermetallic quenching exists between optically active lanthanide ions. The variations in luminescence intensity observed can be related to the crystal structure. The mean distance between the lanthanide ions was estimated as twice the radius of the sphere that has the same volume than the mean volume occupied by a lanthanide ion. In our structure, the mean volume is roughly $\tilde{v} = 445$ Å^3 per metallic ion. It

corresponds to the volume of a sphere with a radius of 4.8 Å (r= (3 ṽ/4π) $^{1/3}$). With this rather rough mode, the mean distance between two lanthanide ions is 9.6Å. Therefore the mean distance between two Tb^{3+} ions in the compounds $[Gd_{2-2x}Tb_{2x}(hip)_2(H_2O)_{10}, (hip), 4H_2O]_\infty$ with $x \geq 0.1$ is greater than 10 Å that is often considered as the distance above which intermetallic energy transfer becomes less efficient.

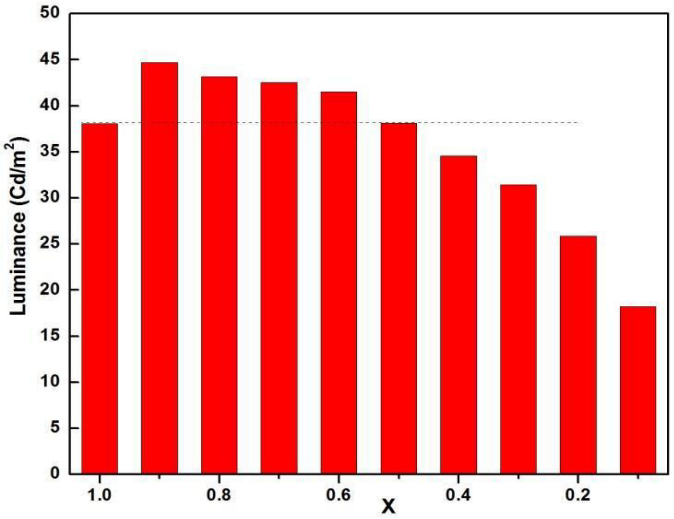

Figure 4.37 Luminance data for $[Gd_{2-2x}Tb_{2x}(hip)_2(H_2O)_{10}, (hip), 4H_2O]_\infty$ versus x.

These results can be used in technological applications to enhance the brightness without modifying the color of compounds containing optically active rare earth ions (Tb^{3+} or Eu^{3+}) by adding a few percents of inactive lanthanide ions (Gd^{3+} or Y^{3+}). This has an impact on the cost of the product because inactive lanthanide ions are significantly less expensive than active lanthanide ions.

4.9.2 $[Eu_{2-2x}Tb_{2x}(hip)_2(H_2O)_{10}, (hip), 4H_2O]_\infty$.

In order to estimate the tunable character of the luminescent properties of the hetero-nuclear compounds, compounds $[Eu_{2-2x}Tb_{2x}(hip)_2(H_2O)_{10}, (hip), 4H_2O]_\infty$ ($0 \leq x \leq 1$) have been synthesized.

First, an excitation/emission 3D scan ($280nm \leq \lambda_{ex} \leq 420$ nm and 450 nm $\leq \lambda_{em} \leq 750$ nm) was performed for $[Eu_1Tb_1(hip)_2(H_2O)_{10}, (hip), 4H_2O]_\infty$ (Figure 4.38) and shows that emission is strongly dependent on excitation wavelength. On the basis of this 3D scan, three different excitation wavelength were chosen to study the luminescent properties of compounds $[Eu_{2-2x}Tb_{2x}(hip)_2(H_2O)_{10}, hip), 4H_2O]_\infty$ ($0 \leq x \leq 1$):

(1). 345nm which corresponds to an excitation of the ligand;
(2). 375nm which corresponds to a direct excitation of both Eu^{3+} and Tb^{3+} ions ($^7F_0 \rightarrow {}^5G_5$ and $^7F_6 \rightarrow {}^5D_3$, respectively);
(3). 395nm which corresponds to a direct excitation of Eu^{3+} ions only ($^7F_0 \rightarrow {}^5L_6$).

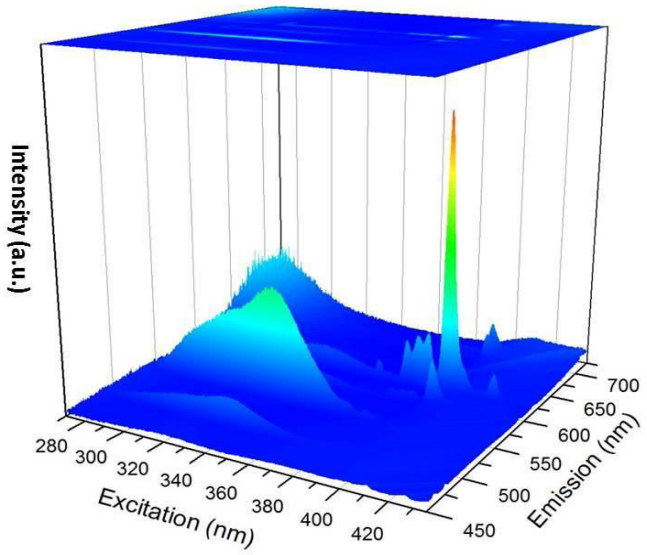

Figure 4.38 Excitation and emission 3D scan for $[Eu_1Tb_1(hip)_2(H_2O)_{10}, (hip), 4H_2O]_\infty$.

Emission spectra and colorimetric coordinates were recorded under 345 nm, 375 nm, and 395 nm, respectively (Figure 4.39a, 4.39b, 4.39c and Table 4.9).

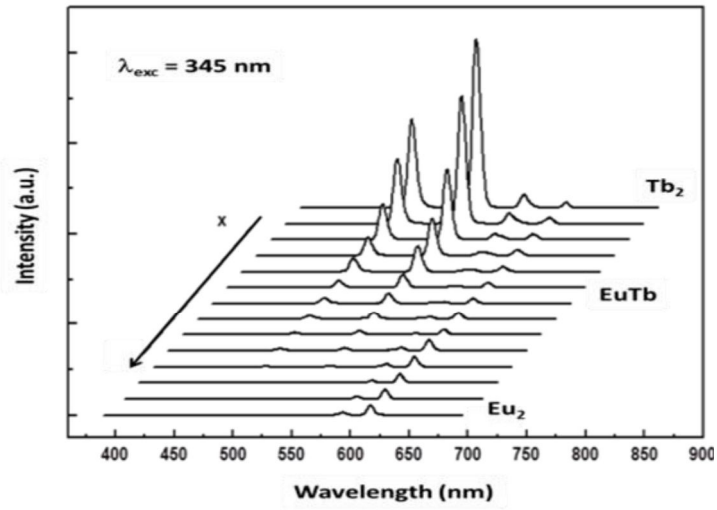

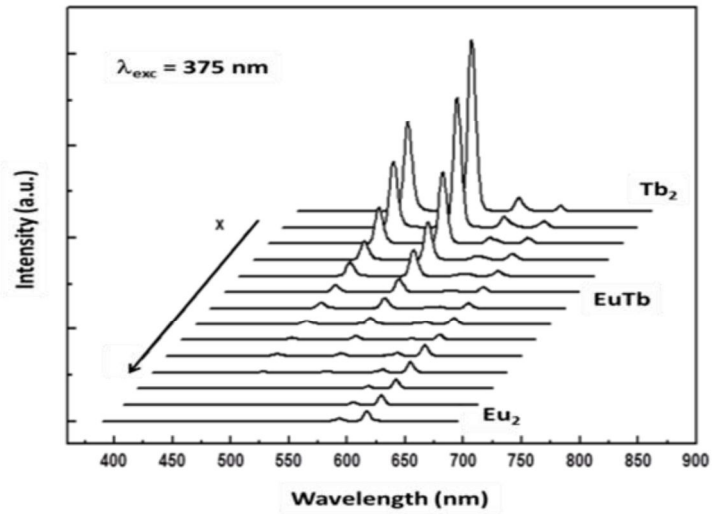

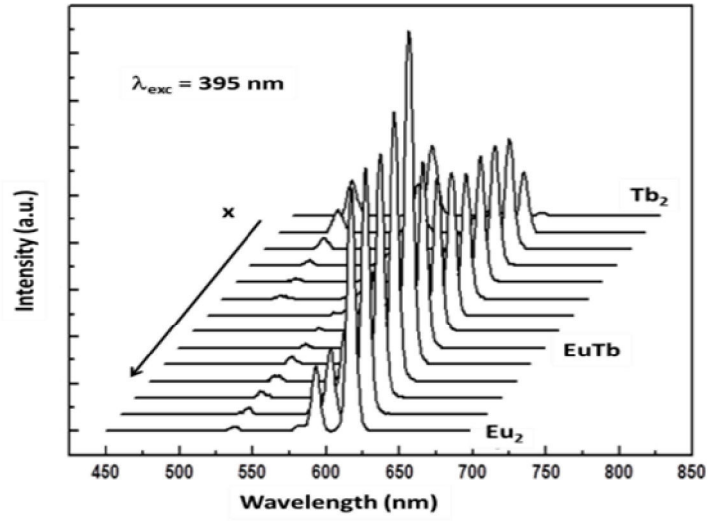

Figure 4.39a Emission spectra of $[Eu_1Tb_1(hip)_2(H_2O)_{10}, (hip), 4H_2O]_\infty$under three different excitation wavelength.

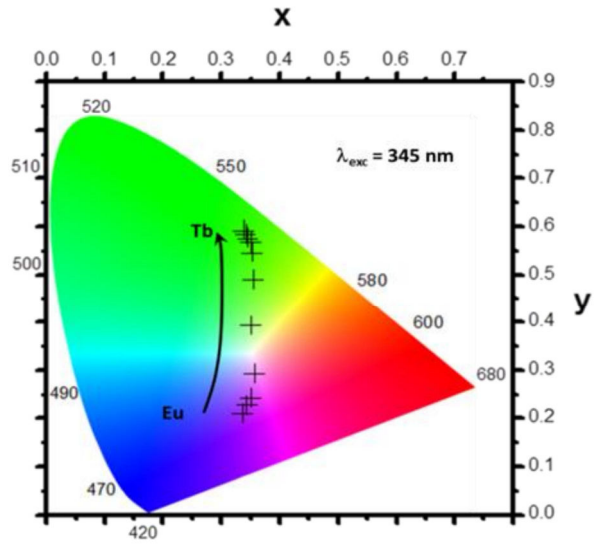

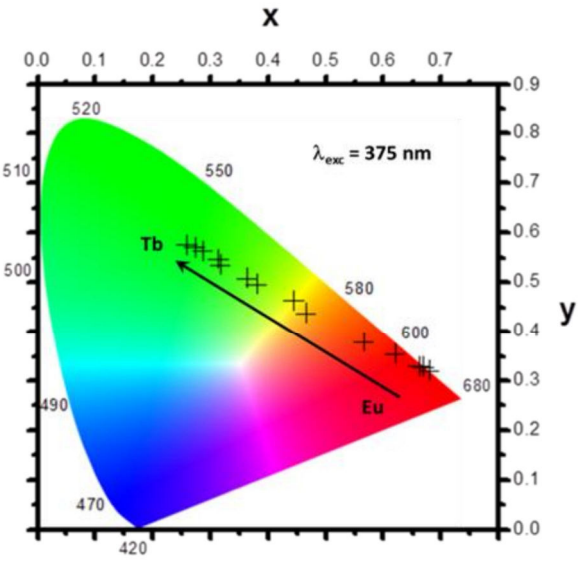

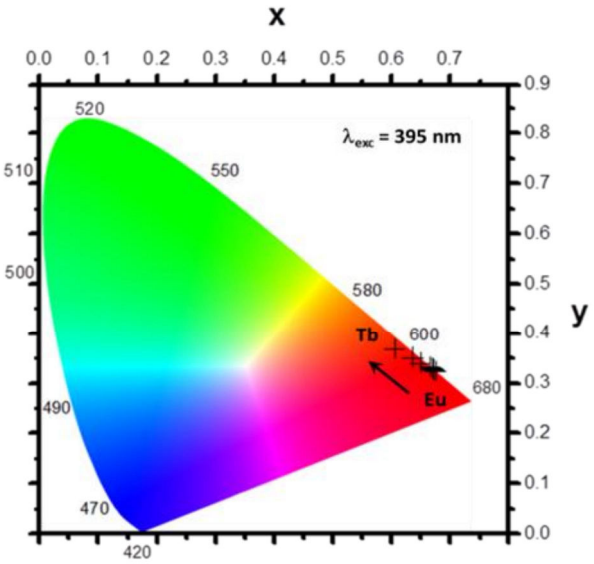

Figure 4.39b Colorimetric coordinates for $[Eu_1Tb_1(hip)_2(H_2O)_{10}$, (hip), $4H_2O]_\infty$under three different excitation wavelength.

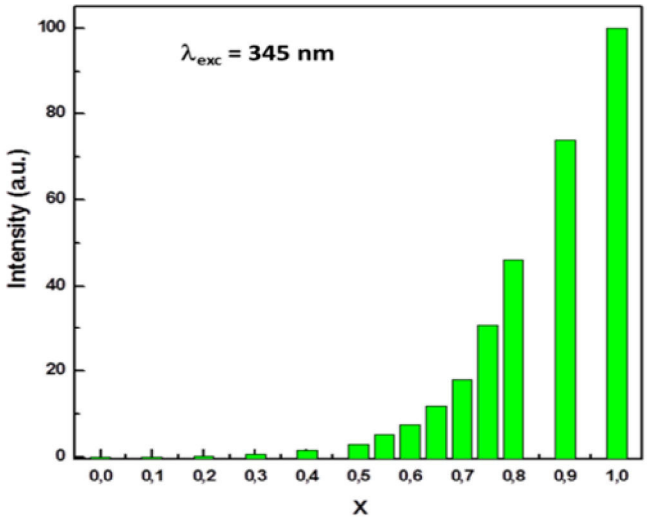

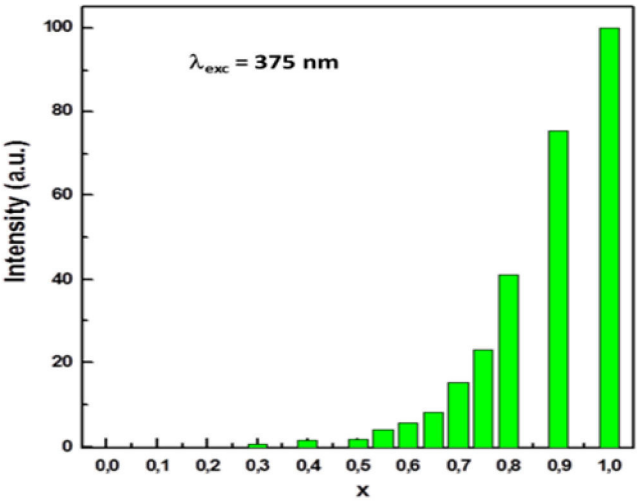

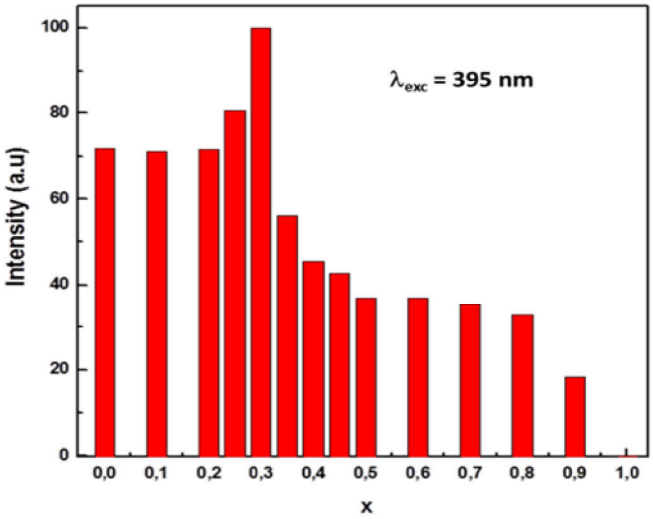

Figure 4.39c Integrated intensity of a Tb^{3+} characteristic emission peak (green bars 545 nm) or a Eu^{3+} characteristic emission peak (red bars 615 nm) versus x.

Table 4.9 colorimetric coordination for $[Eu_{2-2x}Tb_{2x}(hip)_2(H_2O)_{10}, (hip), 4H_2O]_\infty$ under three different excitation wavelength (345 nm, 375 nm and 395 nm).

compound	colorimetric coordinates 345 nm		colorimetric coordinates 375 nm		colorimetric coordinates 395 nm	
x	x	y	x	y	x	y
1	0.34	0.59	0.26	0.57		
0.9	0.34	0.58	0.27	0.57	0.65	0.32
0.8	0.34	0.57	0.29	0.56	0.60	0.37
0.75	0.36	0.52	0.31	0.55	0.64	0.35
0.7	0.35	0.57	0.32	0.53	0.65	0.34
0.65	0.36	0.46	0.36	0.51	0.65	0.34
0.6	0.35	0.54	0.38	0.50	0.66	0.33
0.55	0.36	0.36	0.44	0.46	0.67	0.33
0.5	0.35	0.48	0.47	0.44	0.67	0.32
0.4	0.35	0.39	0.57	0.38	0.67	0.33
0.3	0.35	0.29	0.62	0.35	0.67	0.33
0.2	0.35	0.24	0.66	0.33	0.67	0.33
0.1	0.34	0.23	0.67	0.33	0.67	0.33
0	0.34	0.21	0.68	0.32	0.67	0.33

Integrated intensities of one out of the two lanthanide ions components in the emission spectra versus x have been plotted. Theses integrated intensities were estimated by integration of an emission peak that does not overlap with any peak of the other lanthanide ion and assuming that all compounds are iso-structural that is all peaks of the considered lanthanide ion in the emission spectra present identical relative intensities (Tb^{3+} $^5D_4 \rightarrow {}^7F_5$ transition (545nm) was chosen under 345nm and 375nm irradiation, Eu^{3+} transition $^5D_0 \rightarrow {}^7F_2$ (615nm) was chosen under 395nm irradiation).

For future industrial applications, we have also studied their luminescent behavior under 312nm irradiation which is a cheap commercially available irradiation wavelength. Emission spectra, colorimetric data and luminance data were recorded under 312nm irradiation (Figure 4.40 and Table 4.10). We also report pictures of these compounds under 312nm irradiations (Figure 4.41).

Table 4.10 Colorimetric coordinates for $[Eu_{2-2x}Tb_{2x}(hip)_2(H_2O)_{10}$, (hip), $4H_2O]_\infty$ under 312nm irradiation.

compound	colorimetric coordinates	
x	x	y
1	0.34	0.59
0.9	0.34	0.58
0.8	0.34	0.57
0.75	0.35	0.56
0.7	0.36	0.52
0.65	0.36	0.45
0.6	0.35	0.54
0.55	0.35	0.35
0.5	0.35	0.48
0.4	0.35	0.39
0.3	0.35	0.29
0.2	0.35	0.24
0.1	0.34	0.22
0	0.33	0.20

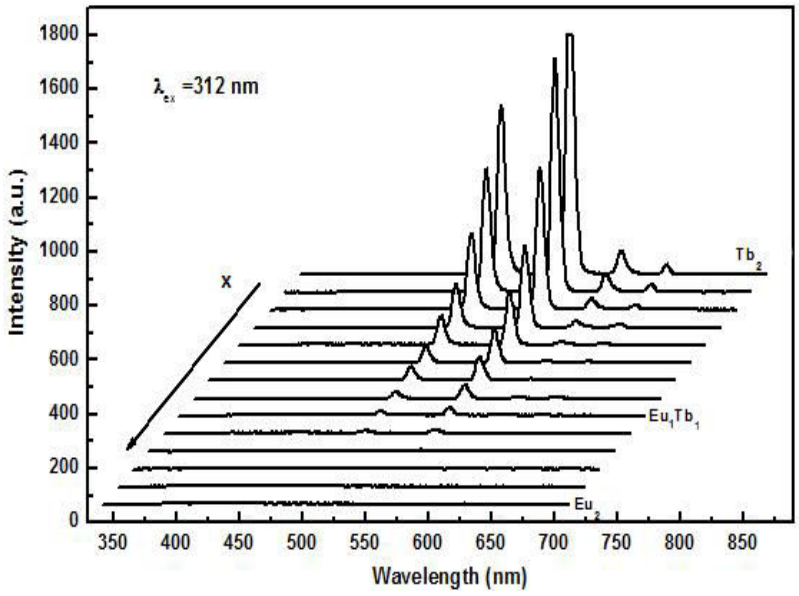

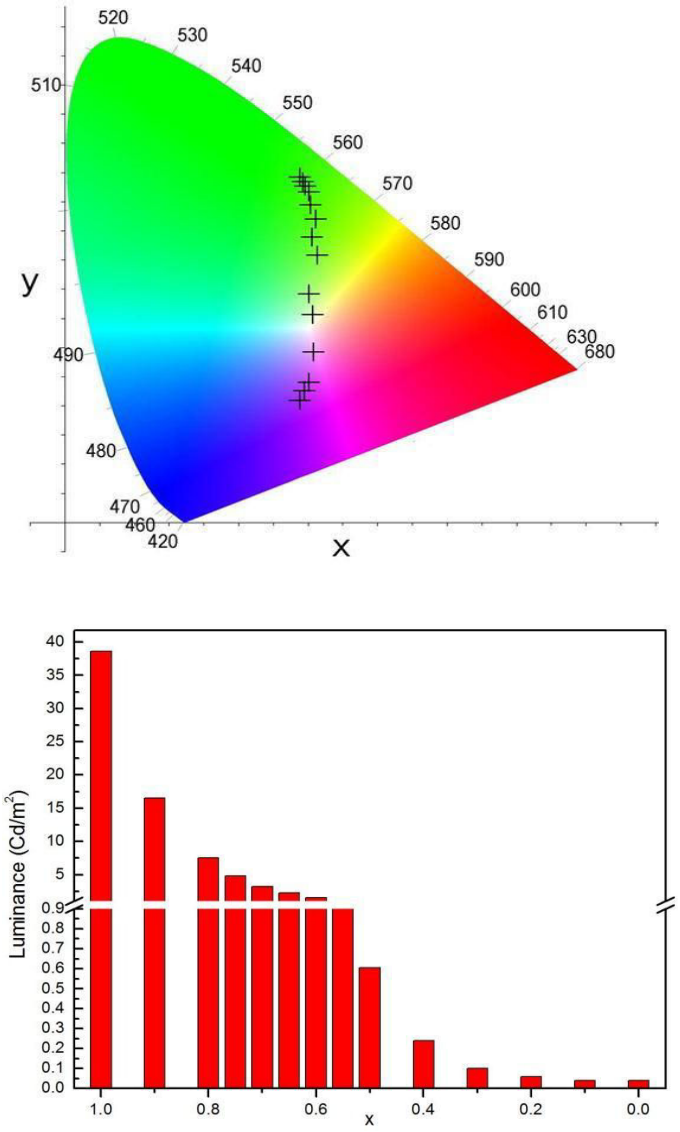

Figure 4.40 Emission spectra, colorimetric coordinates and luminance for $[Eu_{2-2x}Tb_{2x}(hip)_2(H_2O)_{10}, (hip), 4H_2O]_\infty$ under irradiation at 312 nm.

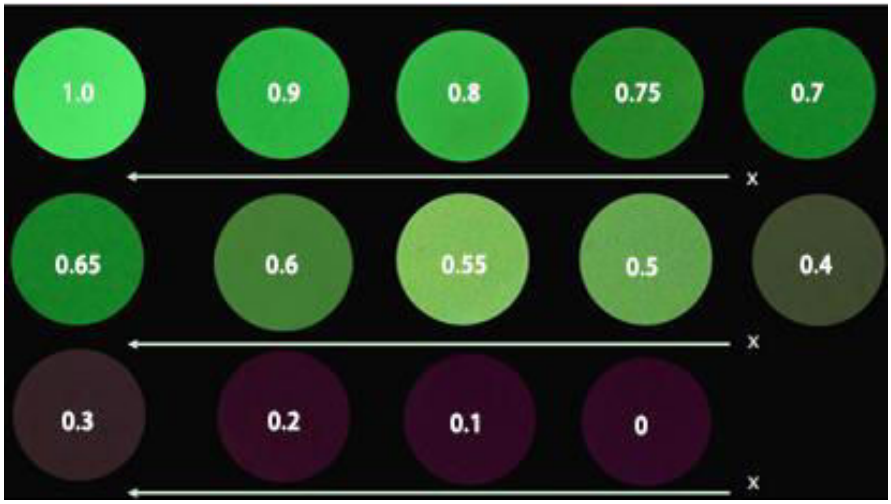

Figure 4.41 Pictures under UV irradiation at 312 nm for $[Eu_{2-2x}Tb_{2x}(hip)_2(H_2O)_{10}, (hip), 4H_2O]_\infty$.

All these results show that these compounds exhibit completely different luminescent properties versus the excitation wavelength. These different luminescent behaviors can be related to a competition between two main mechanisms: a photo-induced electron transfer (PET) and an intermetallic energy transfer. The compound $[Eu_1Tb_1(hip)_2(H_2O)_{10}, (hip), 4H_2O]_\infty$ was chosen for a detailed study in order to better understand how these mechanisms interact.

Comparison of the colorimetric coordinates under different excitation wavelength for compound $[Eu_1Tb_1(hip)_2(H_2O)_{10}, (hip), 4H_2O]_\infty$ (Table 4.11) reveals that its luminescent properties strongly depend on the excitation wavelength. Colorimetric coordinates under 345nm irradiation clearly show that both intermetallic energy transfer and photo-induced electron transfer occur.

Table 4.11 Colorimetric coordinates for $[Eu_1Tb_1(hip)_2(H_2O)_{10}, (hip), 4H_2O]_\infty$ under different excitation wavelengths.

Excitation wavelength (nm)	colorimetric coordinates	
	x	y
345	0.34	0.60
375	0.35	0.48(1)
395	0.67	0.32

First, intermetallic energy transfer was studied. The intrinsic quantum yields and luminescent lifetimes of four compounds $[Tb_2(hip)_2(H_2O)_{10}, (hip), 4H_2O]_\infty$ $[Gd_1Tb_1(hip)_2(H_2O)_{10}, (hip), 4H_2O]_\infty$, $[Eu_1Tb_1(hip)_2(H_2O)_{10}, (hip), 4H_2O]_\infty$ and $[Eu_2(hip)_2(H_2O)_{10}, (hip), 4H_2O]_\infty$ were measured under 375 nm excitation wavelength (Table 4.12). Indeed, this excitation wavelength provokes a direct excitation of both Eu^{3+} and Tb^{3+} ions and no antenna effect nor PET are expected. Their emission spectra were also recorded (Figure 4.42).

Table 4.12 Quantum yields and luminescent lifetimes under 375 nm excitation wavelength for $[Tb_2(hip)_2(H_2O)_{10}, (hip), 4H_2O]_\infty$, $[Gd_1Tb_1(hip)_2(H_2O)_{10}, (hip), 4H_2O]_\infty$, $[Eu_1Tb_1(hip)_2(H_2O)_{10}, (hip), 4H_2O]_\infty$ and $[Eu_2(hip)_2(H_2O)_{10}, (hip), 4H_2O]_\infty$.

	Q_{Tb}^{Tb}(%)	τ (ms)	Q_{Eu}^{Eu} (%)	τ (ms)
$[Tb_2(hip)_2(H_2O)_{10}\cdot(hip)\cdot 4H_2O]_\infty$	7.5(7)	0.48(4)	-	-
$[Gd_1Tb_1(hip)_2(H_2O)_{10}\cdot(hip)\cdot 4H_2O]_\infty$	7.4(7)	0.48(4)	-	-
$[Eu_1Tb_1(hip)_2(H_2O)_{10}\cdot(hip)\cdot 4H_2O]_\infty$	0.10(5)	0.33(3)	0.60(6)	0.17(2)
$[Eu_2(hip)_2(H_2O)_{10}\cdot(hip)\cdot 4H_2O]_\infty$	-	-	0.50(5)	0.16(2)

Intermetallic energy transfer can be calculated using the relationship:

$$\eta_{et} = 1 - \frac{\tau_{obs}}{\tau_o}$$

Where τ_{obs} and τ_o are respectively the lifetime in the presence and in the absence of an acceptor.[12] Since Gd^{3+} ion has its first excited state above the excitation it cannot act as an

acceptor, in this case τ_{obs} is about 0.33(3) ms and τ_o is about 0.48(4) ms. Therefore, intermetallic energy transfer is about 32%. On the other hand, the intrinsic quantum yields of $[Tb_2(hip)_2(H_2O)_{10}, (hip), 4H_2O]_\infty$ and $[Gd_1Tb_1(hip)_2(H_2O)_{10}, (hip), 4H_2O]_\infty$ are almost the same (7.5% and 7.4%). This is in agreement with the quite large Tb-Tb mean distance in the crystal structure.

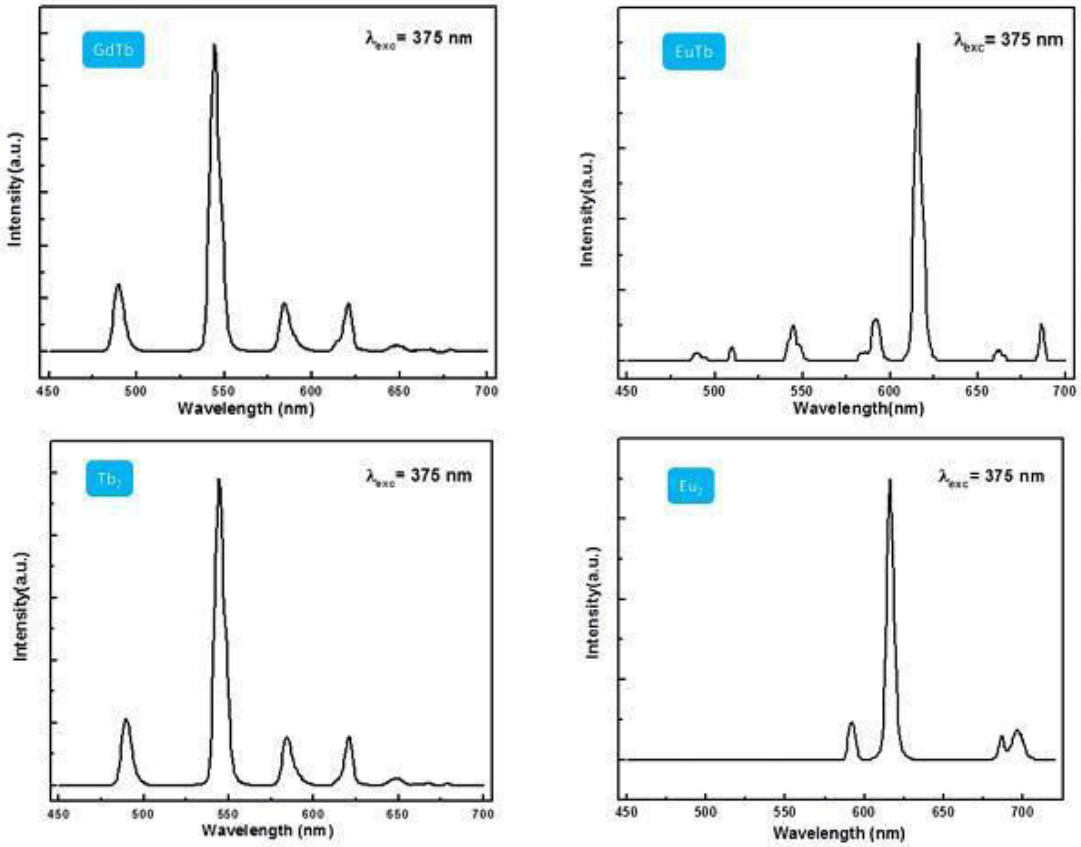

Figure 4.42 Emission spectra under 375 nm excitation wavelength of $[Tb_2(hip)_2(H_2O)_{10}, (hip), 4H_2O]_\infty$, $[Gd_1Tb_1(hip)_2(H_2O)_{10}, (hip), 4H_2O]_\infty$, $[Eu_1Tb_1(hip)_2(H_2O)_{10}, (hip), 4H_2O]_\infty$and $[Eu_2(hip)_2(H_2O)_{10}, (hip), 4H_2O]_\infty$.

Emission spectra recorded under 395 nm excitation wavelength for $[Eu_{2-2x}Tb_{2x}(hip)_2(H_2O)_{10}, (hip), 4H_2O]_\infty$ compounds show Tb^{3+} characteristic emission peaks around 490 and 545 nm corresponding to the transitions ($^5D_4 \rightarrow {}^7F_6$ and $^5D_4 \rightarrow {}^7F_5$) for $x \geq 0.3$, this was unexpected because the homo-nuclear Tb-containing compound excitation spectrum does not present any peaks at 395 nm. In contrast, excitation spectra recorded for $[Eu_1Tb_1(hip)_2(H_2O)_{10}, (hip), 4H_2O]_\infty$ clearly show the presence of a small excitation peak at 395 nm at 545 nm emission wavelength (Figure 4.43).

The presence of this peak in the excitation spectra can be attributed to an intermetallic energy transfer Eu-to-Tb. The intrinsic quantum yield and luminescent lifetimes were measured under excitation at 395 nm ($\boldsymbol{Q}_{\boldsymbol{Eu}}^{\boldsymbol{Eu}}$ is about 0.64(6)% and τ_{obs}=0.17(2) ms) (Figure 4.44). The value is closed to those obtained under excitation at 375nm. This suggests that the Eu-to-Tb intermetallic transfer is weak.

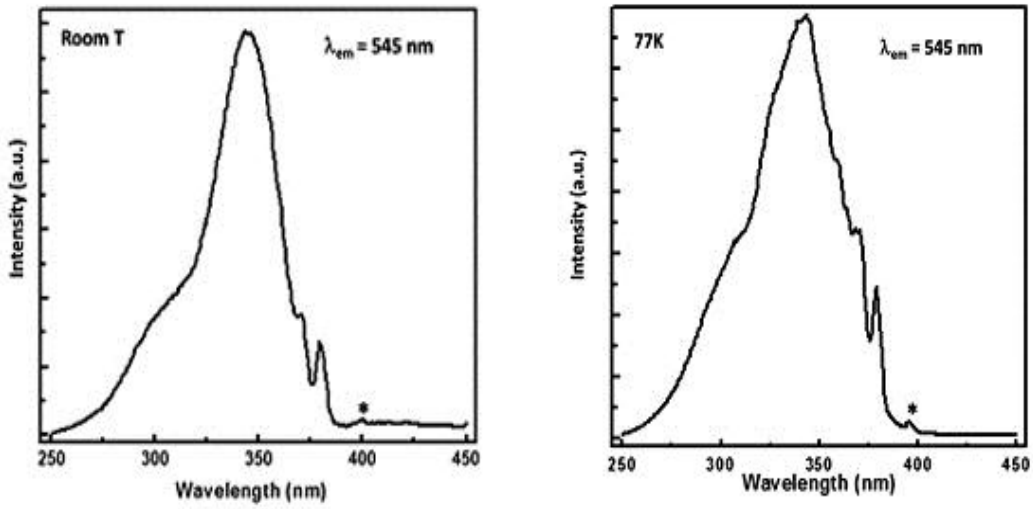

Figure 4.43 Excitation spectra of $[Eu_1Tb_1(hip)_2(H_2O)_{10}, (hip), 4H_2O]_\infty$ at room temperature and 77K under 545nm emission wavelength.

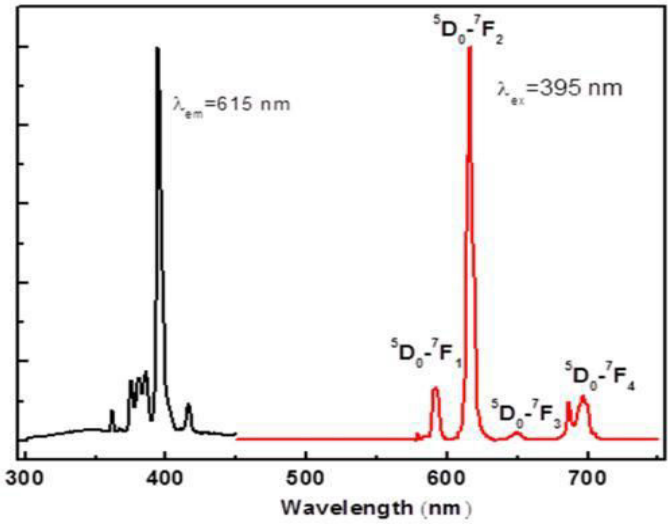

Figure 4.44 Excitation and emission spectra of $[Eu_1Tb_1(hip)_2(H_2O)_{10}, (hip), 4H_2O]_\infty$.

Second PET transfer was considered. Because the PET transfer strongly depend on the temperature, excitation spectra of $[Eu_1Tb_1(hip)_2(H_2O)_{10}, (hip), 4H_2O]_\infty$ were recorded at room temperature and 77K for a 615nm emission wavelength (Figure 4.45). An excitation band centered at 345 nm is present which is in agreement with the presence of a PET mechanism.

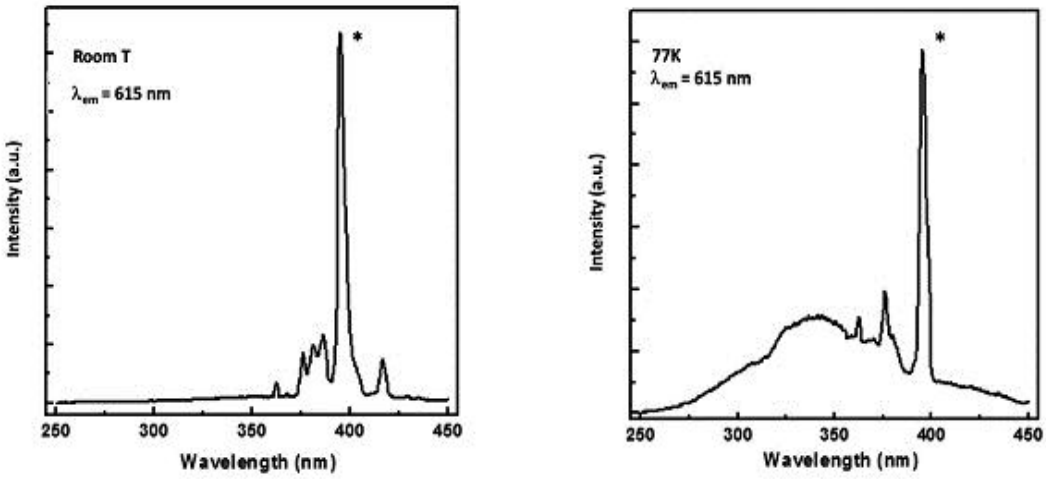

Figure 4.45 Excitation spectra of $[Eu_1Tb_1(hip)_2(H_2O)_{10}, (hip), 4H_2O]_\infty$ at room temperature and 77 K for a 615 nm emission wavelength.

When excited at 345 nm, that is a wavelength that corresponds to the ligand excitation, the Eu/Tb hetero-nuclear compounds present complex luminescent properties that arise from a competition between intermetallic energy transfer, PET transfer and antenna effect. Excitation and emission spectra were recorded for $[Eu_1Tb_1(hip)_2(H_2O)_{10}, (hip), 4H_2O]_\infty$ and $[Gd_1Tb_1(hip)_2(H_2O)_{10}, (hip), 4H_2O]_\infty$ (Figure 4.46). Quantum yields and luminescent lifetimes were also calculated (Table 4.13). Intermetallic energy transfer is about 32% which is in perfect agreement with what has been calculated from measurements realized at 375 nm excitation wavelength.

Table 4.13 Quantum yields and luminescent lifetimes under 345nm excitation wavelength for $[Gd_1Tb_1(hip)_2(H_2O)_{10}, (hip), 4H_2O]_\infty$, $[Eu_1Tb_1(hip)_2(H_2O)_{10}, (hip), 4H_2O]_\infty$.

	Q_{Tb}^{Tb}(%)	τ (ms)
$[Gd_1Tb_1(hip)_2(H_2O)_{10}, (hip), 4H_2O]_\infty$	25(2)	0.53(5)
$[Eu_1Tb_1(hip)_2(H_2O)_{10}, (hip), 4H_2O]_\infty$	0.78(8)	0.36(4)

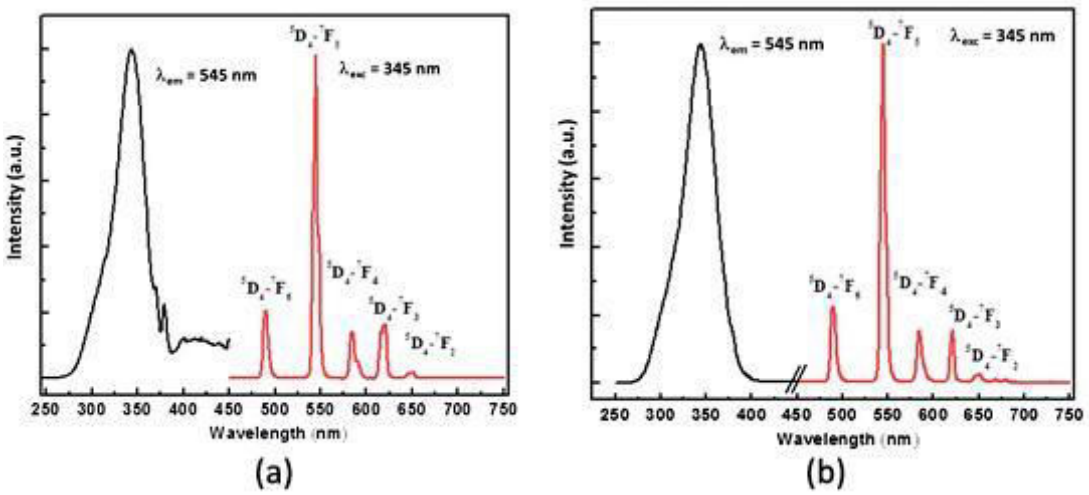

Figure 4.46 Excitation and emission spectra for (a) $[Eu_1Tb_1(hip)_2(H_2O)_{10}, (hip), 4H_2O]_\infty$ and (b) $[Gd_1Tb_1(hip)_2(H_2O)_{10}, (hip), 4H_2O]_\infty$

4.10 Diagram of energy transfers.

The luminescent behaviors of the Eu/Tb hetero-nuclear compounds can be illustrated by using the simple diagram of energy transfer which shows the main radiative and non-radiative processes at different excitation wavelengths (Figure 4.47).

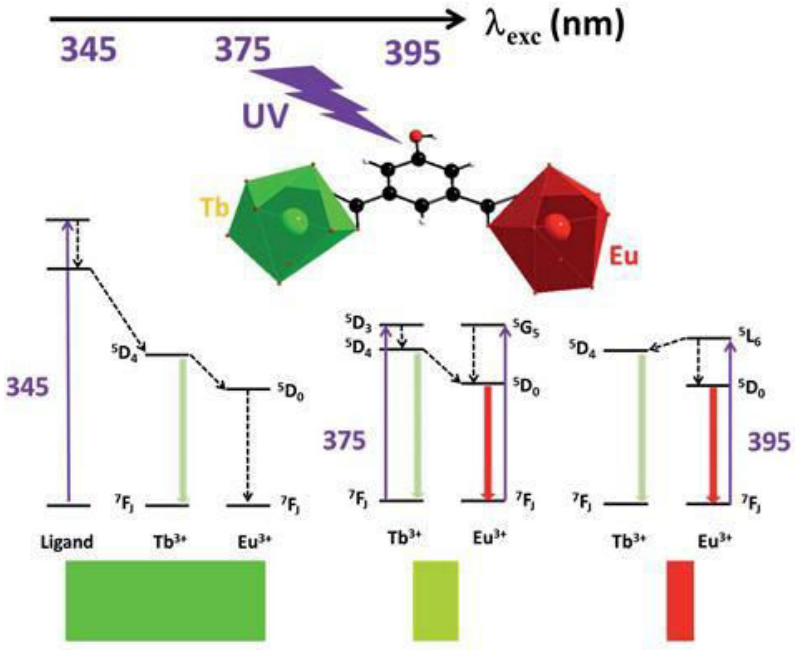

Figure 4.47 Energy transfer diagram at different excitation wavelengths.

Conclusion

We have synthesized the microcrystalline powders for all the rare earth elements at different temperatures and classified them on the basis of their powder X-ray diffraction diagrams. We got two novel crystal structures for family 2 and family 3. Crystal growth for other families is in progress. We have studied in details the luminescent properties of the compounds that constitute family 3 for homo-nuclear compounds and hetero-nuclear compounds and evidenced the different mechanisms that originate them.

References:

[1]. S. Freslon, Y. Luo, G. Calvez, C. Daiguebonne, O. Guillou, K. Bernot, V. Michel, X. Fan, Inorganic Chemistry, 53 (2014) 1217-1228.

[2]. (a) T. Terai, K. Kikuchi, S.-y. Iwasawa, T. Kawabe, Y. Hirata, Y. Urano, T. Nagano, Journal of the American Chemical Society, 128 (2006) 6938-6946. (b) C. Galaup, J.-M. Couchet, S. Bedel, P. Tisnès, C. Picard, The Journal of Organic Chemistry, 70 (2005) 2274-2284.

[3]. (a) J. Roger, V. Babizhetskyy, S. Cordier, J. Bauer, K. Hiebl, L. Le Pollès, S. Elisabeth Ashbrook, J.-F. Halet, R. Guérin, Journal of Solid State Chemistry, 178 (2005) 1851-1863.(b) S.E. Ashbrook, K.R. Whittle, G.R. Lumpkin, I. Farnan, The Journal of Physical Chemistry B, 110 (2006) 10358-10364.(c) S.W. Reader, M.R. Mitchell, K.E. Johnston, C.J. Pickard, K.R. Whittle, S.E. Ashbrook, The Journal of Physical Chemistry C, 113 (2009) 18874-18883.(d) M.R. Mitchell, D. Carnevale, R. Orr, K.R. Whittle, S.E. Ashbrook, The Journal of Physical Chemistry C, 116 (2012) 4273-4286.

[4]. (a) C. Daiguebonne, A. Deluzet, M. Camara, K. Boubekeur, N. Audebrand, Y. Gérault, C. Baux, O. Guillou, Crystal Growth & Design, 3 (2003) 1015-1020.(b) N. Mahé, O. Guillou, C. Daiguebonne, Y. Gérault, A. Caneschi, C. Sangregorio, J.Y. Chane-Ching, P.E. Car, T. Roisnel, Inorganic Chemistry, 44 (2005) 7743-7750.(c) Y. Zheng, G. Calvez, N. Kerbellec, C. Daiguebonne, O. Guillou, Inorganica Chimica Acta, 362 (2009) 1478-1484.

[5]. A. Ruiz-Martínez, D. Casanova, S. Alvarez, Chemistry – A European Journal, 14 (2008) 1291-1303.

[6]. H.T. Xu, Y.D. Li, Journal of Molecular Structure, 690 (2004) 137-143.

[7]. R. Shinley, in The CRYSFIRE system for automatic powder indexing, 2002.

[8]. (a) S. Quici, M. Cavazzini, G. Marzanni, G. Accorsi, N. Armaroli, B. Ventura, F. Barigelletti, Inorganic Chemistry, 44 (2005) 529-537. (b) M. Shi, F. Li, T. Yi, D. Zhang, H. Hu, C. Huang, Inorganic Chemistry, 44 (2005) 8929-8936.

[9]. J.-C.G. Bünzli, S. Comby, A.-S. Chauvin, C.D.B. Vandevyver, Journal of Rare Earths, 25 (2007) 257-274.

[10]. F.J. Steemers, W. Verboom, D.N. Reinhoudt, E.B. van der Tol, J.W. Verhoeven, Journal of the American Chemical Society, 117 (1995) 9408-9414.

[11]. M. Latva, H. Takalo, V.-M. Mukkala, C. Matachescu, J.C. Rodríguez-Ubis, J. Kankare, Journal of Luminescence, 75 (1997) 149-169.

[12]. (a) J.-C. G. Bünzli and S. V. Eliseeva, in Lanthanide Luminescence,ed. P. Hänninen and H. Härmä, Springer, Berlin, Heidelberg, 2010, pp. 1–45. (b) J.-C.G. Bünzli, Chemical Reviews, 110 (2010) 2729-2755.

Chapter 5.
Lanthanide coordination polymers based on ligand H_2nip

Chapter 5. Lanthanide coordination polymers based on ligand H_2nip

To further study the influence of the ligand on the luminescent behavior of the lanthanide coordination polymers, another V-shaped ligand, 5-nitro-isophthalic acid, was chosen (Figure 5.1). Our group has studied three V-shaped acid: isophtalic acid (H_2ip), 5-amino-isophtalic acid (H_2aip) and 5-hydroxy-isophthalic acid (H_2hip) (Figure 5.1) and published the work about their lanthanide-based coordination polymers and their luminescent properties.[1] However in all three ligands, 5-position is occupied by an electron-donating group (-H, $-NH_2$ and -OH). On the opposite, 5-nitro-isophthalic (H_2nip) has an electron-withdrawing group ($-NO_2$) in the 5-position. The series of lanthanide containing coordination polymers based on nip^{2-} were prepared and characterized.

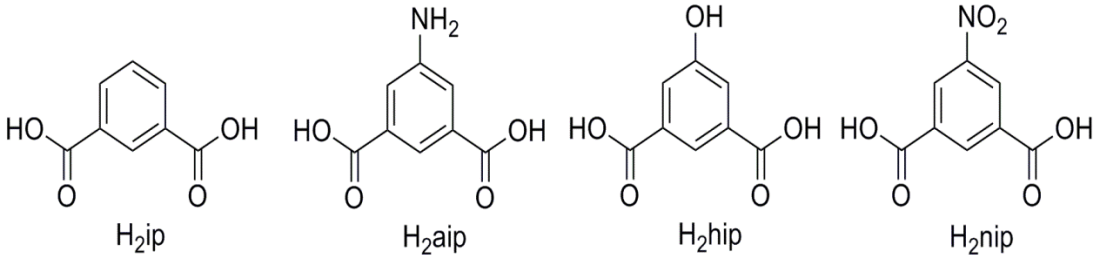

Figure 5.1 Studied V-shaped acids.

5.1 Preparation of the di-sodium salt of 5-nitro-isophthalic acid.

The procedure for synthesizing the di-sodium salt of 5-nitro-isophthalic acid (H_2nip) is similar to the one followed for the synthesis of Na_2cda (Chapter 3) except that chelidonic acid (H_2cda) is replaced by 5-nitro-isophthalic acid (H_2nip). After filtration and drying, the white powder of the di-sodium salt of H_2nip was obtained in 90% yields. The UV-vis absorption spectrum of Na_2nip aqueous solution (1×10^{-5} mol.L^{-1}) was measured. It shows a broad absorption band centered at 300 nm (Figure 5.2).

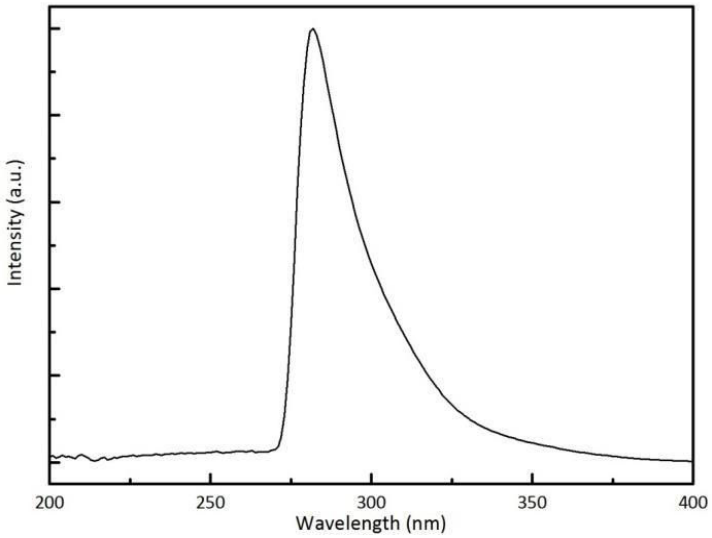

Figure 5.2 UV-vis absorption spectrum of a Na_2nip aqueous solution.

5.2 Preparation of the microcrystalline powders.

Microcrystalline powders of lanthanide-based (La to Yb plus Y) compounds are prepared with the same stoichiometric amounts at different temperatures (2°C, room temperature and 100 °C).

The clear solution of lanthanide chloride (0.5 mmol in 10mL H_2O, La to Eu) was added to a di-sodium salt of H_2nip solution (0.75 mmol in 10 mL H_2O). Precipitation immediately occurred at 2°C and at room temperature. Mixtures were stirred for 10 min. During stirring precipitates aggregated and finally jellified (Figure 5.3). The procedure for synthesizing the other lanthanide -based coordination polymers (Gd to Yb plus Y) were the same except that the precipitates didn't aggregate. The powders were filtered and dried at room temperature. The white resulting powders were obtained in 90% yields. The microcrystalline powders were classified by families (Table 5.1) of iso-structural compounds on the basis of their X-ray powder diffraction diagrams (Figure 5.4).

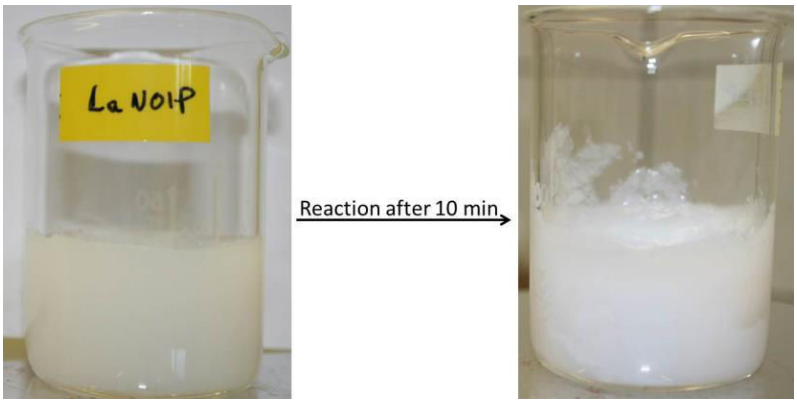

Figure 5.3 Obtained jellified mixtures for the ligthest lanthanide (La to Tb).

Table 5.1 Families of Lanthanide-based compounds.

L=nip^{2-}	La	Ce	Pr	Nd	Sm	Eu	Gd	Tb	Dy	Ho	Y	Er	Yb
2°C													
RT													
100°C													

	Family 1 Novel coordination polymers
	Family 2 No crystal structure.
	Family 3 No crystal structure.
	Family 4 No crystal structure.

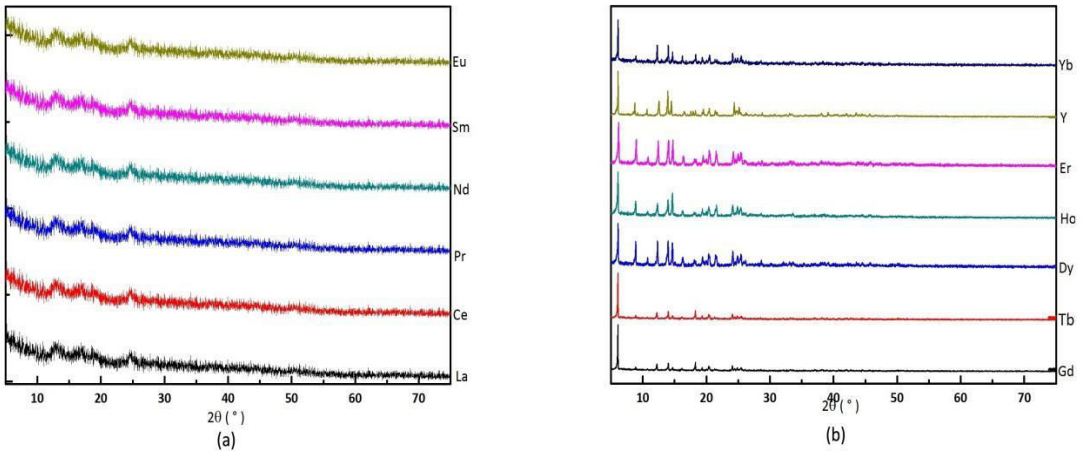

Figure 5.4 XRD patterns of the obtained powders for (a) amorphous and (b) Family 1.

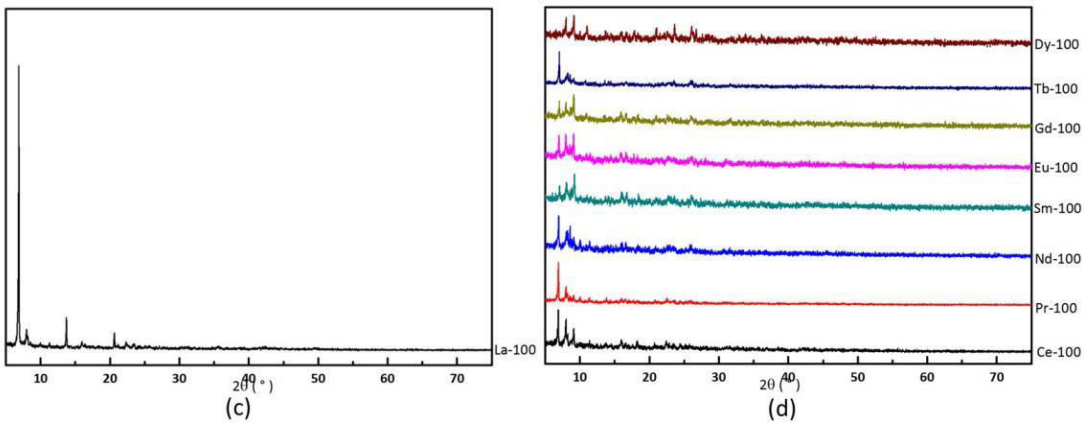

Figure 5.4 XRD patterns of the obtained microcrystalline powders for (c) Family 2 and (d) Family 3.

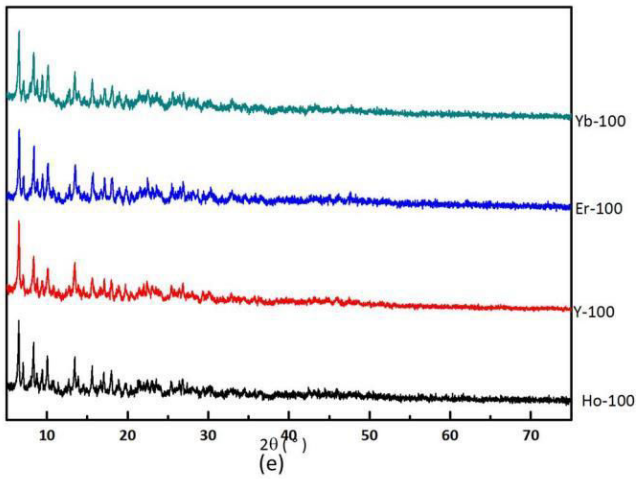

Figure 5.4 XRD patterns of the obtained microcrystalline powders for Family 5.

5.3 Synthesis of single crystals.

Single crystals of lanthanide-based compounds were grown by slow diffusions of lanthanide chloride (0.5 mmol in 10 mL H_2O)and Na_2nip (0.5 mmol in 10 mL H_2O) solutions in H-shaped tubes as well as U-shaped tube containing gels (Agar-Agar, TMOS or TEOS). Details are reported in Appendix I. After a few weeks, single-crystals were obtained in the tubes that were fill with 7.5% gel (TMOS). Slow evaporation of the filtrates obtained during the preparations of the microcrystalline powders lead to single crystals suitable for crystal

structure characterization for Family 1 $[Ln(nip)(Hnip)(H_2O)_4, 3H_2O]_\infty$ with Ln = Gd – Yb plus Y. These crystals are needle-like shaped (Figure 5.5). Single crystals were sealed in glass capilaries for X-ray single crystal data collections in order to avoid potential dehydration. However, compounds that constitute Families 2, 3 and 4 were only obtained as microcrstalline powders. Despite great efforts no high quality single crystals were obtained. The work is still in progress.

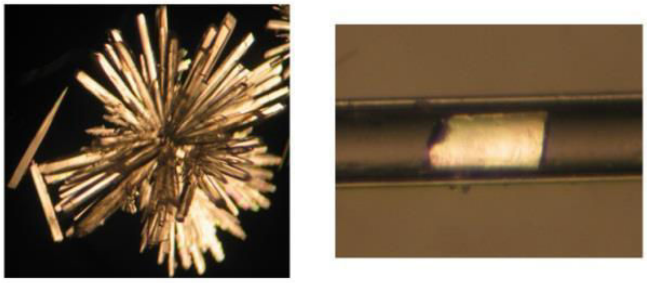

Figure 5.5 Pictures of single crystals of compound $[Gd(nip)(Hnip)(H_2O)_4, 3H_2O]_\infty$.

5.4 Description of the crystal structures.

5.4.1 [Gd(nip)(Hnip)$(H_2O)_4$, 3H_2O].

The single crystal $[Gd_4(nip)_6(H_2O)_{14}, 5H_2O]_\infty$ was gotten by evaporating the filtrate after reaction at room temperature.

$[Gd(nip)(Hnip)(H_2O)_4, 3H_2O]$ crystallizes in the monoclinic system, space group C2/c with the cell parameters : a = 7.5882(1) Å, b = 29.2765(5) Å, c = 20.2535(4) Å and β = 99.3299(7)° (Table 5.2). The best single crystal was obtained by slow evaporation. Atomic parameters and selected bond lengths and angles are listed in Appendix II.

Table 5.2 Crystal datas of $[Gd(nip)(Hnip)(H_2O)_4, 3H_2O]$ and $[Gd_4(nip)_6(H_2O)_{14}, 5H_2O]_\infty$

	1	2
formula	$GdC_{16}O_{16}N_2H_{15}$	$Gd_4C_{48}O_{55}N_6H_{56}$
Mr	701.58	2225.96
Crystal system	Monoclinic	Triclinic
Space group	C 2/c	P -1
a(Å)	7.5882(1)	12.1177(4)
b(Å)	29.2765(5)	13.8644(4)
c(Å)	20.2535(4)	23.3218(7)
α(°)	90	95.6102(16)
β(°)	99.3299(7)	93.8803(16)
ϒ(°)	90	112.7645(16)
V ($Å^3$)	4439.89(20)	3571.82(21)
Z, ρ_{calc} (g/cm^3)	4, 2.13	2, 2.28
GOF on F^2	1.09	1.064
R	0.0916	0.0543
Rw	0.2110	0.265

In this crystal strucutre, the asymmetric unit contains one Gd^{3+} ions, one nip^{2-} ligand, one $Hnip^-$ ligand, four coordination water molecules and three crystallization water

molecules (Figure 5.6a). Gd^{3+} ions are eight-coordinated by two oxygen atoms from nip^{2-} ligand, two oxygen atoms from $Hnip^{-}$ anion and four oxygen atoms from coordination water molecules, that generate a triangular dodecahedron (D_{2d} site symmetry Figure 5.6b) as evidenced by SHAPE calculations (SHAPE Factor is D_{2d}=0.869)[2].

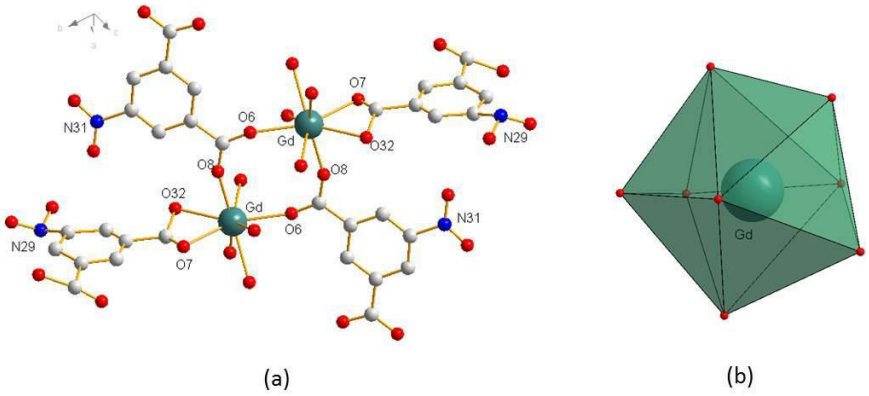

Figure 5.6 (a) Coordination environment and (b) geometry of Gd^{3+} ion in [Gd(nip)(Hnip)$(H_2O)_4$, $3H_2O$].

The crystal structure can be described as 0D (Figure 5.6a) and there are two different coordinated modes in the crystal structure (Figure 5.7a). In the crystal, one Gd^{3+} ion is coordinated by one nip^{2-} ligand and one $Hnip^{-1}$ ligand. Strong π-π stacking interactions (the face to face distance is about 3.822 Å) between the nip^{2-} ligands from adjacent chains result in a 2D layer in the bc plane (Figure 5.7b).

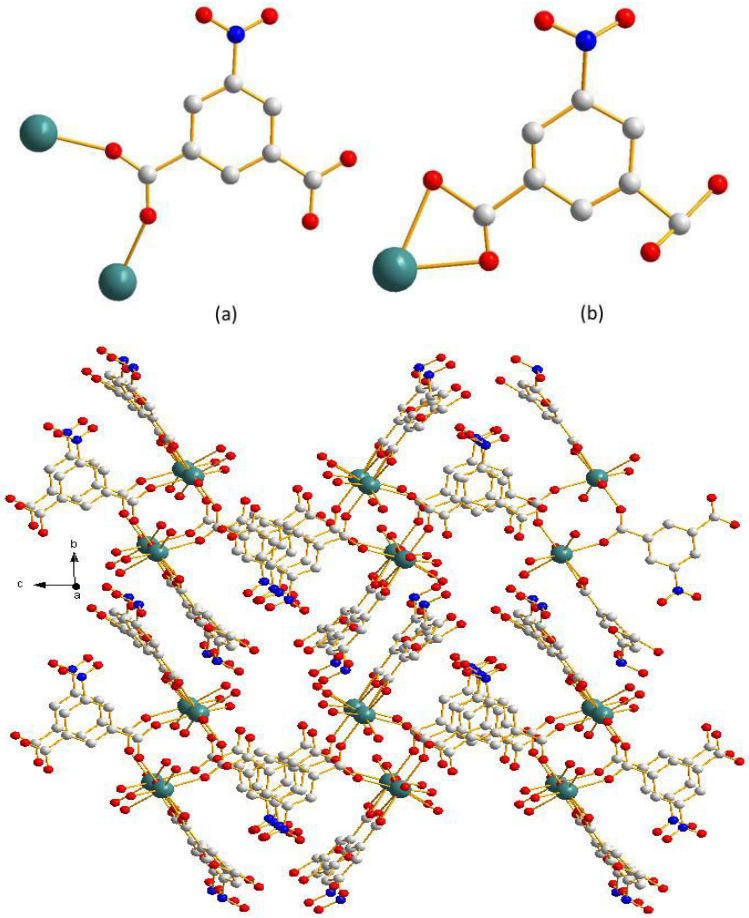

Figure 5.7 coordination mode of ligand and π-π stacking interactions in [Gd(nip) (Hnip)$(H_2O)_4$, $3H_2O$].

Comparison of experimental XRD patterns of the micro-crystalline powders of Family 1 with the simulated X-ray diffraction diagram from this crystal structure (Figure 5.8) reveals that the single crystal and the micro-crystalline powders are iso-structural.

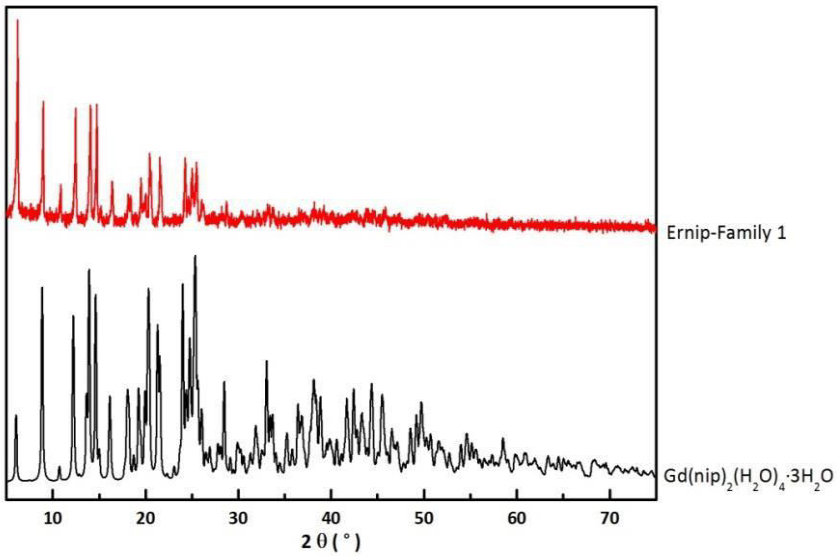

Figure 5.8 Experimental XRPD pattern of a compound that belongs to Family 1 and the simulated XRD diagram from the crystal structure of [Gd(nip)(Hnip) $(H_2O)_4$, $3H_2O$].

5.4.2 $[Gd_4(nip)_6(H_2O)_{14}, 5H_2O]_\infty$.

The single crystal $[Gd_4(nip)_6(H_2O)_{14}, 5H_2O]_\infty$ was gotten by diffusion in the U-shaped tubes which contains gels (TMOS or TEOS).

$[Gd_4(nip)_6(H_2O)_{14}, 5H_2O]_\infty$ crystallizes in the triclinic system, space group P-1 with the cell parameters: a = 12.1177(4) Å, b = 13.8644(4) Å, c = 23.3218(7) Å, α = 95.6102(16)°, β = 93.8803(16)° , ϒ = 112.7645(16) and Z = 2 (Table 5.2). The best single-crystal was obtained in U-shaped tubes containing TMOS 7.5% gel. Atomic parameters and selected bond lengths and angles are listed in Appendix II.

In this crystal strucutre, the asymmetric unit contains four Gd^{3+} ions, six nip^{2-} ligands, fourteen coordination water molecules and five crystallization water molecules (Figure 5.9a). Three out of the four Gd^{3+} ions are eight-coordinated and the last one is seven-coordinated. Gd(1) is surrounded by four oxgen atoms from three different nip^{2-} ligands and four other oxygen atoms from four coordination water molecules which generate a bi-augmented trigonal prism as evidenced by SHAPE calculation (SHAPE Factor is C_{2v}=2.060). Gd(2) and Gd(3) have similar coordination polyhedra that are also best described as bi-augmented trigonal prisms as evidenced by SHAPE calculation (SHAPE Factors are C_{2v}=1.770 and C_{2v}= 1.103 respectively).[2] Gd(4) is seven-coordinated by five oxygen atoms from three different nip^{2-} ligands and two oxygen atoms from two coordination water molecules. Its coordination polyhedron is best described as a distorted capped trigonal prism as evidenced by SHAPE calculations (SHAPE Factor is C_{2v}= 0.711) (Figure 5.9b).[3]

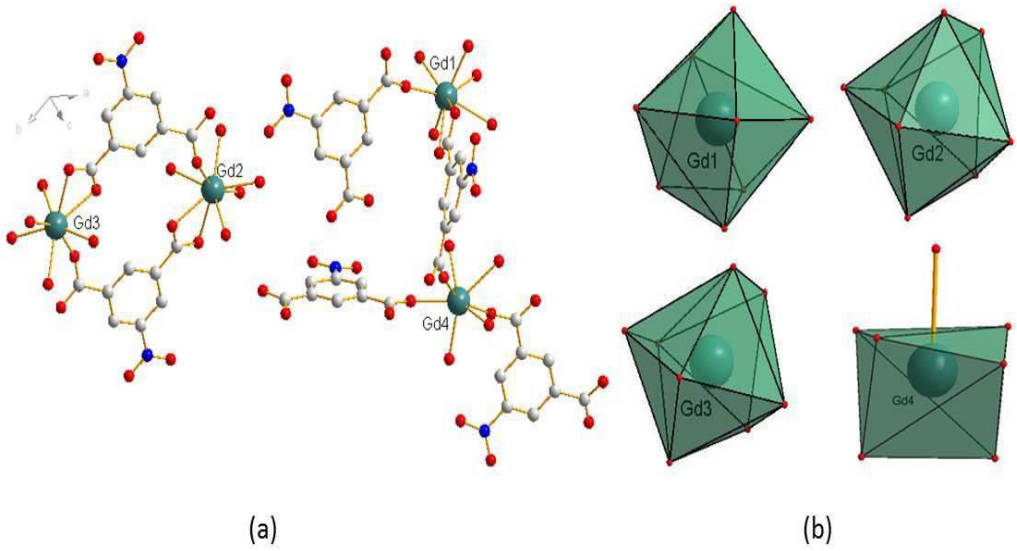

Figure 5.9 (a) Coordination environments and (b) geometries of Gd^{3+} ions in $[Gd_4(nip)_6(H_2O)_{14}, 5H_2O]_\infty$.

The crystal structure is 1D and can be described on the basis of two molecular chains. One chain involves two Gd^{3+} ions (Gd(2) and Gd(3)) and two nip^{2-} ligands. The two carboxylate groups of each nip^{2-} ligand have different coordination modes (Figure 5.10a): one is bidentate and the other one bridges two Gd^{3+} ions to form an infinite 1D chains (Figure 5.10b).

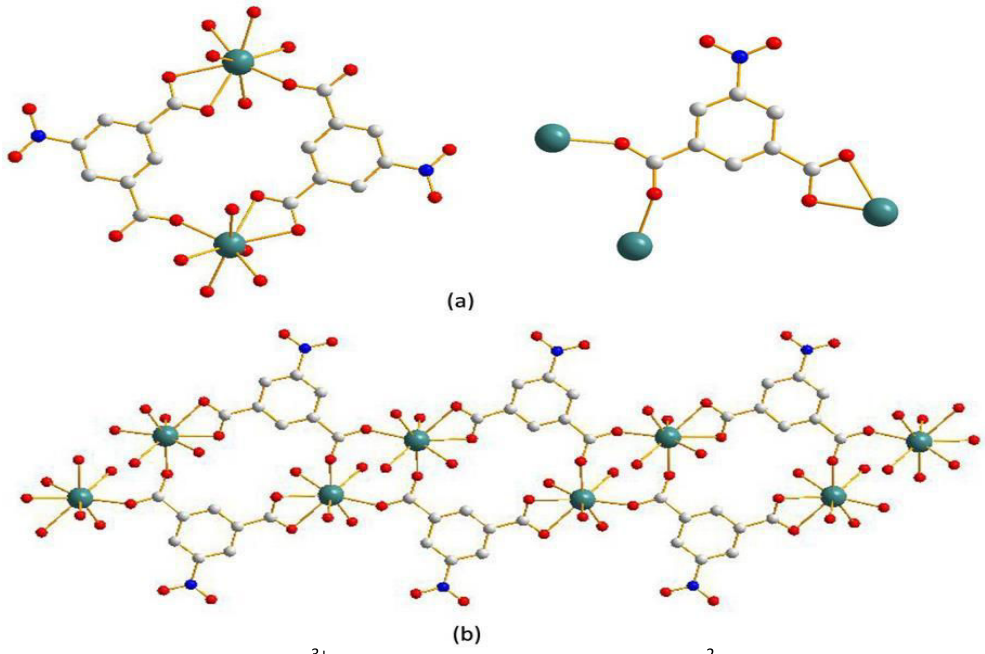

Figure 5.10 (a) environment of the Gd^{3+} ions and coordination mode of nip^{2-} ligands and (b) projection view of the first molecular chain in $[Gd_4(nip)_6(H_2O)_{14}, 5H_2O]_\infty$.

The second chain involves the other Gd^{3+} ions and four different nip^{2-} ligands (Figure 5.10). Carboxylate groups present three different coordination modes (Figure 5.11). Mode a and mode b act as a bridges to bind the Gd^{3+} ions and form the chain, mode c decorates the chains (Figure 5.12).

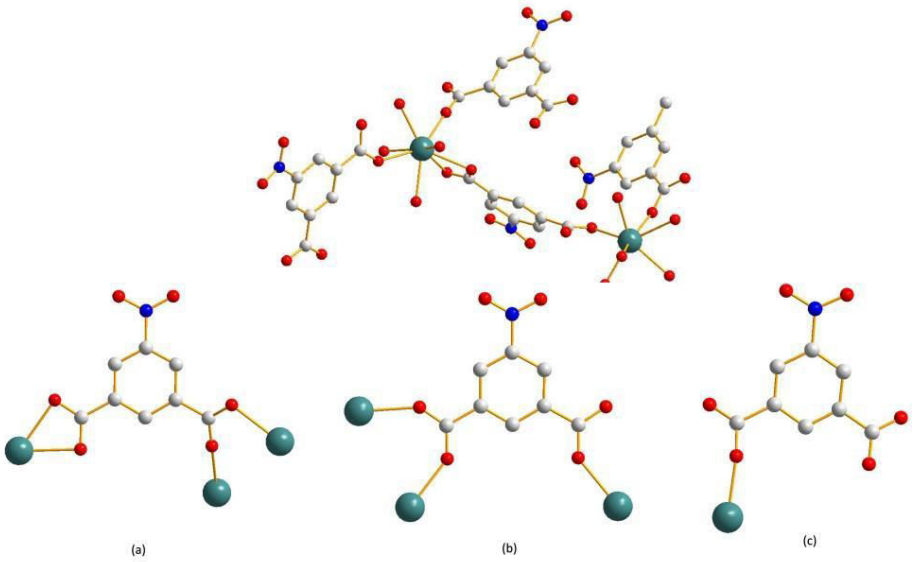

Figure 5.11 Environment of the Gd^{3+} ions and coordinating modes of nip^{2-} ligands in the second molecular chain of $[Gd_4(nip)_6(H_2O)_{14}, 5H_2O]_\infty$.

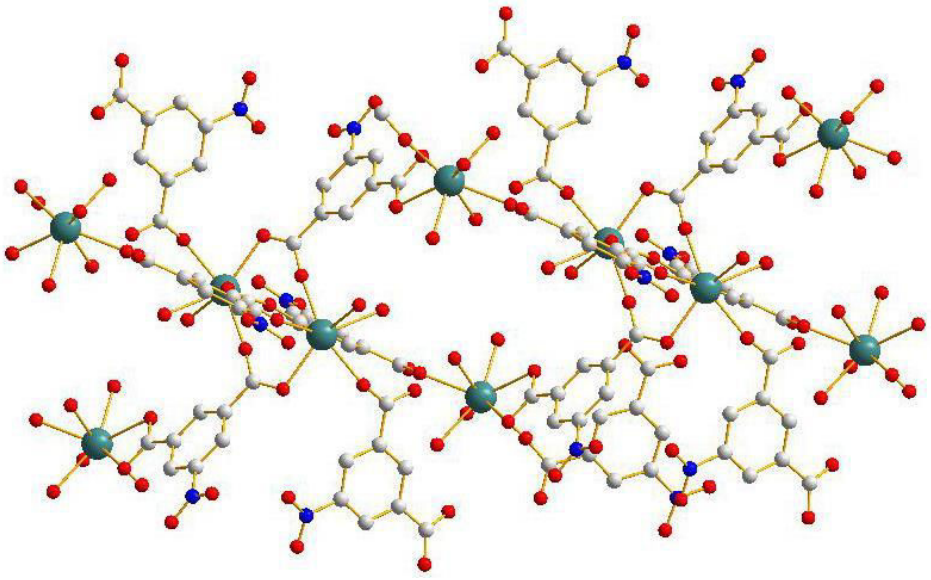

+

Figure 5.12 1D Projection view of the second molecular chain in $[Gd_4(nip)_6(H_2O)_{14}, 5H_2O]_\infty$.

In the strucure, each molecular double-chain motif is constituted by two molecular chains held together by a network of straong hydrogen bonds and π-π stacking interactions (the face to face distance is about 3.747 Å) between the two adjacent chains.

Unfortunately, we did not succeed in preparing microcrystalline powders of this compound.

5.5 Study of the thermal stability.

Thermal stability of the compounds that constitute Family 1 was investigated by TGA/TDA experiments in the 25-995°C temperature range under N_2 atmosphere. The program details about TGA/TDA are given in Appendix I. The Dy-containing compound is taken as example (Figure 5.13).

The thermal analysis shows a 21.5% weight loss from room temperature to 150°C

that corresponds to the departure of 7 water molecules (cal 18%). Then, the anhydrous phasis is stable between 150 to 390°C. Then a violent weight loss after 390°C is attributed to the decomposition of the ligand and is accompanied by an intense exothermic phenomenon at 400°C.

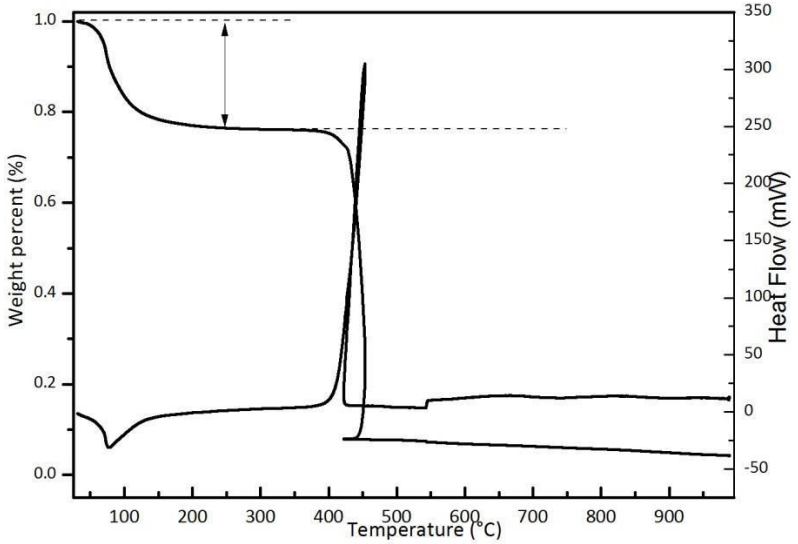

Figure 5.13 TGA/TDA curves for a microcrystalline sample of [Dy(nip)(Hnip)(H_2O)$_4$, 3H_2O].

The TDXD of the Y-containing compound [Y(nip)(Hnip)(H_2O)$_4$, 3H_2O] confirmed the results of the thermal analysis (Figure 5.14). The sample was heated from room temperature to 850°C under N_2 flux. The crystal structure collapsed upon dehydration leading to an amorphous phasis stable between 50°C and 350°C. This behavior is in agreement with 0D character of the crystal strucutre. Finally, the sample completely decomposed leading to Y_2O_3.

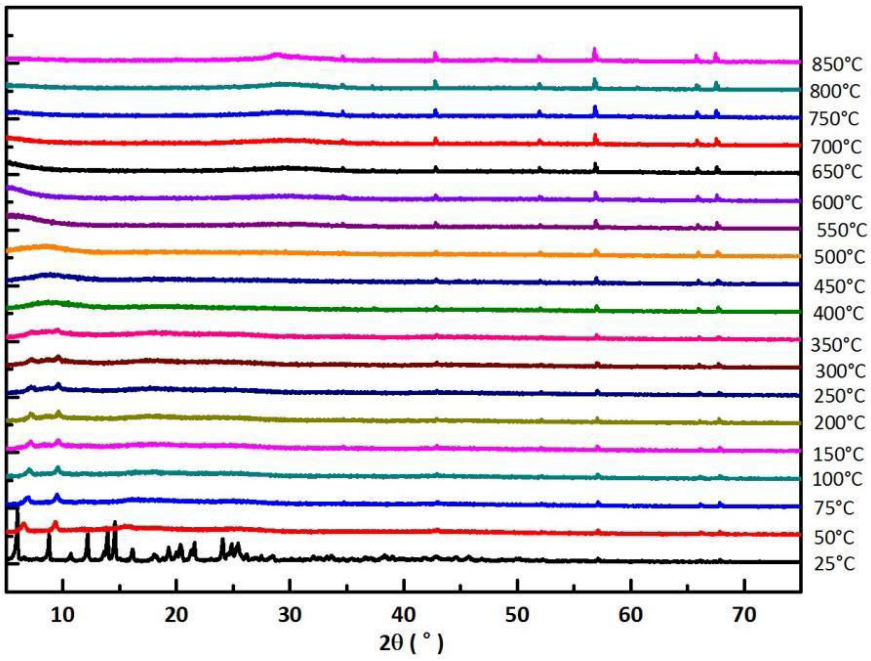

Figure 5.14 TDXD under N_2 flux between room temperature and 850°C for [Y(nip)(Hnip) (H_2O)$_4$, 5H_2O].

5.6 Luminescent properties.

The Eu-containing compound obtained at room temperature is amorphous, so we didn't study its luminescent properties. Moreover, Tb- and Eu-containing compounds obtained at 100°C were not structurally characterized. Therefore, only the Tb-containing compound obtained at room temperature and belonging to Family 1 was studied.

First, solid-state excitation and emission spectra were mesured at λ_{em} = 545 nm and λ_{exc} = 312 nm, respectively (Figure 5.15). There is no obvious emission peaks in the emission spectrum. This is in agreement with results published before.[4] The luminescent behavior can be explained by the intramolecular transfer between the triplet state of the ligand and the lanthanide receiving levels. Energy of the lowest triplet states were reported around 21 786 cm^{-1}. According to Latva's rules,[5] the lowest excited triplet (21 786 cm^{-1}) state is too close of the terbium emitting states (20 500 cm^{-1}) and an energy back-transfer can occur that leads to a quenching of the luminescence of the Tb-containing complex.

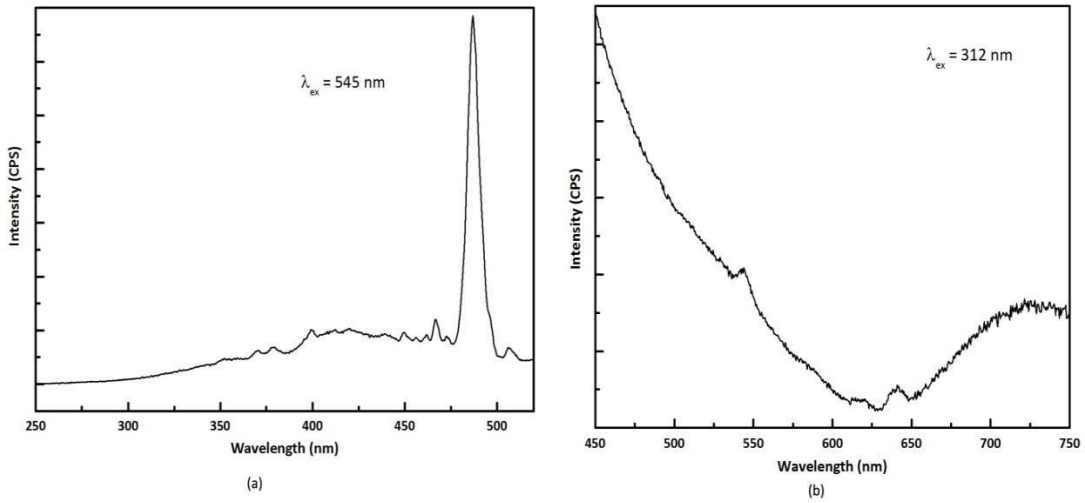

Figure 5.15 Excitation and emission spectra of [Tb(nip)(Hnip) $(H_2O)_4$, $3H_2O$].

Conclusion.

We have synthesized the microcrystalline powders for all the rare earth elements at different temperatures and classified them on the basis of their XPRD patterns. We obtained two novel crystal structures. The growth of single crystals of the other families is in progress. We measured the luminescent properties of the Tb-containing compound of Family 1 and evidenced an energy back-transfer process that quenches its luminescence.

References:

[1]. a) Y. Luo, G. Calvez, S. Freslon, K. Bernot, C. Daiguebonne, O. Guillou, European Journal of Inorganic Chemistry, 2011, 3705, 2011. (b) S. Freslon, Y. Luo, G. Calvez, C. Daiguebonne, O. Guillou, K. Bernot, V. Michel, X. Fan, Inorganic Chemistry, 53, 1217, 2014. (c) X. Fan, S. Freslon, C. Daiguebonne, G. Calvez, L. Le Polles, K. Bernot, O. Guillou, Journal of Materials Chemistry C, 2, 5510, 2014.

[2]. D. Casanova, M. Llunell, P. Alemany, S. Alvarez, Chemistry – A European Journal, 11, 1479, 2005.

[3]. D. Casanova, P. Alemany, J. M. Bofill, S. Alvarez, Chemistry – A European Journal, 9, 1281, 2003.

[4]. Y. Huang, B. Yan, M. Shao, Journal of Solid State Chemistry, 182, 657, 2009.

[5]. M. Latva, H. Takalo, V.-M. Mukkala, C. Matachescu, J.C. Rodríguez-Ubis, J. Kankare, Journal of Luminescence, 75, 149, 1997.

Chapter 6.
Lanthanide coordination polymers based on ligand Hcpb

Chapter 6. Lanthanide coordination polymers based on ligand Hcpb

For synthesizing lanthanide-based coordination polymers, people usually focus their interest on ligands with oxygen donor such as benzene-poly-carboxylates.[1] However new types of ligands could lead to new structural networks and/or new physical properties. That is why we have chosen to use 4-carboxyphenylboronic acid (Hcpb) (Figure 6.1) as ligand. Actually, this rode-like ligand can present a structuring effect via π-stacking and hydrogen bonds, it present two functions with donor oxygen atoms and it can act as an antenna for luminescent properties. 4-carboxyphenylboronic acid presents both the acidic character of a Brönsted acid (carboxylic group) and the Lewis acidic character because of the vacant p orbital of the boron atom (Figure 6.1).[2] This particularity could lead to original structural properties.

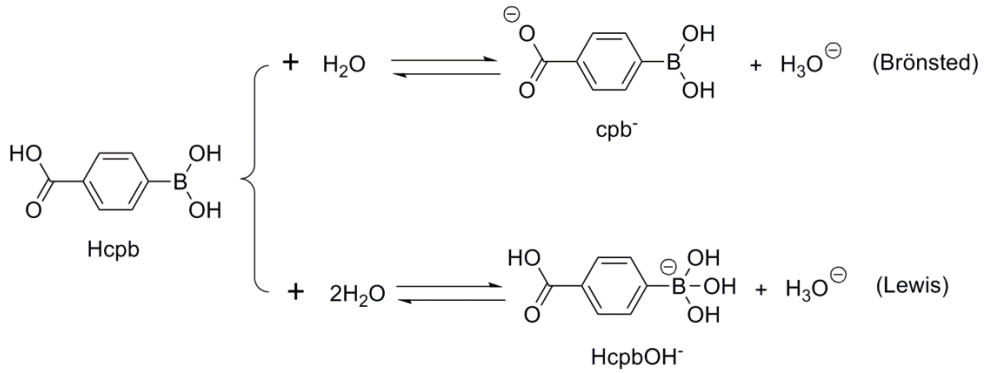

Figure 6.1 Acid/base equilibriums of 4-carboxyphenylboronic acid (Hcpb) in water.

6.1 Preparation of the sodium salt of 4-carboxyphenylboronic acid (Hcpb).

Synthesis of the sodium salt of 4-carboxyphenlboronic acid (Hcpb) is similar to that of Na_2cda (Chapter 3) except that chelidonic acid (H_2cda) is replaced by 4-carboxyphenlboronic acid (Hcpb) and the related ratio Hcpb:NaOH changes to 1:1.2. After filtration and drying, the white powder of the sodium salt of Hcpb was obtained in 90% yields. UV-vis absorption spectrum of an aqueous solution (1×10^{-5} mol.L^{-1}) was measured. It shows a broad absorption band centered at 279 nm (Figure 6.2).

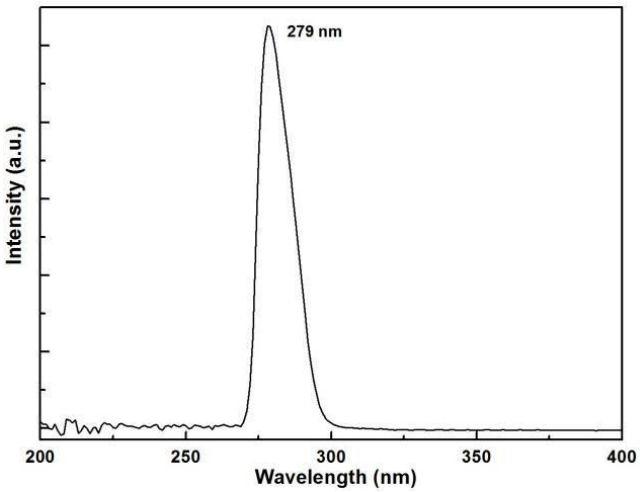

Figure 6.2 UV-vis absorption spectrum of a Nacpb, $0.5H_2O$ aqueous solution.

6.2 Preparation of microcrystalline powders.

6.2.1 Synthesis of microcrystalline powders of homo-nuclear compounds.

Microcrystalline powders of lanthanide-based (La to Lu plus Y) compounds have been synthesized with the same stoichiometric amounts at different temperatures (room temperature or 100 °C).

Clear solution of lanthanide chloride (0.5 mmol in 10 mL H_2O) was added to a sodium salt of Hcpb solution (1 mmol in 10 mL H_2O). Mixture was stirred for 40 min (10 min) at room temperature (100 °C) and a precipitation occurred. Precipitates were filtered and dried at room temperature. The white resulting powders were obtained in 90% yields. Microcrystalline powders were classified by families (Table 6.1) of iso-structural compounds on the basis of their X-ray powder diffraction diagrams (Figure 6.3).

Table 6.1 Families of the obtained Lanthanide-based compounds.

$L=cpb^{-1}$	La	Ce	Pr	Nd	Sm	Eu	Gd	Tb	Dy	Ho	Y	Er	Yb	Lu
RT														
100°C														

	Family 1 ≡ crystal structure of $[La(cpb)_3(H_2O)_2]_\infty$.
	Family 2 ≡ crystal structure of $[Tb(cpbOH)(H_2O)_2, (cpb)]_\infty$.

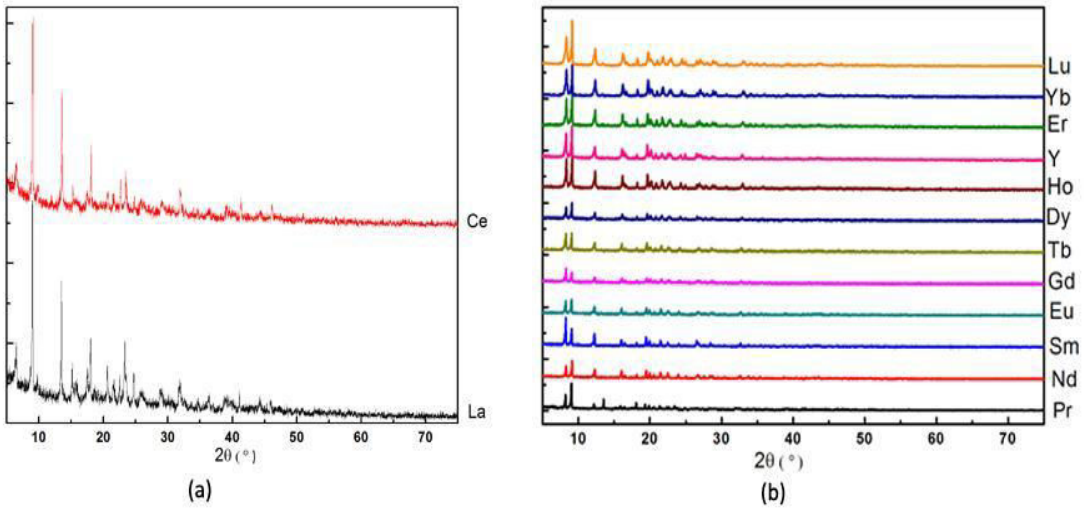

Figure 6.3 XPRD patterns of the microcrystalline powders for (a) family 1 and (b) family 2.

6.2.2 Synthesis of microcrystalline powders of hetero-nuclear compounds.

Microcrystalline powders of hetero-nuclear (Eu/Tb, Tb/Gd, Eu/Gd and Y/Lu) compounds were obtained according to similar procedures by simply replacing the lanthanide chloride solution by the appropriate mixture of lanthanide chlorides solutions in the synthetic process. For hetero-nuclear compounds the relative ratios between the two different lanthanide ions were measured by EDS (Appendix Ⅰ) Results for Eu/Tb and Gd/Tb compounds are listed in Table 6.2.

XPRD patterns of the hetero-nuclear (Eu/Tb and Gd/Tb) compounds (Figure 6.4) reveal that they are iso-structural to the corresponding homo-nuclear compounds (Family 2). XPRD patterns of the hetero-nuclear (Eu/Gd) compounds are reported in Appendix Ⅱ.

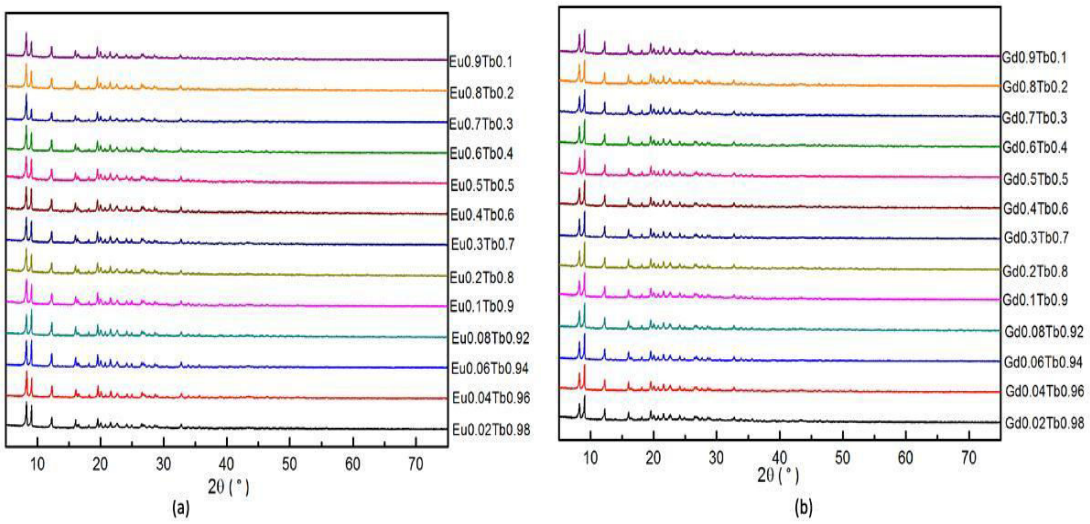

Figure 6.4 XPRD patterns for some hetero-nuclear (Eu/Tb and Gd/Tb) compounds.

Table 6.2 Relative contents of Ln and Ln' for some $[Eu_{1-x}Tb_x(cpbOH)(H_2O)_2, (cpb)]_\infty$ and $[Gd_{1-x}Tb_x(cpbOH)(H_2O)_2, (cpb)]_\infty$ compounds with $0 \leq x \leq 1$.

$[Eu_{1-x}Tb_x(cpbOH)(H_2O)_2, (cpb)]_\infty$			$[Gd_{1-x}Tb_x(cpbOH)(H_2O)_2, (cpb)]_\infty$		
Tb(%)	Eu(%)	x	Tb(%)	Gd(%)	x
100	0	1.00	100	0	1.00
98(2)	2(2)	0.98	98	2	0.98
96(2)	4(2)	0.96	96	4	0.96
94(2)	6(2)	0.94	94	6	0.94
91(2)	9(2)	0.92	91	9	0.92
89(2)	11(2)	0.90	90	10	0.90
80(2)	20(2)	0.80	80	20	0.80
71(2)	29(2)	0.70	71	29	0.70
61(2)	39(2)	0.60	60	40	0.60
51(2)	49(2)	0.50	51	49	0.50
40(2)	60(2)	0.40	42	58	0.40
32(2)	68(2)	0.30	33	67	0.30
21(2)	79(2)	0.20	22	78	0.2
11(2)	89(2)	0.10	13	87	0.1
0	100	0.00	0	100	0

a: experimental values (metal fractions found by elemental analyses).

b: Theoretical values (metal fractions used during the syntheses)

6.3 Distribution of the lanthanide ions over the metallic sites in the hetero-nuclear compounds.

To confirm that the distribution of the lanthanide ions over the metallic sites in the hetero-nuclear compounds is random, both X-ray powder diffraction and solid state ^{89}Y RMN measurements (Appendix I) were used to verify the phenomenon at the X-ray scale and at the local scale.

Four samples have been prepared and their powder X-ray diffraction diagrams have been compared (Figure 6.5).

1). Two homo-nuclear compounds involving two lanthanide ions with very different ionic radii (Nd^{3+} and Y^{3+}): $[Nd(cpbOH)(H_2O)_2, (cpb)]_\infty$ and $[Y(cpbOH)(H_2O)_2, (cpb)]_\infty$.

2). A fifty-fifty mixture of homo-nuclear compounds : $0.5[Nd(cpbOH)(H_2O)_2, (cpb)]_\infty$ and $0.5[Y(cpbOH)(H_2O)_2, (cpb)]_\infty$.

3). The 50/50 hetero-nuclear compound $[Nd_{0.5}Y_{0.5}(cpbOH)(H_2O)_2, (cpb)]_\infty$.

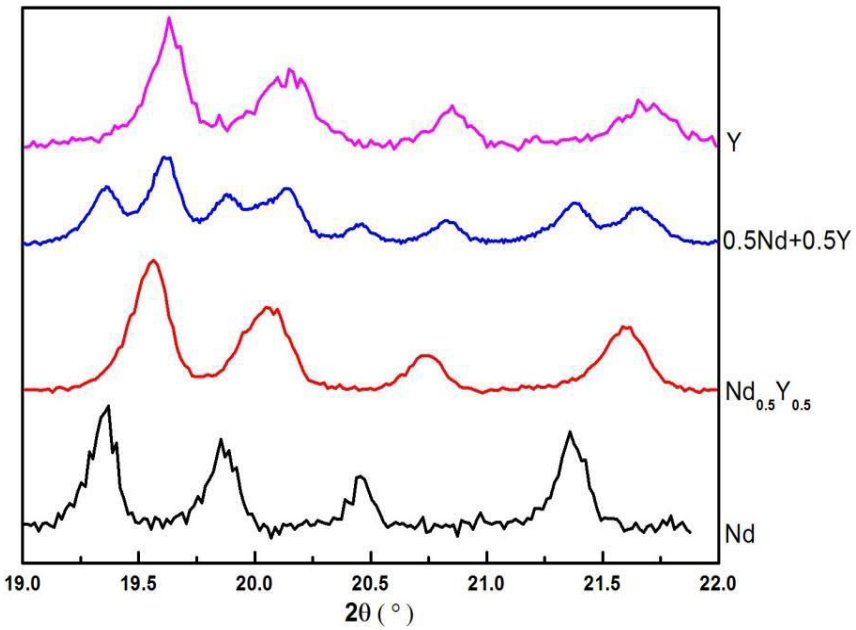

Figure 6.5 XPRD patterns of $[Nd(cpbOH)(H_2O)_2, (cpb)]_\infty$, $[Y(cpbOH)(H_2O)_2, (cpb)]_\infty$, $0.5[Tb(cpbOH)(H_2O)_2, (cpb)]_\infty$+ $0.5[Tb(cpbOH)(H_2O)_2, (cpb)]_\infty$ and $[Nd_{0.5}Y_{0.5}(cpbOH)(H_2O)_2, (cpb)]_\infty$.

These powder X-ray diffraction diagrams show that the diffraction peaks of the hetero-nuclear compounds are not split and are located between the corresponding diffraction peaks of the homo-nuclear (Nd and Y) compounds. Moreover, powder X-ray diffraction patterns of the hetero-nuclear (Eu/Tb and Gd/Tb) compounds (Figure 6.4) indicate that there is neither a long range order nor segregation in hetero-nuclear compounds. Therefore, distribution of the lanthanide ions over metallic sites in hetero-nuclear compounds is random at the X-ray scale.

For ^{89}Y measurements, due to experimental problems, results are not yet available.

6.4 Synthesis of single crystals.

Single crystals of lanthanide-based compounds were synthesized by slow diffusions of lanthanide chlorides (0.25 mmol in 10 mL H_2O) and Nacpb, $0.5H_2O$ (0.25 mmol in 10 mL H_2O) solutions in H-shaped tubes or in U-shaped tubes filled with gels (Agar-Agar, TMOS or TEOS). Details are given in Appendix I. After a few weeks, single-crystals were obtained in the tubes that were filled with 7.5% gel (TMOS or TEOS) or Agar-Agar (0.3% or 0.5%). Slow evaporation of the filtrates obtained during the microcrystalline preparation also offers single crystal. Single crystals suitable for crystal structure determination of Family 1 $\{[Ln(cpb)_3(H_2O)_2]_\infty\}$ (Ln=La and Ce) and Family 2 $\{[Ln(cpbOH)(H_2O)_2, (cpb)]_\infty\}$ (Ln=Pr to Lu, plus Y and except Pm) have similar cell parameters. Therefore, only one crystal structure was solved for each family. Fitted cell parameters of the other compounds were calculated on the basis of their XRPD patterrns using the software Celref3 (Appendix I).[4] These single crystals are needle-like shaped (Figure 6.6). Single crystals were sealed in glass capillaries for X-ray single crystals

data collection in order to avoid potential dehydration.

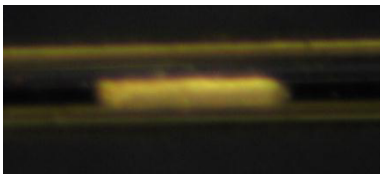

Figure 6.6 Picture of a single crystal of $[Tb(cpbOH)(H_2O)_2, (cpb)]_\infty$.

6.5 Description of the crystal structures.

6.5.1 $[La(cpb)_3(H_2O)_2]_\infty$.

Compound $[La(cpb)_3(H_2O)_2]_\infty$ crystallizes in the monoclinic system, space group P21/n, with the cell parameters: a = 22.7993(5) Å, b = 5.2334(1) Å, c = 23.2460(6) Å, β=118.608(1)° and Z = 4 (Table 6.3). Atomic parameters and selected bond lengths and angles are listed in Appendix II.

Table 6.3 Crystal data of $[La(cpb)_3(H_2O)_2]_\infty$ and $[Tb(cpbOH)(H_2O)_2, (cpb)]_\infty$

Family	1	2
formula	$LaC_{21}B_3O_{14}H_{22}$	$TbC_{14}B_2O_{11}H_{17}$
Mw	669.73	541.82
Crystal system	Monoclinic	Orthorombic
Space group	P21/n (n° 14)	Pbca (n° 61)
a(Å)	22.7993(5)	8.5704(1)
b(Å)	5.2334(1)	19.5441(1)
c(Å)	23.2460(6)	21.4191(3)
β(°)	118.608(1)	90
V ($Å^3$)	2435(1)	3587.71(7)
Z, ρ_{calc} (g/cm^3)	4, 1.799	8, 1.98
GOF on F^2	1.118	1.082
R	0.0706	0.038
Rw	0.1126	0.0901

In this crystal structure, the asymmetric unit contains one La^{3+} ion, three cpb^- ligands and two coordination water molecules. The La^{3+} ion is eight-coordinated by six oxygen atoms from six different cpb^- ligands and two oxygen atoms from two coordination water molecules (Figure 6.7a) that generate a bi-augmented trigonal prim (C_{2v} site symmetry Figure 6.7b) (SHAPE Factor is C_{2v} = 0.762).

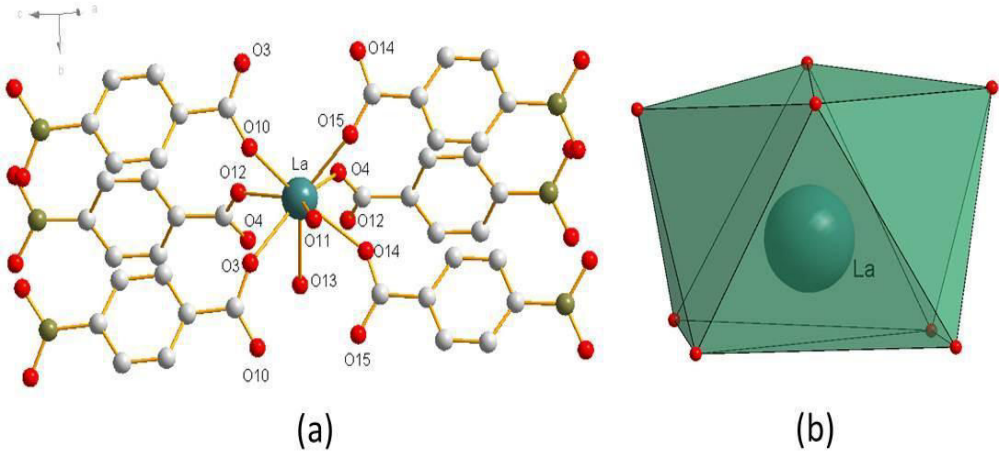

Figure 6.7 (a) Coordination environment and (b) coordination geometry of La^{3+} ions in $[La(cpb)_3(H_2O)_2]_\infty$.

The crystal strucutre can be described as a 1D molecular chain. There is only one coordinated mode for cpb^- ligands (Figure 6.8a). Oxygen atoms from carboxylate groups act as bridges that connect adjacent La^{3+}. There are two types of bridges. First type connects La^{3+} ions to form a straight molecular chain. The other bridges two adjacent chains to form 1D double-chains molecular motifs(Figure 6.8c).

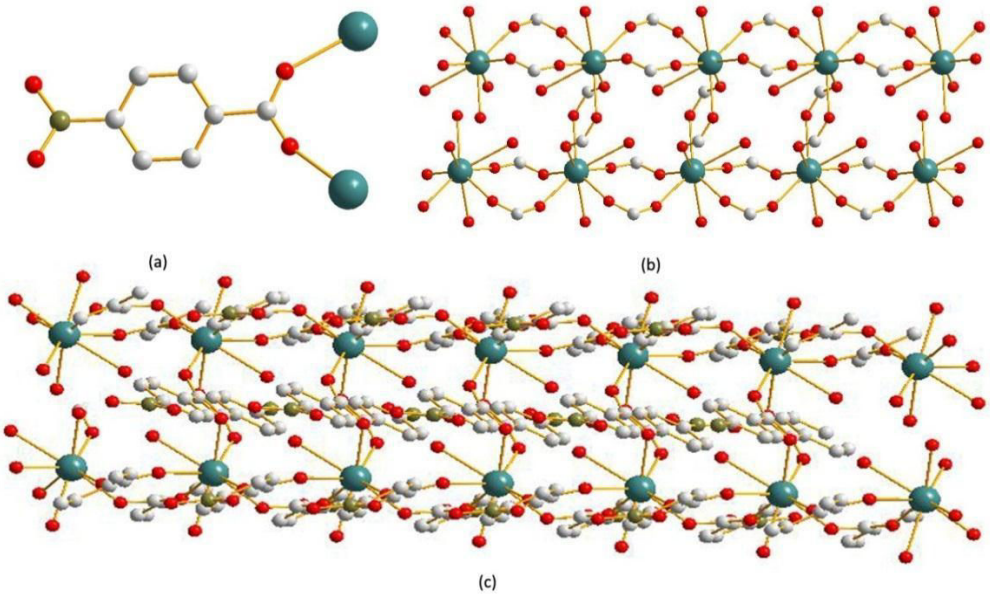

Figure 6.8 (a) coordinated mode of cpb^- ligand, (b) two types of bridges and (c) 1D double-chains molecular motifs of $[La(cpb)_3(H_2O)_2]_\infty$.

XRPD pattern of the micro-crystalline powder of the La-containing compound is similar to the X-ray diffraction diagram simulated on the basis of the crystal structure (Figure 6.9).

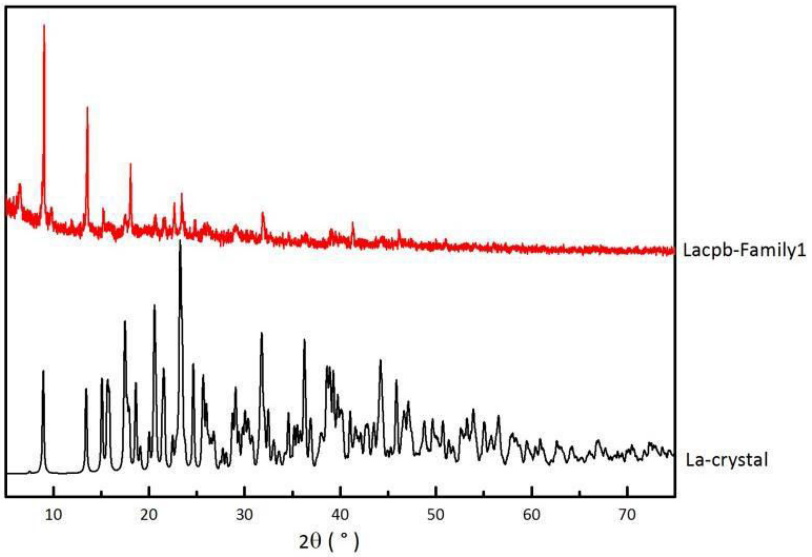

Figure 6.9 Experimental XRPD patterns of the La-containing compound of Family 1 and simulated XRD diagram of $[La(cpb)_3(H_2O)_2]_\infty$.

6.5.2 $[Tb(cpbOH)(H_2O)_2, (cpb)]_\infty$.

$[Tb(cpbOH)(H_2O)_2, (cpb)]_\infty$ crystallizes in the orthorombic system, space group Pbca (n°61), with a = 5.5704(1) Å, b = 19.5441(1) Å, c = 21.4191(3) Å and Z = 8 (Table 6.3). Atomic parameters and selected bond lengths and angles are listed in Appendix II.

It must be noticed that the ligand involved in the molecular motif is di-anionic ($cpbOH^{2-}$). Therefore, the bi-dimensional layers described above are cationic because there are only one Tb^{3+} ion and one $cpbOH^{2-}$ ligand in the asymmetric unit. The overall neutrality is ensured by a free cpb^- ligand that is located between the molecular layers (Figure 6.10b). Tb^{3+} ion is eight coordinated by four oxygen atoms from two $B(OH)_3^-$ groups, two oxygen atoms from two carboxylates groups and two oxygen atoms from coordination water molecules (Figure 6.10a) that form a slightly distorted square antiprism (Figure 6.10c). The coordination polyhedron of the Tb^{3+} ion is best described as a distorted square antiprism (D_{4d} site symmetry) as evidenced by SHAPE calculations (SHAPE Factor is D_{4d} = 2.805).

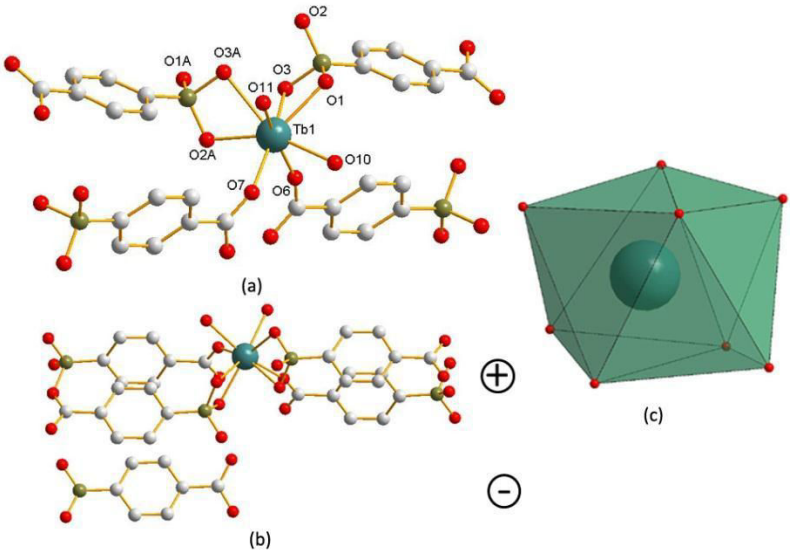

Figure 6.10 (a) coordination environment of Tb^{3+} ion, (b) overall neutrality of the network and (c) coordination geometry of Tb^{3+} ion in $[Tb(cpbOH)(H_2O)_2, (cpb)]_\infty$.

The $cpbOH^{2-}$ ligand links four Tb^{3+} ions. Its carboxylate group bridges two Tb^{3+} ions by two μ_2-O atoms (Figure 6.11). On the other hand, the $B(OH)_3^-$ group bridges two Tb^{3+} ions by two μ_2-OH groups and one μ_3-OH group (Figure 6.11). There is no crystallization water molecule in the framework whose stability is ensured by a complex network of hydrogen bonds as already observed in the crystal structure of Hcpb.[5]

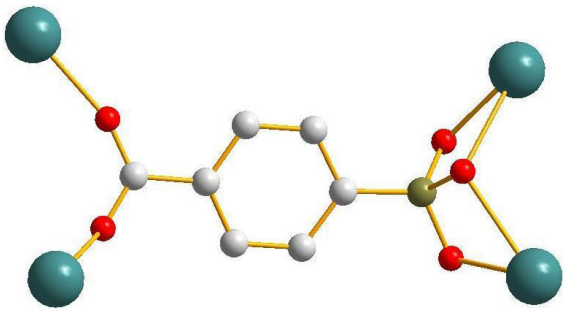

Figure 6.11 Coordination mode of $cpbOH^{2-}$ ligand.

The crystal structure is 2D and can be described as the superimposition of wavy planes that spread parallel to the $(\vec{a}, \vec{b})$ plane. The 2D layer structure were generated by two chains, one chain is formed by two $cpbOH^{2-}$ ligand that connect two adjacent Tb^{3+} ions (Figure 6.12a) and in the other chains adjacent Tb^{3+} ions are connected by two $cpbOH^{2-}$ ligand (Figure 6.12b).The two chains further connect to generate 2D molecular layers that spread parallel to the $(\vec{a}, \vec{b})$ plane (Figure 6.12c).

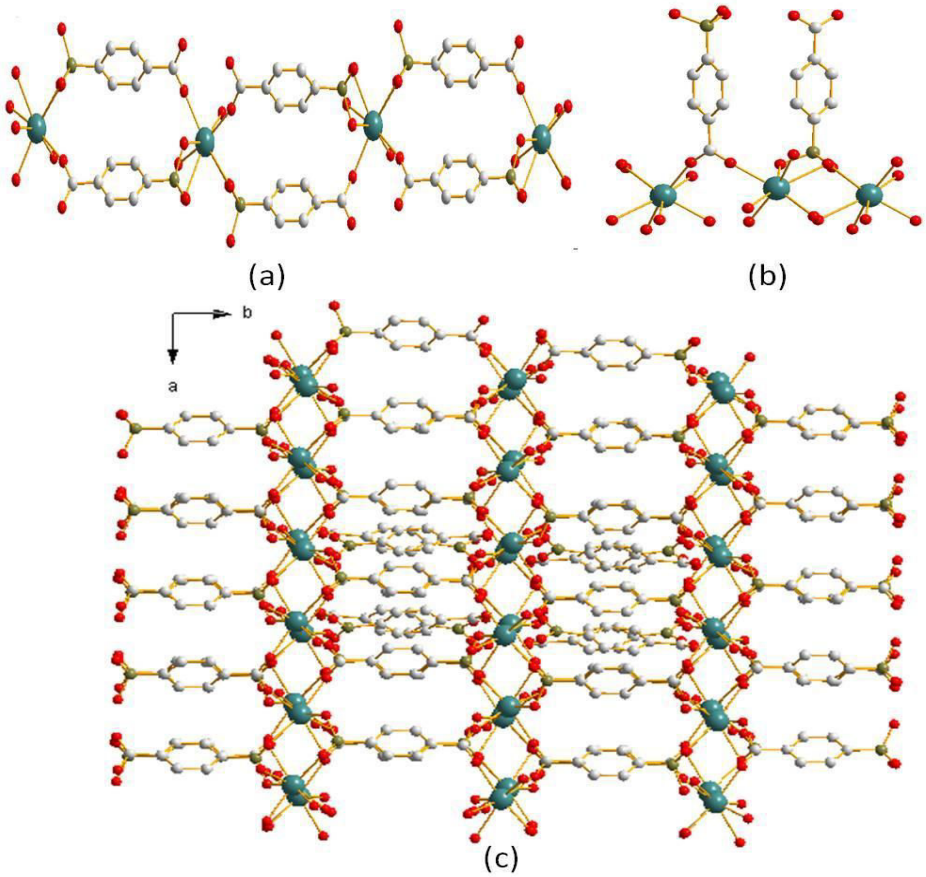

Figure 6.12 (a) and(b) 1D molecular chains that spread in planes (ac) and (bc) and (c) 2D structure parallel (ab) plane.

Tb-Tb distances between Tb^{3+} ions that belong to the same dimeric unit are 4.32Å while they are 5.32Å for Tb^{3+} ions that belong to adjacent dimeric units. These inorganic chains are linked to each other by 4-carboxyphenylborate ligands that are aligned parallel to the $\vec{b}$ axis. The shortest distance between two Tb^{3+} ions that belong to adjacent inorganic chains is 9.79Å (Figure 6.13).

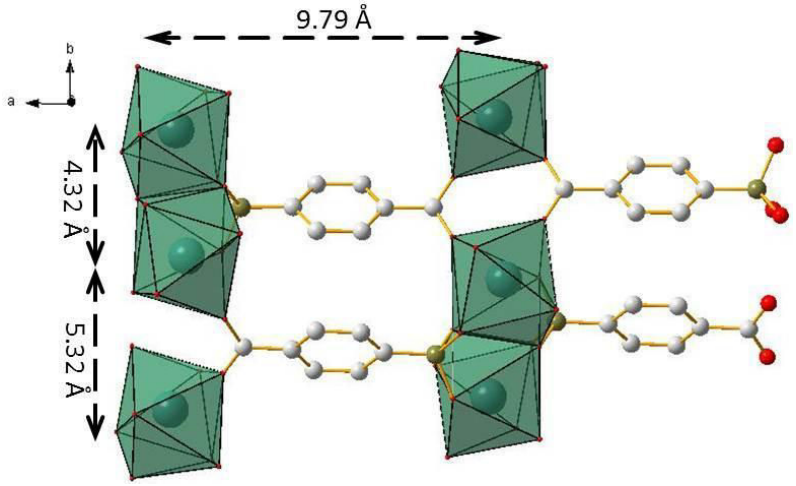

Figure 6.13 Distances between Tb^{3+} ions in $[Tb(cpbOH)(H_2O)_2, (cpb)]_\infty$.

Simulated X-ray diffraction diagram from this crystal structure has been compared with experimental powder X-ray diffraction diagrams (Figure 6.14) of the compounds that constitute Family 2. This comparison revealed that they are all iso-structural to $[Tb(cpbOH)(H_2O)_2, (cpb)]_\infty$. Their cell parameters (Table 6.4 and Figure 6.15) were refined on the basis of their powder X-ray diffraction patterns by the software Celref 3 (Appendix I). The refined cell parameters (a,b and c) are almost identical which indicates a weak influence of the involved lanthanide ions on the cell parameters for Family 2. The cell parameters of the hetero-nuclear (Eu/Tb and Gd/Tb) compounds ($[Ln_xLn'_{1-x}(cpbOH)(H_2O)_2, (cpb)]_\infty$) were also refined using the same method (Table 6.5, 6.6 and Figure 6.16, 6.17), and the results confirmed-a weak influence of the involved lanthanide ions on the cell parameters.

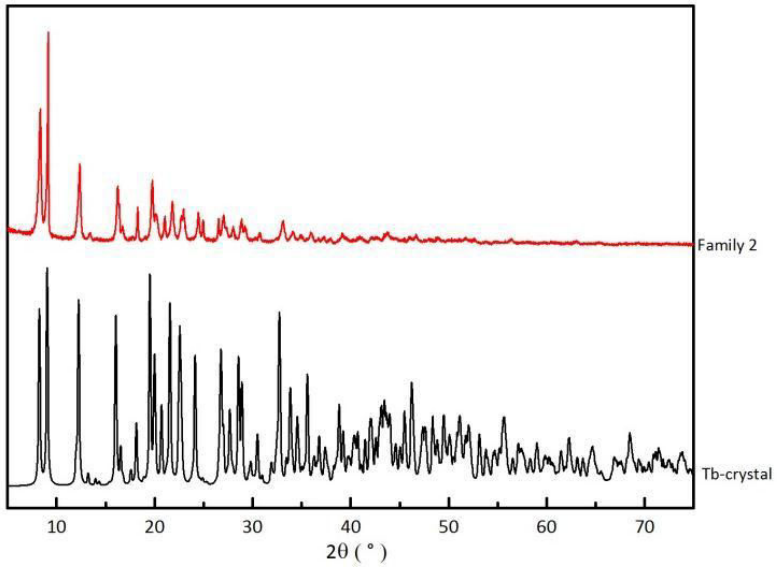

Figure 6.14 Experimental XRPD patterns of compounds that belong to Family 2and simulated XRD diagram of $[Tb(cpbOH)(H_2O)_2, (cpb)]_\infty$.

Table 6.4 Refined cell parameters for $[Ln(cpbOH)(H_2O)_2, (cpb)]_\infty$ (Ln=Pr to Lu, plus Y).

	a(Å)[a]	b(Å)[a]	c(Å)[a]
Pr	8.59	19.54	21.44
Nd	8.58	19.57	21.44
Sm	8.58	19.56	21.46
Eu	8.58	19.56	21.45
Gd	8.58	19.56	21.44
Tb	8.58	19.56	21.45
Dy	8.58	19.55	21.45
Ho	8.58	19.56	21.44
Y	8.58	19.56	21.46
Er	8.58	19.56	21.45
Yb	8.57	19.58	21.45
Lu	8.57	19.55	21.44

a. calculated values (cell parameters calculate by software Celref).

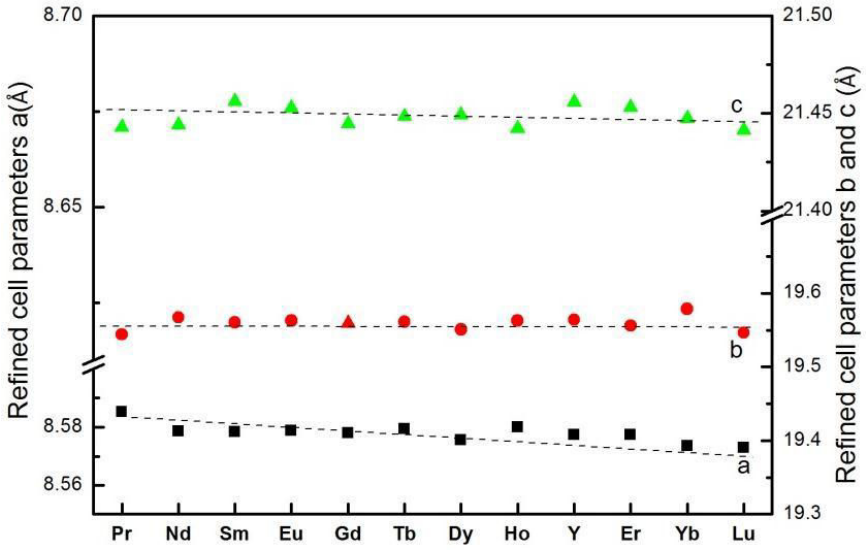

Figure 6.15 Refined cell parameters for $[Ln(cpbOH)(H_2O)_2, (cpb)]_\infty$ (Ln=Pr to Lu, plus Y).

Table 6.5 Refined cell parameters for $[Eu_xTb_{1-x}(cpbOH)(H_2O)_2, (cpb)]_\infty$ $(0 \le x)]$b).

x	a(Å)[a]	b(Å)[a]	c(Å)[a]
0.02	8.57	19.55	21.46
0.04	8.58	19.55	21.46
0.06	8.57	19.55	21.45
0.08	8.58	19.54	21.45
0.1	8.58	19.55	21.45
0.2	8.57	19.56	21.44
0.3	8.57	19.54	21.44
0.4	8.58	19.55	21.45
0.5	8.58	19.54	21.45
0.6	8.58	19.56	21.45
0.7	8.58	19.56	21.45
0.8	8.60	19.54	21.46
0.9	8.59	19.55	21.47

a. calculated values (cell parameters calculate by software Celref).

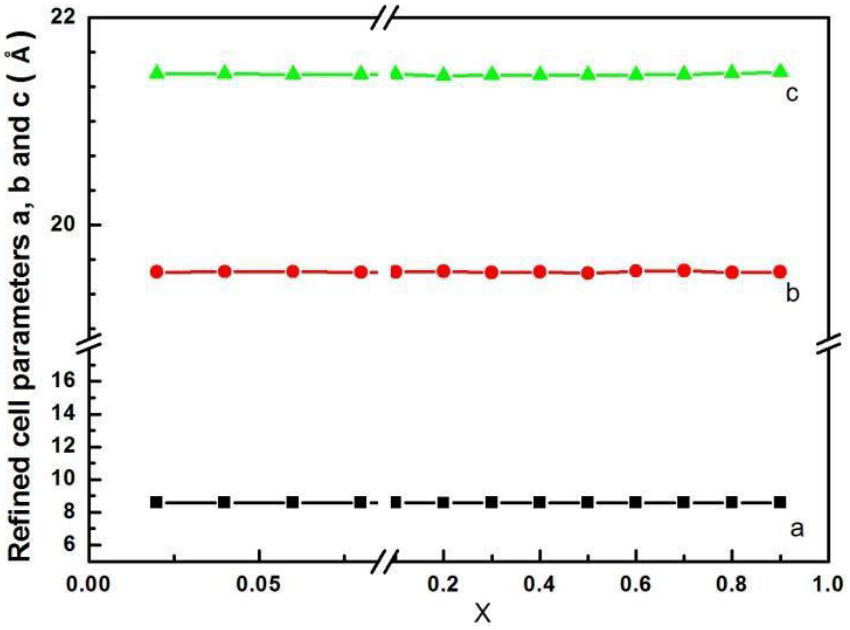

Figure 6.16 Refined cell parameters for $[Eu_xTb_{1-x}(cpbOH)(H_2O)_2, (cpb)]_\infty$ $(0 \le x \le 1)$.

Table 6.6 Refined cell parameters for $[Gd_xTb_{1-x}(cpbOH)(H_2O)_2, (cpb)]_\infty$ $(0 \le x \le 1)$.

x	a(Å)[a]	b(Å)[a]	c(Å)[a]
0.02	8.57	19.54	21.45
0.04	8.57	19.55	21.45
0.06	8.58	19.56	21.43
0.08	8.57	19.54	21.44
0.1	8.57	19.54	21.45
0.2	8.57	19.55	21.45
0.3	8.58	19.56	21.43
0.4	8.57	19.54	21.44
0.5	8.58	19.54	21.44
0.6	8.57	19.56	21.45
0.7	8.57	19.54	21.45
0.8	8.58	19.56	21.45
0.9	8.57	19.56	21.46

a. calculated values (cell parameters calculate by software Celref).

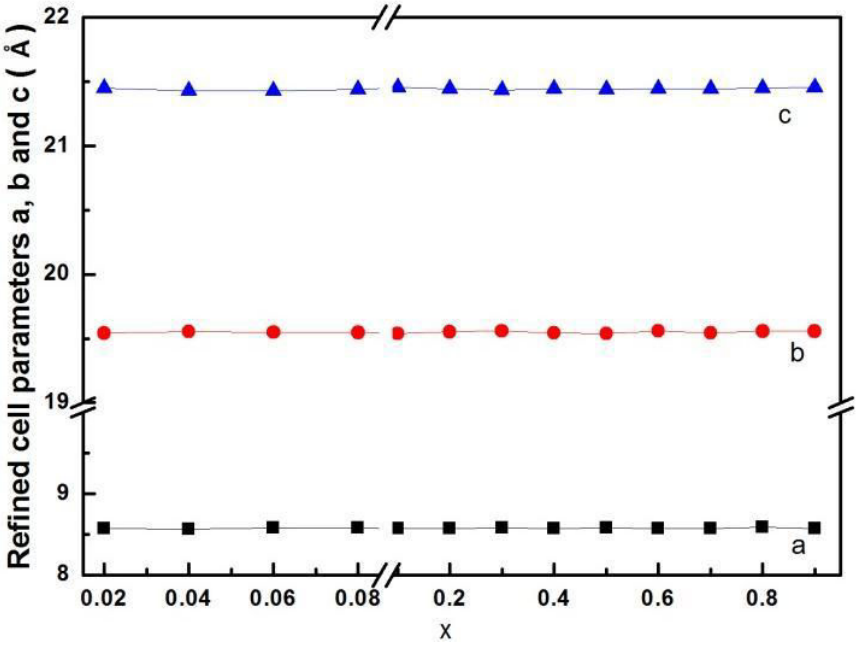

Figure 6.17 Refined cell parameters for $[Eu_xTb_{1-x}(cpbOH)(H_2O)_2, (cpb)]_\infty$ $(0 \le x \le 1)$.

6.6 Study of the thermal stabilities.

Thermal stabilities of both families were investigated by TGA/TDA experiments in the 25-995°C temperature range under N_2 atmosphere. Details are given in Appendix I. The curves obtained for compounds that constitute Family 2 are described as an example (Figure 6.18). Curves for compounds that belong to Family 1 and for sodium salt of Hcpb acid are

reported in Appendix II.

Thermal analyses show a first weight loss at 150°C. This weight loss (13.6%) has been attributed to the departure of 4 water molecules (calc. 13.3%): two coordination water molecules and two water molecules produced by the dehydration of the boronic functions. The obtained anhydrous phasis is stable between 150 to 400°C and then a second weight loss is observed between 400°C and 600°C that has been attributed to the decomposition of the ligand. These experiments demonstrate that this compound is quite thermally stable.

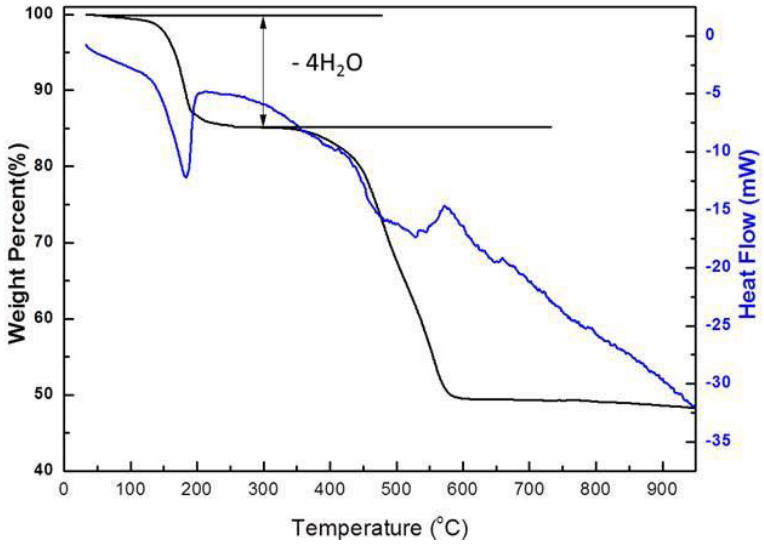

Figure 6.18 TGA/TDA curves for $[Tb(cpbOH)(H_2O)_2, (cpb)]_\infty$.

The thermal behavior of $[Tb(cpbOH)(H_2O)_2, (cpb)]_\infty$ has also been investigated by thermal dependent powder X-ray diffraction (TDXD) (Figure 6.19a). TDXD measurements show that the crystal structure is unchanged from room temperature to 150°C (Figure 6.19b). Then the crystal structure collapses and the powder becomes amorphous.

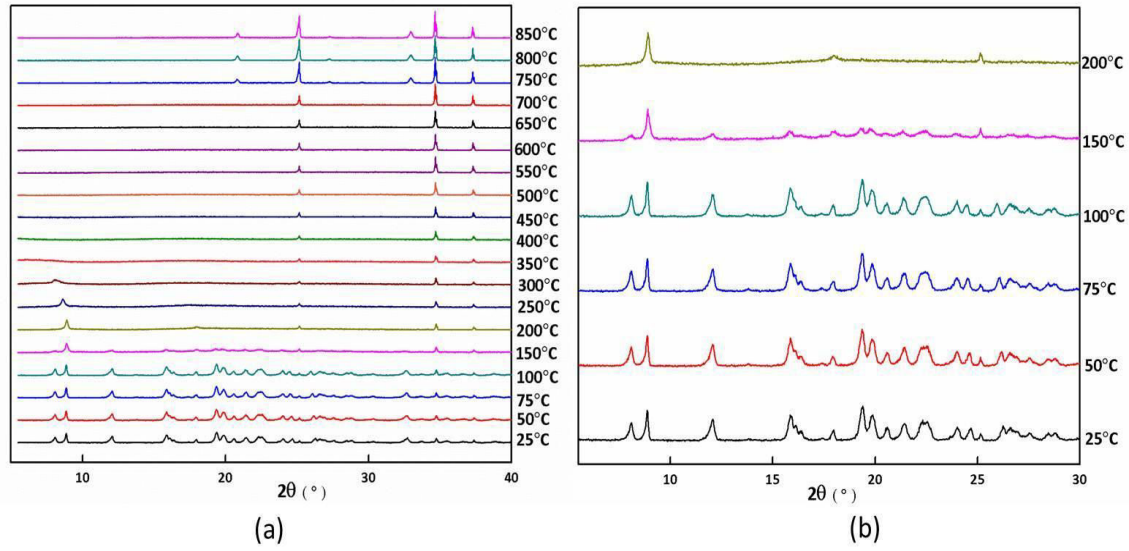

Figure 6.19 (a) TDXD diagrams recorded under N_2 flux between room temperature and 850°C and (b) zoom from 25 to 200°C for $[Tb(cpbOH)(H_2O)_2, (cpb)]_\infty$.

6.7 UV-Vis absorption measurements.

Solid-state UV-vis absorption spectrum of compound $[Gd(cpbOH)(H_2O)_2, (cpb)]_\infty$ has been recorded for estimating the energy of the lowest singlet excited states of cpb^- ligand (Figure 6.20). The lowest singlet excited state of cpb^- ligand was estimated on the basis of the wavelength of the UV-vis absorbance edges (325 nm ≈30 750 cm^{-1}).

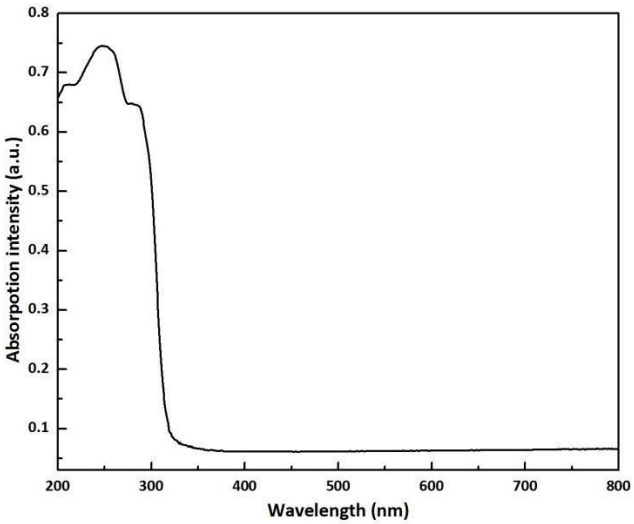

Figure 6.20 Solid state absorption spectrum of $[Gd(cpbOH)(H_2O)_2, (cpb)]_\infty$.

Highly luminescent compounds should present an important absorption cross-section; however, because of the insolubility of the compound in common solvents, molar absorption coefficients of these compounds could not be determined, which prevented us to estimate their luminescent efficiency ($f_{lum} \approx Q_{Ln}^{ligand} \times \varepsilon_\lambda$; f_{lum} is the luminescence efficiency, Q_{Ln}^{ligand} is the overall quantum yield and ε_λ is the molar absorption coefficient). Therefore, molar absorption coefficient of the deprotonated acid can be calculated from a series of dilute aqueous solution (Table 6.7) of the sodium salt (Figure 6.21).

Table 6.7 the absorbance of dilute aqueous solution of sodium salt of Hcpb acid.

Concentration (mol. L^{-1})	absorbance
8.10^{-4}	0.9385
6.10^{-4}	0.7342
$5.\ 10^{-4}$	0.6167
$4.\ 10^{-4}$	0.5356
$2.\ 10^{-4}$	0.2689
$1.\ 10^{-4}$	0.1714

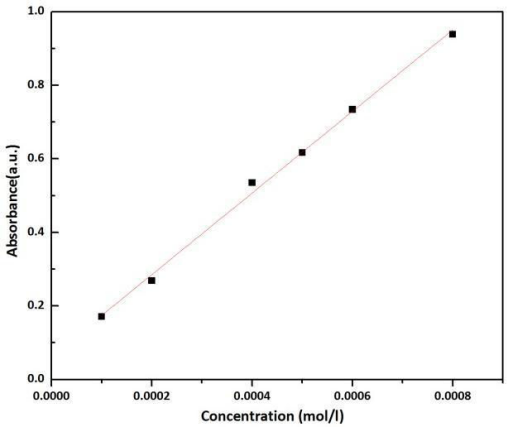

Figure 6.21 Absorbance versus concentration of dilute aqueous solutions of Nacpb, $0.5H_2O$.

The molar absorption coefficient of the deprotonated Hcpb acid was estimated: ε_{max}=1

100 L mol^{-1} cm^{-1}. This is quite low and can explain the moderate luminance (which will be showed in the following Figure 6.27) of these compounds.

6.8 Luminescent properties of the homo-nuclear compounds.

Before working on hetero-nuclear compounds, we firstly studied the luminescence properties of the homo-nuclear compounds $[Ln(cpbOH)(H_2O)_2, cpb)]_\infty$ (Ln=Sm, Eu, Tb, and Dy) that constitute Family 2. Therefore their solid-state excitation and emission spectra were recorded (Figure 6.22).

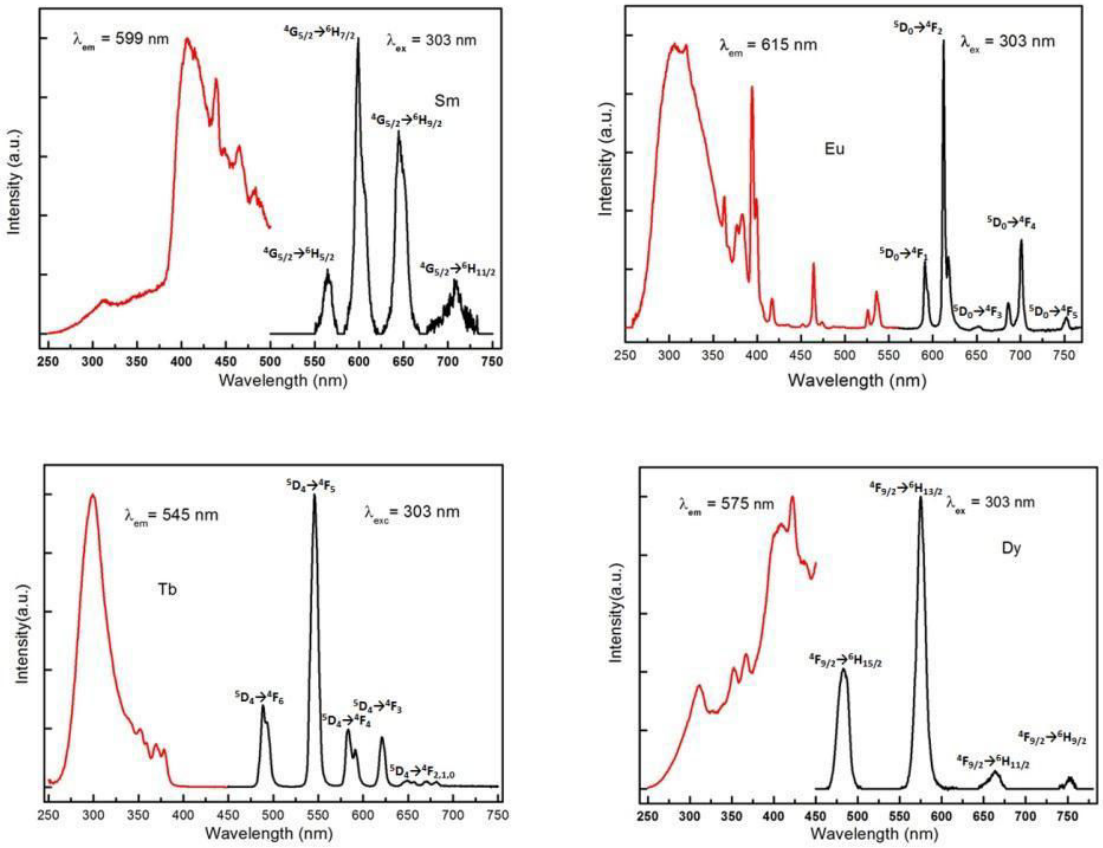

Figure 6.22 Excitation and emission spectra for $[Ln(cpbOH)(H_2O)_2, (cpb)]_\infty$ (Ln=Sm, Eu, Tb and Dy).

All the four spectra present a band centered at 303 nm. This confirms that for these four ions (Sm^{3+}, Eu^{3+}, Tb^{3+} and Dy^{3+}) the Hcpb ligand exhibits an antenna effect. However, it must be noticed that according to excitation spectra, this antenna effect is more efficient for the Tb- and Eu-based compounds.

Sm-containing microcrystalline powder exhibits four emission peaks at 560, 598, 641 and 708 nm which respectively correspond to the typical transitions: $^4G_{5/2}\rightarrow{}^6H_{5/2}$, $^4G_{5/2}\rightarrow{}^6H_{7/2}$, $^4G_{5/2}\rightarrow{}^6H_{9/2}$ and $^4G_{5/2}\rightarrow{}^6H_{11/2}$ under 303nm irradiation (Figure 6.23a). Transitions $^4G_{5/2}\rightarrow{}^6H_{7/2}$ and $^4G_{5/2}\rightarrow{}^6H_{9/2}$ at 598 and 641 nm respectively dominate the emission spectrum. Its overall quantum yield is 0.11% and the observed luminescent lifetime

is about 5.3 μs; its luminescent decay rate is mono-exponential (Figure 6.23b).

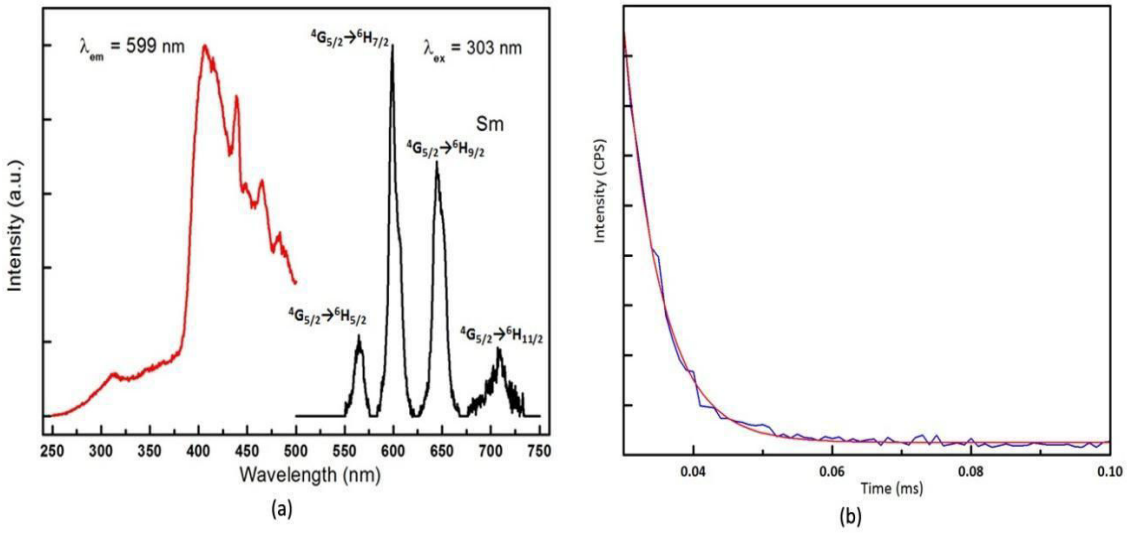

Figure 6.23 (a) Excitation and emission spectra and (b) luminescent decay for $[Sm(cpbOH)(H_2O)_2, (cpb)]_\infty$.

Eu-containing microcrystalline powder displays typical Eu^{3+} transitions: $^4D_0 \rightarrow {}^7F_1$, $^4D_0 \rightarrow {}^7F_2$, $^4D_0 \rightarrow {}^7F_3$, $^4D_0 \rightarrow {}^7F_4$ and $^4D_0 \rightarrow {}^7F_5$ at 591, 615, 651, 688 and 751 nm respectively and is dominated by the $^4D_0 \rightarrow {}^7F_2$ transition centered at 615nm under 303nm irradiation (6.24a). Its overall quantum yield is 6.0% and the observed luminescent lifetime is about 0.217 ms. Its luminescent decay rate is mono-exponential (Figure 6.24b).

Luminescence lifetime and intrinsic quantum yield have been measured for the Eu-based coordination polymer under an excitation wavelength that corresponds to a f-f transition that does not overlap with the absorption band of the ligand: 395 nm ($^7F_0 \rightarrow {}^5D_3$ transition for Eu^{3+}). Its intrinsic quantum yield (Q_{Ln}^{Ln}) is 7.1% and the observed lifetime under 395 nm irradiation is 0.214 ms.

Efficiency of the overall ligand-to-metal energy transfer (η_{sens}) is an important parameter. For lanthanide containing compounds it is defined as the efficiency with which energy is transferred from the feeding levels of the ligand to the lanthanide ion excited states:[6]

$$Q_{Ln}^{Ligand} = \eta_{sens} \times Q_{Ln}^{Ln} = \eta_{sens} \times \frac{\tau_{obs}}{\tau_{rad}}$$

For the Eu-containing compound, Q_{Ln}^{Ligand} is 6.0% and Q_{Ln}^{Ln} is 7.1%. Therefore, efficiency of the overall ligand-to-metal energy transfer (η_{sens}) is about 84.9%.

On the other hand, for Eu-containing compounds a simplified equation leads to the radiative lifetime:[7]

$$\frac{1}{\tau_{rad}} = A_{MD,0} \times n \times \left(\frac{I_{tot}}{I_{MD}}\right)$$

Where $A_{MD,0}$, a constant equal to 14.65 s^{-1}, is the spontaneous emission probability of the magnetic dipole $^5D_0 \rightarrow {}^7F_1$, n is the refractive index, I_{tot} is the integrated emission of the $^5D_0 \rightarrow {}^7F_J$ (J=0-6) transitions and I_{MD} is the integrated emission of the $^5D_0 \rightarrow {}^7F_1$ transition. Refractive index has been estimated to 1.50 on the basis of similar compounds (Table 6.8).

Table 6.8 Integrated emission of the $^5D_0 \rightarrow {}^7F_J$ (J=0-6) transitions and η_{sens}.

580	590	615	650	700	
576-580	581-604	604-635	645-661	681-710	
Int 0-0	Int 0-1	Int 0-2	Int 0-3	Int 0-4	Int_{tot}
1198.696	78520.12	276261.9	9274.271	152424.4	517679.3
0.02	1	3.52	0.12	1.94	

$1/\tau_{rad}$ (s^{-1})	τ_{rad}(ms)	τ_{obs} (ms)	Q_{Eu-Eu} (%)	Q_y (%)	η_{sens} (%)
325.98	3.068	0.22	7	6.01	85.1

With this assumption, $\boldsymbol{Q_{Ln}^{Ln} = 7.0(1)\%}$ and η_{sens} = 85.1 %.Both set of values (84.9% and 85.1%) are in perfect agreement and show that ligand-to-Eu energy transfer is efficient.

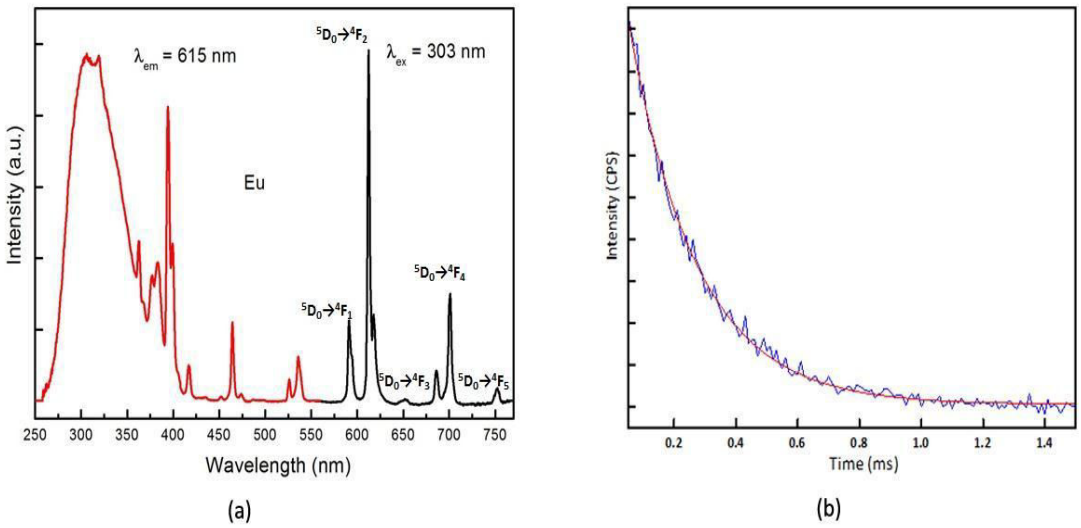

Figure 6.24 (a) Excitation and emission spectra and (b) luminescent decay for $[Eu(cpbOH)(H_2O)_2, (cpb)]_\infty$.

Microcrystalline powder of the Tb-containing compound presents seven emission peaks at 490, 545, 585, 621, 650, 665 and 678 nm which respectively correspond to the typical transitions: $^4D_4 \rightarrow {}^7F_6$, $^4D_4 \rightarrow {}^7F_5$, $^4D_4 \rightarrow {}^7F_4$, $^4D_4 \rightarrow {}^7F_3$, $^4D_4 \rightarrow {}^7F_2$, $^4D_4 \rightarrow {}^7F_1$ and $^4D_4 \rightarrow {}^7F_0$ under 303nm irradiation (Figure 6.25a). The dominating peak corresponds to the $^5D_4 \rightarrow {}^7F_5$ transition at 545 nm. Its overall quantum yield is 46% and the observed luminescent lifetime is about 0.843 ms. Its luminescent decay rate is also mono-exponential (Figure 6.25b). The

Tb-containing compound emits intense green light.

We also tried to estimate the efficiency of the ligand-to-Tb energy transfer. Unfortunately, this has not been possible because the previous relationship ($\frac{1}{\tau_{rad}} = A_{MD,0} \times n \times \left(\frac{I_{tot}}{I_{MD}}\right)$) is only valid for Eu^{3+}-based compounds and all usable f-f transition overlap with the absorption band of the ligand for the Tb-containing compound.

Nevertheless, these results indicate that ligand-to-metal energy transfer efficiency is not responsible of the significant difference between overall quantum yields that have been measured for both the Tb- and Eu-based compounds. This suggests that non radiative deactivation of the Eu^{3+} is important. This can be related to the presence of two coordination water molecules and one chelating $-B(OH)_3^-$ group per lanthanide ion. Indeed, it is known that the luminescence of Eu^{3+} ion is more sensitive to deactivation by O-H oscillators than that of Tb^{3+} ions.

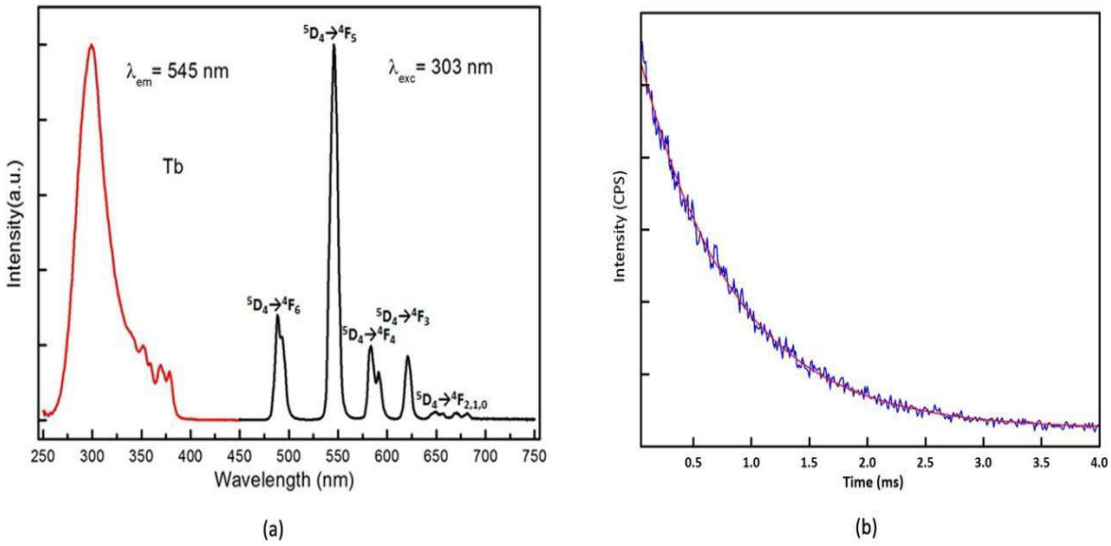

Figure 6.25 (a) Excitation and emission spectra and (b) luminescent decay for $[Tb(cpbOH)(H_2O)_2, (cpb)]_\infty$.

Microcrystalline powder of the Dy-containing compound exhibit four emission peaks at 478, 572, 660 and 750 nm which respectively correspond to the typical transitions: $^4F_{9/2} \rightarrow {}^6H_{15/2}$, $^4F_{9/2} \rightarrow {}^6H_{13/2}$, $^4F_{9/2} \rightarrow {}^6H_{11/2}$ and $^4F_{9/2} \rightarrow {}^6H_{9/2}$ under 343nm irradiation (Figure 6.26a). Overall quantum yield is 0.19% and the observed luminescent lifetime is about 1.9 µs; its luminescent decay rate is also mono-exponential (Figure 6.26b).

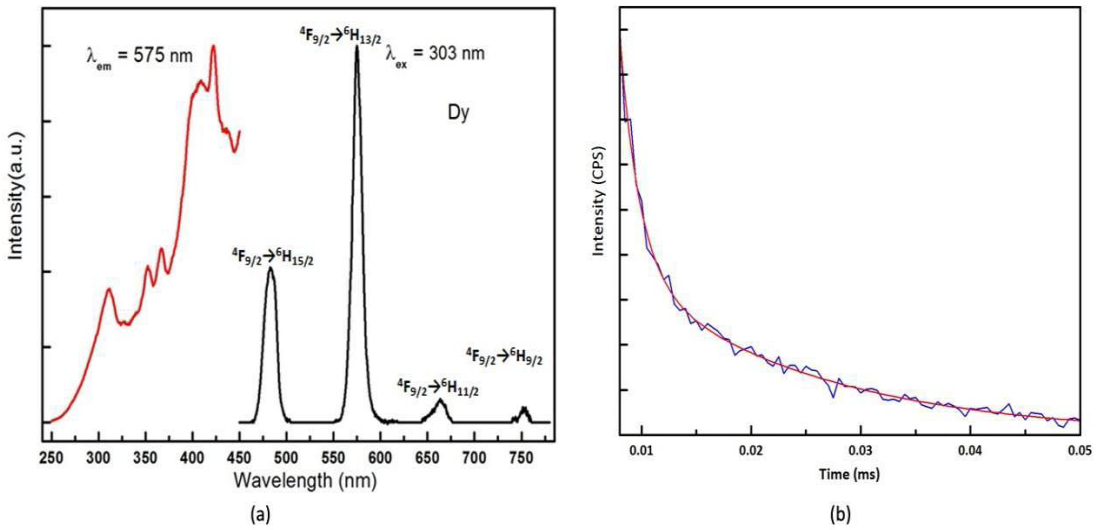

Figure 6.26 (a) Excitation and emission spectra and (b) luminescent decay for $[Dy(cpbOH)(H_2O)_2, (cpb)]_\infty$.

Luminance and colorimetric coordinates under UV irradiation (λ_{exc} = 312 nm) have also been measured for $[Ln(cpbOH)(H_2O)_2,(cpb)]_\infty$ (Ln= Sm, Eu, Gd, Tb and Dy) (Table 6.9 and Figure 6.28).

Table 6.9 Colorimetric coordinates and luminance for $[Ln(cpbOH)(H_2O)_2, (cpb)]_\infty$ (Ln= Sm, Eu, Gd, Tb and Dy) under 312 nm irradiation.

	Colorimetric coordinate		Luminance (Cdm^{-2})
	x	y	
Sm	0.32	0.24	0.51
Eu	0.57	0.32	2.43
Gd	0.29	0.36	4.2
Tb	0.35	0.57	50.65
Dy	0.29	0.21	0.71

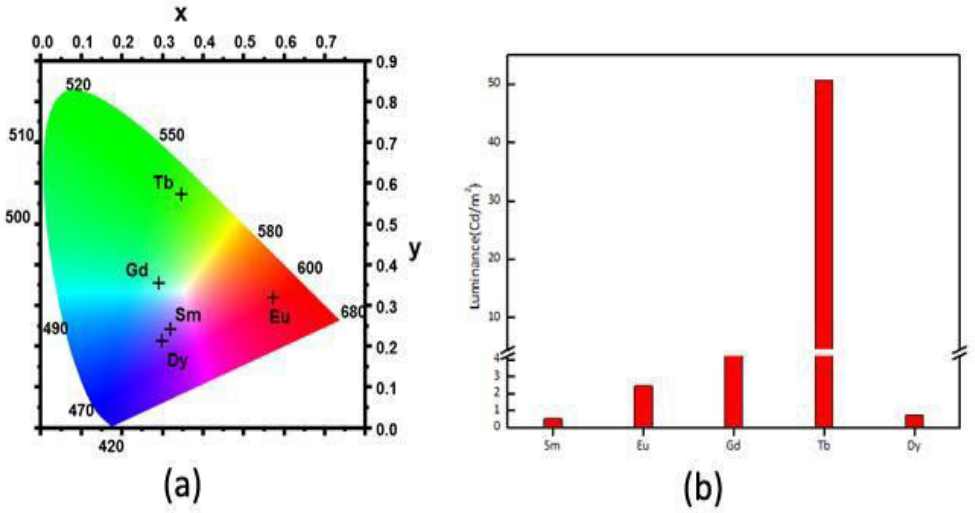

Figure 6.27 (a) colorimetric coordinates and (b) luminancefor $[Ln(cpbOH)(H_2O)_2, (cpb)]_\infty$ (Ln= Sm, Eu, Gd, Tb and Dy) under 312 nm irradiation.

From these results it can be first noticed that the luminance of the Tb- and Eu-based compounds are quite sizeable but lower than those measured for other coordination polymers that present comparable overall quantum yields. This can be explained by the lower value (1 100 $L.mol^{-1}.cm^{-1}$) of the molar absorption coefficient of the deprotonated ligand compared with other ligands.

Second, colorimetric coordinates of the Gd-, Sm- and Dy-based compounds present a quite strong blue component. Obviously this is related to the luminescence of the ligand because, Gd^{3+}-containing compounds cannot exhibits Gd^{3+}-induced luminescence under this excitation wavelength.

At last, the luminance of the Gd-based compound is unusually strong (even stronger than that of the Eu-containing compound). This suggests that the phosphorescence of the ligand could be used for obtaining the blue component that is often lacking for lanthanide-based coordination polymers.

Triplet state phosphorescence is known for being highly thermo-dependent. Therefore, in order to support our assumption, we have recorded emission spectra of the Gd-based compound versus temperature (Figure 6.28).

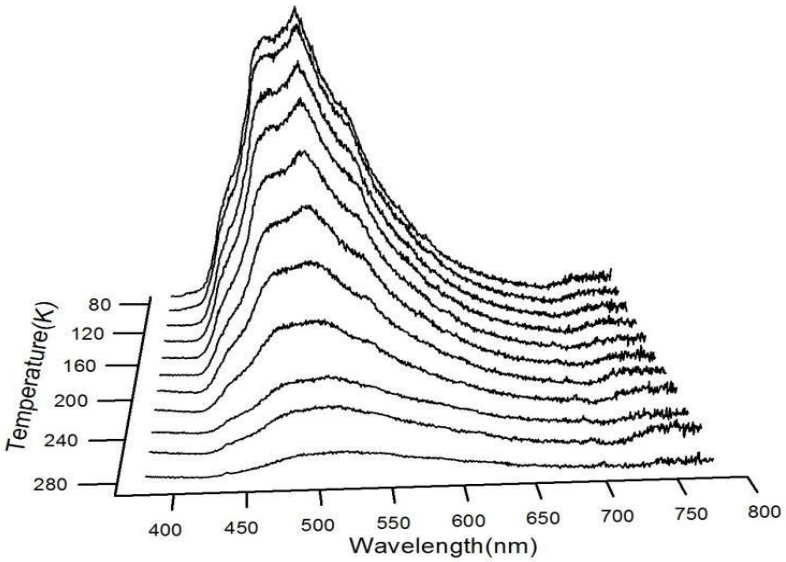

Figure 6.28 Emission spectra versus temperature under 303nm irradiation of $[Gd(cpbOH)(H_2O)_2, (cpb)]_\infty$.

As expected, the ligand phosphorescence drastically increases as the temperature is lowered. This could be of interest as far as potential applications are targeted. At the same time, the triplet state of cpb^- ligand was estimated on the basis of the shortest wavelength of the phosphorescent band of the emission spectrum of $[Gd(cpbOH)(H_2O)_2, (cpb)]_\infty$ at 77 K under 303 nm irradiation (400 nm ≈ 25000 cm^{-1}) (Figure 6.29).[8]

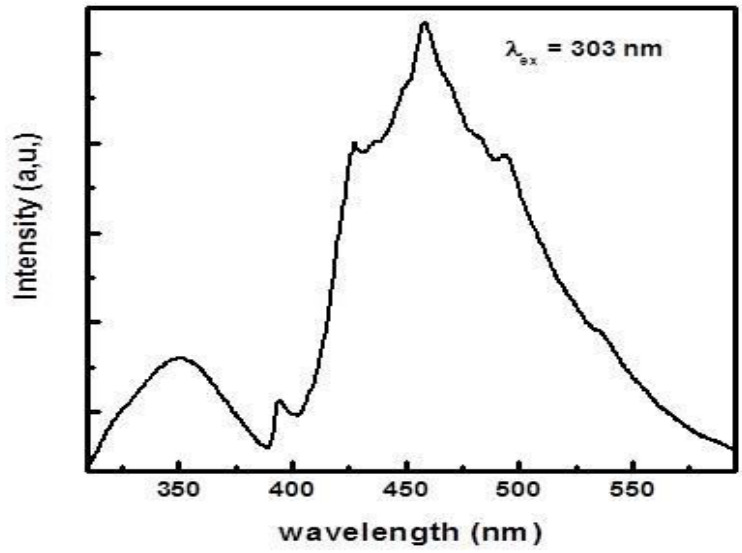

Figure 6.29 Emission spectrum of $[Gd(cpbOH)(H_2O)_2, (cpb)]_\infty$ at 77 K.

According to Reinhoudt's empirical rules,[9] the inter-system crossing is efficient when $\Delta E(^1\pi\pi^* \rightarrow {}^3\pi\pi^*)$ is greater than 5000 cm^{-1}. In this case, the singlet excited and triplet state of cpb^- ligand were respectively 30750 and 25000 cm^{-1}, so the energy gap $\Delta E(^1\pi\pi^* \rightarrow {}^3\pi\pi^*)$ is about 5750 cm^{-1}, which is favorable for an efficient intersystem crossing process. Moreover,

according to Latva's rules,[10] the lowest excited triplet (25000 cm^{-1}) state is supposed to favor efficient ligand to metal energy transfer without significant back-transfer for Eu^{3+} (17300cm^{-1}) and Tb^{3+} (20500cm^{-1}) containing compounds.

In order to evaluate the potential interest of the compounds that belong to this family of homo-nuclear coordination polymers, we have compared the variation of the luminescence versus temperature of the ligand and of the lanthanide ion for both the Tb- and Eu-containing compounds. Emission spectra and colorimetric coordinates versus temperature are reported for both compounds (Figure 6.30 and Figure 6.31).

These results reveal that the colorimetric coordinates vary over a large range with temperature. For Eu-containing compound, color changes from faint violet (at 80 K) to red (280K) and for Tb-containing compound; it changes from light blue (80 K) to green (280 K). These measurements also confirm that these homo-nuclear coordination polymers are of interest as far as molecular thermometers are targeted.

Actually, the luminescence of the cpb^- ligand and the one of the lanthanide ions (Tb^{3+} or Eu^{3+}) varies differently with the temperature. For each spectrum, contributions that can be attributed to both the ligand phosphorescence and the lanthanide ion (Tb^{3+} or Eu^{3+}) luminescence have been estimated and integrated (Figure 6.32 and Figure 6.33).

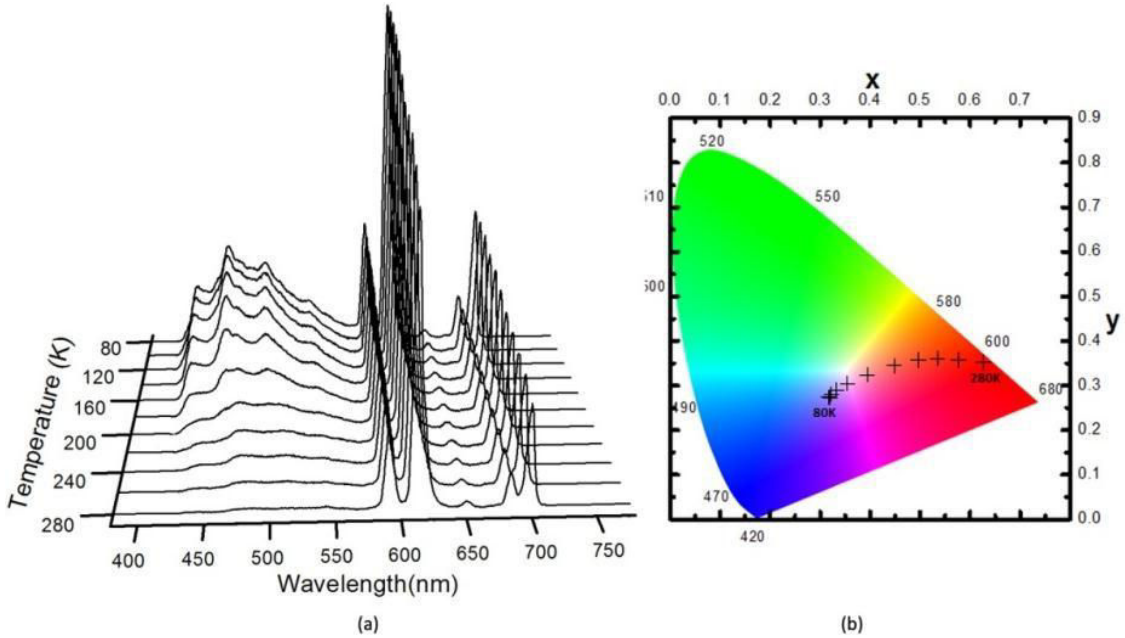

Figure 6.30 (a) Emission spectra versus temperature and (b) colorimetric coordinates under 303nm irradiation of $[Eu(cpbOH)(H_2O)_2, (cpb)]_\infty$.

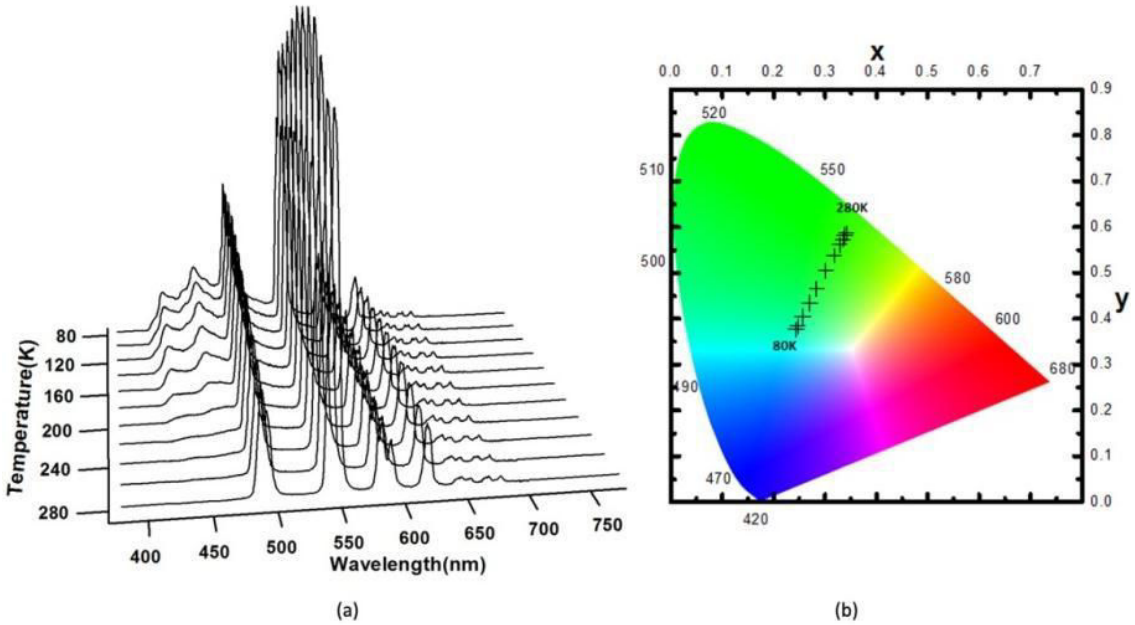

Figure 6.31 (a) Emission spectra versus temperature and (b) colorimetric coordinates under 303nm irradiation of [Tb(cpbOH)$(H_2O)_2$, (cpb)]$_\infty$.

Table 6.10 Colorimetric data versus temperature under 303nm irradiation for [Eu(cpbOH)$(H_2O)_2$, (cpb)]$_\infty$ and [Td(cpbOH)$(H_2O)_2$, (cpb)]$_\infty$.

Temperature (K)	[Eu(cpbOH)$(H_2O)_2$, (cpb)]$_\infty$		[Tb(cpbOH)$(H_2O)_2$, (cpb)]$_\infty$	
	x	y	x	y
80	0.32	0.27	0.24	0.38
100	0.32	0.28	0.25	0.38
120	0.32	0.28	0.26	0.4
140	0.33	0.29	0.27	0.43
160	0.35	0.31	0.28	0.47
180	0.39	0.32	0.3	0.51
200	0.45	0.34	0.32	0.54
220	0.5	0.36	0.33	0.56
240	0.53	0.36	0.34	0.57
260	0.58	0.36	0.34	0.58
280	0.63	0.35	0.34	0.59

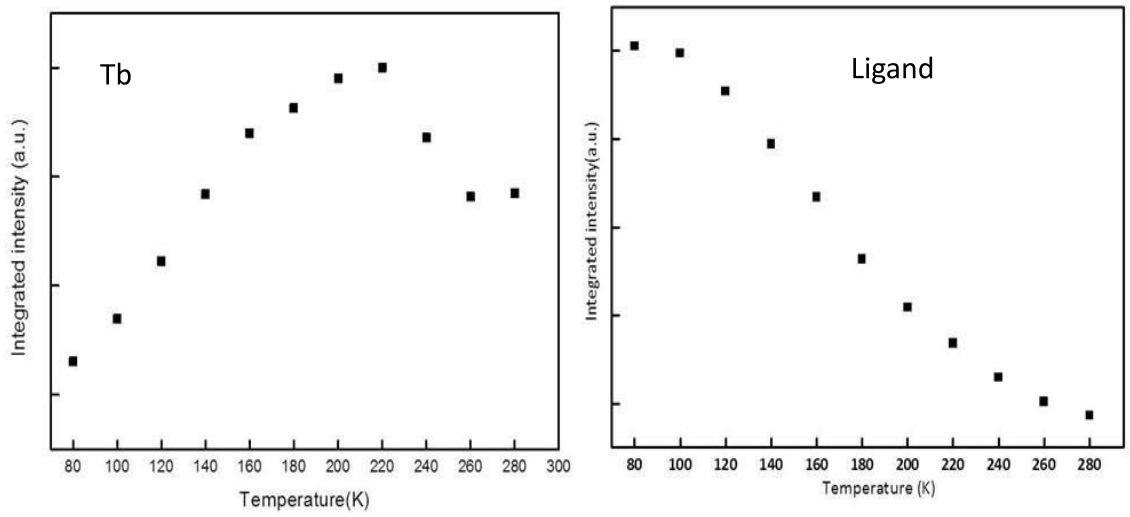

Figure 6.32 Integrated intensities of the emission spectra of $[Tb(cpbOH)(H_2O)_2, (cpb)]_\infty$, Contributions of Tb^{3+} ion (left) and of the ligand (right) are integrated separately

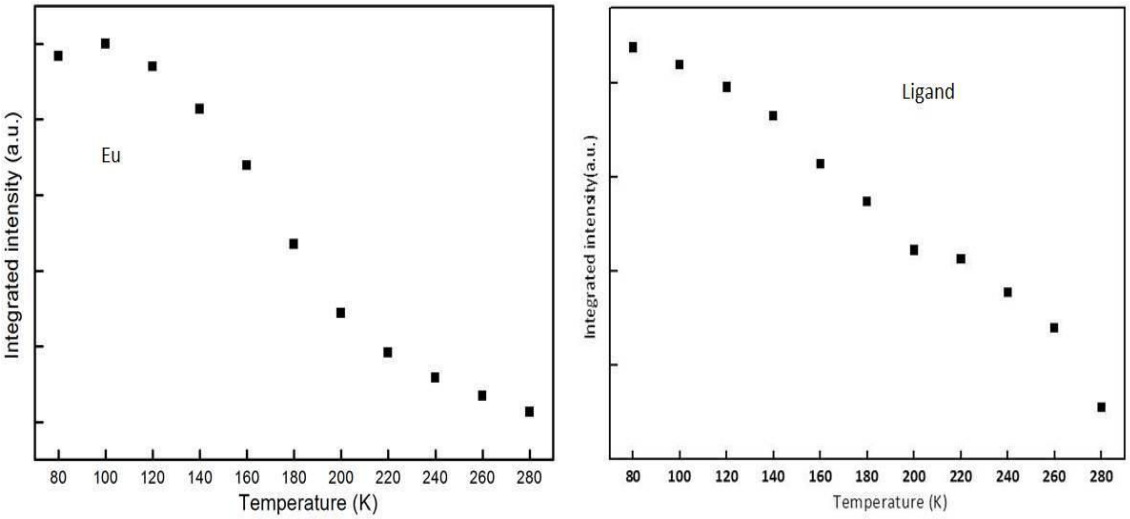

Figure 6.33 Integrated intensities of the emission spectra of $[Eu(cpbOH)(H_2O)_2, (cpb)]_\infty$. Contributions of Eu^{3+} ion (left) and of the ligand (right) are integrated separately.

Overall, all the intensities decrease as the temperature increases because of the thermal activation of non-radiative pathways. However, decreasing is not linear because they result in the combination of different mechanisms with different thermal behaviors (ligand de-activation, ligand-to-metal energy transfer, metal deactivation…). In order to compare the potential efficiency of these compounds as molecular thermometer with already reported compounds a parameter Δ that has been defined elsewhere has been calculated:[11]

$$\Delta = I_{Ln}/I_{Ligand}$$

where I_{Ln} is the integrated intensity of the contribution of the lanthanide ion to the emission spectrum and I_{Ligand} is the integrated intensity of the contribution of the ligand to the emission spectrum. It is noticeable that this parameter is independent of the emission scale

and can be used for designing molecular thermometers that need no calibration (Table 6.11 and Figure 6.34).

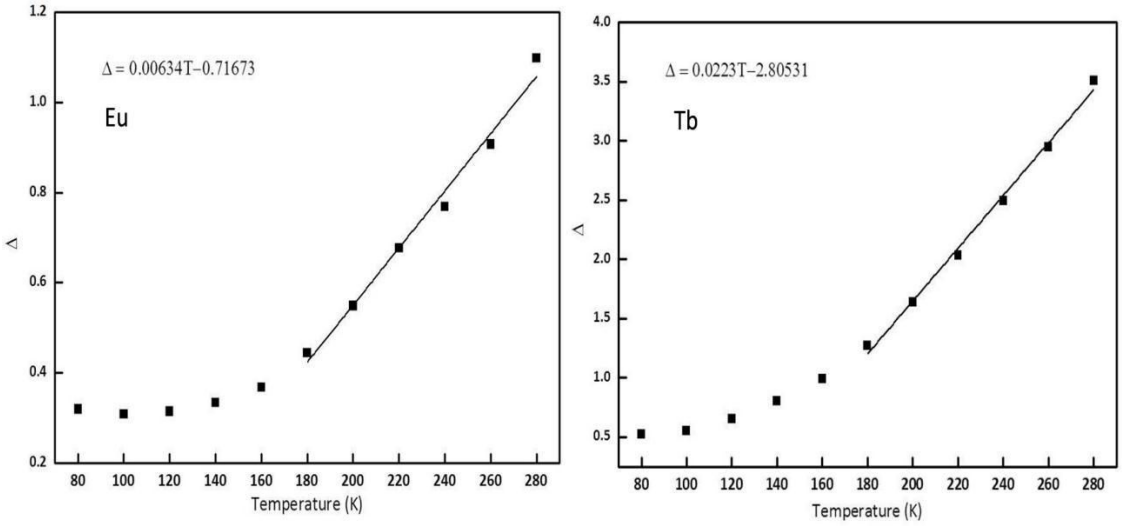

Figure 6.34 parameter Δ versus T for $[Eu(cpbOH)(H_2O)_2, (cpb)]_\infty$ and $[Tb(cpbOH)(H_2O)_2, (cpb)]_\infty$.

These results demonstrate that temperature can be correlated with the empirical parameter Δ between 200K and 300K for both compounds. However, the Tb-based compound constitutes a much more sensitive thermometer (≈ 2.4%) than the Eu-based one (≈0.7%). This value is quite sizeable and can be compared with the best ones reported so far (3.5%).

Table 6.11 Integrated intensities of the emission spectra and parameter Δ versus T for $[Eu(cpbOH)(H_2O)_2, (cpb)]_\infty$ and $[Tb(cpbOH)(H_2O)_2, (cpb)]_\infty$.

Temperature(K)	int. Tb	int. ligand	Δ(Tb/L)	int. Eu	int. ligand	Δ(Eu/L)
80	1.32E+07	2.53E+07	0.52136	1.54E+07	4.82E+07	0.31922
100	1.38E+07	2.49E+07	0.5546	1.52E+07	4.92E+07	0.3086
120	1.48E+07	2.27E+07	0.65155	1.50E+07	4.76E+07	0.31443
140	1.58E+07	1.97E+07	0.80223	1.47E+07	4.38E+07	0.33423
160	1.66E+07	1.67E+07	0.9933	1.41E+07	3.84E+07	0.36803
180	1.68E+07	1.32E+07	1.2732	1.37E+07	3.09E+07	0.44434
200	1.71E+07	1.05E+07	1.63721	1.32E+07	2.41E+07	0.54895
220	1.72E+07	8.42E+06	2.03761	1.31E+07	1.94E+07	0.67735
240	1.62E+07	6.47E+06	2.49872	1.28E+07	1.66E+07	0.7692
260	1.51E+07	5.11E+06	2.95012	1.24E+07	1.37E+07	0.90746
280	1.51E+07	4.31E+06	3.51184	1.15E+07	1.05E+07	1.09812

6.9 Luminescent properties of the hetero-nuclear compounds.

6.9.1 $[Gd_{1-x}Tb_x(cpbOH)(H_2O)_2, (cpb)]_\infty$ $(0 \leq x \leq 1)$.

According to the crystal structure, lanthanides ions are close enough from each other (≤ 10Å) to give rise to intermetallic quenching. The hetero-metallic coordination polymers that involve Tb^{3+} ion (luminescent lanthanide ion) and Gd^{3+} ion (optically non-active lanthanide ion) as optical dilutors were synthesized.

Solid state emission spectra and luminescence intensities of the Gd/Tb hetero-nuclear compounds were recorded (Figure 6.35). The emission spectra of compounds $[Gd_{1-x}Tb_x(cpbOH)(H_2O)_2, (cpb)]_\infty$ show that the luminescent properties of the compounds do not depend on the content of optically non-active lanthanide ions (Gd^{3+}) .Colorimetric coordinates of these hetero-nuclear compounds are almost identical as well (Table 6.12 and Figure 6.36). Because lanthanide ions are randomly distributed over the metallic sites of the crystal structure, the addition of an optically non-active lanthanide ion provokes an increase in the mean distance between the luminescent ions without perturbing the crystal structure.

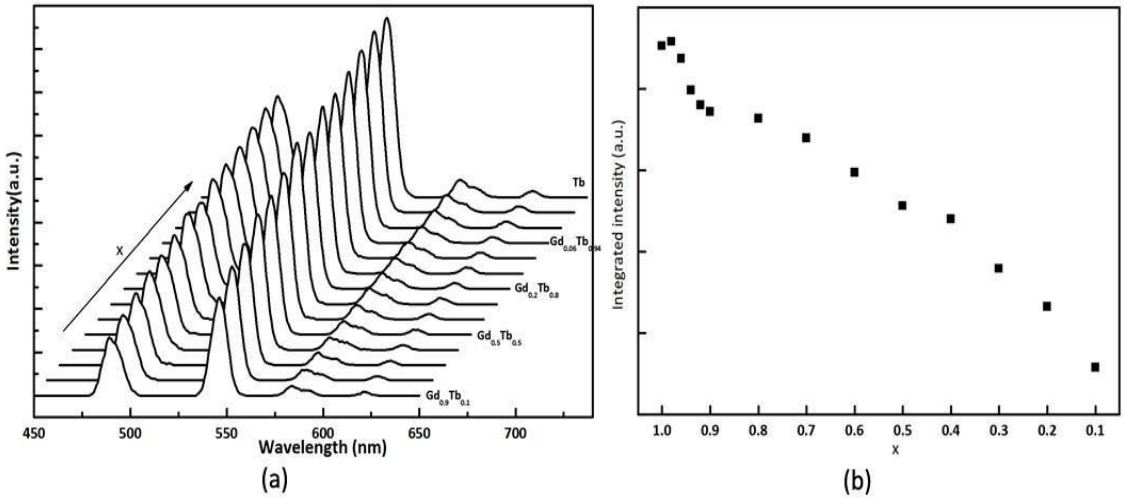

Figure 6.35 Emission spectra under 303 nm irradiation and Integrated intensity of the Eu-based of $[Gd_{1-x}Tb_x(cpbOH)(H_2O)_2, cpb)]_\infty$ with $0 \leq x \leq 1$.

Table 6.12 Colorimetric coordinates for $[Gd_{1-x}Tb_x(cpbOH)(H_2O)_2, (cpb)]_\infty$ $(0.1 \leq x \leq 1)$ under 303 nm irradiation.

x	Colorimetric coordinates	
	x	y
1	0.26	0.55
0.98	0.26	0.55
0.96	0.26	0.55
0.94	0.26	0.55
0.92	0.26	0.55
0.9	0.26	0.55
0.8	0.26	0.55
0.7	0.26	0.55
0.6	0.26	0.55
0.5	0.26	0.55
0.4	0.26	0.55
0.3	0.26	0.55
0.2	0.26	0.55
0.1	0.26	0.55

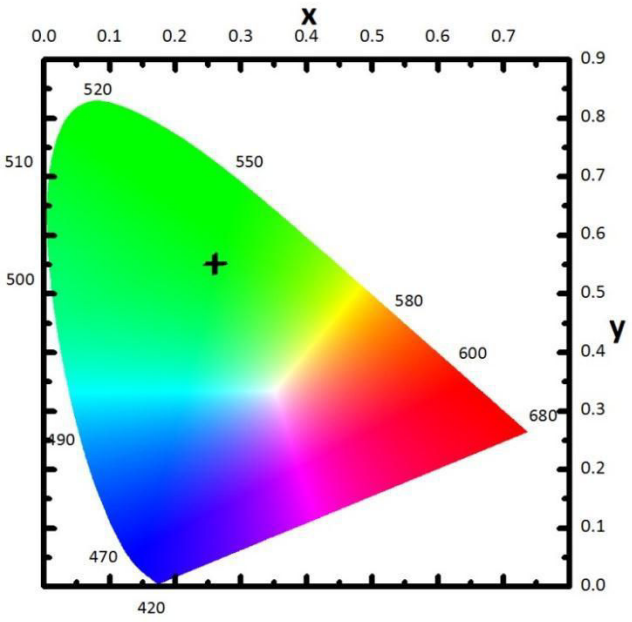

Figure 6.36 Colorimetric coordinates for $[Gd_{1-x}Tb_x(cpbOH)(H_2O)_2, (cpb)]_\infty$ under 303 nm .

However, these compounds exhibit different luminance (Figure 6.37). The dilution resulted in a decreasing in luminance until a value that is comparable to that of the pure Tb-containing compound. When $0.7 \leq x \leq 0.98$, the luminance changed a little, and the dilution can be considered beneficially, and when the $x \geq 0.6$, the effect was detrimental. It must be noticed that these results are in good agreement with relative values that have

been obtained by integrating the peak centered at 545 nm in the emission spectra (Figure 6.35b).

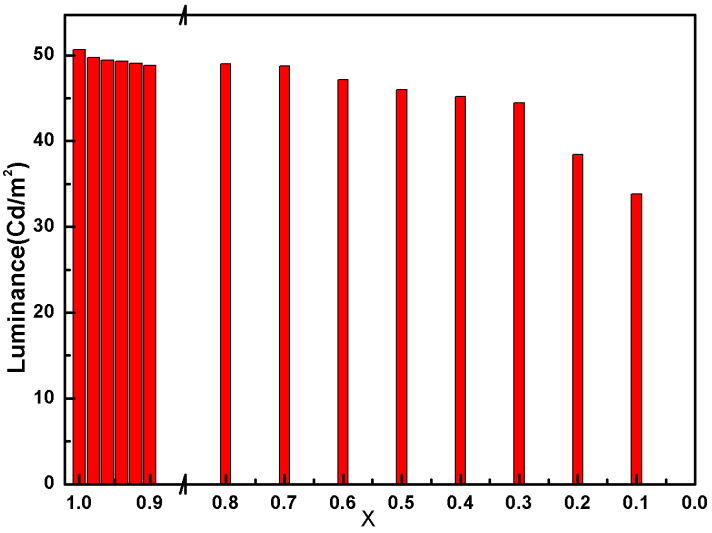

Figure 6.37 Luminance versus x for $[Gd_{1-x}Tb_x(cpbOH)(H_2O)_2, (cpb)]_\infty$ (λ_{ex}=312 nm).

These results confirm that some intermetallic quenching exists between optically active lanthanide ions. The observed variations in luminescence intensity can be related to the crystal structure. Indeed, it is commonly admitted that dipole-dipole intermetallic energy transfer is less efficient if the metallic ions are more than 10 Å apart from each other. In the present case, a specific lanthanide ion is surrounded by eight other metal ions in a sphere with approximately 10Å radius (Figure 6.38) and the mean distance between the lanthanide ions was estimated as twice the radius of the sphere that has the same volume than the mean volume occupied by a lanthanide ion. In this crystal structure, the mean volume is roughly $\tilde{v}$ = 224.23 $Å^3$ per metallic ion. It corresponds to the volume of a sphere with a radius of 3.8 Å ($r = (3\,\tilde{v}/4\pi)^{1/3}$). With this rather rough model, the mean distance between two lanthanide ions is 7.6 Å. Therefore, a given optically active lanthanide ion is statistically surrounded by eight optically non-active lanthanide ion if x is greater than 1/9 (x≈0.1) and by eight optically active lanthanide ions if x is smaller than 8/9 (x≈0.9). In fact, the shortest distance in the crystal structure is about 4.3 Å, the optically non-active lanthanide ions can easily change the distance between Tb^{3+} ions and so the intermetallic quenching effect.

This suggests that, as far as Eu^{3+} or Tb^{3+} are concerned; the most relevant parameter for intermetallic deactivation is not the mean distance between optically active lanthanide ions but the absence or presence of another optically active lanthanide ion in the neighborhood. This is agreement with what has already been published previously.[12]

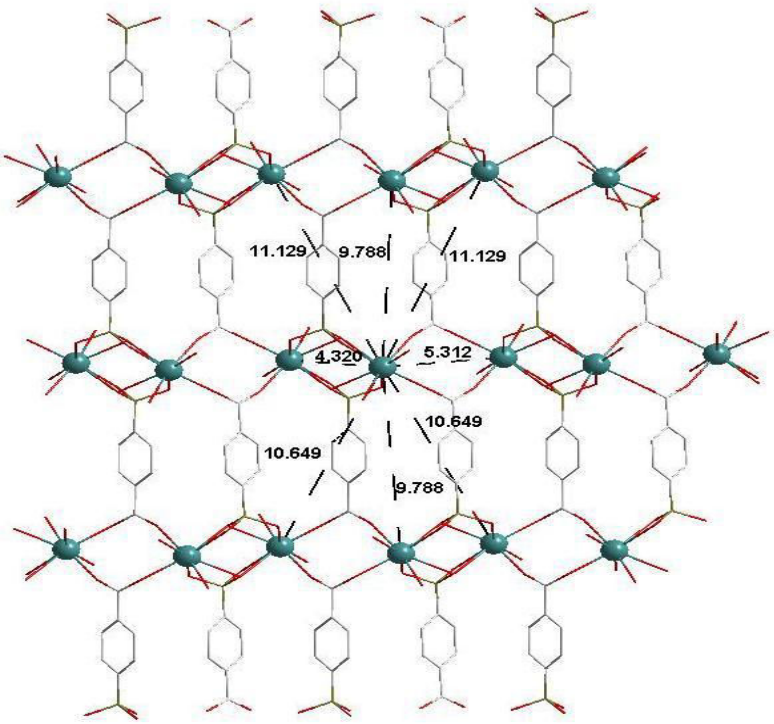

Figure 6.38 Shortest intermetallic distances in $[Tb(cpbOH)(H_2O)_2, (cpb)]_\infty$.

Overall quantum yields of six samples with general chemical formula $[Gd_{1-x}Tb_x(cpbOH)(H_2O)_2, (cpb)]_\infty$ were measured to ensure the conclusion. When x is greater than 0.9, the overall quantum yields are almost not changed (Table 6.12).

Table 6.12 The overall quantum yields of compounds $[Gd_{1-x}Tb_x(cpbOH)(H_2O)_2, (cpb)]_\infty$.

Sample	Q_y
Tb	46(3)
$Gd_{0.02}Tb_{0.98}$	45(5)
$Gd_{0.04}Tb_{0.96}$	45(5)
$Gd_{0.06}Tb_{0.94}$	45
$Gd_{0.08}Tb_{0.92}$	45
$Gd_{0.5}Tb_{0.5}$	42(4)

6.9.2 $[Eu_{1-x}Tb_x(cpbOH)(H_2O)_2, (cpb)]_\infty$ ($0 \leqslant x \leqslant 1$).

In order to estimate the tunable character of the luminescent properties of the hetero-nuclear compounds, compounds with general chemical formula $[Eu_{1-x}Tb_x(cpbOH)(H_2O)_2, (cpb)]_\infty$ ($0 \leq x \leq 1$) were synthesized. Their emission spectra, luminance intensities and colorimetric coordinates were recorded under 303 nm irradiation (Figure 6.39 and Figure 6.40).

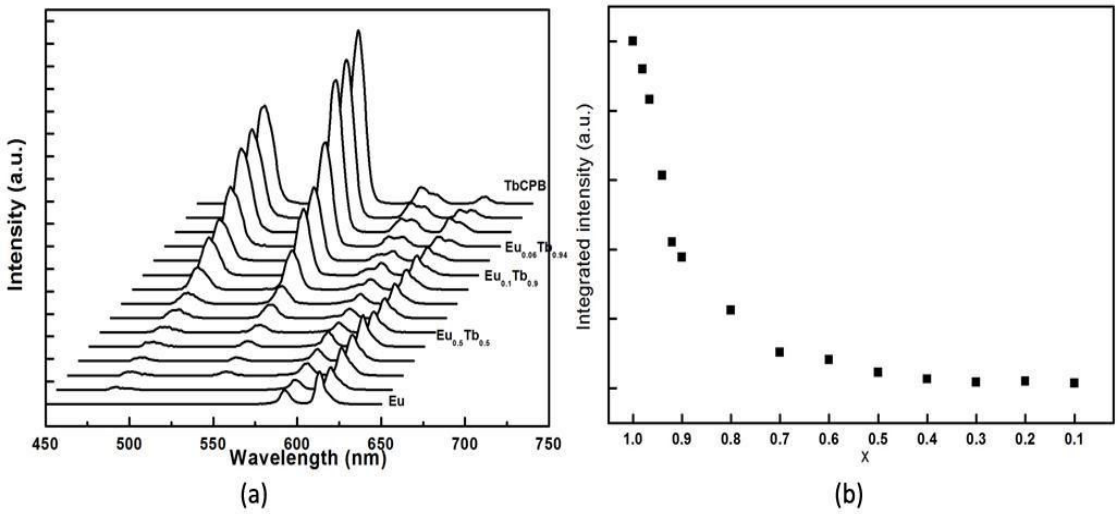

Figure 6.39 Emission spectra under 303 nm irradiation and integrated intensity of the Tb^{3+} component for $[Eu_{1-x}Tb_x(cpbOH)(H_2O)_2, (cpb)]_\infty$ ($0 \le x \le 1$).

Table 6.13 Colorimetric data for compounds $[Eu_{1-x}Tb_x(cpbOH)(H_2O)_2, (cpb)]_\infty$ ($0.1 \leqslant x \leqslant 1$) under 303 nm irradiation.

x	Colorimetric coordinates	
	x	y
1	0.26	0.55
0.98	0.28	0.55
0.96	0.29	0.54
0.94	0.29	0.54
0.92	0.31	0.53
0.9	0.34	0.51
0.8	0.38	0.49
0.7	0.45	0.45
0.6	0.47	0.43
0.5	0.52	0.4
0.4	0.58	0.36
0.3	0.6	0.35
0.2	0.6	0.36
0.1	0.63	0.33
0	0.64	0.34

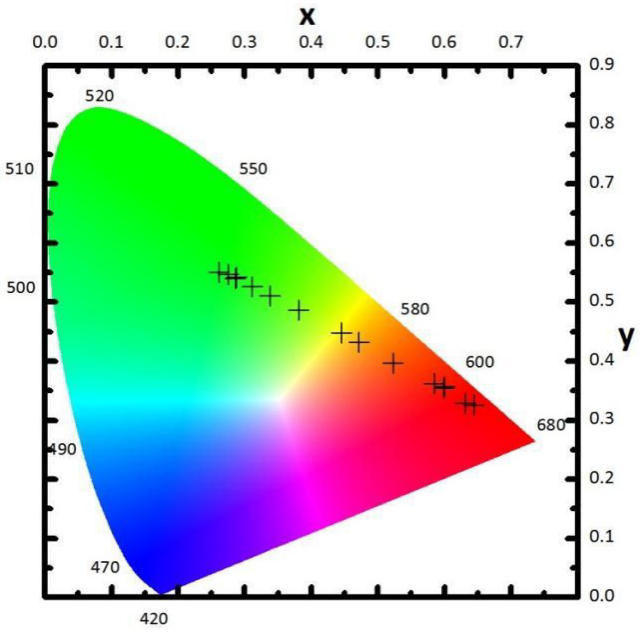

Figure 6.40 Colorimetric coordinates for $[Eu_{1-x}Tb_x(cpbOH)(H_2O)_2, (cpb)]_\infty$ under 303 nm.

Emission spectra and colorimetric coordinates reveal a nonlinear evolution of the colorimetric and spectroscopic properties of these compounds versus the Tb/Eu ratio (Table 6.13). However, the colorimetric coordinated of these series of compounds are localized on a straight line extending from the coordinates of the Eu-containing homo-nuclear compound to the coordinates of the Tb-containing one. Integrated intensities of one out of the two lanthanide ions component in the emission spectra versus x are plotted. Theses integrated intensities were estimated by integration of an emission peak that does not overlap with any peak of the other lanthanide ion and assuming that all compounds are iso-structural that is all peaks of the considered lanthanide ion in the emission spectra present identical relative intensities. Tb^{3+} $^5D_4 \rightarrow {}^7F_5$ transition (545nm) was chosen. Integrated intensities present the same variation than that of the luminance intensity measured under 312nm irradiation (Figure 6.41).

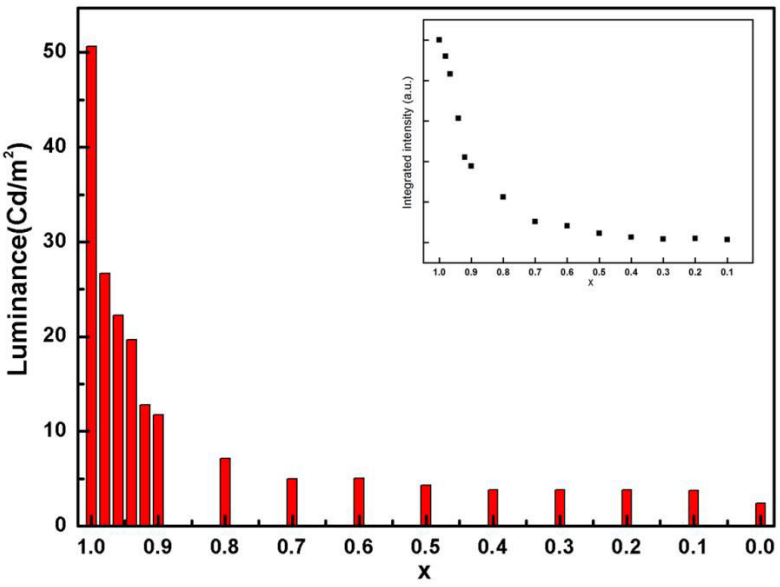

Figure 6.41 luminance data for $[Eu_{1-x}Tb_x(cpbOH)(H_2O)_2, (cpb)]_\infty$ with λ_{ex}=312nm.

We also took pictures of these compounds and measured their colorimetric coordinates under 312nm irradiations (Table 6.14, Figure 6.42 and Figure 6.43).

Table 6.14 Colorimetric data for compounds $[Eu_{1-x}Tb_x(cpbOH)(H_2O)_2, (cpb)]_\infty$ ($0.1 \leqslant x \leqslant 1$) under 312 nm irradiation.

x	colorimetric coordinates	
	x	y
1	0.35	0.57
0.98	0.35	0.57
0.96	0.37	0.54
0.94	0.38	0.52
0.92	0.42	0.48
0.9	0.45	0.45
0.8	0.47	0.4
0.7	0.51	0.37
0.6	0.53	0.35
0.5	0.55	0.34
0.4	0.56	0.33
0.3	0.56	0.33
0.2	0.56	0.32
0.1	0.56	0.32
0	0.57	0.32

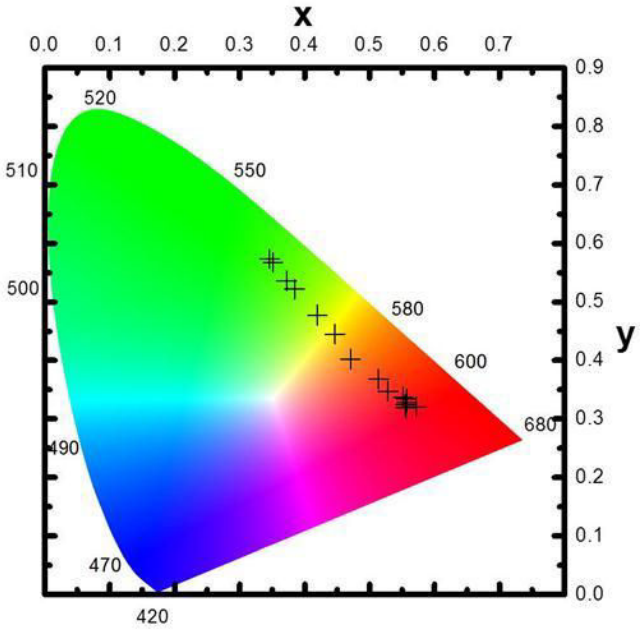

Figure 6.42 Colorimetric coordinates for $[Eu_{1-x}Tb_x(cpbOH)(H_2O)_2, (cpb)]_\infty$ under 312nm.

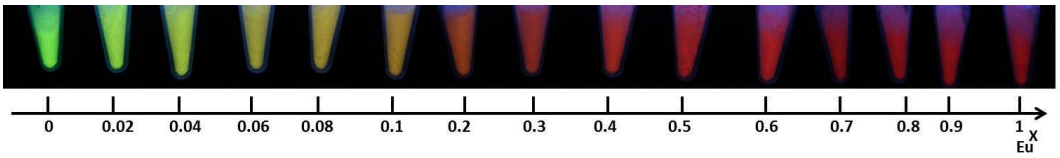

Figure 6.43 Pictures of compound $[Eu_{1-x}Tb_x(cpbOH)(H_2O)_2, (cpb)]_\infty$ under 312 nm irradiation.

To study the intermetallic energy transfer, quantum yields and luminescent lifetimes of $[Eu_{0.5}Tb_{0.5}(cpbOH)(H_2O)_2, (cpb)]_\infty$ and $[Gd_{0.5}Tb_{0.5}(cpbOH)(H_2O)_2, (cpb)]_\infty$ were measured under 303 nm (Table 6.15 and Figure 6.44). Intrinsic quantum yields of Eu^{3+} ion were also measured under 395nm (Figure 6.44c).

Table 6.15 Quantum yields and luminescent lifetimes obtained under 303 nm or 395nm for $[Eu_{0.5}Tb_{0.5}(cpbOH)(H_2O)_2, (cpb)]_\infty$ and $[Gd_{0.5}Tb_{0.5}(cpbOH)(H_2O)_2, (cpb)]_\infty$.

	Q_L^{Tb}	τ_{obs}	Q_L^{Eu}	τ_{obs}	Q_{Eu}^{Eu}	τ_{obs}
$[Eu_{0.5}Tb_{0.5}(cpbOH)(H_2O)_2, (cpb)]_\infty$	0.51	0.36	6(3)	0.22	21(4)	0.21
$[Gd_{0.5}Tb_{0.5}(cpbOH)(H_2O)_2, (cpb)]_\infty$	42	0.82	-	-	-	-

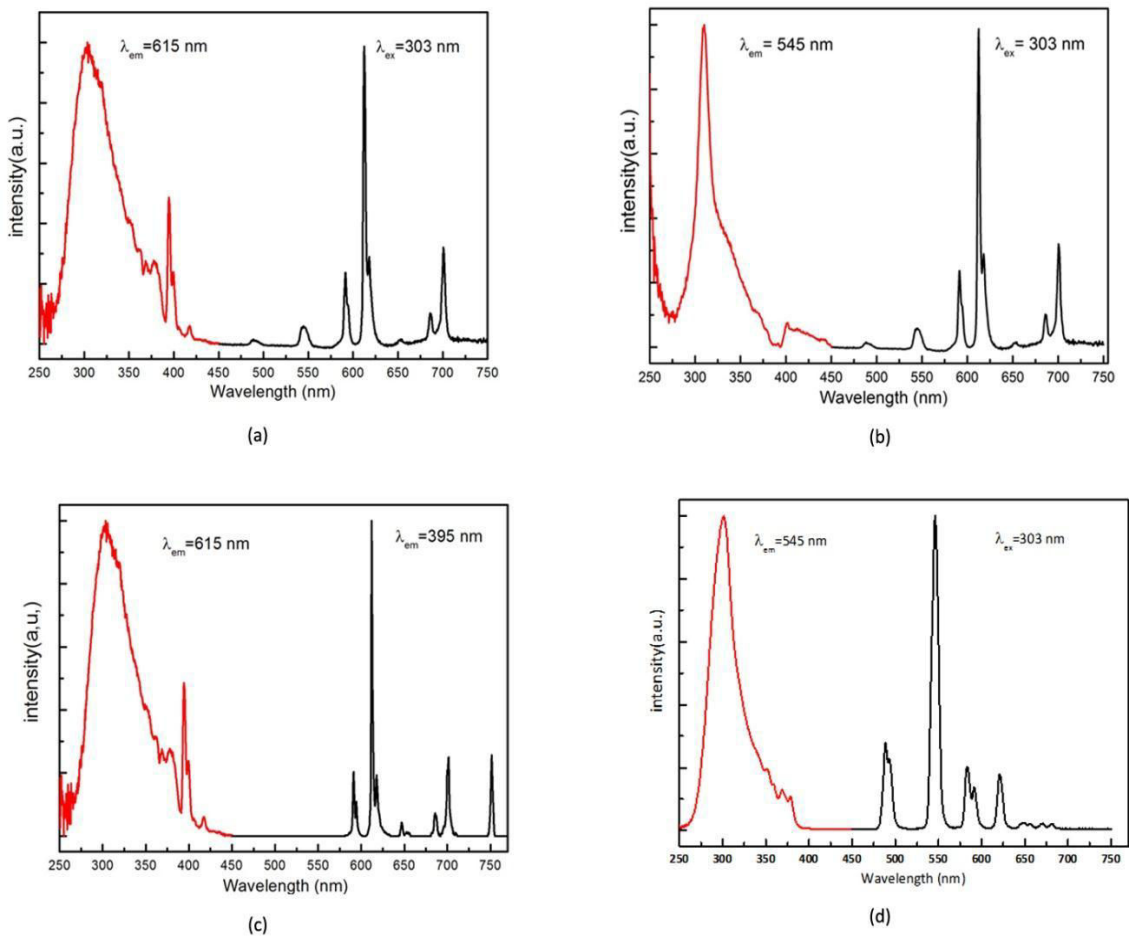

Figure 6.44 (a) emission and excitation spectra of $[Eu_{0.5}Tb_{0.5}(cpbOH)(H_2O)_2, (cpb)]_\infty$ with λ_{ex} = 303nm and λ_{em} = 615nm. (b) emission and excitation spectra of $[Eu_{0.5}Tb_{0.5}(cpbOH)(H_2O)_2, (cpb)]_\infty$ with λ_{ex} = 303 nm and λ_{em} =545 nm. (c) emission and excitation spectra of $[Eu_{0.5}Tb_{0.5}(cpbOH)(H_2O)_2, (cpb)]_\infty$ with λ_{ex}=395 nm and λ_{em}=615nm. (d) emission and excitation spectra of $[Gd_{0.5}Tb_{0.5}(cpbOH)(H_2O)_2, (cpb)]_\infty$ with λ_{ex}=303 nm and λ_{em}=545 nm.

Under direct excitation of the Eu^{3+} ion (λ_{ex}= 395nm which corresponds to $^7F_0 \rightarrow {}^5D_3$ transition)., no Tb^{3+} transition is observed Intrinsic quantum yield of Eu^{3+} ion can be estimated to 21(4)%. In $[Eu_{0.5}Tb_{0.5}(cpbOH)(H_2O)_2 \cdot (cpb)]_\infty$ the efficiency of the ligand-to-Eu energy transfer was about 21.4%.

The intermetallic energy transfer can be calculated using the relationship:[13]

$$\eta_{et} = 1 - \frac{\tau_{obs}}{\tau_o}$$

Where τ_{obs} and τ_o are respectively the lifetime in the presence and in the absence of an acceptor. Since Gd^{3+} ion has its first excited state above the excitation it cannot act as an acceptor, in this case τ_{obs} is about 0.362 ms and τ_o is about 0.82 ms. The intermetallic energy transfer is about 56%. The different energy migration process in the compound $[Eu_{0.5}Tb_{0.5}(cpbOH)(H_2O)_2 \cdot (cpb)]_\infty$ can be simply demonstrated (Figure 6.45).

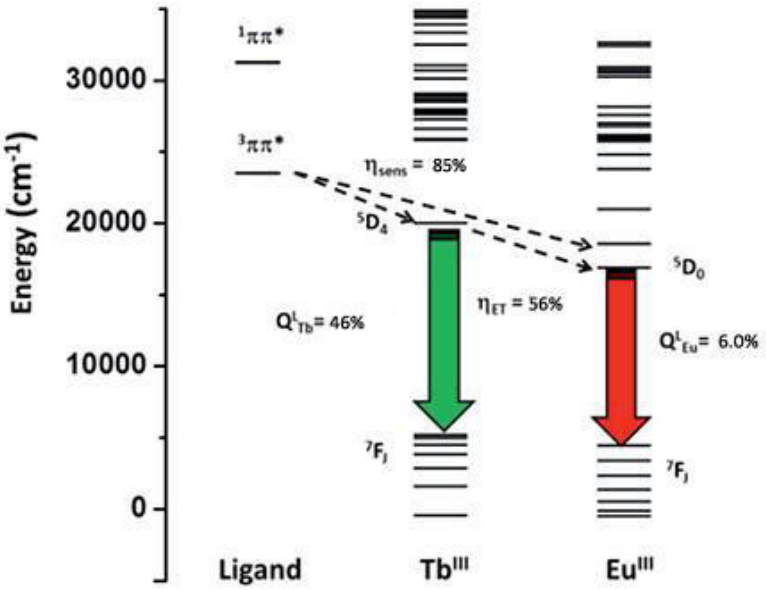

Figure 6.45 Mechanism of energy transfer and luminescence sensitization in $[Eu_{0.5}Tb_{0.5}(cpbOH)(H_2O)_2, (cpb)]_\infty$.

6.10 Magnetic Properties of homonuclear $[Ln(cpbOH)(H_2O)_2,(cpb)]_\infty$ (Ln=Dy or Yb).

Ac and dc magnetic measurements have been performed in order to evaluate the capability of some derivatives of the family to behave as Single Molecule Magnets (SMMs). SMMs are molecules that behave as magnets but with a magnetic bi-stability that as a molecular origin.[14] Given the square antiprism coordination environment of the lanthanide ion in the reported family, the Dy^{3+}- and Yb^{3+}-based compounds are the derivatives that most likely can present SMM properties.[15]

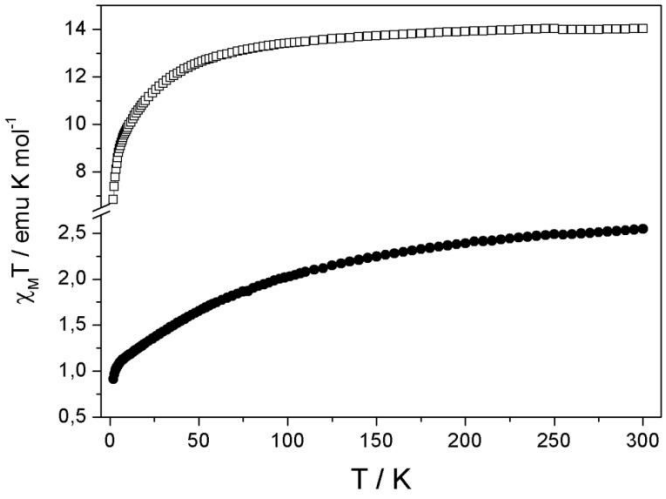

Figure 6.46: Temperature dependence of $\chi_M T$ for the Dy^{3+} (squares) and Yb^{3+} derivatives (dots).

$\chi_M T$ vs T curves have been measured through dc magnetometry (Figure 6.46) on both

derivatives and room temperature value of $\chi_M T$ of 14.07 and 2.54 cm^3 K mol^{-1} are observed for Dy^{III} and Yb^{III} derivatives respectively. This is in agreement with what is expected for the corresponding isolated ions (Dy^{III} : J=15/2, and g_j= 4/3 ; Yb^{III} : J=7/2 and g_j= 8/7).[16] On lowering T, $\chi_M T$ values decrease as a consequence of the progressive depopulation of the M_J sublevels (Figures 6.47). Evaluation of the coupling between the anisotropic lanthanides ions is complicated by this temperature dependence of the M_J population that induce thermal variation of several order of magnitude higher than the coupling itself. Moreover in our case, two interaction pathways have to be considered: one through the carboxylic moiety (O7-C7-O6) that bridges two Ln^{3+} ions and another one through the three OH^- moieties (O1A, O3A) at the other extremity of the ligand. Consequently, tentative fits of the $\chi_M T$ *vs* *T* curves considering two magnetic interactions (J1, J2) at low temperature provide senseless values, letting us suspect that these interactions are extremely small.

Ac magnetic measurements have been performed on both derivatives (Figures 6.47) to estimate their capabilities to behave as SMMs. In absence of dc field, no χ_M" signals have been detected and zero-field fast tunneling (quantum tunneling) is suspected to hampers magnetic slow relaxation has commonly seen on similar compounds (Appendix II).[17] However as a small dc field is applied to remove degeneracy of M_J sublevels, clear χ_M" signal is observed (Figure 6.48).

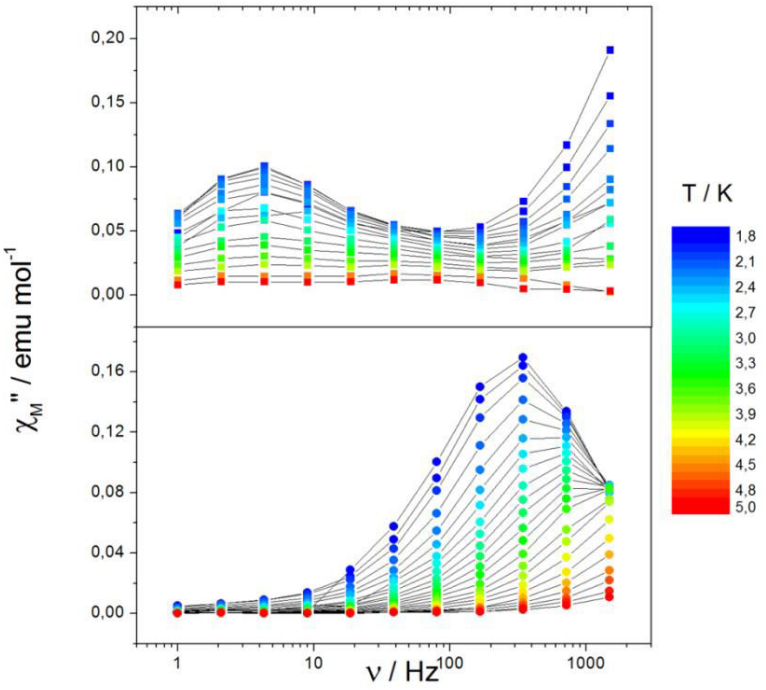

Figure 6.47 **:** Frequency dependence of the out-of phase component of the magnetic susceptibility (χ_M") for $[Dy(cpbOH)(H_2O)_2,(cpb)]_\infty$ and $[Yb(cpbOH)(H_2O)_2,(cpb)]_\infty$ between 1.8 and 5K.

Optimum dc field are found to be 2200 Oe and 1600 Oe for Dy^{3+} and Yb^{3+} derivatives respectively (Appendix II). Frequency dependence of χ_M" is then observed between 1.8K and

5K for both derivatives. For $[Dy(cpbOH)(H_2O)_2,(cpb)]_\infty$ two relaxation regimes are visible and only the slowest one is investigable. For this regime, temperature dependence of the magnetic relaxation is very small and the external dc field only promotes a slow quantum tunneling regime for the relaxation. More interesting is $[Yb(cpbOH)(H_2O)_2,(cpb)]_\infty$ for which clear frequency dependence is observed that witnesses for a thermally activated magnetic slow relaxation. Consequently χ_M'' *vs frequency* curves can be fitted considering Arrhenius law and the relaxation time (Appendix II) is $\tau = \tau_0 \exp(\Delta/k_B T)$ where τ_0 is the characteristic relaxation time and Δ the energy barrier that the molecule has to overcome to reverse its spin(Figure 6.48). Extracted values are $\tau_0 = 2.88\ 10^{-5}$ s and $\Delta = 6.5$K. For comparison the Dy derivative relaxes with $\tau_0 = 3.9\ 10^{-2}$ s but with an energy barrier that is almost zero.

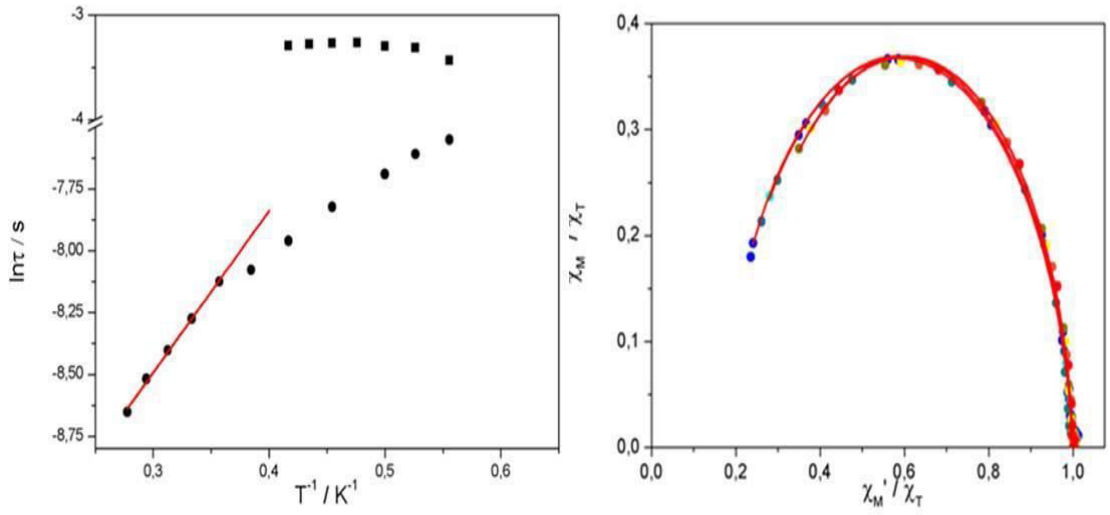

Figure 6.48 : (Left) Arrhenius plots of the relaxation times extracted for $[Dy(cpbOH)(H_2O)_2,(cpb)]_\infty$ (squares) and $[Yb(cpbOH)(H_2O)_2,(cpb)]_\infty$ (circles) with linear best fit (red). (Right) Argand plot for $[Yb(cpbOH)(H_2O)_2,(cpb)]_\infty$ with some of the best fits (red).

The distribution of the relaxation time of a sample can be characterized by plotting χ_M'' vs χ_M' in an Argand plot (Figure 6.49). The resulting curves can be fitted with the Debye model and $\chi(\omega) = \chi_S + (\chi_T - \chi_S)/(1+(i\omega\tau)^{1-\alpha})$ in which χ_T and χ_S are the isothermal and adiabatic susceptibility respectively, ω the frequency of the ac field and α the parameter that accounts for the distribution of the relaxation times.[18] Consequently $\alpha = 0$ corresponds to a unique relaxation time (expected for an ideal SMM) and $\alpha = 1$ to an infinite distribution of the relaxation time (expected for a spin-glass).[19] For $[Yb(cpbOH)(H_2O)_2,(cpb)]_\infty$ α is around 0.06 at 1.8 K which is an excellent agreement with a SMM-like behavior. Moreover $1-(\chi'_M/\chi'_M T)$ is close to 0.85 (Appendix II) meaning that a very significant fraction of the sample is concerned by the magnetic slow relaxation.

Consequently on the $[Ln(cpbOH)(H_2O)_2,(cpb)]_\infty$ family the Yb^{3+} derivative possesses clearly more significant SMM properties that its Dy^{3+} analogue which is quite rare in the library of Ln^{3+}-based SMMs. This is probably due to the distortion of the coordination

polyhedron around the lanthanide ion that is far from an ideal D_{4d} symmetry. Thus this deformation may offer an organization of the electrostatic surrounding of the lanthanide that favor the “prolate“ nature of the Yb^{3+} ion over the “oblate” one of the Dy^{3+}.

Conclusion

To the best of our knowledge the first example of lanthanide-based coordination polymer with a boronic acid as ligand has been described herein. It has been structurally characterized by single-crystal X-ray diffraction. Luminescent (Homo-nuclear and hetero-nuclear compounds) and the strong and thermo-dependent phosphorescence of the ligand have also been studied. Meanwhile magnetic properties have been explored.

References:

[1]. (a) Reneike, T. M.; Eddaoudi, M.; Fehr, M.; Kelley, D.; Yaghi, O. M., J. Am. Chem. Soc. 121, 1651-1657, 1991; (b) Daiguebonne, C.; Kerbellec, N.; Guillou, O.; Bünzli, J. C. G.; Gumy, F.; Catala, L.; Mallah, T.; Audebrand, N.; Gérault, Y.; Bernot, K.; Calvez, G., Inorg. Chem. 47, 3700, 2008; (e) Wang, Z.; Yang, Y.; Cui, Y.; Wang, Z.; Qian, G., J. Alloys Compd. 510, L5, 2012; (f) Decadt, R.; Van Hecke, K.; Depla, D.; Leus, K.; Weidenberg, D.; Van Driessche, I.; Van der Voort, P.; Van Deun, R., Inorg. Chem. 51, 11623, 2012;

[2]. Hall, D. G., Boronic acids. Wiley-VCH Verlag: Weinheim, 2005.

[3]. (a) J. Roger, V. Babizhetskyy, S. Cordier, J. Bauer, K. Hiebl, L. Le Pollès, S. Elisabeth Ashbrook, J.-F. Halet, R. Guérin, Journal of Solid State Chemistry, 178 (2005) 1851-1863.(b) S.E. Ashbrook, K.R. Whittle, G.R. Lumpkin, I. Farnan, The Journal of Physical Chemistry B, 110 (2006) 10358-10364.(c) S.W. Reader, M.R. Mitchell, K.E. Johnston, C.J. Pickard, K.R. Whittle, S.E. Ashbrook, The Journal of Physical Chemistry C, 113 (2009) 18874-18883.(d) M.R. Mitchell, D. Carnevale, R. Orr, K.R. Whittle, S.E. Ashbrook, The Journal of Physical Chemistry C, 116 (2012) 4273-4286.

[4]. R. Shinley, in The CRYSFIRE system for automatic powder indexing, 2002.

[5]. Lekshmi, N. S.; Pedireddi, V. R., Crystal Growth & Design 2007, 7 (5), 944-949.

[6]. (a) Comby, S.; Bünzli, J. C. G.; Gschneider, K. A.; Pecharsky, V. K., Lanthanide Near-Infrared Luminescence in Molecular Probes and Devices. In Handook on the Physics and Chemistry of Rare Earths, Elsevier: Amsterdam, 2007; Vol. 37, pp 1-353; (b) Werts, M. H. V.; Jukes, R. T. F.; Verhoeven, J. W., Physical Chemistry Chemical Physics 2002, 4, 1542-1548. 47. (c) Arakcheeva, A.; Logvinovich, D.; Chapuis, G.; Morozov, V.; Eliseeva, S. V.; Bünzli, J. C. G.; Pattison, P., Chemical Science 2012, 3, 384-390.

[7]. Chauvin, A. S.; Gumy, F.; Imbert, D.; Bünzli, J. C. G., Spectroscopy letters 2004, 37, 512-537.

[8]. (a) Shi, M.; Li, F.; Yi, T.; Zhang, D.; Hu, H.; Huang, C.-H., Inorg. Chem. 2005, 44, 8929; (b) Prodi, L.; Maestri, M.; Ziessel, R.; Balzani, V., Inorg. Chem. 1991, 30 (20), 3798-3802; (c) Quici, S.; Cavazzini, M.; Marzanni, G.; Accors, i. G.; Armaroli, N.; Ventura, B.; Barigelletti, F., Inorg. Chem. 2005, 44 (3), 529-537; (d) Bünzli, J. C. G.; Eliseeva, S. V., Basics of lanthanide photophysics. In Lanthanide Luminescence, Hänninen, P.; Härmä, H., Eds. Springer Berlin Heidelberg: 2010; pp 1-45.

[9]. F.J. Steemers, W. Verboom, D.N. Reinhoudt, E.B. van der Tol, J.W. Verhoeven, Journal of the American Chemical Society, 117 (1995) 9408-9414.

[10]. M. Latva, H. Takalo, V.-M. Mukkala, C. Matachescu, J.C. Rodríguez-Ubis, J. Kankare, Journal of Luminescence, 75 (1997) 149-169.

[11]. Rao, X.; Song, T.; Gao, J.; Cui, Y.; Yang, Y.; Wu, C.; Chen, B.; Qian, G., *2013* 2013, *135*, 15559-15564.

[12]. (a) V. Haquin, M. Etienne, C. Daiguebonne, S. Freslon, G. Calvez, K. Bernot, L. Le Pollès, S.E. Ashbrook, M.R. Mitchell, J.-C. Bünzli, S.V. Eliseeva, O. Guillou, European Journal of Inorganic Chemistry, 2013 (2013) 3464-3476. (b) M.O. Rodrigues, J.D.L. Dutra, L.A.O. Nunes, G.F. de Sá, W.M. de Azevedo, P. Silva, F.A.A. Paz, R.O. Freire, S. A. Júnior, The Journal of Physical Chemistry C, 116 (2012) 19951-19957.

[13]. a) J.-C. G. Bünzli and S. V. Eliseeva, in Lanthanide Luminescence,ed. P. Hänninen and H. Härmä, Springer, Berlin, Heidelberg, 2010, pp. 1–45. (b) J.-C.G. Bünzli, Chemical Reviews, 110 (2010) 2729-2755.

[14]. Gatteschi, D.; Sessoli, R.; Villain, J., Oxford University Press: Oxford, 2006.

[15]. Rinehart, J. D.; Long, D.-L., *Chemical Science* 2011, *2*, 2078-2085.

[16]. Benelli, C.; Gatteschi, D., *Chemical reviews* 2002, *102*, 2369-2387.

[17]. Woodruf, D. N.; Winpenny, R. E. P.; Layfield, R. A., *Chem. Rev.* 2013, *113*, 5110-5148.

[18]. Cole, K. S.; Cole, R. H., *Journal of Chemical Physic* 1941, *9*.

[19]. Mydosh, J. A., *Spin glasses : an experimental introduction*. Taylor & Francis: London, 1993.

Conclusion and outlook

In this thesis, four different ligands (H_2cda, H_2hip, H_2nip and Hcpb) were chosen to synthesize new lanthanide-containing coordination polymers that could present an interest as far as technological applications are concerned. Their physical-chemical properties were studied in details.

The four ligands are non-toxic, low cost and commercially available. Furthermore, syntheses of the lanthanide-containing coordination polymers were conducted in water, at moderate temperature (≤ 100°C) and in good yields (> 90%) according to the green chemistry principles. These conditions are mandatory as far as potential industrial production is targeted.

Although a lot of single crystal structures have been already reported with ligand H_2cda, we found three new crystal structures based on ligand cda^{2-} and a new crystal structure based on oxalate ligand which comes from the decomposition of the ligand cda^{2-} during the reaction.

a). $[Na(Hcda)(H_2O)]_\infty$ which is 2D.
b). $[Lu(cda)_{1.5}(H_2O)_5, 2H_2O]_\infty$ which is 1D.
c). $[Yb_2(cda)_2(ox)(H_2O)_7, 6H_2O]_\infty$ which is 1D.
d). $[Yb_2(ox)_3(H_2O)_4, 2H_2O]_\infty$ which is 2D.

Unfortunately, despite great efforts, we did not obtain single crystals iso-structural with the microcrystalline powders of Family 2 (Ln=Pr to Dy synthesized at room temperature) and Family 6 (Ln=Nd to Lu synthesized at 100°C). Therefore we simply studied the luminescent properties of the Eu- and Tb-containing compounds that belong to these families. They exhibit red and green light respectively. The near-infrared luminescent of Yb-containing compound of Family 4 with chemical formula $\{[Yb_2(cda)_2(ox)(H_2O)_7], 6H_2O\}_\infty$ was measured at room temperature and 77 K. It presents typical $^2F_{5/2} \rightarrow {}^2F_{7/2}$ Yb^{3+} transition at 980nm. Its magnetic properties were also studied. This study revealed that $[Yb_2(cda)_2(ox)(H_2O)_7, 6H_2O]_\infty$ presents a SMM behavior.

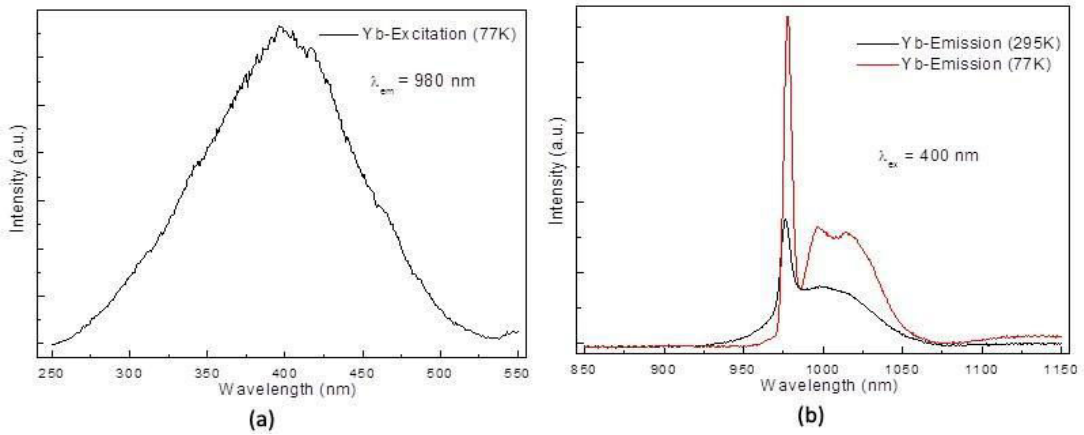

Solid state excitation spectrum at 77K (λ_{em}=980 nm) and emission spectra at 295K and 77K (λ_{ex}=400 nm) of $[Yb_2(cda)_2(ox)(H_2O)_7, 6H_2O]_\infty$.

With ligand hip^{2-}, two new crystal structures were found:

(a). $[Ce_2(hip)_3(H_2O)_9, 6H_2O)]_\infty$ which is 1D.

(b). $[La_2(hip)_2(H_2O)_{10}, hip), 4H_2O]_\infty$ which is 1D and iso-stuctural with microcrystalline powders that belong to Family 2 (Ln=Pr to Lu synthesized at room temperature and 2°C).

Despite great efforts, single crystals iso-structural with microcrystalline powders of Family 1 (Ln=La at room temperature), Family 4 (Ln=La to Pr at 100°C) and Family 5 (Ln=Nd to Lu at 100°C) were not obtained. Hetero-nuclear compounds of Family 2 were also prepared.

Luminescent properties of homo-nuclear compounds (Sm-, Eu-, Tb- and Dy-containing compounds) and of hetero-nuclear compounds (Gd/Tb and Eu/Tb) belonging to Family 2 were studied and revealed the presence of a PET-mechanism for Eu-containing compounds. This study also revealed that adding a few percent of inactive lanthanide ions (Gd^{3+} or Y^{3+}) can enhance the brightness without modifying the color. At last, luminescent properties can be tuned from green to red by modifying the ratio between Eu and Tb. This family of compounds could be used to design taggants with complex luminescent signatures.

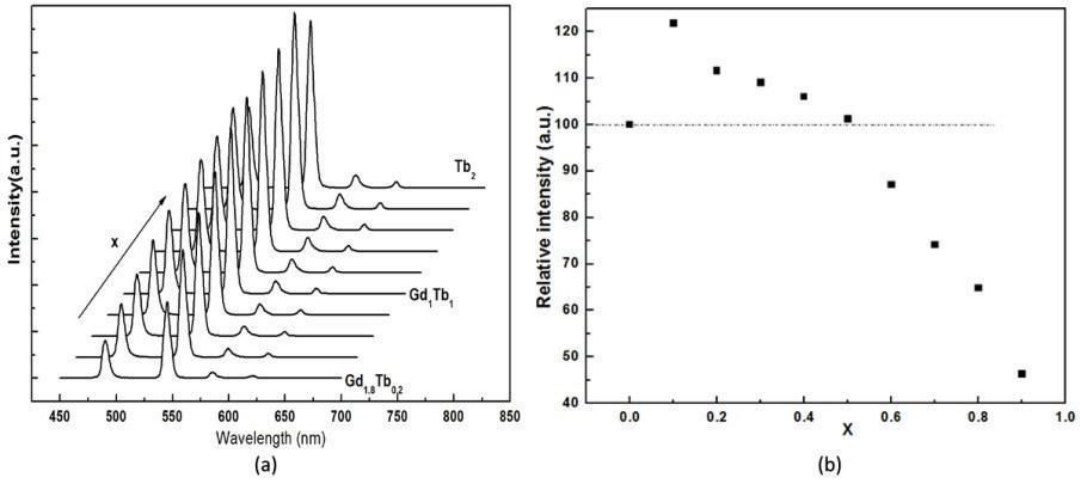

Emission spectra under 345 nm irradiation and integrated intensity of the emission transitions (545 nm) of $[Gd_{2-2x}Tb_{2x}(hip)_2(H_2O)_{10}, (hip), 4H_2O]_\infty$ versus x.

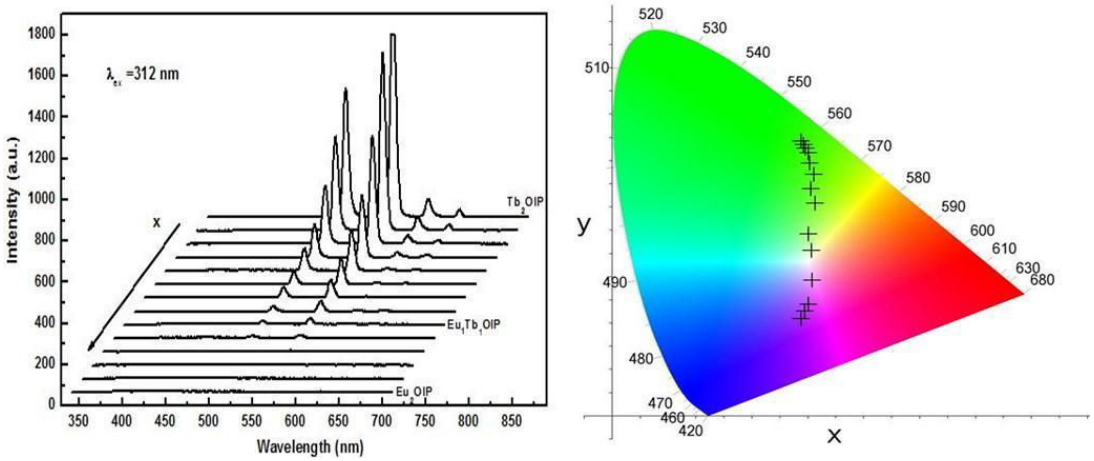

Emission spectra and colorimetric coordinates versus x for $[Eu_{2-2x}Tb_{2x}(hip)_2(H_2O)_{10}, (hip), 4H_2O]_\infty$ under 312 nm excitation wavelength.

Unfortunately, results with ligand nip^{2-} are quite scarce. Actually, compounds involving one lanthanide ions comprised between La^{3+} and Eu^{3+} and synthesized at room temperature are amorphous. Moreover, single crystals iso-structural with the microcrystalline powders of Family 2 (Ln=La to Ce synthesized at 100°C), Family 3 (Ln=Pr to Dy synthesized at 100°C) and Family 4 (Ln=Ho to Yb synthesized at 100°C) were not obtained despite great crystal growth efforts. However, two new crystal structures were obtained:

(a). $[Gd(nip)(Hnip)(H_2O)_4, 3H_2O]$ which is 0D.
(b). $[Gd_4(nip)_6(H_2O)_{14}, 5H_2O]_\infty$ which is 1D.

Because the first excited triplet state of the ligand is closed to the terbium emitting state a back-transfer process occurs that quenches the luminescence of the Tb-containing compound.

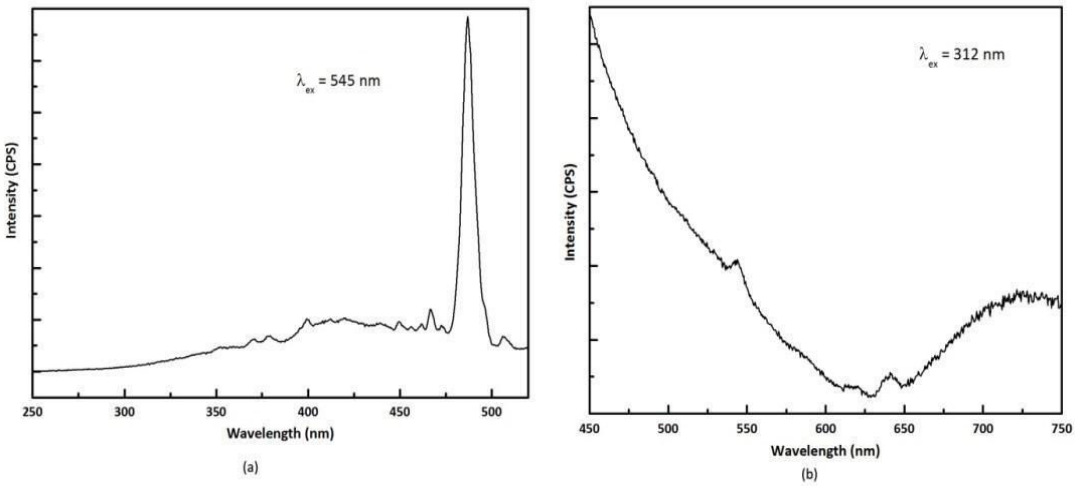

Excitation and emission spectra of $[Tb(nip)(Hnip)(H_2O)_4, 3H_2O]_\infty$.

Hcpb is the first boronic acid that leads to a lanthanide-containing coordination polymer. Two different new crystal structures were obtained.

(a). $[La(cpb)_3(H_2O)_2]_\infty$ which is 1D.
(b). $[Tb(cpbOH)(H_2O)_2, (cpb)]_\infty$ which is 2D.

In both crystal structures, ligand cpb^- presents both the Brönsted and the Lewis acidic characters because of the vacant p orbital of the boron atom. Luminescent properties of homo-nuclear compounds (Sm-, Eu-, Tb- and Dy-containing compounds) and hetero-nuclear compounds (Gd/Tb and Eu/Tb) that belong to Family 2 were studied in details. The luminescence versus temperature for both the Eu- and the Tb-containing compounds was studied, and the emission spectra and colorimetric coordinates versus temperature were recorded. Luminescent behavior could be of interest as far as potential applications are targeted. Study of the luminescent properties of hetero-nuclear compounds (Gd/Tb and Eu/Tb) revealed that adding a few percent of inactive lanthanide ions (Gd^{3+} or Y^{3+}) can enhance the brightness without modifying the color. Furthermore, luminescent properties can be tuned from green to red by modifying the ratio between Eu^{3+} and Tb^{3+} ions., Study of the magnetic properties revealed that the compounds that belong to Family 2 (Ln=Dy or Yb)

present SMM-like magnetic behaviors.

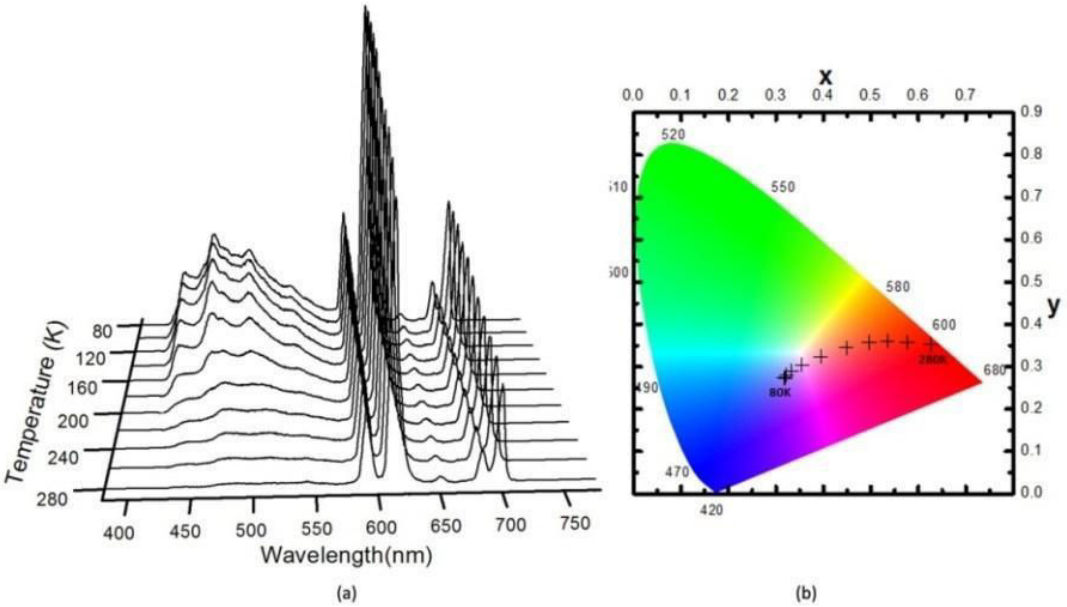

Emission spectra and colorimetric coordinates under 303nm irradiation versus temperature of $[Eu(cpbOH)(H_2O)_2, (cpb)]_\infty$.

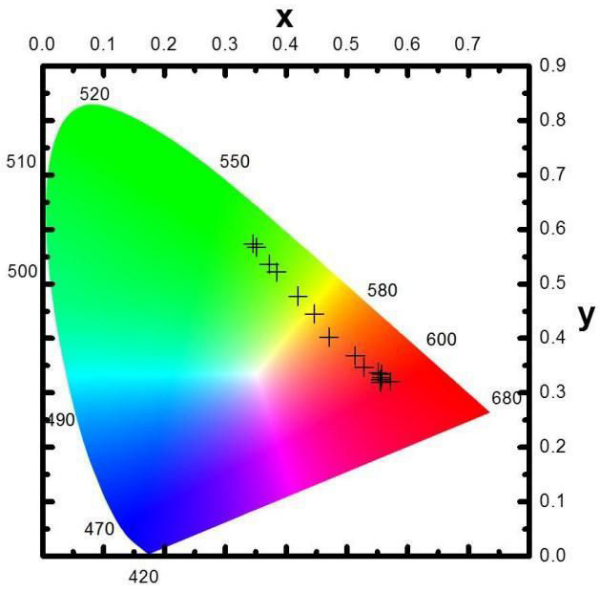

Colorimetric coordinates versus x for $[Eu_{1-x}Tb_x(cpbOH)(H_2O)_2, (cpb)]_\infty$ under 312nm irradiation.

As a summary, lanthanide-based coordination polymers exhibiting interesting luminescent and magnetic properties have been deeply investigated. This systematic work has also brought us to understand luminescent mechanisms of lanthanide-containing compounds and we hope that these compounds can be useful in future industrial applications.

Appendix I

Experimental techniques

1. X-ray powder diffraction

Diagrams have been collected using a Panalytical X'Pert Pro diffractometer with a X'Celerator detector. The typical recording conditions were 45 kV, 40 mA for Cu-Kα (λ = 1.542Å), the diagrams were recorded in θ/θ mode in 5 or 60 min between 5° and 75° (8378 measurements) with a step size of 0.0084° and a scan time of 50s. The calculated patterns were produced using the Powdercell and WinPLOTR software programs. For Pattern indexing, the extractions of the peak positions were carried out via the WinPLOTR software. The pattern indexing was performed by the program McMaille, and the refinement of the unit-cell parameters by means of the Chekcell program which is a modified version of Cellref from CRYSFIRE suite.

Thermal dependent X-ray diffraction experiments (TDXD) have been performed with a Panalytical X'Pert Pro diffractometer equipped with an X'celerator detector using Cu $K\alpha_1$ radiation in the 5 - 75° 2θ range. Heating of the samples (from room temperature to 1000°C) was performed using an Anton Paar HTK 1200 furnace under nitrogen atmosphere.

2. Thermal Analyses.

Thermo-gravimetric and thermo-differential analyses were performed in platinum crucibles under a nitrogen atmosphere between room temperature and 1000 °C with a heating rate of 5 °C.min^{-1} using a Perkin Elmer Pyris-Diamond thermal analyzer. At the end of the experiments, the compounds were maintained for one hour at 1000°C under air atmosphere in order to complete the combustion.

3. Single crystal X-ray diffraction data.

Single-crystals have been sealed in glass capillaries for X-ray single crystal data collection in order to avoid potential dehydration. Single crystals were mounted on a Nonius Kappa CCD diffractometer with Mo Kα radiation (λ = 0.71073 Å). The crystal data collection was performed at room temperature.

Crystal structures were solved by direct methods using the SIR97 program, and then refined with full matrix least-square methods based on F^2 (SHELX-97) with the aid of WINGX program. All non-hydrogen atoms were refined anisotropically using the SHELXL program. Hydrogen atoms bound to the organic ligand were localized at ideal positions. Hydrogen atoms of water molecules have not been localized. Absorption corrections were performed using the facilities included in the WinGX program suite.

4. Solid state luminescent measurements.

Solid state emission spectra have been measured on a Horiba Jobin-Yvon Fluorolog III fluorescence spectrometer with a Xe lamp. Slit widths for excitation and emission were 2 nm for the Eu- and Tb-containing compounds and 5 nm for the Sm- and Dy-containing compounds. Most of the luminescence spectra were recorded between 450 nm and 750 nm at room temperature. Some of them have also been recorded at 77 K using a cold-finger

sample holder. The data were collected at every 0.5 nm with an integration time of 100 ms for each step. The quantum yield measurements were performed using a Jobin-Yvon integrating sphere ($\phi=E_c-E_a)/(L_a-L_c$) with E_c being the integrated emission spectrum of the sample, E_a the integrated "blank" emission spectrum, L_a the "blank" absorption and L_c the sample absorption at the excitation wavelength. Luminescence decays have also been measured using this apparatus. Temperature dependent luminescence measurements have been performed using an Optistat CF2 cryostat from Oxford Instruments.

Comparative solid state luminescent spectra have been measured on a Perkin-Elmer LS-55 spectrometer between 450 nm and 750 nm under identical operating conditions and without turning the lamp off to ensure a valid comparison between the emission spectra. Reproducibility of the measurements as well as surface states of the samples (1.5 cm^2 pellets) have been carefully checked. Slit widths for excitation and emission were 5 nm or 10 nm depending on the series of samples.

Solid state luminescence spectra of the homo-nuclear Gd-containing compounds have been recorded at 77 K in order to obtain the energy levels of the lowest triplet states of the ligands.

Luminescence intensities of the samples expressed in $Cd.m^{-2}$ have been measured with a Gigahertz-Optik X1-1 optometer with an integration time of 200 ms on 1.5 cm^2 pellets. The intensity of the UV flux, 2.5(1) $W.m^{-2}$, has been measured with a VilberLourmat VLX-3W radiometer.

5. UV-visible Absorption Measurements.

UV-vis absorption spectra have been recorded on a Perkin-Elmer Lambda 650 spectrometer. Solid state measurements were recorded using a 60 mm integrating sphere. Solid state UV-vis absorption spectrum of the compounds have been recorded for estimating the energy of the lowest singlet excited states of the ligands. Liquid state measurements have been performed for evaluating molar absorption coefficients of the ligand.

6. Colorimetric measurements.

CIE (Commission International de l'Eclairage) (x,y) emission color coordinates were obtained using a MSU-003 colorimeter (Majantys) with the PhotonProbe 1.6.0 Software (Majantys). Color measurements: 2°, CIE 1931, step 5 nm, under 312 nm UV light. $X = k \times \int_{380nm}^{780nm} I_\lambda \times x_\lambda$, $Y = k \times \int_{380nm}^{780nm} I_\lambda \times y_\lambda$ and $Z = k \times \int_{380nm}^{780nm} I_\lambda \times z_\lambda$ with k constant for the measurement system I_λ sample spectrum intensity, wavelength depending, x_λ, y_λ, z_λ trichromatic values x = X/(X+Y+Z), y = Y/(X+Y+Z) and z = Z/(X+Y+Z). Mean xyz values are given for each sample, which act as light sources (luminescent samples). Standards from Phosphor Technology used, calibrated at 312 nm: red phosphor Gd_2O_2S:Eu (x = 0.667, y = 0.330) and green phosphor Gd_2O_2S:Tb (x = 0.328, y = 0.537).

For other excitation wavelengths than 312 nm colorimetric coordinates have been calculated on the basis of emission spectra that have been measured on a Perkin-Elmer LS-

55 spectrometer. Both apparatus present different geometries which induces a little discrepancy between the results.

7. Solid state NMR spectroscopy

Solid-state NMR spectra were acquired using a Bruker Avance III spectrometer equipped with a 14.1 T magnet (^{89}Y Larmor frequency 29.4 MHz). Samples were packed into 7 mm rotors rotated at a spinning rate of 4 kHz. ^{89}Y MAS NMR spectra were acquired using cross polarization (CP) from 1H using a contact time of 5 ms (ramped for ^{1}H), SPINAL64 ^{1}H decoupling during acquisition with an rf field strength of about 60 kHz and a recycle interval of 3 s. Chemical shift scales are shown relative to 1 M YCl_3 in aqueous solution.

8. Energy dispersive spectroscopy

All EDS measurements were carried out with a Hitachi TM-1000, Tabletop microscope version 02.11 (Hitachi High-Technologies, Corporation Tokyo Japan) with an EDS analysis system (SwiftED-TM, Oxford Instruments Link INCA). The detector is a silicon drift detector, with an energy resolution of 165 eV which allows us to detect the element from Na to U. With SwiftD-TM software, qualitative and quantitative analyses can be performed. All samples were observed by means of an electron beam accelerated at 15 kV, under high vacuum. Samples were assembled on carbon discs, stuck on an aluminum stub fixed at 7 mm from the EDX beam, with an angle of measurement of 22°. Reproducibility of the elemental analyses was carefully checked by reproducing several times the measurements on different takings for each sample.

9. Granulometry

Microcrystalline powders were analyzed by laser granulometry using a CILAS Laser Sizer 1180.

10. Crystal growth in gel media (U-shaped tubes)

Gels constitute media in which two reactants slowly diffuse toward each other and react to form crystals in the U-shape tube. Two reactants are respectively added in the two different sides of U-tube. The gel bridge allows the two reactants to slowly diffuse in the media and react. Finally, the crystals grow in the gel bridge. The typically experimental conditions used during this work are: 10mL of a solution containing 0.25 mmol of Ln^{3+} salt on one side and 10mL of a solution containing 0.25 mmol of sodium salt of ligand on the other side.

11. Crystal growth in H-shaped tubes.

A H-shaped tube can be described as two test tubes connected by a bridge. The two reactants are respectively added in the two different sides of the H-shaped tube. The distilled water is slowly and carefully added upon the solutions of reactants till the bridge is filled. The reactants solutions must not be disturbed, otherwise, precipitation immediately occurs. Then the tube is sealed to avoid evaporation. At last, the crystals form in the bridge.

The typically experimental conditions used during this work are: 10mL of a solution containing 0.25 mmol of Ln^{3+} salt on one side and 10mL of a solution containing 0.25 mmol of sodium salt of ligand in the other side.

Appendix II

1. Ligand H_2cda

Crystallographic data

1.1 **[**Na(cda)(H_2O)**]**$_\infty$

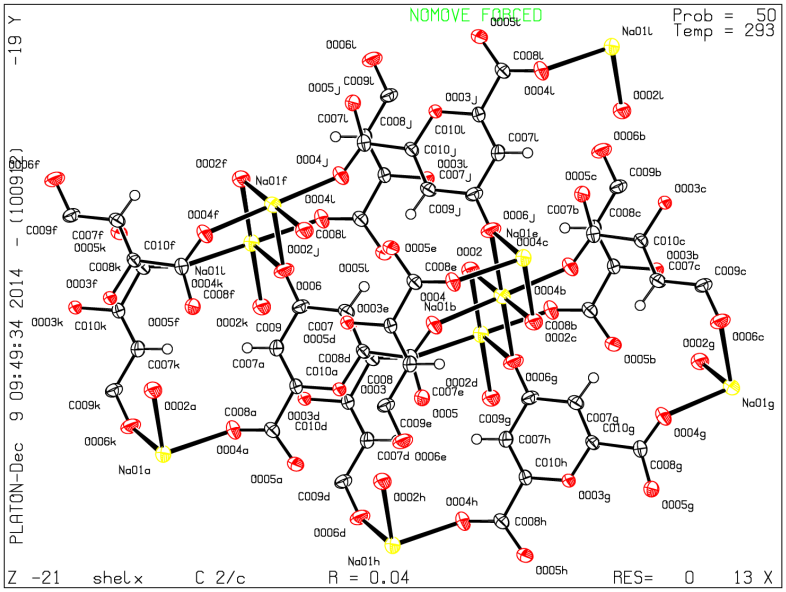

Table 1.1a Atomic parameters for [Na(cda)(H_2O)]$_\infty$

Atom	x/a	y/b	z/c
Na01	1.0000	0.0000	0.5000
O002	1.0000	0.14825(17)	0.2500
O003	0.5000	-0.04743(14)	0.2500
O004	0.78290(11)	-0.00834(12)	0.49255(17)
O005	0.67838(11)	-0.18517(11)	0.40440(16)
O006	0.5000	0.34513(16)	0.2500
C007	0.59841(14)	0.14981(16)	0.33476(19)
H007	0.6647	0.1911	0.3933
C008	0.69611(14)	-0.06243(16)	0.41588(18)
C009	0.5000	0.2262(2)	0.2500
C010	0.59495(12)	0.02051(14)	0.32979(17)

Table 1.1b Selected bond lengths (Å) and angles (°) for **[**Na(cda)(H_2O)**]**$_\infty$

Atoms	d (Å)	Atoms	Angle (°)
Na01—O004	2.3575(12)	O004—Na01—O006^{ii}	90.84(3)
Na01—O004^{i}	2.3576(12)	O002—Na01—O006^{ii}	99.01(4)
Na01—O002	2.3980(11)	O004—Na01—O006^{iii}	89.16(3)
Na01—O002^{i}	2.3980(11)	O002—Na01—O006^{iii}	80.99(4)
Na01—O006^{ii}	2.4426(11)	O006^{ii}—Na01—O006^{iii}	180
Na01—O006^{iii}	2.4426(11)	O004—Na01—O002^{i}	88.09(3)
Na01—Na01^{iv}	3.6805	O002—Na01—O002^{i}	180
Na01—Na01^{v}	3.6805	O004—Na01—O002	91.91(3)
		O004—Na01—O004^{i}	180

1.2 **{**$[Lu(cda)_{1.5}(H_2O)_5]$, $2H_2O$**}**$_\infty$

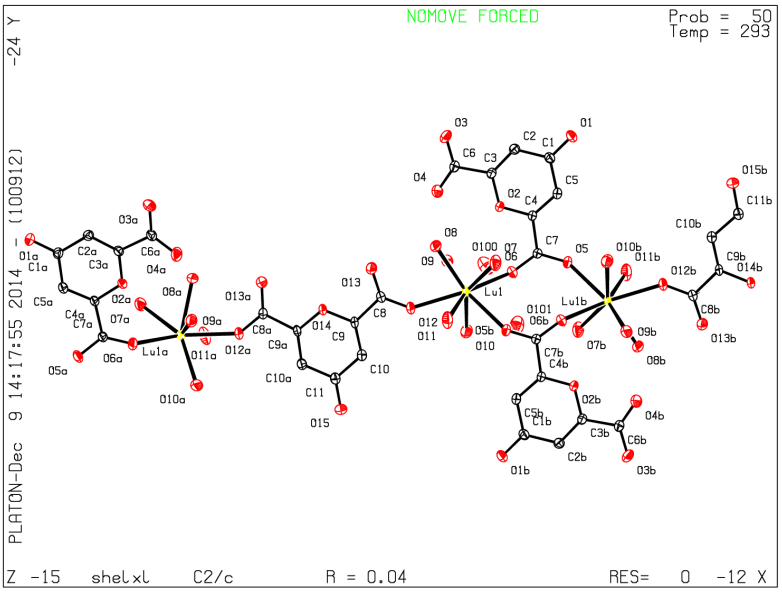

Table 1.2a Atomic parameters for **{**$[Lu(cda)_{1.5}(H_2O)_5] \cdot 2H_2O$**}**$_\infty$

Atom	x/a	y/b	z/c	Atom	x/a	y/b	z/c
C1	1.08085(14)	0.9595(2)	-0.03144(14)	O101	0.92620(16)	0.3570(3)	-0.19678(16)
C10	0.57174(14)	0.3967(2)	-0.20770(14)	O11	0.79664(13)	0.5127(3)	0.03705(13)
C11	0.5000	0.3280(3)	-0.2500	O12	0.70543(10)	0.53881(18)	-0.12836(12)
C2	1.00235(14)	1.0078(2)	-0.08148(14)	O13	0.63205(11)	0.70483(18)	-0.15928(12)
C3	0.93872(15)	0.9354(2)	-0.11597(15)	O14	0.5000	0.5794(2)	-0.2500
C4	1.01710(13)	0.7669(2)	-0.05825(13)	O15	0.5000	0.2154(3)	-0.2500
C5	1.08438(14)	0.8313(2)	-0.02243(15)	O2	0.94463(10)	0.81524(15)	-0.10399(11)
C6	0.85465(14)	0.9763(2)	-0.17350(14)	O3	0.84638(14)	1.08559(19)	-0.18428(14)
C7	1.01391(13)	0.6324(2)	-0.05246(13)	O4	0.80396(13)	0.8965(2)	-0.20618(13)
C8	0.64131(13)	0.5955(2)	-0.16158(13)	O5	1.07856(12)	0.58049(18)	-0.02899(14)
C9	0.56873(12)	0.5174(2)	-0.20851(13)	O6	0.94895(12)	0.58540(18)	-0.07146(13)
Lu1	0.84073(0)	0.56609(1)	-0.05656(1)	O7	0.92808(13)	0.6746(2)	0.06402(13)
O1	1.14079(11)	1.02406(19)	0.00136(12)	O8	0.79209(12)	0.75276(18)	-0.05649(13)
O10	0.81830(13)	0.4019(2)	-0.13965(14)	O9	0.79887(12)	0.64827(19)	-0.19474(12)
O100	0.8730(2)	0.5652(2)	-0.2948(2)				

Table 1.2b Selected bond lengths (Å) and angles (°) for **{**$[Lu(cda)_{1.5}(H_2O)_5] \cdot 2H_2O$**}**$_\infty$

Atoms	d (Å) or Angle (°)	Atoms	d (Å) or Angle (°)
O5—Lu1^{ii}	2.286(2)	O6—Lu1—O5^{ii}	77.71(7)
O6—Lu1	2.251(2)	O6—Lu1—O10	83.27(8)
O7—Lu1	2.368(2)	O5^{ii}—Lu1—O10	74.10(8)
O8—Lu1	2.295(2)	O6—Lu1—O8	108.57(7)
O9—Lu1	2.439(2)	O5^{ii}—Lu1—O8	143.00(8)
O10—Lu1	2.294(2)	O10—Lu1—O8	141.89(8)
O11—Lu1	2.338(2)	O6—Lu1—O12	143.82(7)
O12—Lu1	2.3097(19)	O5^{ii}—Lu1—O12	120.27(7)
Lu1—O5^{ii}	2.286(2)	O10—Lu1—O12	73.63(8)
O11—Lu1—O9	143.75(7)	O8—Lu1—O12	76.67(7)
O7—Lu1—O9	120.31(8)	O6—Lu1—O11	143.85(7)
O12—Lu1—O7	134.31(7)	O5^{ii}—Lu1—O11	71.46(8)
O11—Lu1—O7	78.08(9)	O10—Lu1—O11	105.37(10)
O6—Lu1—O9	72.28(7)	O8—Lu1—O11	86.38(9)
O5^{ii}—Lu1—O9	139.25(7)	O12—Lu1—O11	70.65(7)
O10—Lu1—O9	75.57(8)	O6—Lu1—O7	77.32(8)
O8—Lu1—O9	74.16(7)	O5^{ii}—Lu1—O7	77.71(8)
O12—Lu1—O9	75.19(7)	O10—Lu1—O7	148.55(8)
O8—Lu1—O7	68.76(7)		

1.3 **{**$[Yb_2(cda)_2(H_2O)_9]$, $5H_2O$**}**$_\infty$

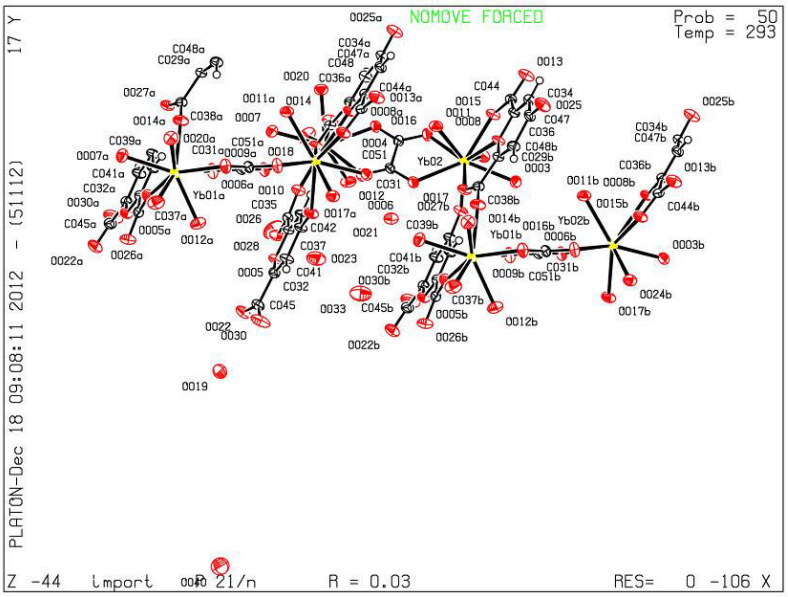

Table 1.3a Atomic parameters for **{**$[Yb_2(cda)_2(H_2O)_9]$, $5H_2O$**}**$_\infty$

Atom	x/a	y/b	z/c	Atom	x/a	y/b	z/c
Yb02	1.37171(2)	0.15376(1)	0.91412(1)	O009	0.9518(4)	0.16295(15)	0.6780(3)
Yb01	0.83313(2)	0.09230(1)	0.54402(1)	O008	1.5684(3)	0.22061(14)	0.9073(3)
O040	0.0412(6)	0.9992(3)	0.8795(5)	O007	0.6562(4)	0.09886(16)	0.3643(3)
O033	0.8490(6)	0.4435(2)	0.8324(5)	O006	1.1470(3)	0.18319(15)	0.8204(3)
O030	0.3899(4)	0.39190(17)	0.6759(4)	O005	0.5020(3)	0.25814(14)	0.6237(3)
O028	0.4569(6)	0.0325(2)	0.6723(4)	O004	1.0528(3)	0.06397(14)	0.6416(3)
O027	0.8610(3)	0.24691(14)	0.4327(3)	O003	1.5395(3)	0.17106(18)	1.0925(3)
O026	0.5080(4)	0.14494(15)	0.6322(3)	C051	1.1279(5)	0.09477(19)	0.7217(4)
O025	1.8455(4)	0.32160(17)	0.8674(4)	C048	1.1540(5)	0.1867(2)	0.4088(4)
O024	1.4147(4)	0.06292(15)	1.0012(3)	C047	1.7642(5)	0.2285(2)	0.8734(4)
O023	0.7571(5)	0.48522(19)	0.5978(4)	C045	0.3876(5)	0.3398(2)	0.6564(4)
O022	0.3025(4)	0.30402(16)	0.6579(3)	C044	1.6542(5)	0.13186(19)	0.8804(4)
O021	1.0414(4)	0.29598(16)	0.7949(3)	C042	0.6864(5)	0.2613(2)	0.5702(4)
O020	0.8994(4)	0.04370(15)	0.4118(3)	C041	0.5863(5)	0.3489(2)	0.6011(4)
O019	0.1681(4)	0.45761(17)	0.6675(3)	C039	0.6860(5)	0.3223(2)	0.5689(4)
O018	0.7431(5)	0.00185(17)	0.5231(3)	C038	0.9375(5)	0.20624(19)	0.4372(4)
O017	1.2652(4)	0.14873(15)	1.0410(3)	C037	0.5971(4)	0.2318(2)	0.5968(4)
O016	1.2462(3)	0.08356(15)	0.7862(3)	C036	1.6692(5)	0.1969(2)	0.8870(4)
O015	1.5495(3)	0.11258(15)	0.8861(3)	C035	0.5891(5)	0.1669(2)	0.5990(4)
O014	0.9238(4)	0.15440(14)	0.4547(3)	C034	1.7626(5)	0.2903(2)	0.8816(4)
O013	1.7464(4)	0.10413(16)	0.8722(4)	C032	0.4998(5)	0.3165(2)	0.6255(4)
O012	0.8445(4)	0.05949(17)	0.7217(3)	C031	1.0693(5)	0.15215(19)	0.7409(4)
O011	1.3378(4)	0.18727(16)	0.7258(3)	C029	1.0620(4)	0.22163(19)	0.4177(4)
O010	0.6696(4)	0.14121(16)	0.5672(3)				

Table 1.3b Selected bond lengths (Å) and angles (°) for **{**$[Yb_2(cda)_2(H_2O)_9]$, $5H_2O$**}**$_\infty$

Atoms	d (Å) or Angle (°)	Atoms	d (Å) or Angle (°)
Yb01—O010	2.235(3)	O014—Yb01—C051	80.01(13)
Yb01—O018	2.295(4)	O004—Yb01—C051	20.62(12)
Yb01—O014	2.296(3)	O012—Yb01—C051	69.97(13)
Yb01—O004	2.321(3)	O007—Yb01—C051	157.35(13)
Yb01—O012	2.353(4)	O009—Yb01—C051	49.16(12)
Yb01—O007	2.352(4)	O020—Yb01—C051	90.57(13)
Yb01—O009	2.359(3)	O010—Yb01—C031	96.57(13)
Yb01—O020	2.372(3)	O018—Yb01—C031	132.92(14)
Yb01—C051	3.124(5)	O014—Yb01—C031	74.88(13)
Yb01—C031	3.132(5)	O004—Yb01—C031	49.13(12)
Yb02—O015	2.317(3)	O012—Yb01—C031	69.85(13)
Yb02—O003	2.329(3)	O007—Yb01—C031	148.75(13)
Yb02—O027^{i}	2.333(3)	O009—Yb01—C031	20.61(12)
Yb02—O016	2.336(3)	O020—Yb01—C031	113.51(12)
Yb02—O017	2.342(4)	C051—Yb01—C031	28.56(12)
Yb02—O024	2.350(3)	O015—Yb02—O003	80.75(13)
Yb02—O006	2.369(3)	O015—Yb02—O027^{i}	120.33(12)
Yb02—O011	2.416(3)	O003—Yb02—O027^{i}	77.33(13)
Yb02—O008	2.683(3)	O015—Yb02—O016	84.17(12)
Yb02—C051	3.140(4)	O003—Yb02—O016	145.51(14)
Yb02—C031	3.170(5)	O027^{i}—Yb02—O016	136.54(12)
O010—Yb01—O018	98.92(16)	O015—Yb02—O017	139.63(12)
O010—Yb01—O014	105.64(13)	O003—Yb02—O017	75.20(13)
O018—Yb01—O014	140.31(14)	O027^{i}—Yb02—O017	85.45(12)
O010—Yb01—O004	141.69(13)	O016—Yb02—O017	97.76(13)
O018—Yb01—O004	96.10(15)	O015—Yb02—O024	71.21(12)
O014—Yb01—O004	83.60(14)	O003—Yb02—O024	76.04(13)
O010—Yb01—O012	77.16(13)	O027^{i}—Yb02—O024	148.53(12)
O018—Yb01—O012	70.80(14)	O016—Yb02—O024	69.76(13)
O014—Yb01—O012	144.69(14)	O017—Yb02—O024	71.80(12)
O004—Yb01—O012	74.90(14)	O015—Yb02—O006	143.74(12)
O010—Yb01—O007	72.83(13)	O003—Yb02—O006	134.69(12)
O018—Yb01—O007	78.28(14)	O027^{i}—Yb02—O006	71.39(12)
O014—Yb01—O007	79.80(14)	O016—Yb02—O006	69.12(12)
O004—Yb01—O007	145.09(13)	O017—Yb02—O006	70.47(13)
O012—Yb01—O007	132.38(14)	O024—Yb02—O006	118.25(12)
O010—Yb01—O009	77.72(13)	O015—Yb02—O011	77.77(12)
O018—Yb01—O009	144.26(14)	O003—Yb02—O011	132.22(13)
O014—Yb01—O009	72.57(14)	O027^{i}—Yb02—O011	77.70(12)
O004—Yb01—O009	69.69(12)	O016—Yb02—O011	73.24(13)
O012—Yb01—O009	73.81(14)	O017—Yb02—O011	141.55(12)
O007—Yb01—O009	131.91(13)	O024—Yb02—O011	133.34(12)
O010—Yb01—O020	145.32(13)	O006—Yb02—O011	71.45(12)

O018—Yb01—O020	73.53(15)	O015—Yb02—O008	60.27(11)
O014—Yb01—O020	68.48(13)	O003—Yb02—O008	66.46(12)
O004—Yb01—O020	72.89(12)	O027^{i}—Yb02—O008	60.07(11)
O012—Yb01—O020	128.18(13)	O016—Yb02—O008	129.77(12)
O007—Yb01—O020	72.49(13)	O017—Yb02—O008	132.43(12)
O009—Yb01—O020	127.96(13)	O024—Yb02—O008	121.67(11)
O010—Yb01—C051	122.87(13)	O006—Yb02—O008	119.96(11)
O018—Yb01—C051	111.89(14)	O011—Yb02—O008	65.80(11)

1.4 $[Yb_2(ox)_3(H_2O)_4, 2H_2O]_\infty$

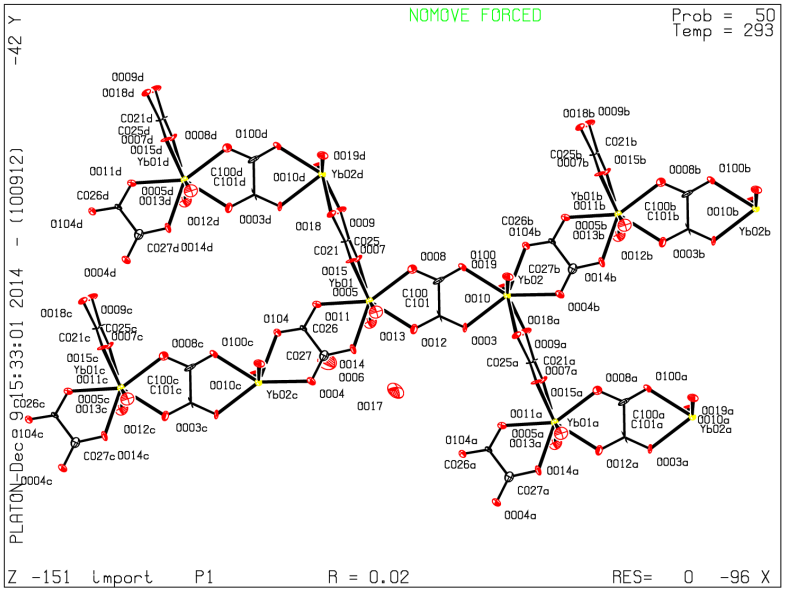

Table 1.4a Atomic parameters for $[Yb_2(ox)_3(H_2O)_4, 2H_2O]_\infty$

Atom	x/a	y/b	z/c	Atom	x/a	y/b	z/c
Yb01	0.41089(3)	0.81404(3)	0.56523(2)	O014	0.386(3)	0.854(3)	0.3275(16)
Yb02	-0.19341(3)	0.19613(3)	0.95080(2)	O015	0.686(2)	0.7757(19)	0.7142(14)
O003	-0.040(2)	0.335(2)	0.7105(13)	O017	0.352(4)	0.405(3)	0.2865(19)
O004	0.524(3)	1.004(3)	0.0893(15)	O018	0.539(2)	1.259(2)	0.8040(15)
O005	0.083(2)	1.036(2)	0.5199(17)	O019	-0.4371(17)	0.468(2)	1.0090(11)
O006	0.902(4)	0.566(4)	0.236(2)	C100	0.128(2)	0.531(2)	0.8289(14)
O007	0.3962(18)	1.0955(17)	0.6696(12)	C021	0.6876(16)	0.8992(18)	0.7653(12)
O008	0.263(2)	0.666(2)	0.8058(13)	O104	0.824(3)	1.148(3)	0.2001(16)
O009	0.839(2)	0.912(2)	0.8631(14)	O100	0.048(2)	0.4346(18)	0.9457(10)
O010	0.123(2)	-0.033(3)	0.9917(17)	C025	0.517(2)	1.0911(19)	0.7352(12)
O011	0.692(3)	1.002(3)	0.4174(16)	C026	0.698(3)	1.050(3)	0.2849(15)
O012	0.175(2)	0.5750(18)	0.5699(12)	C027	0.521(3)	0.964(3)	0.2262(19)
O013	0.646(2)	0.535(2)	0.5011(14)	C101	0.0796(19)	0.4775(15)	0.6894(10)

Table 1.4b Selected bond lengths (Å) and angles (°) for compound $[Yb_2(ox)_3(H_2O)_4, 2H_2O]_\infty$

Atoms	d (Å) or Angle (°)	Atoms	d (Å) or Angle (°)
Yb02—O104^{ii}	2.355(14)	O005—Yb01—O008	91.8(5)
Yb02—O100	2.335(12)	O007—Yb01—O011	77.9(5)
Yb02—O019	2.316(11)	O014—Yb01—O011	69.3(5)
Yb02—O018^{i}	2.290(13)	O015—Yb01—O011	74.4(5)
Yb02—O010	2.341(14)	O012—Yb01—O011	143.2(4)
Yb02—O009^{i}	2.234(12)	O013—Yb01—O011	80.4(6)
Yb02—O004^{ii}	2.358(18)	O005—Yb01—O011	105.3(6)
Yb02—O003	2.356(12)	O008—Yb01—O011	145.3(4)
Yb01—O015	2.363(10)	O009^{i}—Yb02—O104^{ii}	118.1(5)
Yb01—O014	2.261(14)	O009^{i}—Yb02—O019	143.7(4)
Yb01—O013	2.346(13)	O104^{ii}—Yb02—O019	77.5(5)
Yb01—O012	2.311(12)	O009^{i}—Yb02—O100	132.9(5)
Yb01—O011	2.365(18)	O104^{ii}—Yb02—O100	78.7(4)
Yb01—O008	2.361(14)	O019—Yb02—O100	80.2(4)
Yb01—O007	2.327(9)	O009^{i}—Yb02—O018^{i}	75.2(4)
Yb01—O005	2.384(14)	O104^{ii}—Yb02—O018^{i}	136.7(6)
O007—Yb01—O014	122.9(5)	O019—Yb02—O018^{i}	72.4(4)
O007—Yb01—O015	66.9(3)	O100—Yb02—O018^{i}	124.4(4)
O014—Yb01—O015	138.0(6)	O009^{i}—Yb02—O004^{ii}	75.8(5)
O007—Yb01—O012	135.1(4)	O104^{ii}—Yb02—O004^{ii}	70.0(5)
O014—Yb01—O012	77.0(5)	O019—Yb02—O004^{ii}	80.4(5)
O015—Yb01—O012	127.8(4)	O100—Yb02—O004^{ii}	146.0(4)
O007—Yb01—O013	142.5(4)	O018^{i}—Yb02—O004^{ii}	74.8(5)
O014—Yb01—O013	75.8(6)	O009^{i}—Yb02—O003	80.4(5)
O015—Yb01—O013	78.0(4)	O104^{ii}—Yb02—O003	147.2(5)
O012—Yb01—O013	77.4(5)	O019—Yb02—O003	104.1(4)
O007—Yb01—O005	71.2(4)	O100—Yb02—O003	69.5(4)
O014—Yb01—O005	74.1(6)	O018^{i}—Yb02—O003	71.7(5)
O015—Yb01—O005	137.2(4)	O004^{ii}—Yb02—O003	142.8(4)
O012—Yb01—O005	78.4(5)	O009^{i}—Yb02—O010	64.5(4)
O013—Yb01—O005	144.8(4)	O104^{ii}—Yb02—O010	76.0(6)
O007—Yb01—O008	79.5(4)	O019—Yb02—O010	149.4(3)

O014—Yb01—O008	145.4(5)	O100—Yb02—O010	80.0(5)
O015—Yb01—O008	72.6(5)	O018^{i}—Yb02—O010	138.2(4)
O012—Yb01—O008	69.2(4)	O004^{ii}—Yb02—O010	104.3(6)
O013—Yb01—O008	102.9(5)	O003—Yb02—O010	90.4(6)

ATG curves of Family 2 and Family 6

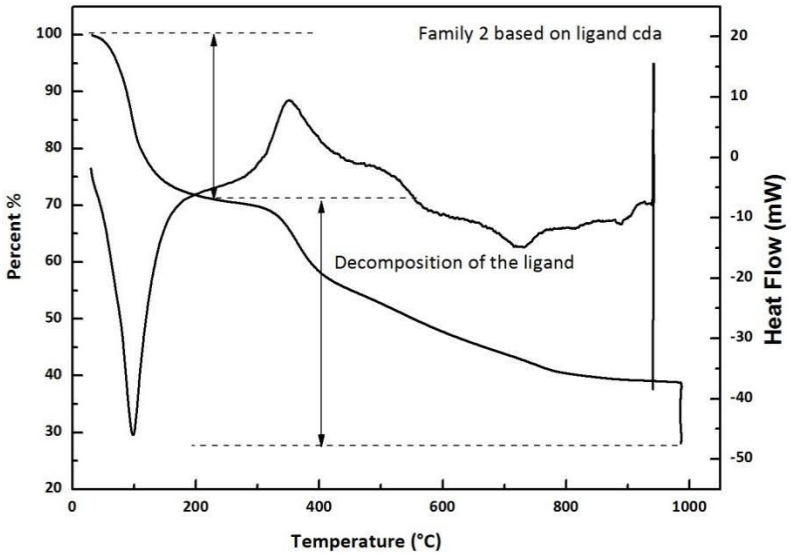

TGA/TDA curves for microcrystalline powders of Family 2 (Pr)

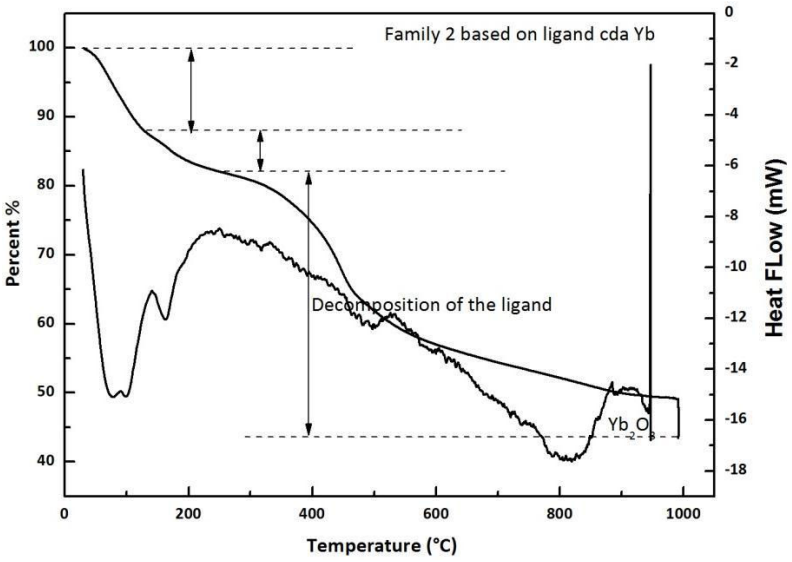

TGA/TDA curves for microcrystalline powders of Family 6 (Yb)

Emission spectra of Family 6 Eu- and Tb- containing compounds

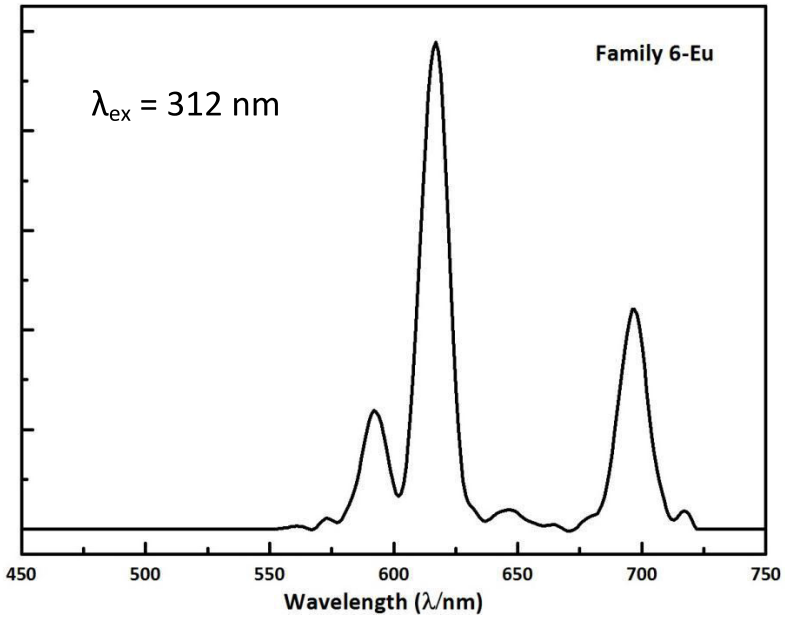

Emission spectrum of Eu-containing compounds of Family 6.

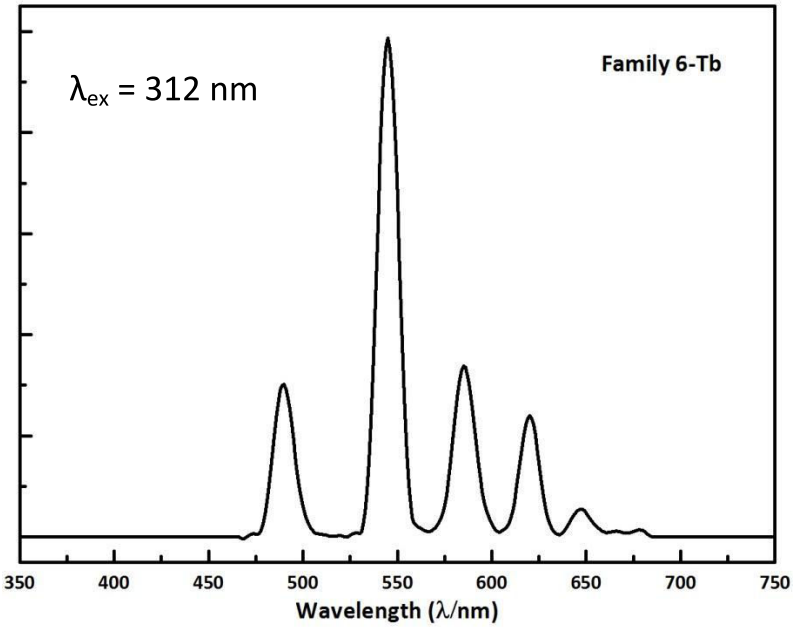

Emission spectrum of Tb-containing compounds of Family 6.

2. Ligand H_2hip

Crystallographic data

2.1 $[Ce_2(hip)_3(H_2O)_9, 6H_2O)]_\infty$

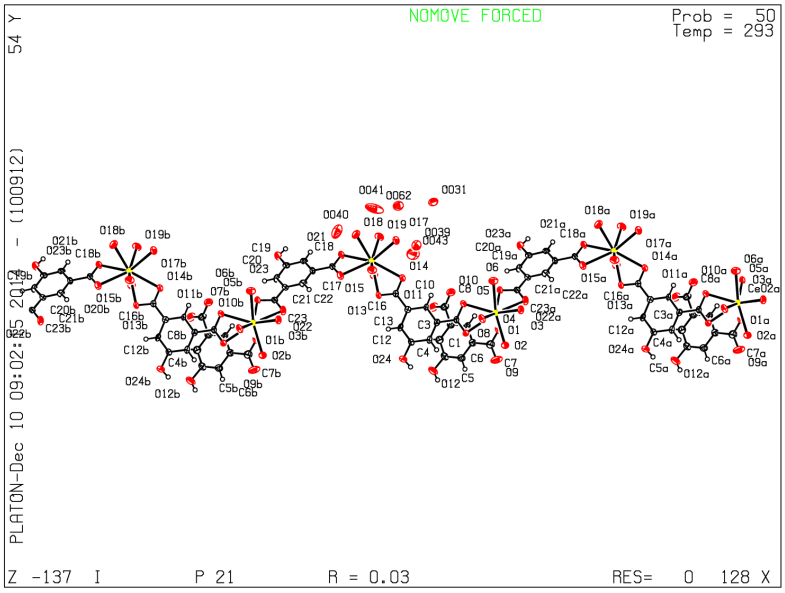

Table 2.1a Atomic parameters for $[Ce_2(hip)_3(H_2O)_9, 6H_2O)]_\infty$

Atom	x/a	y/b	z/c	Atom	x/a	y/b	z/c
Ce02	-0.09386(3)	-0.17680(2)	0.43639(2)	O040	0.9556(7)	0.2267(8)	0.9363(4)
Ce01	0.41401(3)	0.24387(2)	0.93383(2)	O041	0.7366(5)	0.3758(5)	0.6657(3)
O1	-0.2915(4)	-0.1863(6)	0.4900(3)	O043	0.0113(9)	0.4268(7)	0.8389(5)
O2	-0.1740(6)	-0.3895(5)	0.4201(4)	O062	0.6949(12)	0.4499(7)	0.8118(5)
O3	-0.0650(4)	-0.2417(6)	0.2878(3)	C1	-0.2908(5)	-0.2073(5)	0.6356(3)
O4	0.1035(5)	-0.3001(4)	0.4469(3)	C2	-0.2623(6)	-0.0890(7)	0.6513(4)
O5	-0.1871(5)	0.0359(5)	0.4380(3)	C3	-0.2388(6)	-0.0448(5)	0.7329(4)
O6	0.0562(5)	-0.0267(5)	0.3903(4)	C4	-0.2356(7)	-0.1266(7)	0.7987(5)
O7	0.0222(5)	-0.0881(5)	0.5720(3)	C5	-0.2608(6)	-0.2468(6)	0.7823(4)
O8	-0.0332(4)	-0.2760(5)	0.5848(3)	C6	-0.2890(7)	-0.2886(7)	0.7013(4)
O9	-0.3620(7)	-0.3564(5)	0.5332(3)	C7	-0.3178(6)	-0.2537(6)	0.5476(4)
O10	-0.1659(5)	0.1477(5)	0.7003(3)	C8	-0.2093(5)	0.0866(5)	0.7523(4)
O11	-0.2280(5)	0.1265(5)	0.8207(3)	C9	0.0620(5)	-0.1749(9)	0.7087(4)
O12	-0.2567(6)	-0.3242(6)	0.8488(3)	C10	0.1235(6)	-0.0678(7)	0.7442(4)
O13	0.3159(5)	0.0347(5)	0.9375(3)	C11	0.1685(7)	-0.0628(7)	0.8300(4)
O14	0.2396(5)	0.1407(5)	0.8273(3)	C12	0.1522(6)	-0.1618(8)	0.8802(4)
O15	0.2114(5)	0.2612(7)	0.9922(3)	C13	0.0919(7)	-0.2633(9)	0.8450(4)
O16	0.5583(5)	0.0895(5)	0.8858(3)	C14	0.0475(6)	-0.2705(8)	0.7595(4)
O17	0.4363(5)	0.3130(7)	0.7868(3)	C15	0.0151(5)	-0.1805(8)	0.6172(3)
O18	0.6138(5)	0.3616(5)	0.9462(3)	C16	0.2435(6)	0.0422(7)	0.8668(4)
O19	0.3267(6)	0.4552(6)	0.9144(4)	C17	0.5720(5)	0.2446(8)	1.2076(3)
O20	0.5303(5)	0.1566(5)	1.0705(3)	C18	0.5606(6)	0.3457(6)	1.2558(4)
O21	0.4677(5)	0.3430(5)	1.0803(3)	C19	0.6016(6)	0.3407(7)	1.3409(4)
O22	0.7420(5)	-0.0684(5)	1.3244(3)	C20	0.6592(6)	0.2379(8)	1.3782(4)
O23	0.5879(5)	0.4413(5)	1.3872(3)	C21	0.6733(6)	0.1379(6)	1.3288(4)
O24	0.0788(6)	-0.3584(6)	0.8981(3)	C22	0.6280(7)	0.1435(7)	1.2434(5)
O031	0.5264(5)	0.4336(5)	0.5427(3)	C23	0.7462(6)	0.0292(6)	1.3654(4)
O039	0.4958(6)	0.1826(6)	0.6563(4)	C24	0.5212(5)	0.2492(8)	1.1144(4)

Table 2.1b Selected bond lengths (Å) and angles (°) for $[Ce_2(hip)_3(H_2O)_9, 6H_2O)]_\infty$

Atoms	d (Å) or Angle (°)	Atoms	d (Å) or Angle (°)
Ce01—O18	2.484(5)	O14—Ce01—O17	71.60(16)
Ce01—O19	2.524(6)	O18—Ce01—O21	70.48(16)
Ce01—O16	2.532(5)	O19—Ce01—O21	74.57(19)
Ce01—O20	2.537(5)	O16—Ce01—O21	122.12(18)
Ce01—O15	2.540(5)	O20—Ce01—O21	50.48(16)
Ce01—O13	2.555(6)	O15—Ce01—O21	71.14(16)
Ce01—O14	2.570(5)	O13—Ce01—O21	112.52(17)
Ce01—O17	2.579(5)	O14—Ce01—O21	144.97(16)
Ce01—O21	2.600(5)	O17—Ce01—O21	133.6(2)
Ce02—O1	2.444(4)	O1—Ce02—O4	137.05(18)
Ce02—O4	2.498(4)	O1—Ce02—O2	72.3(2)
Ce02—O2	2.510(6)	O4—Ce02—O2	76.09(18)
Ce02—O6	2.529(5)	O1—Ce02—O6	141.2(2)
Ce02—O7	2.527(5)	O4—Ce02—O6	78.68(17)
Ce02—O5	2.566(6)	O2—Ce02—O6	144.37(17)
Ce02—O22^{i}	2.584(5)	O1—Ce02—O7	90.98(16)
Ce02—O3	2.610(4)	O4—Ce02—O7	83.36(17)
Ce02—O8	2.632(5)	O2—Ce02—O7	124.14(19)
O18—Ce01—O19	79.27(19)	O6—Ce02—O7	76.71(17)
O18—Ce01—O16	79.28(18)	O1—Ce02—O5	70.7(2)
O19—Ce01—O16	145.50(18)	O4—Ce02—O5	146.08(17)
O18—Ce01—O20	81.85(18)	O2—Ce02—O5	137.83(14)
O19—Ce01—O20	125.0(2)	O6—Ce02—O5	70.57(17)
O16—Ce01—O20	77.79(17)	O7—Ce02—O5	76.10(18)
O18—Ce01—O15	135.63(19)	O1—Ce02—O22^{i}	75.83(16)
O19—Ce01—O15	69.8(2)	O4—Ce02—O22^{i}	139.24(15)
O16—Ce01—O15	141.6(2)	O2—Ce02—O22^{i}	100.96(19)
O20—Ce01—O15	90.52(17)	O6—Ce02—O22^{i}	82.36(19)
O18—Ce01—O13	145.98(19)	O7—Ce02—O22^{i}	126.59(17)
O19—Ce01—O13	134.74(16)	O5—Ce02—O22^{i}	50.57(16)
O16—Ce01—O13	70.74(18)	O1—Ce02—O3	125.93(16)
O20—Ce01—O13	76.54(18)	O4—Ce02—O3	70.36(15)
O15—Ce01—O13	71.0(2)	O2—Ce02—O3	74.92(19)
O18—Ce01—O14	142.58(17)	O6—Ce02—O3	73.12(18)
O19—Ce01—O14	97.19(19)	O7—Ce02—O3	143.08(16)
O16—Ce01—O14	84.00(18)	O5—Ce02—O3	112.29(18)
O20—Ce01—O14	126.84(17)	O22^{i}—Ce02—O3	69.71(16)
O15—Ce01—O14	74.07(18)	O1—Ce02—O8	74.32(15)
O13—Ce01—O14	50.30(16)	O4—Ce02—O8	69.52(14)
O18—Ce01—O17	71.81(18)	O2—Ce02—O8	73.98(18)
O19—Ce01—O17	72.8(2)	O6—Ce02—O8	119.42(18)
O16—Ce01—O17	75.01(19)	O7—Ce02—O8	50.16(16)
O20—Ce01—O17	144.98(17)	O5—Ce02—O8	113.80(16)
O15—Ce01—O17	124.45(18)	O22^{i}—Ce02—O8	149.83(15)
O13—Ce01—O17	113.83(19)	O3—Ce02—O8	133.75(18)

2.2 $[La_2(hip)_2(H_2O)_{10}, (hip), 4H_2O]_\infty$

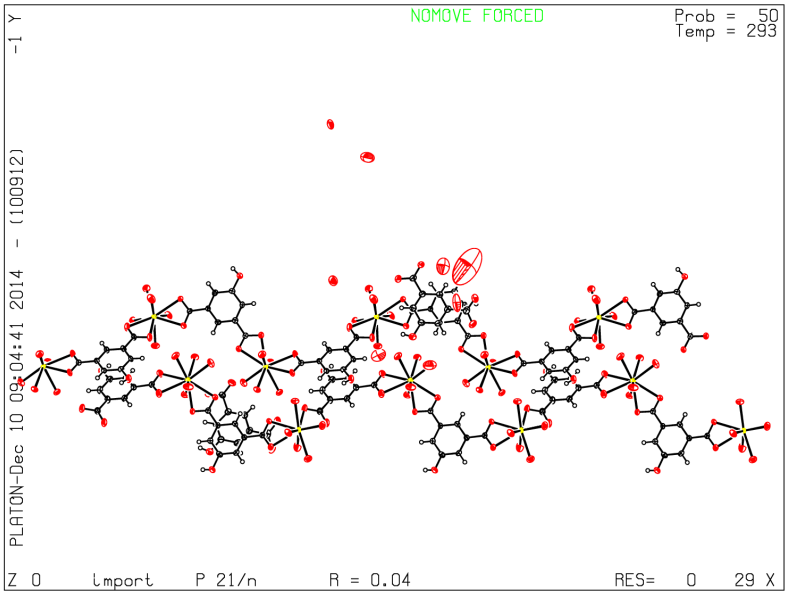

Table 2.2a Atomic parameters for $[La_2(hip)_2(H_2O)_{10}, (hip), 4H_2O]_\infty$

Atom	x/a	y/b	z/c	Atom	x/a	y/b	z/c
La1	0.18112(2)	0.47885(1)	0.03144(2)	O53	0.7171(5)	0.3225(5)	0.7859(4)
La2	0.31306(2)	0.23405(1)	-0.02591(2)	O54	0.4698(4)	0.1902(3)	0.1970(4)
La3	0.80922(2)	0.01992(1)	-0.02443(2)	O55	0.0367(3)	0.5571(3)	0.1884(3)
La4	-0.32394(2)	0.27414(1)	0.01343(2)	O56	0.7615(3)	0.1899(5)	0.7370(4)
O1	0.0683(2)	0.4203(2)	0.0596(2)	O57	0.3689(5)	0.8128(4)	0.7419(5)
O2	0.1759(2)	0.3659(2)	0.0804(2)	O101	0.1149(5)	0.4326(4)	-0.2054(4)
O3	0.1537(2)	0.5925(2)	0.0481(2)	O103	0.7988(19)	0.364(2)	0.7002(13)
O4	0.2108(3)	0.4900(2)	0.1645(2)	C48	0.0603(3)	0.3124(3)	0.0880(3)
O5	0.3177(2)	0.52954(18)	0.0848(2)	C50	-0.0624(3)	0.2635(3)	0.0814(3)
O6	0.3178(2)	0.43437(19)	0.0440(2)	C53	0.5610(3)	0.4393(3)	0.0798(3)
O7	0.2153(2)	0.5341(2)	-0.0674(2)	C56	0.4822(3)	0.5411(3)	0.1135(3)
O8	0.0543(2)	0.5081(2)	-0.0640(2)	C58	-0.0681(3)	0.1807(3)	-0.0865(3)
O9	0.1546(3)	0.40413(19)	-0.0693(2)	C59	0.4411(3)	0.4876(2)	0.0852(3)
O10	0.6067(2)	0.59566(19)	0.1521(2)	C61	0.4463(4)	0.3537(3)	0.2358(3)
O11	0.5662(2)	0.33163(19)	0.0508(2)	C63	0.0511(3)	0.2323(3)	-0.0824(3)
O12	0.6694(2)	0.3876(2)	0.0561(3)	C64	0.4140(3)	0.4095(3)	0.2490(3)
O13	-0.3352(3)	0.3451(2)	-0.0918(2)	C65	0.4806(3)	0.4361(3)	0.0699(3)
O14	-0.4528(2)	0.2494(2)	-0.0771(2)	C66	0.5024(3)	-0.0377(3)	-0.1049(3)
O15	-0.2938(2)	0.2106(2)	-0.0820(2)	C67	0.5624(3)	0.5436(3)	0.1241(3)
O16	-0.3581(2)	0.16370(19)	0.0355(2)	C68	-0.5965(3)	0.2733(3)	-0.2315(3)
O17	-0.2991(2)	0.2598(2)	0.1470(2)	C69	-0.0205(3)	0.3154(3)	0.0723(3)
O18	-0.1846(2)	0.31576(19)	0.0348(2)	C70	-0.1098(3)	0.2348(3)	-0.1126(3)
O19	-0.1890(2)	0.21937(19)	0.0692(2)	C71	-0.6156(3)	0.0989(3)	-0.2652(3)
O20	0.1008(2)	0.15302(19)	0.1500(3)	C72	0.0100(3)	0.2864(3)	-0.1101(3)
O21	0.6712(2)	0.06580(19)	-0.0407(2)	C73	0.6337(3)	0.0156(3)	-0.0604(3)
O22	0.6704(2)	-.03383(18)	-0.0626(2)	C74	-0.1091(3)	0.1240(3)	-0.0709(3)
O23	0.7935(2)	-0.0425(2)	0.0780(2)	C75	-0.4807(3)	0.1264(3)	-0.2444(3)

O24	0.8411(3)	-0.0902(2)	-0.0515(2)	C76	0.5073(3)	0.0710(3)	-0.0743(3)
O25	0.7616(3)	0.0154(3)	-0.1572(2)	C77	-0.0225(3)	0.2082(2)	0.1081(3)
O26	0.9425(2)	-0.0041(2)	0.0640(2)	C79	0.5705(3)	0.4035(3)	0.2525(3)
O27	0.8260(3)	0.09285(19)	0.0798(2)	C81	0.3833(3)	0.0177(3)	-0.1136(3)
O28	-0.1759(2)	0.1308(2)	-0.0622(2)	C82	0.6551(3)	0.3983(3)	0.2519(3)
O29	-0.0780(2)	0.0710(2)	-0.0650(2)	C83	0.5397(3)	0.4593(3)	0.2671(3)
O30	0.1754(2)	0.2824(2)	-0.0652(3)	C84	0.6006(3)	0.3831(3)	0.0613(3)
O31	0.2903(3)	0.2879(2)	0.0780(2)	C85	0.1393(3)	0.2328(3)	-0.0611(3)
O32	0.3449(3)	0.1565(2)	0.0739(2)	C86	0.3545(3)	0.4834(3)	0.0710(3)
O33	0.3149(2)	0.12658(19)	-0.0788(2)	C87	-0.4986(3)	0.1890(3)	-0.2362(3)
O34	0.4227(2)	0.1803(2)	-0.0635(2)	C88	0.6014(3)	0.4935(3)	0.1061(3)
O35	0.4451(2)	0.2632(2)	0.0650(2)	C89	-0.0707(3)	0.2870(3)	-0.1260(3)
O36	0.2612(3)	0.2417(2)	-0.1609(2)	C92	0.5460(3)	0.0162(3)	-0.0807(3)
O37	0.3371(3)	0.3469(2)	-0.0522(2)	C93	0.4612(3)	0.4621(3)	0.2653(3)
O38	-0.1136(2)	0.3391(2)	-0.1546(3)	C96	-0.5752(3)	0.2064(3)	-0.2427(3)
O39	0.3803(2)	-.09090(19)	-0.1460(2)	C97	-0.6344(3)	0.1610(3)	-0.2583(3)
O40	-0.5423(2)	0.3085(2)	-0.1962(2)	C99	0.5238(4)	0.3507(3)	0.2375(3)
O41	-0.6671(2)	0.2902(2)	-0.2554(2)	C101	0.3861(3)	0.1295(3)	-0.0772(3)
O42	-0.3442(3)	0.1473(3)	-0.2089(3)	C102	0.0596(3)	0.2058(2)	0.1242(3)
O43	-0.3830(3)	0.0540(3)	-0.2545(3)	C103	-0.5395(4)	0.0821(3)	-0.2596(3)
O45	0.6967(2)	0.4460(2)	0.2615(3)	C104	0.0130(3)	0.1791(3)	-0.0720(3)
O46	0.6792(3)	0.3448(2)	0.2421(3)	C109	0.4213(3)	-0.0364(3)	-0.1221(3)
O47	0.4013(3)	0.3005(2)	0.2201(3)	C131	0.1034(3)	0.3693(3)	0.0757(3)
O48	0.4729(2)	0.5624(2)	0.3177(2)	C200	-0.3964(4)	0.1070(4)	-0.2363(3)
O49	0.3529(2)	0.5282(2)	0.2632(2)	C201	0.4257(3)	0.5221(3)	0.2822(3)
O50	0.1777(2)	0.1839(2)	-0.0380(3)	C202	0.1001(3)	0.2575(2)	0.1125(3)
O51	-0.6714(2)	0.0527(2)	-0.2793(3)	C203	-0.1499(3)	0.2661(3)	0.0612(3)
O52	0.2216(3)	0.9262(3)	0.7984(2)	C204	0.4259(3)	0.0717(2)	-0.0897(3)

Table 2.2b Selected bond lengths (Å) and angles (°) for $[La_2(hip)_2(H_2O)_{10}, (hip), 4H_2O]_\infty$

Atoms	d (Å) or Angle (°)	Atoms	d (Å) or Angle (°)
La1—O9	2.497(4)	O32—La2—O50	77.41(15)
La1—O3	2.526(4)	O33—La2—O30	111.84(13)
La1—O7	2.526(4)	O33—La2—O34	50.71(12)
La1—O4	2.551(5)	O33—La2—O35	112.74(14)
La1—O8	2.558(4)	O33—La2—O36	70.69(15)
La1—O6	2.568(4)	O33—La2—O37	138.99(14)
La1—O1	2.580(4)	O33—La2—O50	73.44(13)
La1—O5	2.590(4)	O34—La2—O35	72.24(15)
La1—O2	2.621(4)	O34—La2—O50	124.15(13)
La2—O31	2.509(4)	O35—La2—O50	142.83(15)
La2—O32	2.521(5)	O36—La2—O34	77.86(15)
La2—O33	2.536(4)	O36—La2—O35	132.99(16)
La2—O37	2.538(4)	O36—La2—O50	84.14(16)
La2—O30	2.567(4)	O37—La2—O30	76.11(14)
La2—O36	2.569(5)	O37—La2—O34	99.98(14)
La2—O34	2.576(4)	O37—La2—O35	74.77(15)
La2—O35	2.581(4)	O37—La2—O36	75.73(15)
La2—O50	2.595(4)	O37—La2—O50	125.97(14)
La3—O25	2.522(5)	O21—La3—O22	49.29(12)
La3—O24	2.524(4)	O21—La3—O29^{ii}	126.65(13)
La3—O23	2.527(4)	O23—La3—O21	88.02(14)
La3—O28^{ii}	2.530(4)	O23—La3—O22	71.04(13)
La3—O27	2.542(4)	O23—La3—O26	69.29(14)
La3—O26	2.551(4)	O23—La3—O27	71.35(14)
La3—O21	2.588(4)	O23—La3—O28^{ii}	141.70(15)
La3—O29^{ii}	2.630(4)	O23—La3—O29^{ii}	138.82(13)
La3—O22	2.633(4)	O24—La3—O21	126.71(13)
La3—C74^{ii}	2.964(6)	O24—La3—O22	77.56(13)
La4—O16	2.515(4)	O24—La3—O23	76.46(14)
La4—O14	2.516(4)	O24—La3—O26	74.60(15)
La4—O15	2.525(4)	O24—La3—O27	140.42(14)
La4—O13	2.546(4)	O24—La3—O28^{ii}	139.72(14)
La4—O18	2.561(4)	O24—La3—O29^{ii}	94.51(14)
La4—O17	2.578(4)	O25—La3—O21	82.94(15)
La4—O12^{i}	2.590(4)	O25—La3—O22	71.98(15)
La4—O19	2.612(4)	O25—La3—O23	137.85(16)
La4—O11^{i}	2.613(4)	O25—La3—O24	76.48(17)
O1—La1—O2	49.57(12)	O25—La3—O26	131.59(14)
O1—La1—O5	144.93(14)	O25—La3—O27	142.99(16)
O3—La1—O1	104.11(14)	O25—La3—O28^{ii}	75.95(17)
O3—La1—O2	144.15(14)	O25—La3—O29^{ii}	75.00(16)
O3—La1—O4	76.14(16)	O26—La3—O21	145.17(14)
O3—La1—O5	74.87(13)	O26—La3—O22	135.62(14)
O3—La1—O6	124.24(13)	O26—La3—O29^{ii}	69.57(14)

O3—La1—O7	75.74(14)	O27—La3—O21	74.96(13)
O3—La1—O8	72.39(14)	O27—La3—O22	111.85(14)
O4—La1—O1	75.51(15)	O27—La3—O26	72.91(14)
O4—La1—O2	73.72(16)	O27—La3—O29^{ii}	94.78(14)
O4—La1—O5	70.20(14)	O28^{ii}—La3—O21	77.83(13)
O4—La1—O6	92.38(15)	O28^{ii}—La3—O22	120.01(13)
O4—La1—O8	127.38(15)	O28^{ii}—La3—O26	103.48(15)
O5—La1—O2	111.72(13)	O28^{ii}—La3—O27	70.65(14)
O6—La1—O1	125.78(13)	O28^{ii}—La3—O29^{ii}	50.05(13)
O6—La1—O2	76.22(13)	O29^{ii}—La3—O22	146.98(14)
O6—La1—O5	50.36(12)	O12^{i}—La4—O11^{i}	49.48(12)
O7—La1—O1	142.01(14)	O12^{i}—La4—O19	114.26(13)
O7—La1—O2	140.08(15)	O13—La4—O11^{i}	94.28(14)
O7—La1—O4	137.92(14)	O13—La4—O12^{i}	73.16(15)
O7—La1—O5	72.63(13)	O13—La4—O17	149.97(14)
O7—La1—O6	78.49(14)	O13—La4—O18	76.05(13)
O7—La1—O8	71.14(14)	O13—La4—O19	116.75(13)
O8—La1—O1	72.74(14)	O14—La4—O11^{i}	72.40(14)
O8—La1—O2	112.25(14)	O14—La4—O12^{i}	108.02(14)
O8—La1—O5	135.80(14)	O14—La4—O13	73.10(14)
O8—La1—O6	140.24(14)	O14—La4—O15	72.90(14)
O9—La1—O1	83.81(15)	O14—La4—O17	123.22(14)
O9—La1—O2	71.81(14)	O14—La4—O18	145.85(14)
O9—La1—O3	136.59(14)	O14—La4—O19	137.66(14)
O9—La1—O4	145.46(16)	O15—La4—O11^{i}	145.04(13)
O9—La1—O5	121.63(13)	O15—La4—O12^{i}	142.60(14)
O9—La1—O6	77.54(14)	O15—La4—O13	71.56(14)
O9—La1—O7	72.92(15)	O15—La4—O17	134.66(14)
O9—La1—O8	69.52(14)	O15—La4—O18	83.82(14)
O30—La2—O34	146.91(15)	O15—La4—O19	72.35(13)
O30—La2—O35	134.97(15)	O16—La4—O11^{i}	98.60(13)
O30—La2—O36	69.29(16)	O16—La4—O12^{i}	141.95(14)
O30—La2—O50	49.85(13)	O16—La4—O13	137.91(14)
O31—La2—O30	71.62(14)	O16—La4—O14	73.04(14)
O31—La2—O32	72.93(15)	O16—La4—O15	75.15(14)
O31—La2—O33	141.78(15)	O16—La4—O17	71.51(14)
O31—La2—O34	140.76(14)	O16—La4—O18	125.09(13)
O31—La2—O35	69.75(15)	O16—La4—O19	75.29(12)
O31—La2—O36	137.43(15)	O17—La4—O11^{i}	70.82(14)
O31—La2—O37	79.23(15)	O17—La4—O12^{i}	77.51(15)
O31—La2—O50	83.43(15)	O17—La4—O19	70.12(13)
O32—La2—O30	118.24(16)	O18—La4—O11^{i}	124.65(13)
O32—La2—O33	72.58(15)	O18—La4—O12^{i}	76.04(13)
O32—La2—O34	85.69(16)	O18—La4—O17	90.91(14)
O32—La2—O35	70.52(15)	O18—La4—O19	49.95(12)
O32—La2—O37	141.16(15)		

π-stacking interactions. Selected C-C distances

Atom 1	symmetry	Atom 2	symmetry	distance (Å)
C102	x, y, z	C104	x, y, z	3.7834(10)
C58	x, y, z	C77	x, y, z	3.7564(9)
C69	x, y, z	C89	x, y, z	3.8233(10)
C48	x, y, z	C72	x, y, z	3.8141(10)
C63	x, y, z	C202	x, y, z	3.7496(9)

Selected hydrogen bond distances in stair-like double-chains molecular motifs.

Atom 1	symmetry	Atom 2	symmetry	distance (Å)
O2	x, y, z	O31	x, y, z	2.6546(5)
O9	x, y, z	O30	x, y, z	2.6312(6)
O19	x, y, z	O27	-1+x, y, z	2.7248(6)
O15	x, y, z	O28	x, y, z	2.6517(5)
O16	x, y, z	O21	-1+x, y, z	2.7306(5)
O14	x, y, z	O34	-1+x, y, z	2.7561(6)
O11	x, y, z	O35	x, y, z	2.7015(5)

Selected hydrogen bond distances between stair-like double-chains molecular motifs.

Atom 1	Symmetry	Atom 2	symmetry	distance (Å)
O17	x, y, z	O57	-x, 1-y, 1-z	3.2494(5)
O45	x, y, z	O51	1.5+x, 0.5-y, 0.5+z	2.7208(6)
O36	x, y, z	O57	0.5-x, -0.5+y, 0.5-z	2.8414(5)
O31	x, y, z	O47	x, y, z	2.9350(6)
O49	x, y, z	O53	1-x, 1-y, 1-z	3.4662(7)
O4	x, y, z	O49	x, y, z	2.8242(6)
O25	x, y, z	O49	0.5+x, 0.5-y, -0.5+z	2.7631(5)
O15	x, y, z	O42	x, y, z	2.7671(6)
O4	x, y, z	O43	0.5+x, 0.5-y, 0.5+z	2.8200(5)

π−stacking interactions between stair-like double-chains molecular motifs.
Selected C-C distances.

Atom 1	symmetry	Atom 2	symmetry	distance (Å)
C79	x, y, z	C88	x, y, z	3.6755(7)
C67	x, y, z	C83	x, y, z	3.4982(7)
C53	x, y, z	C99	x, y, z	3.8969(7)
C61	x, y, z	C65	x, y, z	3.9559(8)
C56	x, y, z	C93	x, y, z	3.5828(7)
C59	x, y, z	C64	x, y, z	3.8255(8)

ATG curves of Family 1, Family 2, Family 4 and Family 5.

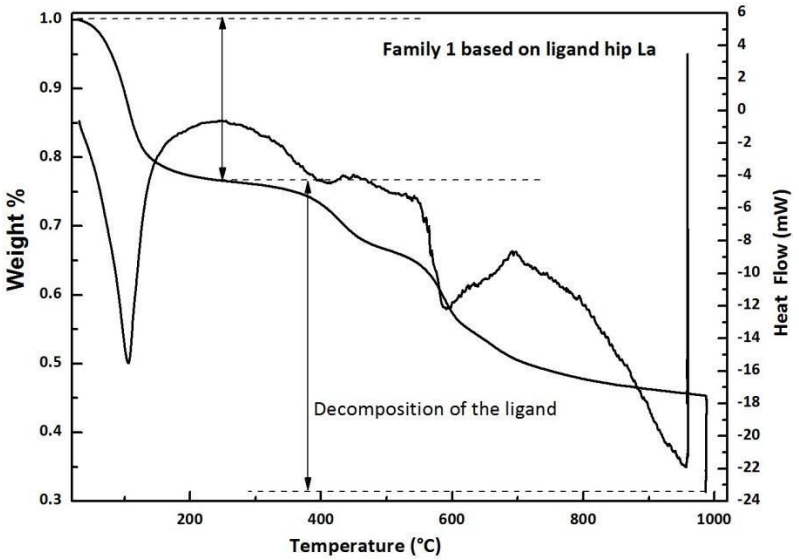

TGA/TDA curves for microcrystalline powders of Family 1 (La)

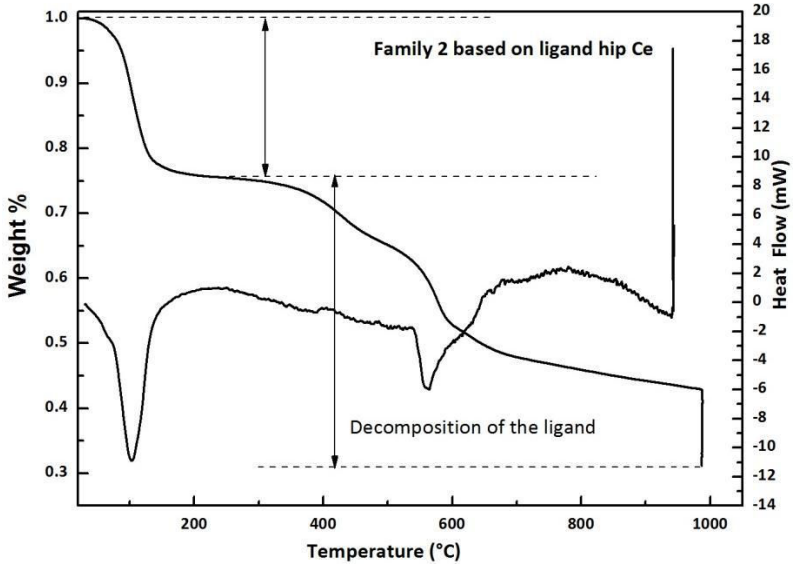

TGA/TDA curves for microcrystalline powders of Family 2 (Ce)

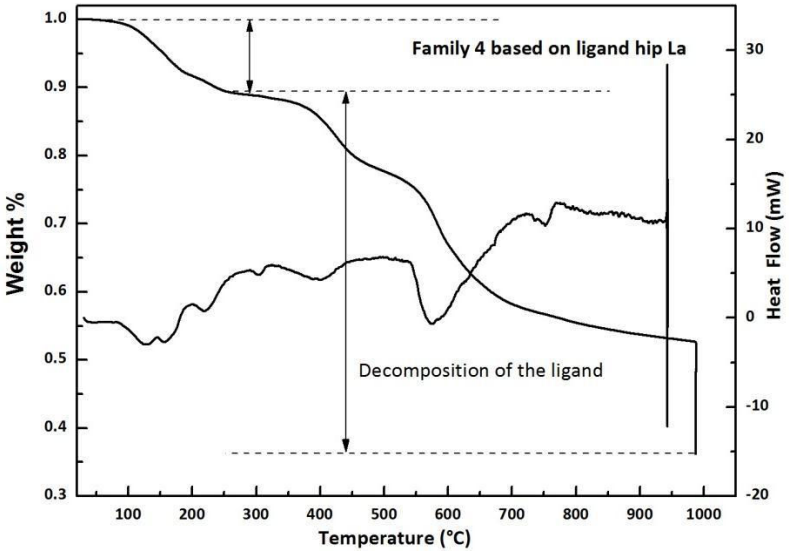

TGA/TDA curves for microcrystalline powders of Family 4 (La)

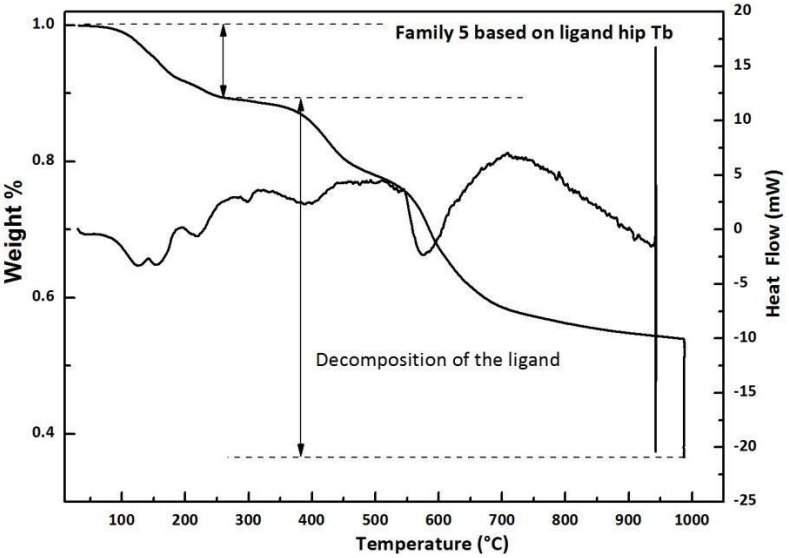

TGA/TDA curves for microcrystalline powders of Family 5 (Tb)

3. Ligand H_2nip

Crystallographic data

3.1 $[Gd(nip)_2(H_2O)_4, 3H_2O]$

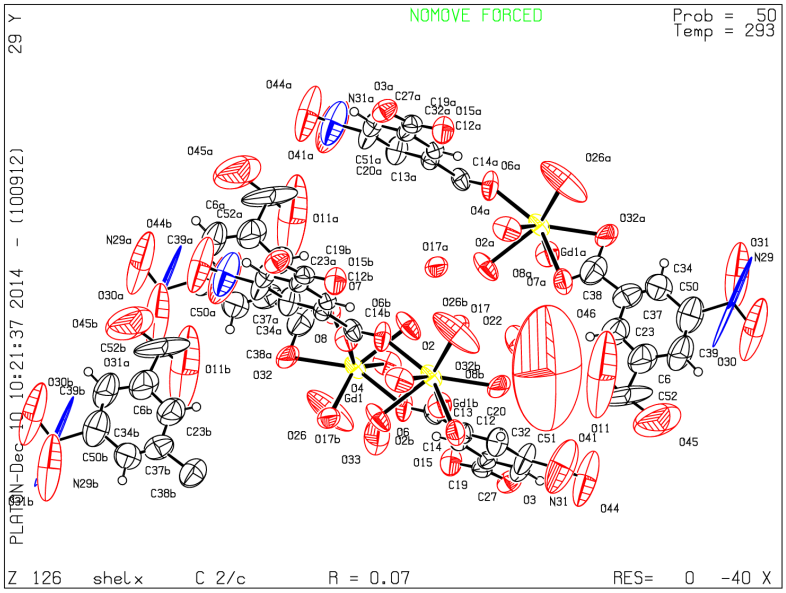

Table 3.1a Atomic parameters for $[Gd(nip)_2(H_2O)_4, 3H_2O]$

Atom	x/a	y/b	z/c	Atom	x/a	y/b	z/c
Gd1	0.41544(6)	-0.08057(2)	0.45364(3)	O46	0.164(11)	0.169(2)	0.452(7)
O2	0.1753(11)	-0.0338(4)	0.4814(4)	N29	-0.592(3)	0.3154(19)	0.394(4)
O3	0.0357(11)	0.0241(3)	0.1045(4)	N31	0.242(3)	0.1627(5)	0.2498(10)
O4	0.1510(12)	-0.0915(3)	0.3692(4)	C6	-0.163(3)	0.2484(6)	0.3894(11)
O6	0.4391(12)	-0.0135(3)	0.3963(4)	C12	0.2789(11)	0.0200(3)	0.2738(4)
O7	0.2449(10)	-0.1350(3)	0.5041(5)	C13	0.3458(12)	0.0488(3)	0.3268(5)
O8	0.5163(11)	-0.0560(3)	0.5611(4)	C14	0.4289(12)	0.0285(4)	0.3928(5)
O11	0.079(5)	0.2342(10)	0.431(3)	C19	0.1197(13)	0.0064(4)	0.1565(5)
O15	0.1438(13)	-0.0352(3)	0.1644(4)	C20	0.3344(18)	0.0959(4)	0.3190(7)
O17	0.2743(11)	0.0709(3)	0.5515(4)	C23	-0.188(3)	0.2107(6)	0.4285(10)
O22	0.0496(17)	0.1082(6)	0.4496(6)	C27	0.1866(19)	0.0852(4)	0.2056(6)
O26	0.4777(18)	-0.1256(7)	0.3624(9)	C32	0.1974(12)	0.0379(4)	0.2123(5)
O30	-0.591(4)	0.3372(7)	0.3400(16)	C34	-0.478(3)	0.2306(5)	0.4365(9)
O31	-0.738(4)	0.2994(6)	0.3979(14)	C37	-0.358(2)	0.2053(6)	0.4490(8)
O32	0.569(3)	-0.1477(4)	0.5062(9)	C38	-0.367(3)	0.1598(6)	0.4881(8)
O33	0.270(3)	-0.1125(6)	0.2399(9)	C39	-0.298(3)	0.2793(5)	0.3668(11)
O41	0.324(3)	0.1864(5)	0.2914(10)	C50	-0.466(3)	0.2717(6)	0.3927(11)
O44	0.148(3)	0.1772(5)	0.2013(9)	C51	0.253(2)	0.1127(4)	0.2591(7)
O45	-0.003(5)	0.2826(7)	0.3173(15)	C52	0.042(6)	0.2522(8)	0.3766(16)

Table 3.1b Selected bond lengths (Å) and angles (°) for [$Gd(nip)_2(H_2O)_4$, $3H_2O$]

Atoms	d (Å) or Angle (°)	Atoms	d (Å) or Angle (°)
Gd1—O8	2.302(7)	O8—Gd1—O32	77.1(5)
Gd1—O6	2.304(8)	O6—Gd1—O32	146.8(4)
Gd1—O26	2.379(11)	O26—Gd1—O32	75.6(7)
Gd1—O7	2.386(8)	O7—Gd1—O32	61.8(4)
Gd1—$O17^{i}$	2.390(8)	$O17^{i}$—Gd1—O32	73.2(4)
Gd1—O32	2.440(11)	O8—Gd1—O2	75.6(3)
Gd1—O2	2.418(7)	O6—Gd1—O2	76.0(4)
Gd1—O4	2.437(8)	O26—Gd1—O2	138.3(4)
O8—Gd1—O6	99.8(3)	O7—Gd1—O2	78.3(3)
O8—Gd1—O26	146.1(5)	$O17^{i}$—Gd1—O2	136.7(4)
O6—Gd1—O26	92.3(6)	O32—Gd1—O2	132.8(3)
O8—Gd1—O7	85.6(3)	O8—Gd1—O4	144.5(3)
O6—Gd1—O7	151.4(3)	O6—Gd1—O4	83.1(3)
O26—Gd1—O7	98.7(6)	O26—Gd1—O4	68.1(4)
O8—Gd1—$O17^{i}$	79.9(3)	O7—Gd1—O4	76.8(3)
O6—Gd1—$O17^{i}$	73.7(3)	$O17^{i}$—Gd1—O4	133.6(3)
O26—Gd1—$O17^{i}$	73.2(4)	O32—Gd1—O4	118.7(6)
O7—Gd1—$O17^{i}$	134.8(3)	O2—Gd1—O4	70.8(3)

3.2 $[Gd_4(nip)_6(H_2O)_{14}, 5H_2O]_\infty$

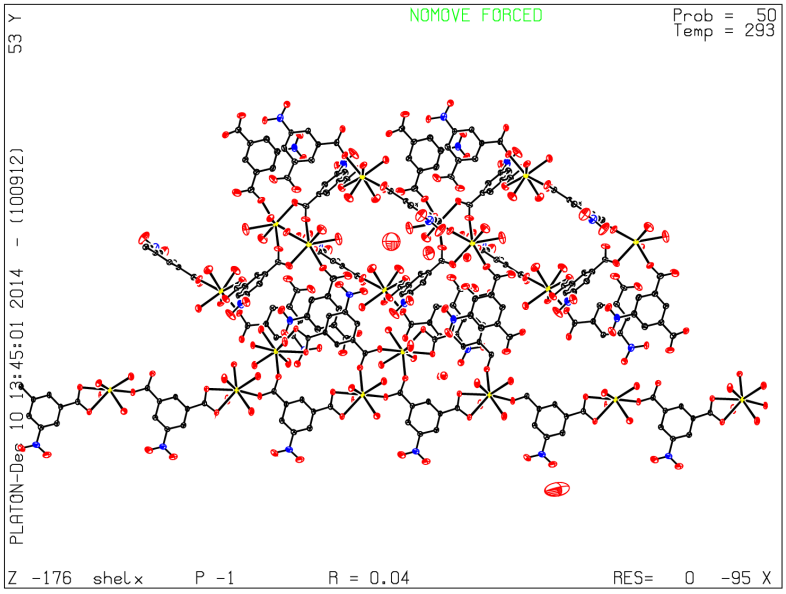

Table 3.2a Atomic parameters for $[Gd_4(nip)_6(H_2O)_{14}, 5H_2O]_\infty$

Atom	x/a	y/b	z/c	Atom	x/a	y/b	z/c
Gd1	0.60932(2)	-0.16490(2)	0.80527(2)	O102	0.8387(11)	0.0153(9)	0.9741(5)
Gd2	0.61795(2)	0.43645(2)	0.42800(2)	O103	0.5196(8)	0.0667(5)	0.9399(3)
Gd3	1.10284(2)	-0.07518(2)	0.42083(2)	O105	0.923(2)	0.9789(8)	0.0803(5)
Gd4	1.07080(2)	0.63715(2)	0.96150(2)	C1	0.7890(3)	0.0912(3)	0.28578(14)
O1	0.7382(4)	0.0894(4)	0.18780(14)	C2	0.8424(3)	0.0506(3)	0.32634(14)
O2	0.8262(6)	-0.0100(5)	0.21044(17)	C3	0.8433(3)	0.0837(2)	0.38485(13)
O3	0.6786(2)	0.3388(2)	0.34668(11)	C4	0.7901(3)	0.1544(2)	0.40117(14)
O4	0.6681(2)	0.28049(19)	0.43164(10)	C5	0.7414(3)	0.1959(2)	0.35920(13)
O5	0.9436(2)	-0.0218(2)	0.41525(11)	C6	0.7411(3)	0.1654(3)	0.30034(14)
O6	0.9169(3)	0.0912(2)	0.48229(11)	C7	0.9048(3)	0.0477(3)	0.43105(14)
O7	1.3124(2)	-0.0260(2)	0.43979(12)	C8	1.1633(3)	-0.2428(3)	0.37732(15)
O8	1.1912(3)	0.1088(2)	0.46588(13)	C9	1.2228(3)	-0.3159(3)	0.35809(14)
O9	1.1512(3)	0.0301(2)	0.34233(12)	C10	1.2186(3)	-0.3483(3)	0.29915(15)
O10	0.9105(3)	-0.2294(3)	0.40568(18)	C11	1.2719(3)	-0.4183(3)	0.28404(15)
O11	1.1415(2)	-0.2351(2)	0.42975(11)	C12	1.3339(3)	-0.4528(3)	0.32411(15)
O12	1.1387(3)	-0.1891(2)	0.34175(11)	C13	1.3410(3)	-0.4160(3)	0.38287(14)
O13	1.2229(5)	-0.4180(4)	0.18664(15)	C14	1.2832(3)	-0.3492(3)	0.39992(15)
O14	1.2872(4)	-0.5364(3)	0.20976(14)	C15	1.4107(3)	-0.4483(3)	0.42757(14)
O15	0.4572(2)	0.4882(2)	0.40982(12)	C16	0.6917(3)	0.2755(2)	0.37990(13)
O16	0.5812(3)	0.4102(2)	0.52080(11)	C17	0.4353(3)	0.1611(2)	0.65027(14)
O17	0.7021(3)	0.6182(2)	0.47523(13)	C18	0.4481(3)	0.2157(3)	0.70568(16)
O18	0.6653(3)	0.5445(2)	0.34969(14)	C19	0.4938(4)	0.1814(3)	0.75248(16)
O19	0.8247(2)	0.4783(2)	0.46501(15)	C20	0.5251(4)	0.0951(3)	0.74717(16)
O21	0.3430(3)	0.2660(2)	0.60732(13)	C21	0.5139(3)	0.0422(3)	0.69104(14)
O22	0.3659(3)	0.1375(3)	0.55025(13)	C22	0.4702(3)	0.0751(3)	0.64324(14)
O23	0.4918(6)	0.3186(4)	0.81471(18)	C23	0.5020(5)	0.2356(4)	0.81063(18)
O24	0.5255(8)	0.1991(5)	0.85150(18)	C24	0.5425(3)	-0.0556(3)	0.68430(15)

O25	0.5527(3)	-0.0917(2)	0.63543(12)	C25	0.4791(3)	-0.4010(3)	0.86136(15)
O26	0.5503(3)	-0.0966(2)	0.72992(12)	C26	0.5056(3)	-0.4760(3)	0.89669(14)
O27	0.6685(3)	-0.2814(2)	0.74427(13)	C27	0.6244(3)	-0.4648(3)	0.91176(14)
O28	0.4060(2)	-0.2848(2)	0.76928(12)	C28	0.6462(3)	-0.5357(3)	0.94537(14)
O29	0.5081(3)	-0.1269(3)	0.88328(16)	C29	0.5509(3)	-0.6164(3)	0.96435(15)
O30	0.7718(3)	-0.1501(3)	0.88013(15)	C30	0.4356(3)	-0.6238(3)	0.94914(15)
O31	0.5676(2)	-0.3218(2)	0.85039(13)	C31	0.4097(3)	-0.5562(3)	0.91461(16)
O32	0.3702(3)	-0.4203(2)	0.84536(14)	C32	0.7735(3)	-0.5227(3)	0.96369(15)
O33	0.2326(3)	-0.7128(4)	0.9554(2)	C33	0.7988(3)	0.0353(3)	0.81053(16)
O34	0.3556(4)	-0.7577(4)	1.0056(2)	C34	0.9050(3)	0.1403(3)	0.81563(16)
O35	1.2147(3)	0.5840(2)	1.00233(13)	C35	0.9959(3)	0.1504(3)	0.78015(16)
O36	0.8592(2)	0.5503(2)	0.94543(13)	C36	1.0909(3)	0.2486(3)	0.78415(15)
O37	0.7972(3)	-0.0406(2)	0.77492(13)	C37	1.0998(3)	0.3360(3)	0.82073(15)
O38	0.7154(3)	0.0245(2)	0.84204(13)	C38	1.0096(3)	0.3239(3)	0.85717(14)
O39	1.1694(4)	0.1850(3)	0.70890(18)	C39	0.9126(3)	0.2270(3)	0.85506(16)
O40	1.2742(3)	0.3427(3)	0.75221(16)	C40	1.0221(3)	0.4174(3)	0.89934(14)
O41	1.0719(3)	0.5079(2)	0.88530(12)	C41	1.0053(4)	0.7374(4)	0.83945(17)
O42	0.9821(3)	0.4016(3)	0.94772(11)	C42	0.9981(3)	0.6932(3)	0.77677(16)
O43	0.9783(3)	0.7700(3)	0.9818(2)	C43	1.0476(3)	0.6192(3)	0.76228(16)
O44	1.2225(3)	0.8035(3)	1.01020(17)	C44	1.0350(3)	0.5787(3)	0.70380(16)
O45	1.2858(3)	0.7162(3)	0.90443(16)	C45	0.9767(3)	0.6073(3)	0.65974(16)
O46	1.0653(3)	0.7112(2)	0.87622(12)	C46	0.9268(3)	0.6811(3)	0.67477(15)
O47	0.9557(5)	0.7982(5)	0.85118(17)	C47	0.9390(3)	0.7242(3)	0.73313(15)
O48	0.7856(2)	0.7527(2)	0.64757(11)	C48	0.8558(3)	0.7114(3)	0.62880(15)
O49	0.8689(3)	0.6930(3)	0.57688(12)	N1	0.7852(4)	0.0558(3)	0.22351(14)
O50	1.0549(3)	0.4480(3)	0.64053(16)	N2	1.2601(4)	-0.4602(3)	0.22219(15)
O51	1.1612(3)	0.4928(3)	0.72480(15)	N3	0.3783(3)	0.1907(3)	0.59862(16)
O52	0.4414(2)	0.2820(2)	0.39888(15)	N4	0.3349(3)	-0.7053(3)	0.97106(18)
O100	0.9695(3)	0.3570(2)	0.48920(14)	N5	1.1859(3)	0.2597(3)	0.74607(16)
O101	0.5699(3)	0.1213(3)	0.50138(15)	N6	1.0866(3)	0.5004(3)	0.68850(16)

Table 3.2b Selected bond lengths (Å) and angles (°) for $[Gd_4(nip)_6(H_2O)_{14}, 5H_2O]_\infty$

Atoms	d (Å) or Angle (°)	Atoms	d (Å) or Angle (°)
O3—Gd2	2.535(2)	O52—Gd2—O17	146.32(10)
O4—Gd2	2.469(2)	O19—Gd2—O17	72.43(10)
O5—Gd3	2.320(2)	O18—Gd2—O17	74.63(11)
O6—Gd3^{i}	2.311(3)	O16—Gd2—O4	81.94(9)
O7—Gd3	2.357(3)	O15—Gd2—O4	143.07(9)
O8—Gd3	2.443(3)	O52—Gd2—O4	71.04(9)
O9—Gd3	2.414(3)	O19—Gd2—O4	65.99(9)
O10—Gd3	2.452(3)	O18—Gd2—O4	122.68(9)
O11—Gd3	2.462(2)	O17—Gd2—O4	135.88(9)
O12—Gd3	2.481(3)	O16—Gd2—O3	134.11(9)
O15—Gd2	2.349(2)	O15—Gd2—O3	119.98(9)
O16—Gd2	2.275(3)	O52—Gd2—O3	76.75(10)
O17—Gd2	2.433(3)	O19—Gd2—O3	79.98(10)
O18—Gd2	2.433(3)	O18—Gd2—O3	71.75(9)
O19—Gd2	2.418(3)	O17—Gd2—O3	133.49(10)
O26—Gd1	2.275(3)	O4—Gd2—O3	52.27(8)
O27—Gd1	2.394(3)	O6^{i}—Gd3—O5	89.63(9)
O28—Gd1	2.412(3)	O6^{i}—Gd3—O7	90.02(10)
O29—Gd1	2.389(3)	O5—Gd3—O7	147.56(10)
O30—Gd1	2.474(3)	O6^{i}—Gd3—O9	151.33(10)
O31—Gd1	2.400(3)	O5—Gd3—O9	79.44(10)
O35—Gd4	2.322(3)	O7—Gd3—O9	85.56(10)
O36—Gd4	2.357(3)	O6^{i}—Gd3—O8	77.8(1)
O37—Gd1	2.465(3)	O5—Gd3—O8	75.82(10)
O38—Gd1	2.466(3)	O7—Gd3—O8	72.41(10)
O41—Gd4	2.401(3)	O9—Gd3—O8	73.85(10)
O42—Gd4^{vii}	2.307(3)	O6^{i}—Gd3—O10	83.40(12)
O43—Gd4	2.524(3)	O5—Gd3—O10	69.80(11)
O44—Gd4	2.432(3)	O7—Gd3—O10	142.24(10)
O45—Gd4	2.882(4)	O9—Gd3—O10	116.53(12)
O46—Gd4	2.334(3)	O8—Gd3—O10	140.69(11)
O52—Gd2	2.366(3)	O6^{i}—Gd3—O11	78.76(9)
O26—Gd1—O29	104.50(13)	O5—Gd3—O11	140.01(10)
O26—Gd1—O27	94.00(11)	O7—Gd3—O11	71.34(9)
O29—Gd1—O27	152.60(12)	O9—Gd3—O11	125.83(9)
O26—Gd1—O31	144.46(11)	O8—Gd3—O11	136.38(9)
O29—Gd1—O31	80.55(12)	O10—Gd3—O11	70.91(10)
O27—Gd1—O31	72.75(11)	O6^{i}—Gd3—O12	131.74(9)
O26—Gd1—O28	73.43(11)	O5—Gd3—O12	123.73(9)
O29—Gd1—O28	80.96(12)	O7—Gd3—O12	78.74(10)
O27—Gd1—O28	85.28(11)	O9—Gd3—O12	75.04(10)
O31—Gd1—O28	72.72(9)	O8—Gd3—O12	138.69(11)
O26—Gd1—O37	74.61(12)	O10—Gd3—O12	78.32(12)
O29—Gd1—O37	125.60(11)	O11—Gd3—O12	53.10(8)

O27—Gd1—O37	78.44(10)	O42^{vii}—Gd4—O35	74.12(11)
O31—Gd1—O37	131.31(10)	O42^{vii}—Gd4—O46	154.78(11)
O28—Gd1—O37	142.81(10)	O35—Gd4—O46	129.90(11)
O26—Gd1—O38	80.95(11)	O42^{vii}—Gd4—O36	76.74(11)
O29—Gd1—O38	72.69(11)	O35—Gd4—O36	130.6(1)
O27—Gd1—O38	131.11(10)	O46—Gd4—O36	88.71(10)
O31—Gd1—O38	132.7(1)	O42^{vii}—Gd4—O41	123.45(11)
O28—Gd1—O38	137.02(10)	O35—Gd4—O41	78.51(11)
O37—Gd1—O38	53.19(9)	O46—Gd4—O41	74.83(11)
O26—Gd1—O30	147.65(12)	O36—Gd4—O41	85.59(11)
O29—Gd1—O30	86.70(13)	O42^{vii}—Gd4—O44	86.83(13)
O27—Gd1—O30	88.28(12)	O35—Gd4—O44	78.05(13)
O31—Gd1—O30	66.57(11)	O46—Gd4—O44	90.98(13)
O28—Gd1—O30	138.86(11)	O36—Gd4—O44	138.75(12)
O37—Gd1—O30	74.27(12)	O41—Gd4—O44	133.83(12)
O38—Gd1—O30	73.50(11)	O42^{vii}—Gd4—O43	82.30(13)
O16—Gd2—O15	93.83(10)	O35—Gd4—O43	140.80(13)
O16—Gd2—O52	86.66(11)	O46—Gd4—O43	73.42(13)
O15—Gd2—O52	72.1(1)	O36—Gd4—O43	70.77(12)
O16—Gd2—O19	84.14(11)	O41—Gd4—O43	140.44(13)
O15—Gd2—O19	150.43(10)	O44—Gd4—O43	69.68(14)
O52—Gd2—O19	136.89(9)	O42^{vii}—Gd4—O45	138.67(10)
O16—Gd2—O18	153.1(1)	O35—Gd4—O45	70.24(10)
O15—Gd2—O18	73.03(10)	O46—Gd4—O45	60.79(10)
O52—Gd2—O18	110.32(12)	O36—Gd4—O45	143.78(10)
O19—Gd2—O18	95.83(12)	O41—Gd4—O45	68.73(10)
O16—Gd2—O17	79.80(11)	O44—Gd4—O45	66.07(12)
O15—Gd2—O17	78.17(10)	O43—Gd4—O45	113.57(12)

ATG curves of disodium salt of ligand H_2nip

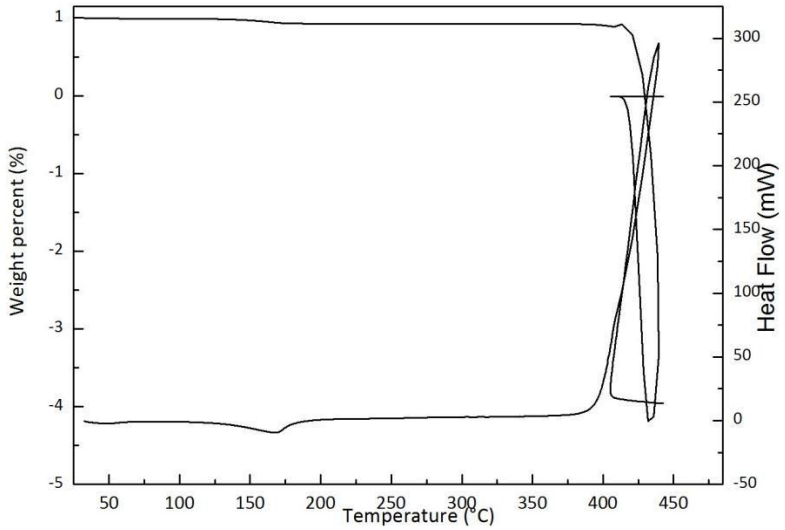

TGA/TDA curves for the microcrystalline powder of Nanip

4. Ligand Hcpb

XPRD patterns of Eu/Gd compounds

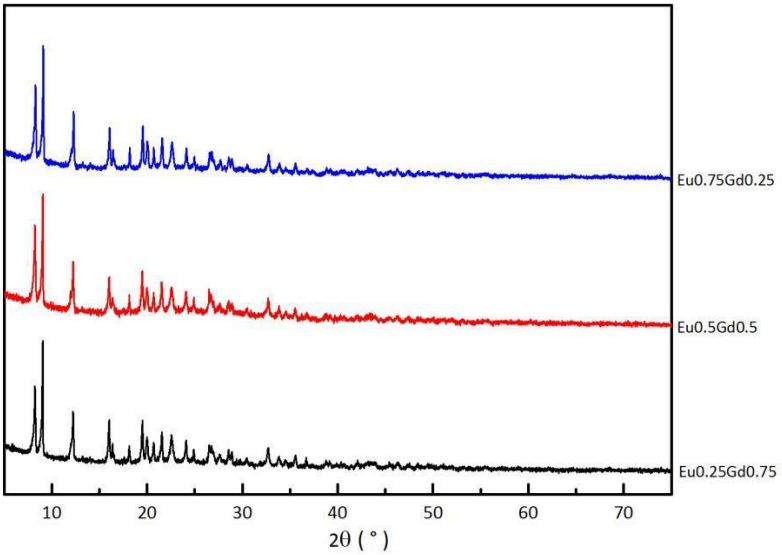

XPRD patterns of microcrystalline powders for mixte Eu/Gd compounds.

Crystallographic data

4.1 $[La(cpb)_3(H_2O)_2]_\infty$

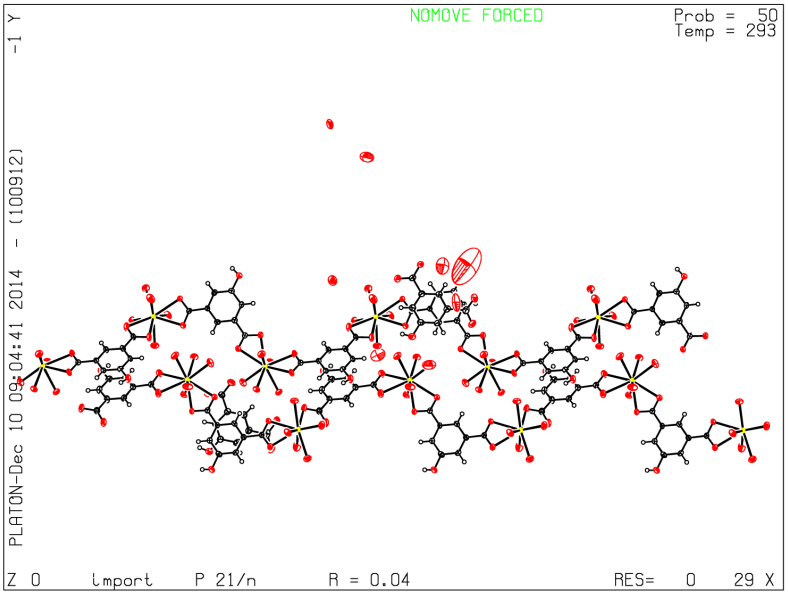

Table 4.1a Atomic parameters for $[La(cpb)_3(H_2O)_2]_\infty$

Atom	x/a	y/b	z/c	Atom	x/a	y/b	z/c
La01	0.87957(1)	0.92510(5)	0.38065(1)	C3	0.7706(2)	1.2628(9)	0.4910(2)
O1	0.6800(3)	1.2942(8)	0.6212(2)	C4	0.7567(2)	1.4562(8)	0.4452(2)
O2	0.6730(2)	1.7382(7)	0.6081(2)	C5	0.7181(2)	1.6650(9)	0.4439(2)
O3	0.80029(19)	1.2208(7)	0.38734(19)	C6	0.6942(2)	1.6782(9)	0.4891(2)
O4	1.00415(17)	0.8360(7)	0.43395(17)	C7	1.0778(2)	0.9825(9)	0.3950(2)
O6	0.9888(2)	0.2895(7)	0.04968(19)	C8	1.0587(2)	0.7870(9)	0.3486(2)
O7	0.9754(2)	0.7328(7)	0.0486(2)	C9	1.0816(2)	0.7865(9)	0.3026(2)
O8	1.1559(2)	1.2222(7)	0.22641(19)	C10	1.1214(2)	0.9854(9)	0.3001(2)
O9	1.1468(2)	0.7796(7)	0.2136(2)	C11	1.1389(2)	1.1810(9)	0.3466(2)
O10	0.79074(19)	0.6416(7)	0.37301(18)	C12	1.1185(2)	1.1782(9)	0.3940(2)
O11	0.7771(2)	0.9995(9)	0.2687(2)	C13	0.9173(2)	0.4414(8)	0.2304(2)
O12	0.91279(18)	0.9014(7)	0.50241(17)	C14	0.9566(2)	0.2554(9)	0.2232(2)
O13	0.94255(16)	1.3762(6)	0.44222(15)	C15	0.9735(2)	0.2758(10)	0.1733(2)
O14	0.9118(2)	1.2034(7)	0.3142(2)	C16	0.9526(2)	0.4827(9)	0.1299(2)
O15	0.8807(2)	0.6107(7)	0.30263(18)	C17	0.9131(2)	0.6684(9)	0.1381(2)
B1	0.9735(3)	0.5031(11)	0.0749(3)	C18	0.8956(2)	0.6483(9)	0.1876(2)
B2	1.1426(3)	0.9942(11)	0.2453(3)	C22	0.9019(2)	0.4171(9)	0.2863(2)
B3	0.6854(3)	1.5053(11)	0.5895(3)	C23	0.7849(2)	1.4390(8)	0.3988(2)
C1	0.7089(2)	1.4852(9)	0.5359(2)	C022	1.0549(2)	0.9745(9)	0.4456(2)
C2	0.7473(2)	1.2800(9)	0.5359(2)				

Table 4.1b Selected bond lengths (Å) and angles (°) for $[La(cpb)_3(H_2O)_2]_\infty$

Atoms	d (Å) or Angle (°)	Atoms	d (Å) or Angle (°)
O3—La01	2.440(3)	O14—La01—O4	79.36(13)
O4—La01	2.540(4)	O3—La01—O12	78.25(13)
O10—La01	2.447(3)	O10—La01—O12	81.21(12)
O11—La01	2.561(4)	O15—La01—O12	132.97(12)
O12—La01	2.559(3)	O14—La01—O12	134.35(13)
O13—La01	2.778(3)	O4—La01—O12	77.40(11)
O14—La01	2.477(3)	O3—La01—O11	67.97(14)
O15—La01	2.458(3)	O10—La01—O11	72.40(13)
O1—B3	1.365(7)	O15—La01—O11	71.29(14)
O2—B3	1.366(7)	O14—La01—O11	71.11(14)
O6—B1	1.382(7)	O4—La01—O11	141.89(12)
O7—B1	1.359(7)	O12—La01—O11	140.71(13)
O8—B2	1.355(7)	O3—La01—O13	69.16(11)
O9—B2	1.371(7)	O10—La01—O13	139.31(11)
O3—La01—O10	77.09(13)	O15—La01—O13	139.76(11)
O3—La01—O15	137.86(13)	O14—La01—O13	65.59(11)
O10—La01—O15	80.89(12)	O4—La01—O13	73.92(11)
O3—La01—O14	96.72(13)	O12—La01—O13	70.43(10)
O10—La01—O14	142.54(14)	O11—La01—O13	112.92(13)
O15—La01—O14	79.76(12)	O7—B1—O6	117.1(4)
O3—La01—O4	140.78(12)	O8—B2—O9	117.7(4)
O10—La01—O4	128.13(12)	O1—B3—O2	117.8(5)
O15—La01—O4	80.35(12)		

4.2 [Tb(cpbOH)$(H_2O)_2$, (cpb)]$_\infty$

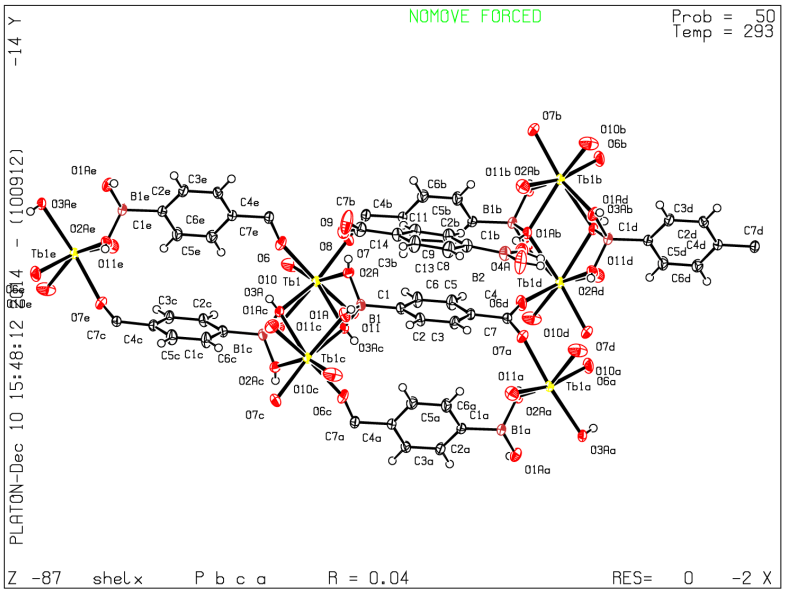

Table 4.2a Atomic parameters for [Tb(cpbOH)$(H_2O)_2$, (cpb)]$_\infty$

Atom	x/a	y/b	z/c	Atom	x/a	y/b	z/c
Tb1	0.21744(2)	0.99314(2)	0.44942(2)	C3	-0.0282(5)	0.70953(17)	0.59041(18)
O1A	-0.0291(4)	0.93650(13)	0.59987(14)	C4	0.0469(4)	0.67635(16)	0.54171(17)
O2A	0.2126(4)	0.93124(13)	0.54107(14)	C5	0.1262(5)	0.71444(18)	0.4971(2)
O3A	0.0249(3)	1.06786(12)	0.50881(12)	C6	0.1270(5)	0.78548(18)	0.5010(2)
O4A	0.2997(4)	0.58168(14)	0.64675(15)	C7	0.0416(5)	0.60037(17)	0.53552(18)
O5A	0.1830(5)	0.58584(15)	0.74775(18)	C8	0.2770(5)	0.69678(19)	0.70079(18)
O6	0.3593(4)	1.07202(13)	0.50099(15)	C9	0.3476(5)	0.73251(18)	0.6523(2)
O7	0.4396(3)	0.93206(13)	0.43444(14)	C10	0.3622(5)	0.80341(18)	0.65281(19)
O8	0.3388(4)	0.94939(13)	0.65497(14)	C11	0.3073(5)	0.84018(18)	0.70423(18)
O9	0.3198(5)	0.94715(15)	0.75728(16)	C12	0.2371(6)	0.80577(19)	0.7533(2)
O10	0.3436(4)	1.04452(18)	0.36269(16)	C13	0.2214(6)	0.7350(2)	0.7514(2)
O11	0.1232(4)	0.91438(14)	0.37181(14)	C14	0.3216(5)	0.91719(19)	0.7054(2)
C1	0.0504(4)	0.82021(16)	0.54895(17)	B1	0.0556(5)	0.90233(18)	0.5487(2)
C2	-0.0255(5)	0.78074(17)	0.59401(19)	B2	0.2517(6)	0.6172(2)	0.6986(2)

Table 4.1b Selected bond lengths (Å) and angles (°) for $[Tb(cpbOH)(H_2O)_2, (cpb)]_\infty$

Atoms	d (Å) or Angle (°)	Atoms	d (Å) or Angle (°)
Tb1—O6	2.253(3)	O6—Tb1—O11	163.36(12)
Tb1—O7	2.270(3)	O7—Tb1—O11	81.23(11)
Tb1—O2A	2.306(3)	O2A—Tb1—O11	104.28(10)
Tb1—O1A^{i}	2.369(3)	O1A^{i}—Tb1—O11	80.48(10)
Tb1—O10	2.373(3)	O10—Tb1—O11	83.27(12)
Tb1—O11	2.405(3)	O6—Tb1—O3A	73.26(11)
Tb1—O3A	2.545(3)	O7—Tb1—O3A	156.41(10)
Tb1—O3A^{i}	2.556(3)	O2A—Tb1—O3A	82.18(9)
B1—O2A	1.469(5)	O1A^{i}—Tb1—O3A	56.48(9)
B1—O1A	1.475(5)	O10—Tb1—O3A	116.37(10)
B1—O3A^{i}	1.527(5)	O11—Tb1—O3A	119.67(10)
O4A—B2	1.372(5)	O6—Tb1—O3A^{i}	125.87(10)
O5A—B2	1.353(6)	O7—Tb1—O3A^{i}	119.06(9)
O6—Tb1—O7	88.65(11)	O2A—Tb1—O3A^{i}	56.15(10)
O6—Tb1—O2A	87.20(11)	O1A^{i}—Tb1—O3A^{i}	82.72(10)
O7—Tb1—O2A	81.92(10)	O10—Tb1—O3A^{i}	147.33(11)
O6—Tb1—O1A^{i}	100.89(10)	O11—Tb1—O3A^{i}	70.77(9)
O7—Tb1—O1A^{i}	144.47(10)	O3A—Tb1—O3A^{i}	64.27(9)
O2A—Tb1—O1A^{i}	132.21(11)	O2A—B1—O1A	111.1(3)
O6—Tb1—O10	81.27(12)	O2A—B1—O3A^{i}	100.2(3)
O7—Tb1—O10	74.30(11)	O1A—B1—O3A^{i}	101.8(3)
O2A—Tb1—O10	153.71(11)	O5A—B2—O4A	122.1(4)
O1A^{i}—Tb1—O10	73.50(11)		

ATG curves of Family 1 and sodium salt of ligand Hcpb

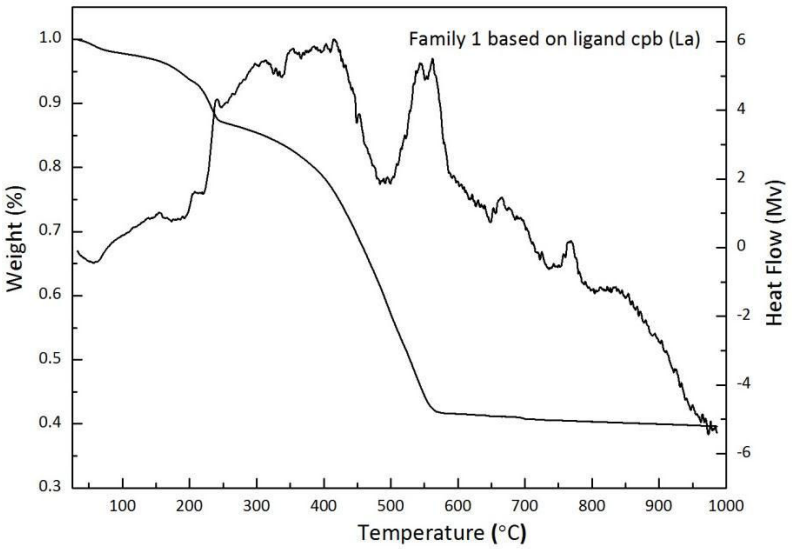

TGA/TDA curves for microcrystalline powders of Family 1 (La)

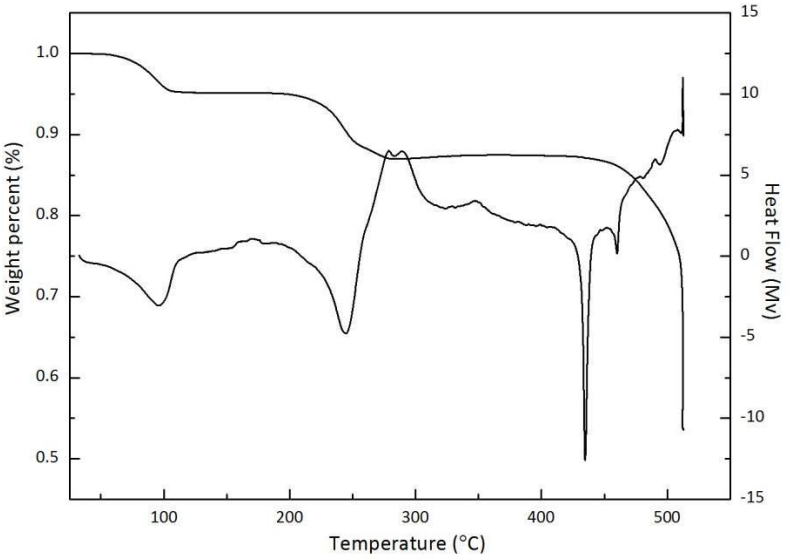

TGA/TDA curves for the microcrystalline powder of Nacpb, $0.5H_2O$.

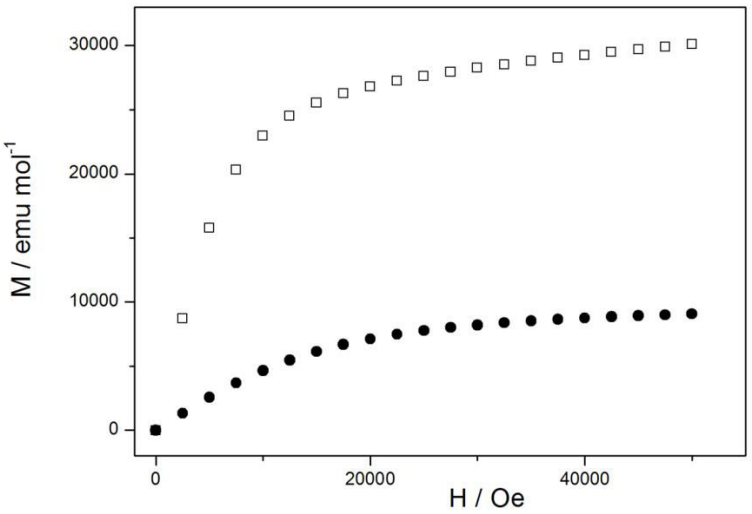

Field dependence of the magnetization for $[Dy(cpbOH)(H_2O)_2,(cpb)]_\infty$ (squares) and $[Yb(cpbOH)(H_2O)_2,(cpb)]_\infty$ (dots).

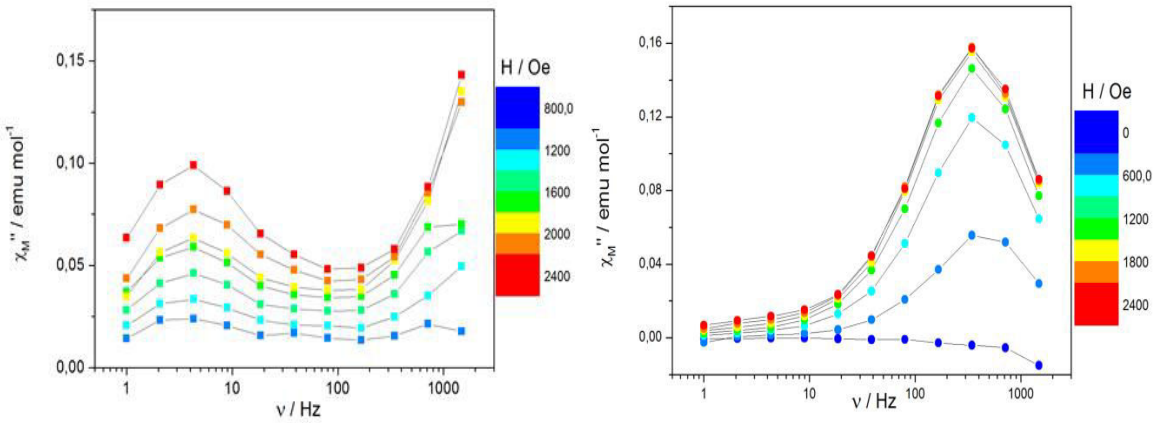

Frequency dependence of the out-of phase component of the magnetic susceptibility (χ_M''") for $[Dy(cpbOH)(H_2O)_2,(cpb)]_\infty$ (left) and $[Yb(cpbOH)(H_2O)_2,(cpb)]_\infty$ (right) for several static magnetic fields (see color mapping).

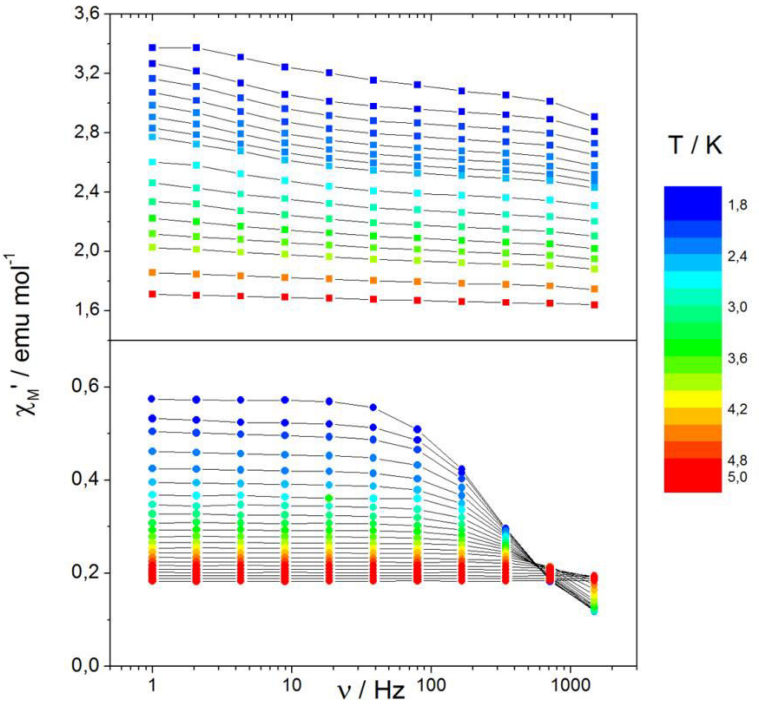

Frequency dependence of the in-phase component of the magnetic susceptibility (χ_M'') for $[Dy(cpbOH)(H_2O)_2,(cpb)]_\infty$ (top) and $[Yb(cpbOH)(H_2O)_2,(cpb)]_\infty$ (bottom) between 1.8 and 5K.

Table Extracted values from the fitting of χ_M'' vs frequency curves of $[Yb(cpbOH)(H_2O)_2,(cpb)]_\infty$

T (K)	τ (μs)
1.8	525.6
1.9	495.5
2.0	457.3
2.2	400.3
2.4	348.9
2.6	310.4
2.8	296.2
3.0	254.8
3.2	224.3
3.4	199.8
3.6	174.7

Table Extracted values from the fitting of χ_M'' vs frequency curves of $[Dy(cpbOH)(H_2O)_2,(cpb)]_\infty$

T (K)	τ (μs)
1.8	32258
1.9	36306
2.0	36903
2.1	38185
2.2	37895
2.3	37650
2.4	37110

Table Extracted values from the Argand plot of $[Yb(cpbOH)(H_2O)_2,(cpb)]_\infty$

T (K)	χ_s (emu.mol^{-1})	χ_T (emu.mol^{-1})	α	R
1.8	0.0784	0.4473	0.0646	0.99674
2.0	0.07034	0.42518	0.08106	0.99487
2.2	0.06724	0.38912	0.07436	0.99569
2.4	0.06195	0.3592	0.07302	0.99658
2.6	0.052	0.33582	0.10276	0.98895
3.0	0.05961	0.29366	0.04883	0.99572
3.2	0.05661	0.27682	0.04861	0.99694
3.4	0.056	0.26191	0.04415	0.99761
3.6	0.05472	0.249	0.03339	0.99728

INSA de RENNES
Service des Formations

AVIS DU JURY SUR LA REPRODUCTION DE LA THESE SOUTENUE

Titre de la thèse:
Heterometallic coordination polymers : toward luminescence modulation

Nom Prénom de l'auteur : FAN XIAO

Membres du jury :
- Madame SIMONNET Corine
- Monsieur LE Eric
- Monsieur GUILLOU Olivier
- Monsieur MIALANE Pierre

Président du jury : M. Pierre MIALANE

Date de la soutenance : 13 Mars 2015

Reproduction de la these soutenue

X Thèse pouvant être reproduite en l'état
Thèse pouvant être reproduite après corrections suggérées

Fait à Rennes, le 13 Mars 2015

Signature du président de jury

Le Directeur,

M'hamed DRISSI